

RIKAGAKU KENKYUSHO

the Institute of Physical and Chemical Research

Wako-shi, Saitama Pref., JAPAN

'80

IPCR cyclotron
Progress Report 1980

Vol. 14

IPCR Cyclotron Progress Report

Vol. 14

The Institute of Physical and Chemical Research
"RIKAGAKU KENKYUSHO" Wako-shi, Saitama, 351 JAPAN
December, 1980

Editors

F. Ambe	Y. Gono
A. Hashizume	Y. Hattori
H. Kamitsubo	T. Nomura
M. Odera	M. Uda
T. Wada	

This volume contains recent information of the IPCR Cyclotron, informal reports and abstracts of papers which will be published at scientific meetings or in publications by staff members, guests, and visitors.

All rights reserved. This report or any part thereof may not be reproduced in any form (including photostatic or microfilm form) without written permission from the publisher.

CONTENTS

	Page
1. INTRODUCTION	1
2. MACHINE OPERATION	2
3. MACHINE DEVELOPMENT AND ACCELERATOR PHYSICS	
3-1. Improved Heavy Ion Source for the Cyclotron	4
3-2. Automatic Frequency Controller of the Cyclotron	6
3-3. Electromotive Slit in the Beam Transport System of the Cyclotron	9
3-4. Present Status of the Baby Cyclotron at the Nakano Hospital	11
4. NUCLEAR PHYSICS	
Scattering and Reactions	
4-1. Analyzing Power-Polarization Inequality in the Inelastic Scattering of Protons on ^{12}C at Incident Energies from 22.0 to 29.0 MeV	13
4-2. Final State Interaction in Heavy Ion Reactions	16
4-3. Study of α -Particle Emission in $^{14}\text{N} + ^{159}\text{Tb}$ Collision I	19
4-4. Study of α -Particle Emission in $^{14}\text{N} + ^{159}\text{Tb}$ Collision II	22
4-5. Angular Momentum Transfer and Alignment Following Preequilibrium α Emission in the $^{209}\text{Bi} + ^{14}\text{N}$ Reaction at 115 MeV	25
4-6. Polarization of Preequilibrium Proton Emission in the $^{93}\text{Nb} + ^{14}\text{N}$ Reaction	28
4-7. Spin Alignment in Heavy Ion Reaction	31
4-8. Reactions between ^{20}Ne and ^{50}Cr	34
4-9. Recoil Range Distributions in the Reaction Induced by 115 MeV ^{14}N on ^{62}Ni	37
4-10. Correlation between the Fragment Mass and the Angular Anisotropy in the Proton-Induced Fission of ^{232}Th	40
4-11. Friction Tensors for Ar + Au and Cu + Au	44
4-12. Numerical Analysis of the $^{63}\text{Cu} + ^{197}\text{Au}$ Reaction Based on the Linear Response Theory	47

4-13.	Semiclassical Treatment of the Direct Reactions Induced by Heavy Ions II.	50
4-14.	Proton Inelastic Scattering to the (1^+ , T=1; 15.1 MeV) State in ^{12}C	53
4-15.	Perturbation Theory of Mass Transport in Nuclear Collision	56
5.	NUCLEAR PHYSICS	
	Nuclear Spectroscopy and Instrumentation	
5-1.	High Spin States in ^{158}Yb	59
5-2.	Calculation of Widths of Hole Analog States	61
5-3.	A Double Scattering Proton Polarimeter	64
6.	ATOMIC AND SOLID-STATE PHYSICS	
6-1.	X-Rays Following Multiple Inner-Shell Ionization (5)	67
6-2.	A Target Chamber for X-Ray-Angular-Distribution Measurement	70
6-3.	Kr $K\beta/K\alpha$ X-Ray Intensity Ratio by 6 MeV/amu Ion Bombardment	72
6-4.	Chemical Effect in Cu L X-Ray Satellite Spectra	74
6-5.	Energy Straggling of C Ions in Metal Foils and Foil Non-Uniformity Effect	77
6-6.	Helium Embrittlement in Precipitation-hardenable Alloys	79
6-7.	Backward Secondary Electron Emission from Al, Cu, Ag, and Au Targets under High Energy N^{7+} and N^{4+} Ion Bombardments	82
6-8.	Measurements of the Compton Profile and Angular Correlation of Positron Annihilation Radiations in Amorphous $\text{Mg}_{70}\text{Zn}_{30}$	84
6-9.	^{119}Sn Emission Mössbauer Study of ^{119}Sb Adsorbed on $\alpha\text{-Fe}_2\text{O}_3$	86
6-10.	X-Rays Induced by Collisions between 110 MeV Ne Ions and Gases	88
7.	RADIOCHEMISTRY AND NUCLEAR CHEMISTRY	
7-1.	Chemical Separation of ^{18}F in the ^3He Activation Analysis of Oxygen	91
7-2.	Recoil Range of ^{18}F Formed by Various Reactions	93

	Page
7-3. Heat Treatment Behavior of Oxygen in Silicon as Measured by Charged Particle Activation	94
7-4. Isomer Shift of ^{119}Sn in Binary Compounds of the Elements from Indium to Iodine	96
7-5. A Mössbauer Emission Study of Defect ^{119}Sn Atoms in Proton- and α -Irradiated SnSe	98
8. RADIATION CHEMISTRY AND RADIATION BIOLOGY	
8-1. Inactivation of Ribonuclease A in Solution by N-Ion Beam	101
8-2. Inactivation of Cultured Normal Human Fibroblasts, IMR-90, Cells with Nitrogen Ions Accelerated in the Cyclotron	102
9. RADIATION MONITORING	
9-1. Routine Monitoring	104
9-2. Leakage-Radiation Measurement at the Underground Passage	106
10. HEAVY ION LINEAR ACCELERATOR PROJECT	
10-1. Status of RILAC	108
10-2. Control System	110
10-3. Design of ECR Ion Source	113
10-4. System for Beam Monitoring with Beam Slit and Stopper	115
10-5. Acceleration Test of the First Cavity	117
10-6. Design of RF Control System	120
10-7. Measurement for Characteristics of RILAC RF System and Excitation Test of Resonators	123
10-8. Magnets for Beam Transport System	126
10-9. Vacuum System of the Beam Transport Lines	129
10-10. Heavy Ion Source for the Linac	132
10-11. Power Supply for Heavy Ion Source	135

10-12.	Multi-Wire Beam Emittance Monitor and Beam Profile Monitor	138
10-13.	A 100 cm Scattering Chamber	141
10-14.	Design of an Electron Spectrometer	143
10-15.	Electron Energy Analyzer	146
10-16.	Design of an Apparatus for RILAC-Beam Irradiation of Biological Samples	148
10-17.	Beam-Foil Spectroscopy	149
10-18.	Multichannel Detection in Normal-Incidence Vacuum Ultraviolet Region	151
10-19.	Spherical Target Chamber for Heavy-Ion Implantation	154
10-20.	On-line Data Processing System at RILAC	156
10-21.	Beam Sharing System between Linac and Separated-Sector Cyclotron	159
11.	SEPARATED-SECTOR CYCLOTRON PROJECT	
11-1.	Status of the Separated-Sector Cyclotron in IPCR (Riken)	162
11-2.	Design of the Sector Magnet for the SSC	164
11-3.	Design Study of the Canted Injection Scheme for the IPCR SSC (I)	167
11-4.	Design Study of the Canted Injection Scheme for the IPCR SSC (II)	170
11-5.	Model Study of the Injection Bending Magnet of the IPCR SSC	173
11-6.	Magnetic Field Measuring System for the Model Injection-Bending Magnet of the SSC	176
11-7.	Microcomputer System with CAMAC for Measuring Magnetic Field of a SSC Model Magnet	179
11-8.	Design Study of RF Resonator for the SSC	182
11-9.	Design Study of Oscillator for the SSC	185

	Page
11-10. Measurement of RF Field Distribution for a Quarter Wave-Length Vertical Type Resonator	187
11-11. Some Properties of Accelerated-Beam Orbit in the Separated-Sector Cyclotron	189
11-12. Design of Beam Transport System for the IPCR SSC	192
11-13. Vacuum System of the SSC (I) Vacuum Considerations in Some Aspects	195
11-14. Vacuum System of the SSC (II) A Preliminary Design of the Vacuum Chamber for the SSC	198
11-15. Design and Operational Performance of Superconducting Coil for Model Sector Magnet of the IPCR SSC	201
11-16. Present Status of Radiation Shielding for the Riken SSC Facility	203
12. LIST OF PUBLICATIONS	207
13. LIST OF OUTSIDE USERS AND THEIR THEMES	214
14. LIST OF SEMINARS	216
15. LIST OF PERSONNEL	218
AUTHOR INDEX	223

1. INTRODUCTION

It has passed fifteen years since we had the first beam from IPCR 160 cm cyclotron and experimental studies were started. This cyclotron was the first one in Japan which was used for the studies of diverse research fields. These studies have been performed mainly by using heavy ions.

During the past one year, the cyclotron was operated in good condition as before. New developed heavy ion source was tested. An automatic RF frequency control system was installed and made the stable operation of the cyclotron possible.

A majority of research works have been carried out with heavy ions. In the field of nuclear physics, polarization of the outgoing protons from heavy ion collision was measured to get more detailed information of the reaction mechanism. Final state interaction was studied by measuring correlation of two α -particles in the heavy ion reaction. Extensive studies on theoretical analysis of the heavy ion reaction based on the linear response theory was performed in collaboration with JAERI.

X-rays following the inner shell ionization were also extensively studied. Backward secondary electron emission from metallic substances were measured by bombarding heavy ions on them. Study of radiation damage in α -particle bombardment was continued.

Charged particle activation analysis of oxygen contamination was applied to study the behavior of the oxygen on the surface of the pure silicone materials. Study of the radiation chemistry and biology was continued as before.

Construction of the heavy ion linac (Rilac) was finished last year and the beam test has been continued. Construction of the energy booster of Rilac was started in this period. Final design of the separated-sector cyclotron is now underway.

Hiromichi Kamitsubo

Hiromichi Kamitsubo
Editor

2. MACHINE OPERATION

K. Ikegami, S. Kohara, T. Kageyama, K. Ogiwara,
S. Fujita, H. Takebe, and I. Kohno

The cyclotron was operated on the 24 h a day basis during the period from Oct. 23, 1979 to Oct. 22, 1980. The total operation time of 4355.6 h is 4% (179.7 h) shorter than that of the last year. This decrease in operation time is due to some scheduled shut-down shown in Table 1, and is caused by a rise in price of electric power.

Table 2 shows the beam time allotted to various activities in this period. Although the total beam time (5478 h) was decreased by 242 h compared with that of last year, requirement for heavy ion beams continued to increase; its increase was 269 h.

Table 3 shows the distribution of the beam time among particles accelerated. In this period, the beam time of highly charged ions such as N^{5+} and Ne^{6+} was greatly increased. The metal ions as ${}^7Li^{2+}$ and ${}^{11}B^{3+}$ were newly accelerated using the sputtering metal ion source¹⁾ in this beam time.

In order to improve the performance of the heavy ion source and to shorten the time for setting up of the source, a new improved heavy ion source was developed and tested during the time of the overhaul and the periodical inspection. Furthermore, the frequency stabilizer for the radiofrequency system of the cyclotron and the slit system of the beam transport adjusted by remote control were newly installed in this period. These improvements served to make good use of the beam time.

Table 1. Machine Operation.

	Oscillator	Ion-source	Beam
Reading of time meter on Oct. 23, 1979	61899.6 (h)	65865.6 (h)	32873.1 (h)
Reading of time meter on Oct. 22, 1980	66807.1	70893.8	37228.7
Difference	4907.5	5028.2	4355.6
Percentage of 365 days	56 %	57 %	50 %

Schedule in this period			
Beam time		233 (days)	
Overhaul and installation work		59	
Periodical inspection and repair		25	
Vacation and holidays		38	
Other scheduled shut down		10	

Table 2. Scheduled beam time and subjects of activity in the period XV.

Subject		Heavy ion	Light particles	Total
Nucl. Phys.	{ Nuclear reaction	3093 (h)	0 (h)	3093 (h)
	{ In-beam spectroscopy	450	0	450
	{ RI production	24	15	39
Fields others than Nucl. Phys.	{ Nuclear chemistry	0	192	192
	{ Radiation biology	144	120	264
	{ Solid state physics	305	356	661
	{ Inner atomic shell excitation study	441	0	441
Outside users	{ Nuclear fuel study	0	132	132
	{ RI production	0	110	110
	{ Detector calibration	0	96	96
Total		4457	1021	5478
Percent in total		81 %	19 %	100 %

Maintenance, operation and engineering				
Exchange of ion source			114 (h)	
Machine inspection and repair			600 (h)	
Total			714	

Table 3. Distribution of Beam time among particles accelerated.

Particle	(h)	(%)	Particle	(h)	(%)
P	228	4.2	N ⁵⁺	1509	27.5
d	16	0.3	O ⁵⁺	117	2.1
³ He ⁺⁺	142	2.6	²⁰ Ne ⁶⁺	1257	23.0
⁴ He ⁺⁺	635	11.6	⁷ Li ²⁺	21	0.4
C ⁴⁺	402	7.3	¹¹ B ³⁺	21	0.4
N ⁴⁺	1130	20.6	Total	5478	100.0

Reference

- 1) K. Ikegami, T. Kageyama, and I. Kohno: Japan. J. Appl. Phys., 19, 1745 (1980).

3. MACHINE DEVELOPMENT AND ACCELERATOR PHYSICS

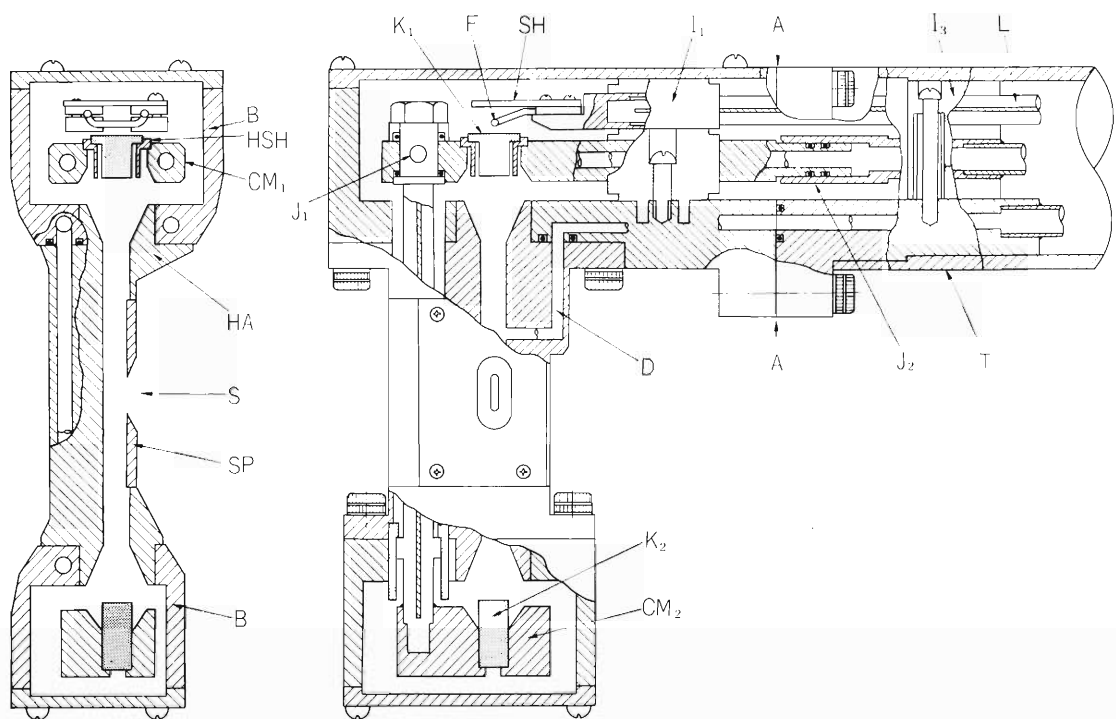
3-1. Improved Heavy Ion Source for the Cyclotron

T. Kageyama, K. Ikegami, and I. Kohno

In order to extend the life time of the heavy ion source and shorten the time to revive it we developed an improved heavy ion source for the cyclotron.

Figures 1 and 2 show a cross-sectional view and a photograph of this improved source. This ion source is supported by a single supporting tube (T), while the old type source was supported by two tubes.¹⁾ The head part of the improved source can be removed from the supporting stem at a position indicated by A in Fig. 1.

When the life time of the source is over, the head part is taken away and new one is attached in several minutes. Furthermore, this source is improved from the old one in exactness of alignment of the geometrical center of anode chimney and two cathodes (K_1 , K_2). By this



K_1 : hot cathode (W or Ta)

K_2 : reflector (W)

F: filament (W)

SH: electron shield (Mo)

CM_1 , CM_2 : cathode mount (copper,
water-cooled)

HSH: cathode heat shield (W)

SP: slit plate (Mo)

J_1 , J_2 : cooling channel joint

I_1 , I_2 , I_3 : insulator (ceramic)

D: distribution plenum

S: source aperture

L: leading tube

T: supporting tube (stainless steel)

B: anode box (copper)

HA: hot anode (copper)

Fig. 1. Cross-sectional view of the source.

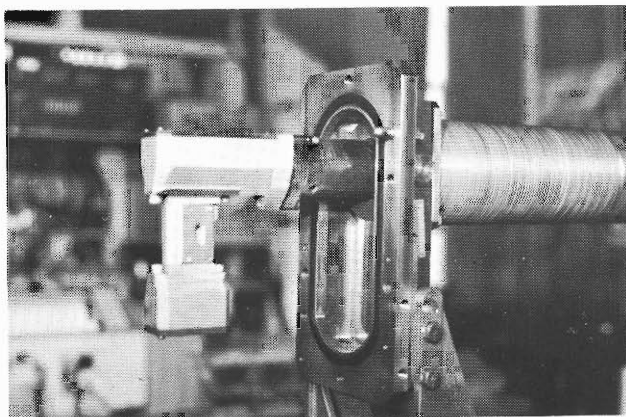


Fig. 2. A photograph of the ion source.

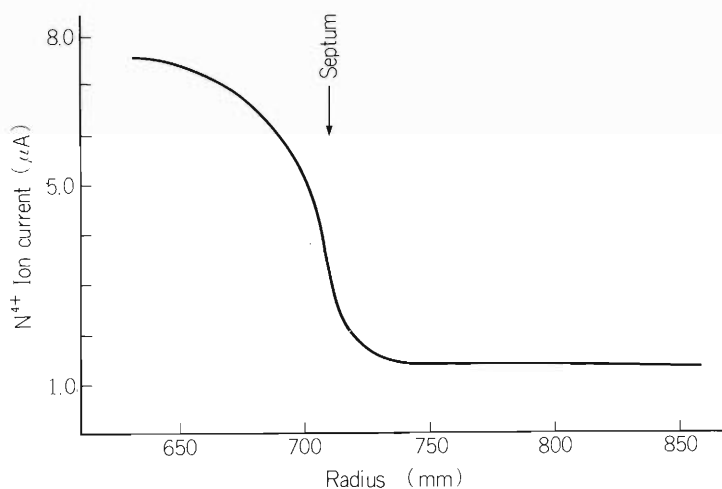


Fig. 3. A typical variation of beam intensity with radius in the cyclotron for 95 MeV N^{4+} ion.

improvement the life time of the source was extended to about twice of the old one.

Using this improved source several kinds of ions (Ne^{6+} , N^{5+} , N^{4+} , and C^{4+}) have been produced and accelerated in the cyclotron. Figure 3 shows a typical radial variation of beam intensity in the cyclotron for 95 MeV N^{4+} ions. As is shown in this figure, the intensity ratio of the external beam to the internal beam is poor (about 1/5) and this reason is being studied.

In Table 1 the results of accelerating test of several ions are summarized. At present, this source is used to accelerate Ne^{6+} ions.

Table 1. Particles, energy ranges and particle yields.

Particle	Energy (MeV)	Extracted beam current
$^{20}Ne^{6+}$	82-160	$0.2\mu A$ *
C^{4+}	49-100	$2.0\mu A$
N^{4+}	57-100	$2.0\mu A$
N^{5+}	57-125	$1.0\mu A$

* Pulsed operation.

Reference

- 1) Y. Miyazawa, I. Kohno, T. Tonuma, T. Inoue, A. Shimamura, and S. Nakajima: IPCR Cyclotron Technical Report, No. 2 (1972).

3-2. Automatic Frequency Controller of the Cyclotron

H. Takebe, K. Ogiwara, and Y. Yamada*

The RF (radio frequency) system of the cyclotron¹⁾ has a self-excited oscillator whose frequency is determined by the geometrical condition of the RF resonator. The resonant frequency drifts due to the mechanical deformation of the resonator occurred thermally in about an hour after RF power has been switched on. Figure 1 shows the frequency change by a thermal deformation of the resonant cavity in thirty minutes from the starting time of the RF power. In the first 20 min, the resonant frequency decreases by about 7 kHz, the mean decreasing rate depending on the dee voltage. The resonant frequency is changed not only by thermal deformation of the cavity but also by positions of the beam probe, deflector, ion source and the small (west) compensator, arc power strength of the ion source, and a discharge in the dee-earth gap. Therefore, the resonant frequency had to be adjusted by manual operation whenever any operating parameter was changed. In order to avoid such a complicated procedure an automatic frequency controller has been developed and equipped to the cyclotron.

A block diagram of this control system is shown in Fig. 2. BCD presets (F_p) in six digits which are set by a rotary encoder and the up-down counter are subtracted from the six digits' BCD data (F_c) of the frequency

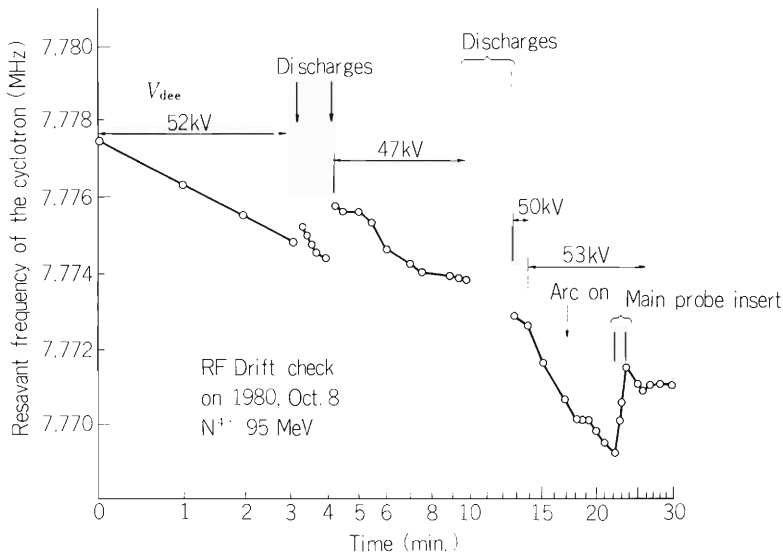


Fig. 1. Resonant frequency drifts in the first 30 min at various dee-voltage and conditions of the resonant cavity.

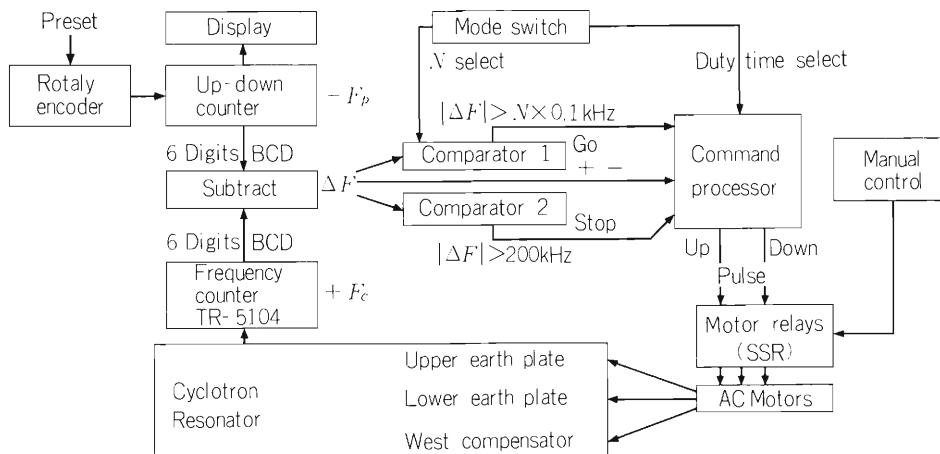


Fig. 2. Block-diagram of the automatic frequency controller.

Table 1 (a)

The command processor makes up or down signal according to N-number which is determined by the ΔF mode switch.

$\Delta F > 200$ kHz	STOP
$\Delta F > N \times 0.1$ kHz	DOWN
$ \Delta F \leq N \times 0.1$ kHz	STOP
$\Delta F < N \times 0.1$ kHz	UP
$\Delta F < 200$ kHz	STOP

$$\Delta F = F_c - F_p$$

Table 1 (b)

The position of the ΔF mode switch (N-number) is selected in accordance with the beam course and particle's energy. Sample rate of the frequency counter is set by about 0.3 sec usually in any ΔF mode.

Mode	No.1	No.2	No.3	No.4
N	2	3	4	6
Sample rate (sec)	0.2 - 0.4	0.2 - 0.4	0.3 - 0.6	0.3 - 1.0
Duty time (sec)	0.2	0.3	0.3	0.5

counter (TR5104²) of the cyclotron RF system. If the difference $\Delta F (= F_c - F_p)$ is positive with the value greater than $N \times 0.1$ kHz (N is indicated in Table 1 (b)), the up-down command processor gives a frequency lowering signal to a device which may be the upper earth plate, the lower earth plate or the west compensator in order to decrease the resonant frequency. These parameters of each mode are shown in Table 1. When $|\Delta F|$ is greater than 200 kHz, the processor commands nothing but indicates the situation by "Over" lamp because the resonator may be unusual: For instance RF discharge in the dee chamber or a parasitic oscillation is excited ($|F| > 200$ kHz).

The up-down command is transferred to the AC motor drive units as pulses shown in Fig. 3. As mechanical structures of the movable earth plates and the west compensator have a large inertia which may cause an over-shooting, the command signals should not be too long so that the device stops changing frequency before the next gate time of the frequency counter begins. The sample rate of the frequency counter and a duty time of the command pulses can be selected by a mode-switch as shown in Table 1 (b). In accordance with the beam line used, kind of accelerated particles and energy of particles, the mode switch should be selected by the operator.

This automatic frequency controller is in the form of a compact box with a simple front panel using the latest digital electronics as shown in Fig. 4. A conventional relay units and AC motor driving relays had been used to move the upper earth plate in the previous control system. They were exchanged with solid

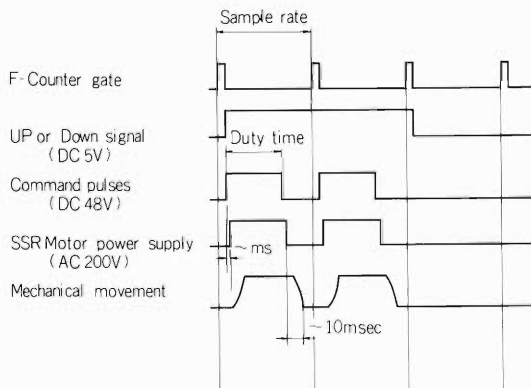


Fig. 3. Time chart of the up or down command pulses and movement of the resonating device. The command pulses of the processor should not be too long to avoid over-shooting.

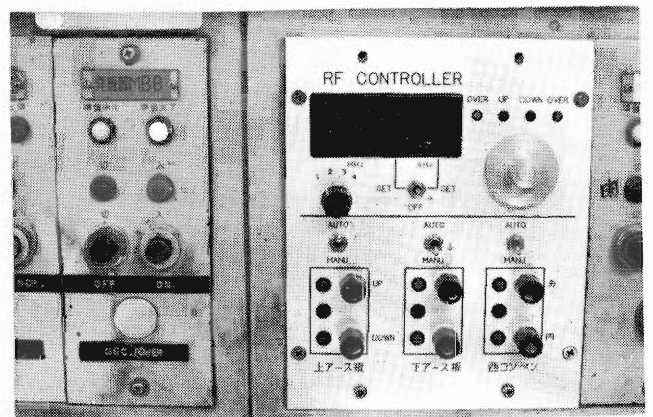


Fig. 4. A front panel of the new system equipped on the control desk.

state relays (SSR: D2W201B, I.O.R. Co.) with circuits for detection of zero-crossing phase of AC 200V. The new relay system is shown in Fig. 5.

It has been found enough to use only the upper earth plate in the automatic mode of this frequency controller to make the resonant frequency constant for any ΔF mode and in any resonant frequency (6 – 12MHz) of the cyclotron. The daily operation of the cyclotron has become much easier than before because of this device.

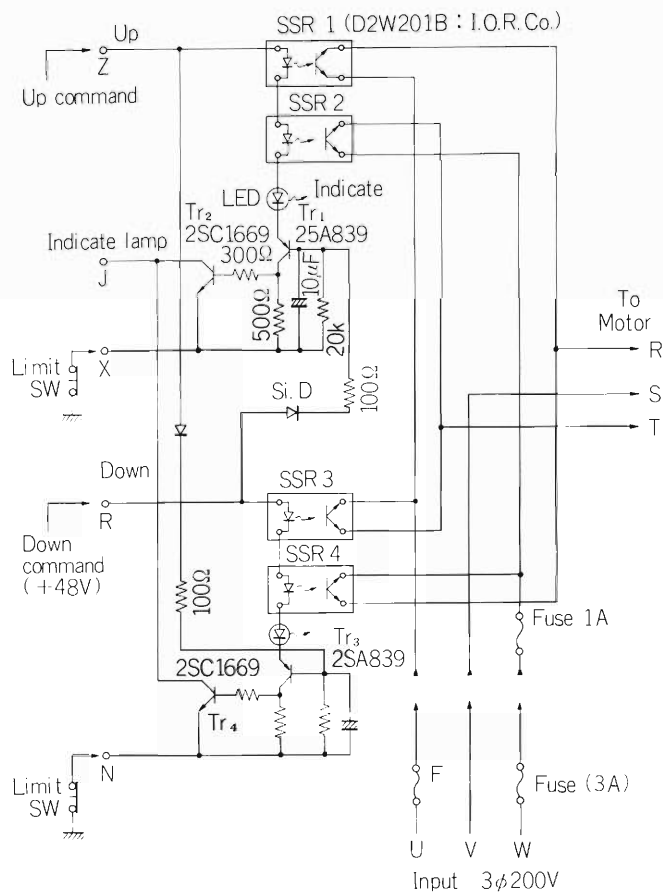


Fig. 5. Solid-state relay circuit. Up command should keep stopping another command until 7 msec after the up pulse by Tr 3 to avoid short-circuit of the AC 200 V power line; the time interval of the up and down signal of the power supply should be longer than 6.67 msec ($T = 1/(3 \times 50 \text{ Hz})$) because the delay in action by the zero-crossing circuit in the three phase of AC power supply.

References

- 1) M. Odera, Y. Chiba, T. Fujisawa, Y. Miyazawa, and O. Terajima: The Radio frequency System of the IPCR Variable Energy Multi-Particle Cyclotron; IPCR Technical Rep., 8 (1973).
- 2) TR5104, Takeda Riken BCD parallel out.

3-3. Electromotive Slit in the Beam Transport System of the Cyclotron

S. Kohara, I. Takeshita, K. Hagiwara,* and Y. Nomiya*

There are many slit boxes in the beam transport system of the cyclotron. Each slit box has four blades moved by hand operation and a beam shutter moved by electric power remotely. In the case of RI production the aperture and position of beams at the target are determined by positions of four movable blades in the slit box installed at about 200 mm in front of the target. Therefore, it is very convenient for operators and experimenters to be able to adjust the positions of four blades observing image of the aperture and position of beams on a quartz plate set at the position of the target using an ITV. For this reason we developed a new slit box which has four blades moved by electric power remotely.

Figure 1 shows a photograph of this slit box installed in the beam line for RI production. The slit system consists of a left blade, a right blade, an upper blade and a lower blade. The left blade can be moved from the center of the beam line to the left direction or outside direction up to 30 mm and to the right direction or inside direction up to 10 mm. The other blades can also be moved in a similar way. Driving speed of these blades are 0.33 mm/sec.

Figure 2 shows a photograph of the controller for the slit box. The positions of four blades are indicated by digital numbers in the front plate and several switches for operation of blades and a beam shutter are equipped. Safety circuits are provided to prevent the collision between the left and the right blade, and between the upper and the lower blade, respectively. This electromotive slit serves to make efficient use of beam time of the cyclotron.

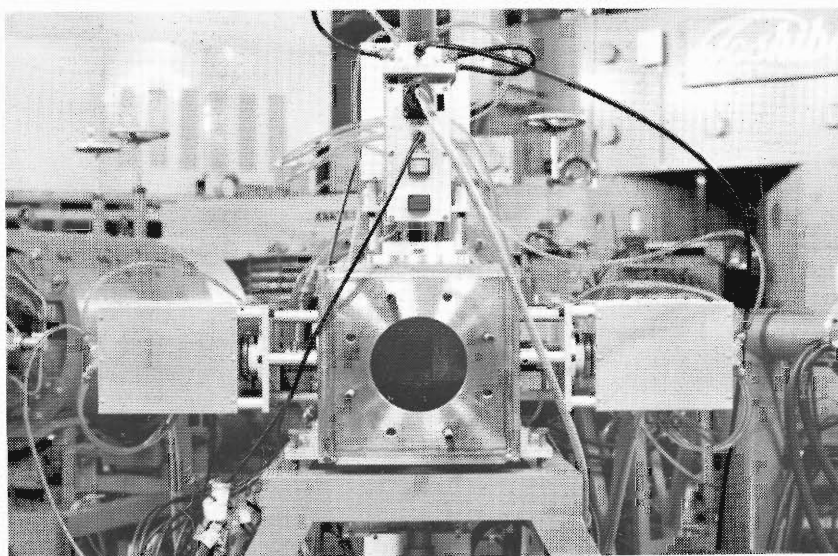


Fig. 1. Photograph of the slit box.

* Work Shop of this Institute.

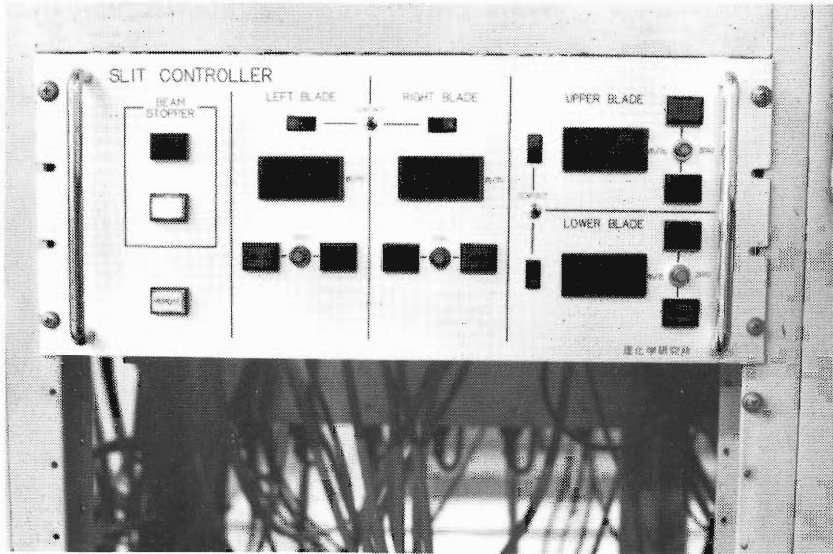


Fig. 2. Photograph of the controller for the slit box.

3-4. Present Status of the Baby Cyclotron at the Nakano Hospital

T. Karasawa, T. Nozaki, and S. Iida*

During this year, the cyclotron has been working satisfactorily for the production of radio-isotopes used in diagnosis and in experiments of labelled compounds synthesis. The beam currents at the target box were $10 \mu\text{A}$ and several μA for protons and deuterons, respectively. The beam shape has been improved by the insertion of the magnetic channel.¹⁾ Radial and

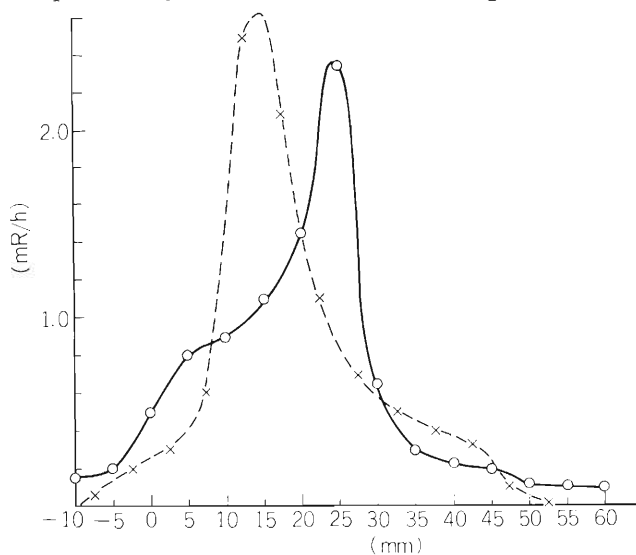


Fig. 1. Radial distributions of the beam at the target. Deflection voltages were 35 kV for ○ and 34 kV for ×.

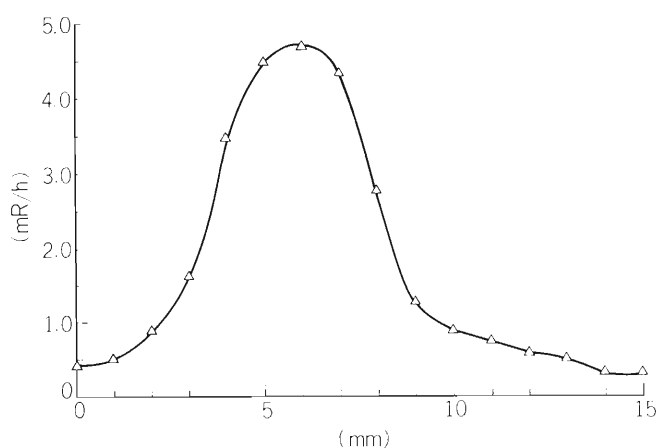


Fig. 2. Vertical distribution at the target. Copper plate was bombarded to induce $^{63}\text{Cu}(p, n)^{63}\text{Zn}$ reaction. ^{63}Zn activity was measured with position resolution of 2 mm. The radial distribution was affected by operating parameters.

* Japan Steel Work Co.

vertical beam distributions are shown in Figs. 1 and 2, respectively. Usually the aperture of the target box window is kept 5 cm in width and 2 cm in height.

One of the main features of the cyclotron is the self radiation shielding.²⁾ Radiation levels around the cyclotron room were surveyed.³⁾ It can be estimated from the result that the radiation level is below 10 mrem/week for 40 h operation per week with 30 μ A proton beam at all measurement points except at those nearer than 0.5 m from the wall of the cyclotron room.

A water-cooled cone of the ion source and an oil-cooled electrode of the deflector are under preparation for higher beam intensities and more reliable operation. Those improvements have already been applied satisfactorily to the second Baby Cyclotron.

A mixture of glucose-¹¹C and fructose-¹¹C has been routinely prepared by photosynthesis and used for diagnosis of lung cancer. A glass vessel containing spinach leaf pieces (0.5 g) and ¹¹CO₂ prepared by the cyclotron is illuminated for 7 min, and the photosynthetic product is extracted into hot EtOH containing HCl. The extract, after removal of ether-extractable substances, is concentrated by partial evaporation by microwave heating, and treated with an anion exchange column to give a mixture of ¹¹C glucose and fructose. It takes 35 min for the total process, and from 50 mCi of the ¹¹CO₂ about 10 mCi of the product is obtained. The product is orally administered to the patient and the ¹¹C distribution in lung is examined. This ¹¹C has been found to behave differently from ¹⁹⁷Hg glutathione and ⁶⁷Ga compounds. About 60 patients have ever been submitted to this diagnosis. The photosynthetic process has been partly automatized and its complete automation is under way.

Automatic synthesizers for ¹¹C palmitic acid and ¹¹CH₃I have been set up. The distribution of ¹³NH₃ in rat brain was examined by radio-autography with its time change. A few other ¹¹C compounds were synthesized and their behaviour in experimental animals were studied.

References

- 1) T. Karasawa and T. Nozaki: *IPCR Cyclotron Progr. Rep.*, 13, 20 (1979).
- 2) T. Karasawa: Japan patent 818015, USA patent 3921019, and France patent 2209272.
- 3) T. Karasawa, T. Tanaka, and T. Yoshida: *Proc. of the 3rd Symp. on Accelerator Science and Technology*, Aug., p.93 (1980).

4. NUCLEAR PHYSICS

Scattering and Reactions

4-1. Analyzing Power-Polarization Inequality in the Inelastic Scattering of Protons on ^{12}C at Incident Energies from 22.0 to 29.0 MeV

T. Fujisawa, N. Kishida, T. Kubo,
T. Hasegawa,* M. Sekiguchi,* N. Ueda,*
M. Yasue,* Y. Wakuta,** and A. Nagao**

NUCLEAR REACTIONS $^{12}\text{C}(p, p'\gamma)$, 4.43 MeV state, $E = 22.0 - 29.0$ MeV, polarized beam; measured cross section, asymmetry, spin flip probability, spin flip asymmetry; deduced difference between asymmetry and polarization.

A large number of studies for elastic and inelastic scatterings of protons on ^{12}C has been performed over the incident energy range of about 20 to 30 MeV.^{1) - 5)} It, however, is in question whether the giant resonance of ^{12}C contributes in this energy region or not.^{3) - 5)} Spin-dependent observables are more sensitive to a reaction mechanism than cross-sections. Particularly it is important to measure the difference between analyzing power (A) and polarization (P).^{6), 7)} Direct measurement of the polarization, however, is very difficult because it requires a double scattering. Therefore, we measured the A, spin flip probability (SF) and spin flip asymmetry (SFA) simultaneously using polarized protons and deduced the (A-P) at incident energies from 22 to 29 MeV.

The observables for nucleon scatterings are expressed as follows if the Z-axis is chosen along the normal to the scattering plane:

$$\sigma_0 = (\sigma_{++} + \sigma_{+-} + \sigma_{-+} + \sigma_{--}) / 2, \quad A = (\sigma_{++} + \sigma_{+-} - \sigma_{-+} - \sigma_{--}) / 2\sigma_0,$$

$$P = (\sigma_{++} - \sigma_{+-} + \sigma_{-+} - \sigma_{--}) / 2\sigma_0, \quad \text{SF} = (\sigma_{+-} + \sigma_{-+}) / 2\sigma_0,$$

$$\text{SFA} = (\sigma_{+-} - \sigma_{-+}) / (\sigma_{+-} + \sigma_{-+}) = (A - P) / (2 \cdot \text{SF}),$$

where σ_{+-} is the partial differential cross section for scattering from an incoming spin-up state (+) to a final spin-down state (-).⁸⁾ It is easy to see from the above equations that the measurement of spin flip probability using a polarized beam determines individually $\sigma_{\alpha\beta}$ and so all of the observables in these equations are deduced.⁸⁾

The measurement was carried out by using the $(pp'\gamma)$ method, i.e., by measuring the angular correlation between protons scattered inelastically from the first 2^+ excited state and the E2 ($2^+ \rightarrow 0^+$ ground) de-excitation γ -rays emitted perpendicularly to the scattering plane.⁹⁾ Polarized protons were obtained from an atomic beam type polarized ion source and were accelerated by the SF Cyclotron at the Institute for Nuclear Study, University of Tokyo. The ion source was constructed at the Institute of Physical and Chemical Research. The beam current on the target was about 10 nA and the beam polarization was about 50 %. The beam polarization was reversed about every one minute by the RF transition units of the ion source which were controlled automatically with signal from a beam current integrator to eliminate systematic errors. The ^{12}C target was a self-supporting foil of natural carbon with thickness of 5.65 mg/cm^2 . The γ -rays were detected with a shielded NaI (Tl) crystal of $7.6 \text{ cm} \times 7.6 \text{ cm}$ mounted on a 56 AVP photomultiplier. This detector had a lead slit of an aperture of $57 \text{ mm}\phi$ with 10 cm of thickness at position 20 cm from the target. The scattered protons were

* Institute for Nuclear Study, University of Tokyo.

** Kyushu University.

detected by four pairs of solid state detectors which were set symmetrically on both sides of the beam direction. A defining slit of 10 mm ϕ was placed in front of each detector at a position 10 cm from the target. In Fig. 1 the data obtained are shown. It was remarkable that the SFA and the (A-P) have such large values and change drastically with the incident energy in contrast with a rather monotonous change of the inelastic scattering cross section.¹⁾ The effect of some resonance on the reaction must be strong since the (A-P) and SFA depend on interferences between partial waves of which angular momentum are different. A coupled-channel calculation with Breit-Wigner terms is in progress.

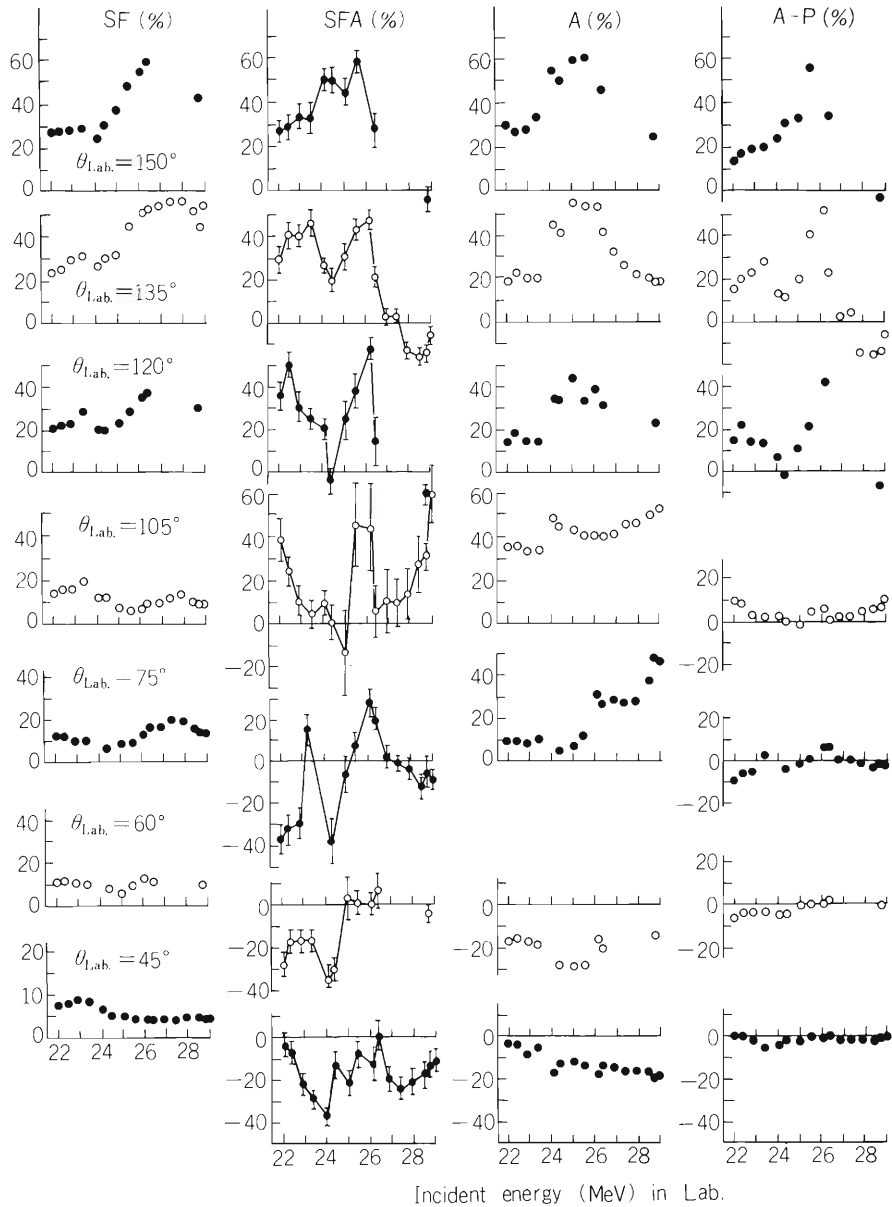


Fig. 1. Excitation curves of the spin flip probability (SF), spin flip asymmetry (SFA), analyzing power(A) and A-P in the inelastic scattering of protons on ^{12}C at the lab. scattering angles of 45°, 60°, 75°, 105°, 120°, 135°, and 150°. The line is to guide the eye.

References

- 1) J. K. Dickens, D. A. Haner, and C. N. Waddell: *Phys. Rev.*, 132, 2159 (1963).
- 2) T. Tamura and T. Terasawa: *Phys. Lett.*, 8, 41 (1964).
- 3) R. M. Craig, J. C. Dore, G. W. Greenlees, J. Lowe, and D. L. Watson: *Nucl. Phys.*, 83, 493 (1966); *ibid*, 79, 177 (1966).
- 4) H. V. Geramb, K. Amos, R. Sprickman, K. T. Knöfle, M. Rogge, D. Ingham, and C. Mayer-Boricke: *Phys. Rev. C*, 12, 1679 (1975).
- 5) R. DE. Leo, G. D'Erasmus, F. Ferrero, A. Pantaleo, and M. Pingnanelli: *Nucl. Phys. A*, 254, 156 (1975).
- 6) G. R. Satchler: *Phys. Lett.*, 19, 312 (1965); H. Sherif: *Canad. J. Phys.*, 49, 983 (1971).
- 7) C. Glashausser: *Proc. 4th Intern. Symp. on Pol. Phen. in Nucl. Reac.*, p. 333, Zurich (1975).
- 8) R. N. Boyd, D. Slater, R. Avida, H. F. Glavish, C. Glashausser, G. Bissinger, D. Davis, C. F. Haynes, and A. B. Robbins: *Phys. Rev. Lett.*, 29, 955 (1972).
- 9) F. H. Schmidt, R. E. Brown, J. B. Gerhart, and W. A. Kolasinski: *Nucl. Phys.*, 52, 353 (1964).

4-2. Final State Interaction in Heavy Ion Reactions

S. Kohmoto, M. Ishihara, H. Kamitsubo, T. Nomura,
Y. Gono, H. Utsunomiya, T. Sugitate, and K. Ieki

NUCLEAR REACTIONS $^{27}\text{Al}(^{14}\text{N}, \alpha\alpha)$, $^{93}\text{Nb}(^{14}\text{N}, \alpha\alpha)$ $E = 115$ MeV,
measured $(d^4\sigma/dE_1 d\Omega_1 dE_2 d\Omega_2)$ at $\theta_1 = \theta_2 = 50^\circ$. Final state Interaction
analysis in terms of α - α rescattering.

We have made an attempt to study the temporal and spatial size for light particle emissions in low energy (≈ 8 MeV/A) heavy-ion reactions detecting directly two light particles in coincidence mode.

Measurements were performed for the following reactions: $^{27}\text{Al}(^{14}\text{N}, \alpha\alpha)$ and $^{93}\text{Nb}(^{14}\text{N}, \alpha\alpha)$ with 115 MeV incident energy, using targets of 2.69 mg/cm² and 13.4 mg/cm², respectively. Four sets of counter telescopes which consist of 30 μm and 2000 μm Si detectors were arrayed at different azimuthal angles ϕ but with the same polar angle $\theta = 50^\circ$ with respect to the beam direction. Correlations between any two sets were measured simultaneously. Thus, correlations for 24 and 30 different $\Delta\phi$ from 22° to 180° were obtained for the $^{27}\text{Al} + ^{14}\text{N}$ and $^{93}\text{Nb} + ^{14}\text{N}$ reactions, respectively.

In the special case of $E_1 = E_2 = E$, where E_1 and E_2 are the kinetic energies of the two α -particles in the laboratory system, the relative energy E_{12} is given by $E_{12} = E \sin^2\theta (1 - \cos\Delta\phi)$

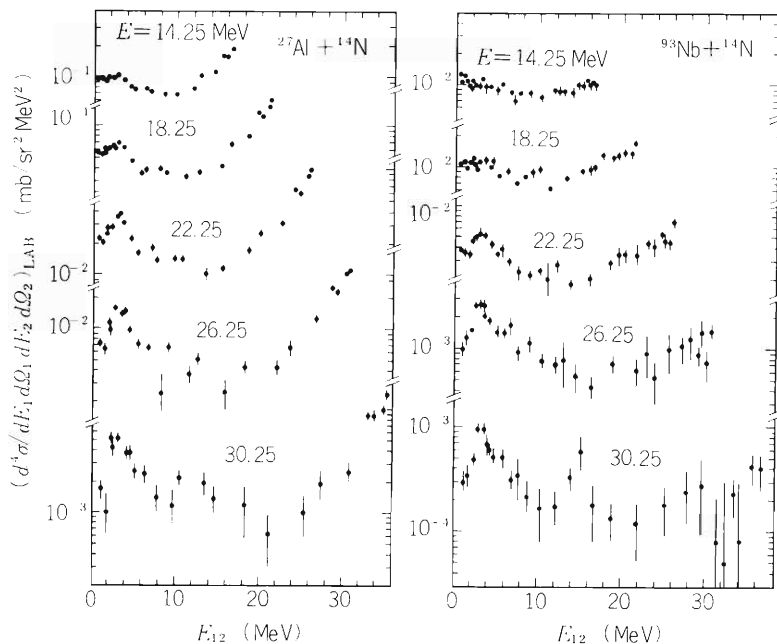


Fig. 1. Cross sections $(d^4\sigma/dE_1 d\Omega_1 dE_2 d\Omega_2)$ for the reactions $^{27}\text{Al}(^{14}\text{N}, \alpha\alpha)$ and $^{93}\text{Nb}(^{14}\text{N}, \alpha\alpha)$ at $\theta = 50^\circ$ plotted against the relative energy E_{12} between two α -particles with the condition $E_1 = E_2 = E$.

The cross sections of the α - α correlation under this condition are plotted against E_{12} in Fig. 1. There, we observe increases toward the left and right sides (i.e. $\Delta\phi=0^\circ$ and 180° , respectively) in each curve, which appear generally in heavy-ion reactions. A remarkable aspect is the enhancement appeared at $E_{12} \approx 3$ MeV in all curves, which corresponds to the 2^+ resonance energy of ^8Be nucleus. Following two processes are examined as the origin of this enhancement: a) break-up of excited ^8Be nucleus b) final state interaction (FSI) between two α -particles. We discuss the first process. The break-up cross section has been estimated using the cross sections of the $^{7,9}\text{Be}$ productions and the Q_{gg} rule¹⁾ established generally in heavy-ion reactions and by assuming an isotropic distribution of α -particles after the break-up of excited ^8Be nucleus. The value thus obtained was found to be 1/5 to 1/10 of the observed enhanced cross section. In view of the difference of the cross sections, we concluded that the FSI is dominant. The same effect is observed also at $E_{12} \approx 11$ MeV which corresponds to the 4^+ resonance energy.

To deduce a temporal information from the coincidence cross section, we apply the following rescattering approximation.²⁾ First, an α -particle 1 is emitted to a direction ω_1 with an energy ε_1 . After a time delay Δt , an emission of a second α -particle occurs with an energy ε_2 greater than that of the first, to the same direction $\omega_2 = \omega_1$. The second catches up the first at a distance D from the parent-nucleus, and, if the relative energy is around 3 MeV, we observe the rescattering as the enhancement in the cross section. In this approximation, the enhanced cross section over the background cross section is written by the following relation:

$$\left(d^4\sigma / dE_1 d\Omega_1 dE_2 d\Omega_2 \right)_{\text{en}} = \left(d^4\sigma / d\varepsilon_1 d\omega_1 d\varepsilon_2 d\omega_2 \right) \left(d\sigma / d\Omega \right)_{\alpha-\alpha} \langle 1/D^2 \rangle J,$$

where the first term on the right hand side is the cross section for the emission of two primary α -particles with energies ε_1 and ε_2 and toward the same direction ($\omega_1 = \omega_2$). The second is the cross section for α - α elastic scattering, which is 600 mb/sr at the 2^+ resonance. The choice $E_1 = E_2$ corresponds to the 90° scattering of two α -particles in their center-of-mass system. The mean value of $1/D^2$ is expressed by the third term of which reciprocal has linear dependence on a time constant τ , if the time delay Δt is distributed as $\exp(-\Delta t/\tau)$. The last is the Jacobian

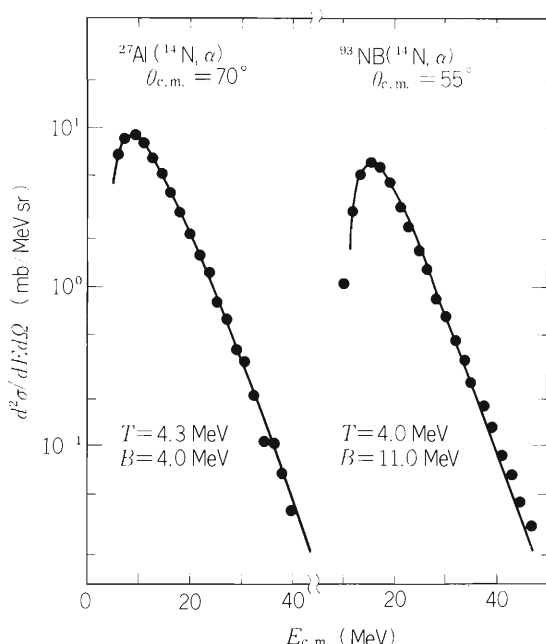


Fig. 2. Singles spectra for the reactions $^{27}\text{Al}(^{14}\text{N}, \alpha)$ and $^{93}\text{Nb}(^{14}\text{N}, \alpha)$ in the center-of-mass system.

for the transformations of the coordinates. The cross section $(d^4\sigma/dE_1 \dots)_{en}$ is evaluated for $E = 14 - 31$ MeV as a function of E , assuming the background properly. For $E < 14$ MeV, it is difficult to subtract the background without any great ambiguity; for $E > 31$ MeV, the statistical error of the cross section is too large. The cross section $(d^4\sigma/d\varepsilon_1 \dots)$ is estimated extrapolating the cross section at the energy set $(\varepsilon_1, \varepsilon_2)$ to $\Delta\phi \rightarrow 0^\circ$.

In the range of $E = 14 - 31$ MeV, we obtained $\tau \approx 5 \times 10^{-22}$ sec. nearly independently of E for both of the two reactions. In Fig. 2 are shown center-of-mass singles spectra of the $^{27}\text{Al}(^{14}\text{N}, \alpha)$ and $^{93}\text{Nb}(^{14}\text{N}, \alpha)$ reactions at $\theta_{\text{cm}} = 70^\circ$ and 55° . In the energy range mentioned above, these angles roughly correspond to $\theta = 50^\circ$ in the laboratory system. The spectra show nearly equal temperature $T \approx 4$ MeV when we fit them using the evaporation formula.³⁾ In spite of the same temperature at $\theta = 50^\circ$, the $^{27}\text{Al} + ^{14}\text{N}$ system forms compound nucleus and the $^{93}\text{Nb} + ^{14}\text{N}$ system is in preequilibrium state, according to the angle dependence of the singles cross sections and of the temperatures. Series of experiments with other temperatures and/or with proton detection are in progress.

It is necessary to consider also the spatial effect⁴⁾ of α -particle emission for further quantitative discussion.

References

- 1) V.V. Volkov: Proc. Intern. Conf. on Reactions between Complex Nuclei, (Ed. by R.L. Robinson et al.) Nashville, II, 363 (1974).
- 2) S. Kato, H. Orihara, S. Kubono, J. Kasagi, H. Ueno, T. Nakagawa, and T. Tohei: Nucl. Phys., A195, 534 (1972).
- 3) T. Ericson: Advan. Phys., 9, 425 (1960).
- 4) H. Sato and K. Yamazaki: to be published.

4-3. Study of α -Particle Emission in $^{14}\text{N} + ^{159}\text{Tb}$ Collision I

H. Utsunomiya, T. Nomura, M. Ishihara, Y. Gono,
T. Sugitate, K. Ieki, and S. Kohmoto

NUCLEAR REACTION $^{159}\text{Tb}(^{14}\text{N}, \alpha xn), (^{14}\text{N}, 2\alpha xn), (^{14}\text{N}, 3\alpha n), E = 115 \text{ MeV};$
measured $\sigma(E, \theta), \alpha\text{-}\gamma, \alpha\text{-}\gamma\text{-}\gamma$ coin; deduced $\sigma(E_\alpha, \theta_\alpha)$ in coin with final nuclei.

In recent years there has been considerable interest in fast (high-energy) α -particle emission in heavy-ion collisions. Typical features of the above emission at relatively low bombarding energies, i.e., at 6–10 MeV/amu, can be summarized as follows: (i) The angular distribution is strongly forward-peaked. (ii) The energy spectrum is continuous with strong enhancement at the high-energy part when compared with that expected in a nuclear compound reaction. (iii) The rest of projectile and target nuclei fuse together, producing final reaction products similar to evaporation residues.

Since the third feature is essential in fast α emission, the measurement of α -particles in coincidence with final reaction products is particularly important. In the present work we have measured energy and angular distributions

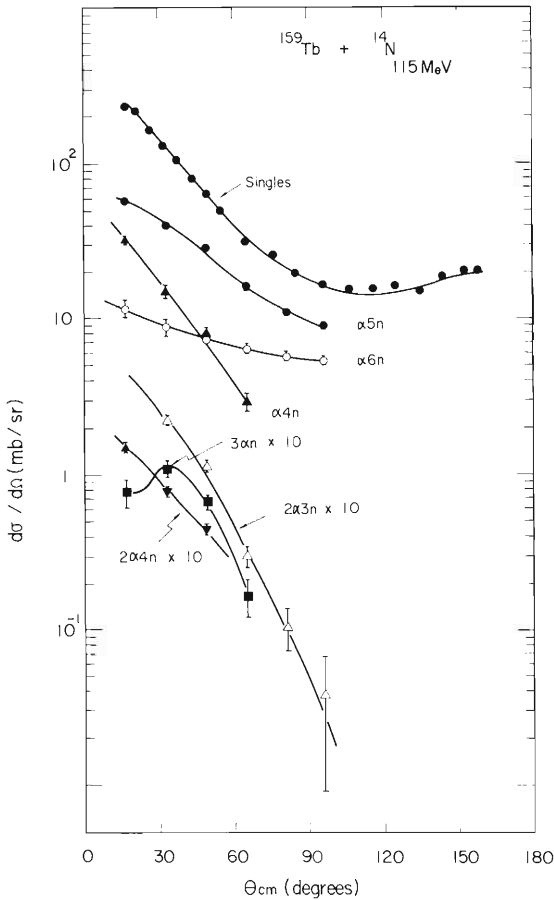


Fig. 1. Angular distributions for various reaction channels associated with α -particle emission in the $^{159}\text{Tb} + ^{14}\text{N}$ reaction at 115 MeV: $^{159}\text{Tb}(^{14}\text{N}, \alpha xn)$ $^{169-x}\text{Yb}$, $x = 4, 5, 6$; $^{159}\text{Tb}(^{14}\text{N}, 2\alpha xn)$ $^{165-x}\text{Er}$, $x = 2, 3$; $^{159}\text{Tb}(^{14}\text{N}, 3\alpha n)$ ^{160}Dy . Solid curves are to guide the eye.

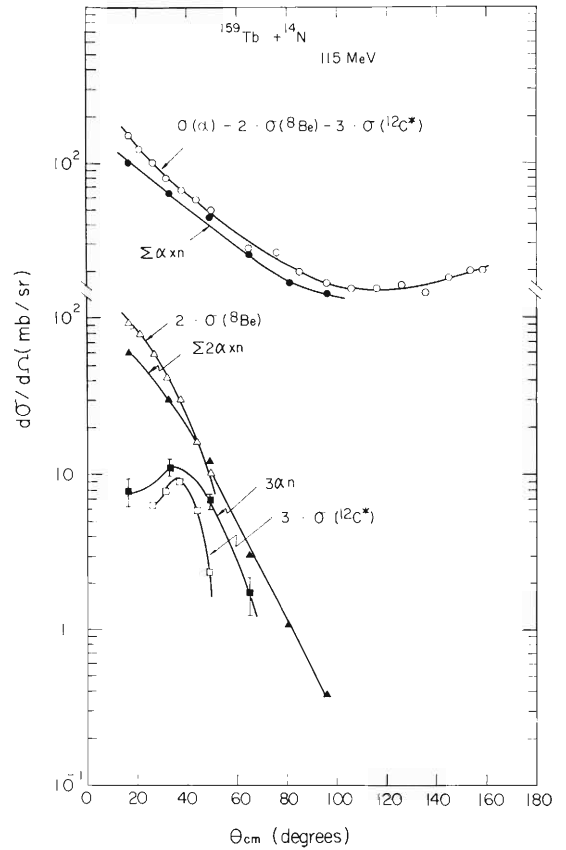


Fig. 2. Lower: Experimental and estimated angular distributions of $2\alpha xn$ and $3\alpha n$ channels. Upper: Comparison of angular distributions of α -particles for αxn channels obtained in the inclusive and exclusive measurements.

of α -particles at six different angles between 15° and 90° in coincidence with discrete γ -rays to specify various final nuclei produced in the 115 MeV ^{14}N bombardment of ^{159}Tb through reactions of ($^{14}\text{N}, \alpha xn$), ($^{14}\text{N}, 2\alpha xn$), and ($^{14}\text{N}, 3\alpha n$). A metallic ^{159}Tb foil of 2.1 mg/cm^2 in thickness was used. Charged particles with $Z \geq 2$ were detected with counter telescopes consisting of $50 \mu\text{m}$ and 2 mm Si detectors, while γ -rays were measured with a $75 \text{ cm}^3 \text{ Ge(Li)}$ counter placed in the reaction plane at 90° with respect to the beam.

Figure 1 shows angular distributions of α -particles in coincidence with γ -rays specifying final residual nuclei mentioned above. The following points should be noted:

(i) The angular distributions of the ($^{14}\text{N}, \alpha xn$) reactions depend very much on values of x . For instance, the yield for the $\alpha 4n$ channel shows a very rapid increase with the decrease of the emission angle, while the $\alpha 6n$ channel has a much more flat angular distribution. This is considered to be due to kinetic energy dependence of angular distribution; in fact, the average energy of α -particles corresponding to the $\alpha 4n$ channel is much higher than that for $\alpha 6n$ as will be mentioned later.

(ii) The angular distribution of the ($^{14}\text{N}, 3\alpha n$) reaction is peaked around 35° , being similar to that for carbon observed in the inclusive measurements carried out simultaneously. This indicates that the main origin of α -particles observed in the $3\alpha n$ channel is break-up of an excited ^{12}C ($^{12}\text{C}^*$) into three α -particles.

(iii) The angular distributions of the ($^{14}\text{N}, 2\alpha xn$) reactions are also similar to those of Be. This fact together with that pointed out in (ii) suggests that the contribution of ^8Be should be important in the $2\alpha xn$ channel.

In order to clarify the above points mentioned in (ii) and (iii), we estimated the contribution of ^8Be and $^{12}\text{C}^*$ in the following way. We first assumed that their angular distributions are the same as those of the corresponding isotopes. The yields of ^8Be and $^{12}\text{C}^*$ are then assumed to follow the so-called Q_{gg} systematics, where the Q-value for ^{12}C is calculated for the 7.6 MeV state in ^{12}C which is known to be the lowest excited level to break up into three α -particles. We assumed further that α -particles originating from the break-up have the same angular distribution as that for the parent nucleus. In spite of the very crude assumptions used, the results thus estimated turned out to reproduce fairly well the experimental yields of α -particles leading to $2\alpha xn$ and $3\alpha n$ channels as shown in the lower part of Fig. 2. The fact that the calculated angular distributions are somewhat sharper than the experimental ones is clearly due to the last assumption mentioned above. We therefore conclude that a dominant part of $2\alpha xn$ and $3\alpha n$ channels originate from the break-up of ^8Be and $^{12}\text{C}^*$. In other words, α -particles corresponding to the above reaction channels should not be included in the study of the fast α emission.

As shown in the upper part of Fig. 2, the cross section of α -particles corresponding to αxn ($x = 4 - 6$) channels amounts to about 80 % of the inclusive cross section when the above break-up contribution is subtracted. A part of the difference must be attributed to the fact that all of the final nuclei were not included in the α - γ measurement, especially at forward angles, where very high-energy α -particles leading to the $\alpha 3n$ channel is significant.

Energy spectra of α -particles leading to various final nuclei measured at 15° are shown in Fig. 3(a). The average energy (E_{av}) for the $\alpha 6n$, $\alpha 5n$, and $\alpha 4n$ channels are 21.2, 23.7, and 31.6 MeV, respectively. The very small difference of E_{av} between $\alpha 6n$ and $\alpha 5n$ is due to the fact that the lower limit of α -particle energy for $\alpha 6n$ is determined by the Coulomb barrier. The angle dependence of energy spectra is shown in Fig. 3(b) and 3(c). The spectra for the same channel are similar to each other, being almost independent of emission angles. This is quite natural because the Q-value is the most decisive factor to determine final residual nuclei. On the other hand, energy spectra obtained by summing up all αxn channels depend very much on emission angles but always have the following features characteristic of preequilibrium emission: the spectral shape is characterized by a Maxwell-Boltzmann distribution and is thus similar to an evaporation spectrum with high nuclear temperature even at forward angles. The temperature deduced from inclusive spectra in our previous works[1] increases smoothly with the decrease of emission angles. However, the high-energy tails of the spectra at 15° , 30° , and 45° in Fig. 3(c) are quite similar to each other, which might indicate roughly the same temperature. This is considered to be due to the lack of the $\alpha 3n$ channel which must be effective to very high-energy α spectra.

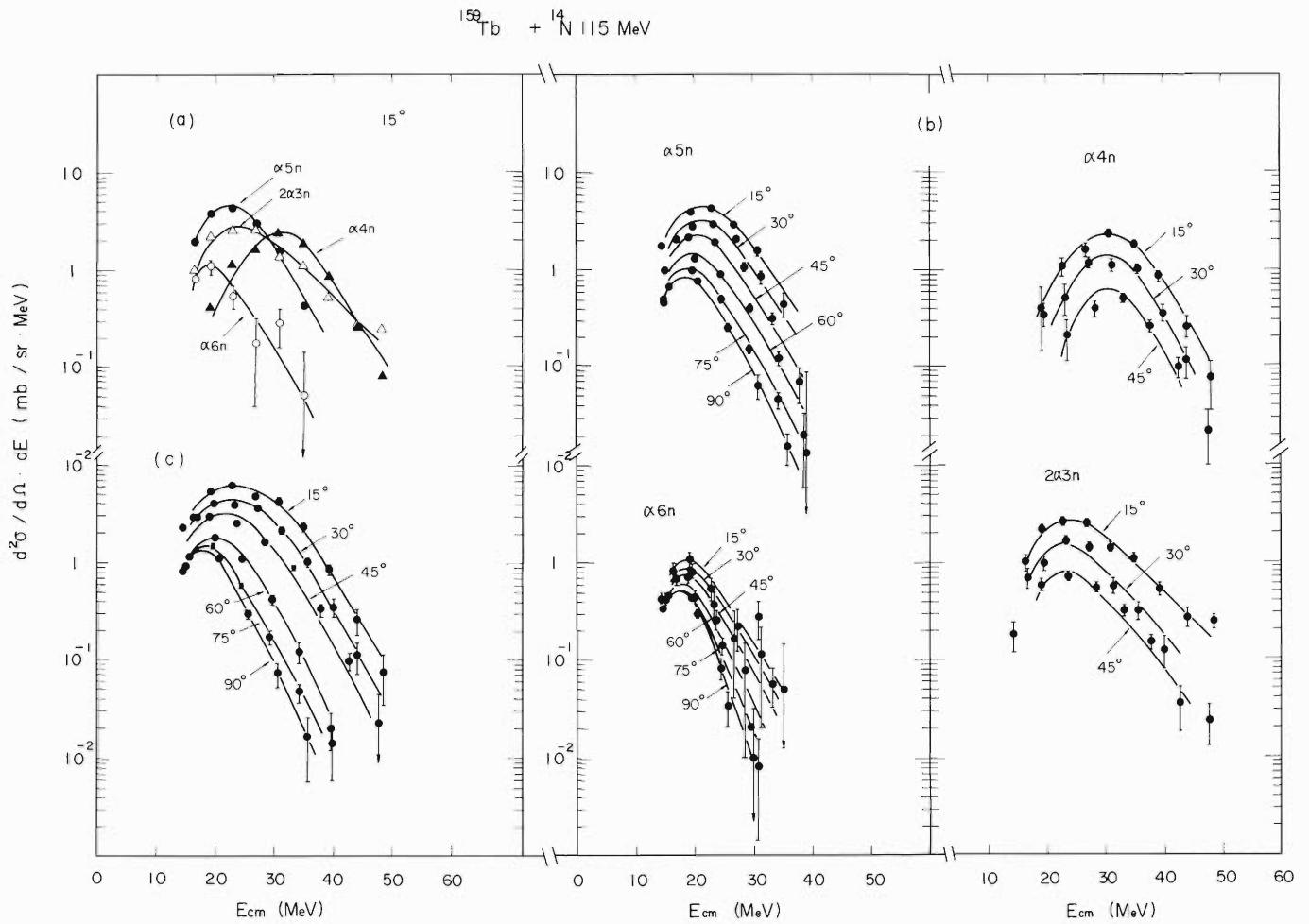


Fig. 3.

- (a) Energy spectra of exclusive α -particles measured at 15° for the $^{159}\text{Tb}(^{14}\text{N}, \alpha xn)^{169-x}\text{Yb}$, $x = 4, 5, 6$, and $^{159}\text{Tb}(^{14}\text{N}, 2\alpha 3n)^{162}\text{Er}$ reaction channels.
- (b) Energy spectra of α -particles measured at various angles for the $^{159}\text{Tb}(^{14}\text{N}, \alpha xn)^{169-x}\text{Yb}$, $x = 4, 5, 6$, and $^{159}\text{Tb}(^{14}\text{N}, 2\alpha 3n)^{162}\text{Er}$ reaction channels. Solid curves are to guide the eye.
- (c) Energy spectra of α -particles obtained after summing up all αxn channels.

Reference

- 1) T. Nomura, H. Utsunomiya, T. Motobayashi, T. Inamura, and M. Yanokura: Phys. Rev. Lett., 40, 694 (1978); J. Phys. Soc. Japan, 46, 335 (1979);
H. Utsunomiya, T. Nomura, T. Inamura, T. Sugitate, and T. Motobayashi: Nucl. Phys., A334, 127 (1980).

4-4. Study of α -Particle Emission in $^{14}\text{N} + ^{159}\text{Tb}$ Collision II

H. Utsunomiya, T. Nomura, M. Ishihara, Y. Gono,
T. Sugitate, K. Ieki, and S. Kohmoto

\left\{ \begin{array}{l} \text{NUCLEAR REACTION } ^{159}\text{Tb}(^{14}\text{N}, \alpha xn)^{169-x}\text{Yb}, E = 115 \text{ MeV: measured} \\ \text{average } \gamma\text{-ray multiplicities } \langle M_\gamma(E_\alpha, \theta_\alpha) \rangle; \text{ average } \ell_i \text{ for } \alpha \text{ emission.} \end{array} \right\}

In the preceding report, energy and angular distributions of emitted α particles associated with $^{159}\text{Tb}(^{14}\text{N}, \alpha xn)^{169-x}\text{Yb}$ reaction channels with $x = 4 - 6$ were presented. In this report, we present average γ -ray multiplicities ($\langle M_\gamma \rangle$) for preequilibrium (PE) α emission and discuss the resultant average initial orbital angular momenta.

α - γ - γ triple coincidence measurement was performed using a 7.6 cm \times 7.6 cm NaI(Tl) detector in addition to a Ge(Li) and α detectors. The NaI(Tl) detector was mounted perpendicularly to the scattering plane, at 90° to the beam and 50 mm from the target.

Table 1 summarizes values of $\langle M_\gamma \rangle$ deduced for the $(^{14}\text{N}, \alpha xn)$ reactions as a function of kinetic energy (E_α) and emission angle (θ_α) of α particles. The following points are to be noted. (1) Because any transitions below the 2^+ (^{164}Yb) or $13/2^+$ ($^{163}, ^{165}\text{Yb}$) states were not detected with the NaI(Tl) counter due to its energy range covered, the given $\langle M_\gamma \rangle$ is smaller than the actual one by one or about three units for the $\alpha 5n$ or $\alpha 4n$ and $\alpha 6n$ channels, respectively. (2) $\langle M_\gamma \rangle$ for any energy bins remains almost constant for the change of θ_α in all reaction channels. (3) $\langle M_\gamma \rangle$ for the $\alpha 5n$ channel clearly decreases with the increase of E_α , while the E_α

Table 1. Average γ -ray multiplicities $\langle M_\gamma \rangle$ as a function of E_α and θ_α for the $^{159}\text{Tb}(^{14}\text{N}, \alpha xn)$ reactions at 115 MeV.

Reaction channel	E_α^* (MeV)	$\langle M_\gamma \rangle$						Weighted average
		$\theta_\alpha = 15^\circ$	30°	45°	60°	75°	90°	
$\alpha 6n$	16–20	13.4 \pm 4.2	12.1 \pm 4.3	12.4 \pm 2.6	12.7 \pm 2.6	13.6 \pm 2.2	12.7 \pm 1.9	12.8 \pm 3.6
	20–24	14.0 \pm 6.6	11.8 \pm 6.4	13.8 \pm 4.4	12.1 \pm 3.8	15.2 \pm 4.0	12.0 \pm 3.5	13.2 \pm 5.9
$\alpha 5n$	16–20	19.1 \pm 2.0	18.6 \pm 2.2	19.5 \pm 2.0	19.6 \pm 2.3	19.2 \pm 1.8	18.9 \pm 1.7	19.1 \pm 2.1
	20–24	16.8 \pm 1.6	16.8 \pm 2.2	17.0 \pm 1.6	17.8 \pm 1.9	16.2 \pm 1.7	18.0 \pm 2.0	17.0 \pm 1.8
	24–28	13.6 \pm 1.7	13.7 \pm 1.8	13.4 \pm 1.7	13.8 \pm 2.2	13.5 \pm 2.4	14.9 \pm 3.0	13.7 \pm 1.8
	28–32	11.4 \pm 2.2	10.8 \pm 2.8	11.7 \pm 2.2	11.7 \pm 2.6	13.4 \pm 4.2	14.9 \pm 4.3	11.5 \pm 2.5
	32–36	9.2 \pm 4.6	9.2 \pm 6.5	10.0 \pm 4.2				9.3 \pm 5.2
$\alpha 4n$	24–28	15.0 \pm 5.3	16.4 \pm 7.1	14.6 \pm 5.5				15.4 \pm 5.8
	28–32	14.6 \pm 3.6	16.6 \pm 5.6	13.9 \pm 4.1				15.2 \pm 4.3
	32–36	13.5 \pm 2.3	15.1 \pm 3.6	13.6 \pm 4.3				14.0 \pm 2.8
	36–40	14.2 \pm 2.8						14.2 \pm 2.8
	40–44	12.9 \pm 3.5						12.9 \pm 3.5

* Energies given in the c.m. system.

dependence is much weaker for the $\alpha 4n$ channel. The similar trend was also reported in Ref. 1.

The experimental values of $\langle M_\gamma \rangle$ are related with the average angular momentum $\langle J_\gamma \rangle$ of “entry states” (levels prior to γ -decays) in the following way. The entry states are usually considered to decay first by several “statistical” transitions, and then by stretched quadrupole de-excitations along the yrast line, or in bands parallel to it. We therefore write

$$\langle J_\gamma \rangle = 2(\langle M_\gamma \rangle - \langle M_s \rangle) + f_s \langle M_s \rangle + J_0, \quad (1)$$

where $\langle M_s \rangle$ is the average number of the statistical γ rays and f_s is the average angular-momentum decrease per statistical transition. J_0 is a constant which depends on spin values of its very low-lying states. J_0 is taken to be 2h or 6.5h for even- or odd-mass nuclei, respectively.

As for values of $\langle M_s \rangle$ and f_s , we follow an empirical analysis of Sarantites et al.²⁾ who obtained $\langle M_s \rangle = 3.1 + 0.019E^*$ for the estimate of $\langle J_\gamma \rangle$ of final nuclei produced in (HI, xn) reactions, where E^* is the excitation energy of a compound nucleus before emitting neutrons. We shall use the same formula for the αxn channels by considering that E^* denotes the excitation energy of intermediate states populated after the α -particle emission; f_s is taken to be constant (0.36), for simplicity, which is a value used in Ref. 2 for the $^{158}\text{Gd} + ^{12}\text{C}$ reaction at 112 MeV.

Neglecting spins of projectile- and target-nuclei, we can relate $\langle J_\gamma \rangle$ with the average angular momentum $\langle \ell_i \rangle$ in the entrance channel leading to the (^{14}N , αxn) reactions by

$$\langle \ell_i \rangle \simeq \langle J_\gamma \rangle + x \Delta_n + \Delta_\alpha, \quad (2)$$

where Δ_n and Δ_α are average decrease of the angular momentum per neutron- and α - emission, respectively. It should be noted that they are not necessarily equal to average orbital angular momenta carried by neutron or α -particle.

The values of Δ_n and Δ_α have been estimated by the statistical model calculation with the assumption that an α -particle is emitted first in the preequilibrium stage of a complex nucleus (projectile and target) and then follows successive evaporation of x neutrons from an intermediate nucleus reaching thermal equilibrium. The preequilibrium nature of the α emission was treated as evaporation from a locally heated system (hot spot).³⁾ More details of the calculation will be described elsewhere.

The energy dependence of $\langle \ell_i \rangle$ estimated from Eqns. (1) and (2) in the case of $\theta_\alpha = 15^\circ$ is shown in Table 2. The values of $\langle \ell_i \rangle$ averaged over both E_α and θ_α are 32.3 ± 6.7 , 37.3 ± 1.8 , and 43.7 ± 4.5 h for the $\alpha 6n$, $\alpha 5n$, and $\alpha 4n$ channels, respectively, clearly increasing with the decreasing number of neutrons emitted as is well known in the case of (HI, xn) reactions. Since E_α leading to the $\alpha 6n$ channel is low, a contribution from the compound reaction must be significant in this channel. The weighted average of $\langle \ell_i \rangle$ for $\alpha 4n$ and $\alpha 5n$ using their cross sections is therefore considered as good indication for the average entrance angular momentum for fast α -particle emission. The $\langle \ell_i \rangle$ was obtained to be 39 h.

Table 2. Angular momenta characterizing the $^{159}\text{Tb}(^{14}\text{N}, \alpha xn)^{169-x}\text{Yb}$ reaction when α -particles are detected at 15° .

Reaction channel	E_α^{cm} (MeV)		E^* (MeV)	$\langle M_\gamma \rangle$	$\langle M_s \rangle$	$\langle J_\gamma \rangle$ (h)	$\langle J_n \rangle^{\text{b)}$ (h)	$\langle \ell_\alpha \rangle^{\text{c)}$ (h)	Δ_α (h)	$\frac{\Delta_\alpha}{\langle \ell_\alpha \rangle}$	$\langle \ell_i \rangle^{\text{d)}$ (h)
	Range	Average ^{a)}									
$\alpha 6n$	16–20	18.1	76.1	13.4±4.2	4.5	25.9	29.5	8.1	5.1	0.630	34.6±8.4
	20–24	21.7	72.5	14.0±6.6	4.5	27.1	30.7	10.5	7.3	0.695	41.2±13.2
$\alpha 5n$	16–20	18.4	75.8	19.1±2.0	4.5	32.8	37.8	8.4	5.4	0.643	43.2±4.0
	20–24	22.0	72.2	16.8±1.6	4.5	28.2	33.2	10.6	7.4	0.698	40.6±3.2
	24–28	25.8	68.4	13.6±1.7	4.4	22.0	27.0	12.7	9.2	0.724	36.2±3.4
	28–32	29.6	64.6	11.4±2.2	4.3	17.7	22.7	14.4	11.0	0.764	33.7±4.4
	32–36	33.5	60.7	9.2±4.6	4.3	13.3	18.3	16.1	12.8	0.795	31.1±9.2
$\alpha 4n$	24–28	26.3	67.9	15.0±5.3	4.4	29.3	33.3	12.9	9.4	0.729	42.7±10.6
	28–32	30.1	64.1	14.6±3.6	4.3	28.6	32.6	14.6	11.1	0.760	43.7±7.2
	32–36	33.8	60.4	13.5±2.3	4.2	26.6	30.6	16.3	12.6	0.773	43.2±4.6
	36–40	37.6	56.6	14.2±2.8	4.2	28.0	32.0	17.6	14.0	0.795	46.0±5.6
	40–44	41.6	52.6	12.9±3.5	4.1	25.6	29.6	19.0	15.2	0.800	44.8±7.0

- a) Weighted average estimated from the energy spectrum at each reaction channel.
b) Average angular momentum of intermediate states populated after the α -particle emission.
c) Average orbital angular momentum carried by α -particle.
d) The given errors are only those associated with $\langle M_\gamma \rangle$.

Table 3 compares the presently deduced values of $\langle \ell_i \rangle$ for fast α emission with some characteristic angular momenta in the entrance channel. The value of the critical angular momentum (ℓ_{cr}) for complete fusion

calculated from models of Wilczyński⁴⁾ and Bass⁵⁾ who consider balance of forces at the close-contact region of projectile- and target-nuclei is around $50 \hbar$ as listed in the second column of Table 2. Therefore, the present result strongly indicates that $\langle \ell_i \rangle$ for fast α emission is close to, but slightly smaller than ℓ_{cr} . This is consistent with interpretation that α - particles of interest are emitted in the precompound decay of a composite nucleus which goes on the way to fusion but does not reach complete equilibrium yet.⁶⁾

Table 3. Average angular momenta $\langle \ell_i \rangle$ (in unit of \hbar) leading to fast α -particle emission and some characteristic angular momenta in the $^{159}\text{Tb} + ^{14}\text{N}$ reaction at 115 MeV.

$\langle \ell_i \rangle_{\text{exp}}$	ℓ_{cr}	ℓ_{gr}^*
$37.3 \pm 1.8 (\alpha 5n)$	52 (Ref. 4)	57
$43.7 \pm 4.5 (\alpha 4n)$	51 (Ref. 5)	
39 (weighted average)	48 (Ref. 4, 7) **	

* Deduced from an optical model analysis for elastic scattering of ^{14}N with ^{159}Tb .

** Wilczyński-model using the half-density radius of Myers.⁷⁾

References

- 1) T. Inamura, T. Kojima, T. Nomura, T. Sugitate, and H. Utsunomiya: Phys. Lett., 84B, 71 (1979).
- 2) D.G. Sarantites, L. Westerberg, M.L. Halbert, R.A. Dayras, D.C. Hensley, and J.H. Barker: Phys. Rev. C, 18, 774 (1978).
- 3) R. Weiner and M. Weström: Nucl. Phys., A286, 282 (1977).
- 4) J. Wilczyński: *ibid.*, A216, 386 (1973).
- 5) R. Bass: *ibid.*, A231, 45 (1974).
- 6) H. Utsunomiya, T. Nomura, T. Inamura, T. Sugitate, and T. Motobayashi: *ibid.*, A334, 127 (1980).
- 7) W.D. Myers: *ibid.*, A204, 465 (1973).

4-5. Angular Momentum Transfer and Alignment Following Preequilibrium α Emission in the $^{209}\text{Bi} + ^{14}\text{N}$ Reaction at 115 MeV

H. Utsunomiya, T. Nomura, M. Ishihara,
T. Sugitate, K. Ieki, and S. Kohmoto

$$\left[\begin{array}{l} \text{NUCLEAR REACTION } ^{209}\text{Bi}(^{14}\text{N}, \alpha f), E = 115 \text{ MeV}; \\ \text{measured angular correlations } \sigma(E_f, \theta, \phi). \end{array} \right]$$

The measurement of the angular distribution for fission fragments in coincidence with reaction products is known to give important informations on angular momenta involved in the nuclear reaction.¹⁾ Dyer et al.²⁾ first applied this method to heavy-ion reactions and successfully studied angular momenta transferred and their alignment in deep-inelastic processes. We applied this technique to the study of fast α -particle emission³⁾⁻⁵⁾ in heavy-ion reactions.

A ^{209}Bi metallic foil of about $800 \mu\text{g}/\text{cm}^2$ in thickness was bombarded with 115 MeV ^{14}N beam provided by the cyclotron. α -particles were detected with Si $\Delta E(50 \mu\text{m}) - E(2 \text{ mm})$ counter telescopes mounted at 20° and 50° with respect to the beam with half-angle acceptances of 3.4° and 4.9° , respectively. Fission fragments were detected with a thin Si($30 \mu\text{m}$) detector and measured at backward angles to avoid the elastically scattered beam and eliminate the evaporation residues.

Figures 1 and 2 show the measured in-plane and out-of-plane angular distributions of fission fragments in coincidence with α -particles emitted at 20° and 50° . The geometry of the experiment is the same as that in Ref. 2. x-axis was chosen along the recoil direction of fissile nucleus and z-axis along the normal to the reaction plane. θ and ϕ are usual polar and azimuthal angles, respectively.

In-plane anisotropy of the angular distribution obtained for α -particles emitted at 20° is larger than that at 50° , while out-of-plane anisotropies at 20° are smaller than those at 50° . This fact suggests that the alignment of the transferred angular momentum in the case of α -particle emission at 50° is larger than that at 20° .

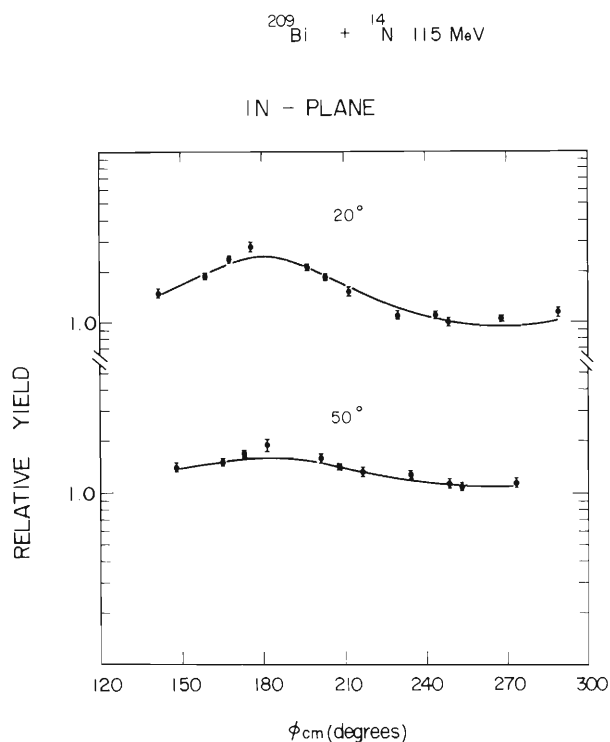


Fig. 1. In-plane angular distributions of fission fragments in coincidence with α -particles emitted at 20° and 50° , respectively. The solid curves show the best fit to the experimental data in the case of one-dimensional disalignment.

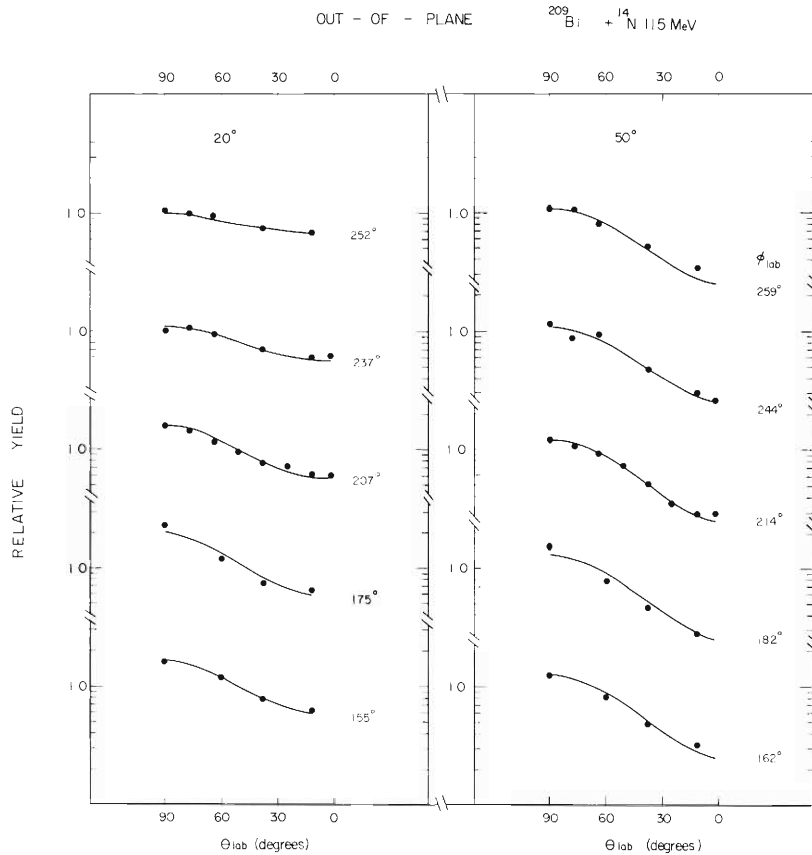


Fig. 2. Out-of-plane angular distributions.

The angular distribution of fission fragments from a nucleus having the intrinsic angular momentum J whose projections on the space-fixed z -axis and the nuclear symmetry axis are M and K , respectively, is usually written by¹⁾

$$W_{MK}^J(\theta) = \frac{1}{2} (2J+1) \left| d_{MK}^J(\theta) \right|^2, \quad (1)$$

where $d_{MK}^J(\theta)$ are rotational wave functions. In order to analyze the experimental data we have to sum Eqn. (1) over J , M and K . Dyer et al.²⁾ have shown that the experimental correlations are sensitive only to the weighted average \bar{J} of the J -distribution when its weight function is proportional to $2J+1$ as is usually adopted. In stead of doing the summation over J with the weight function, we therefore consider Eqn. (1) for $J = \bar{J}$. The K -distribution is assumed here to be given by $\exp\left(-\frac{K^2}{2K_0^2}\right)$, where the width parameter K_0 can be estimated as a function of the nuclear temperature and the effective moment of inertia, both taken at the saddle point deformation.^{1), 6)} Following the procedure given by Back and Bjørnholm,⁶⁾ we obtain $K_0 \approx 11 \hbar$ in the present case.

As for the summation over M , we follow the semi-classical treatment of Dyer et al.;²⁾ that is, the shape of $|M| = J$ angular correlations is taken from Eqn. (1), and a classical prescription is used to account for $M \neq J$ components. If the spin direction is given by polar angle ξ and azimuthal angle η (i.e., $M_x = J \sin \xi \cos \eta$ and $M_y = J \sin \xi \sin \eta$), the angular distribution in the c.m. system of the fissioning nucleus is then given by

$$W(\theta, \phi) \propto \sum_{\xi, \eta} P(\xi, \eta) \sum_{K=-\bar{J}}^{\bar{J}} e^{-\frac{K^2}{2K_0^2}} W_{JK}^{\bar{J}}(\theta') \quad (2)$$

with
$$\theta' = \cos^{-1} \left\{ \cos \theta \cos \xi + \sin \theta \sin \xi (\cos \phi \cos \eta + \sin \phi \sin \eta) \right\}. \quad (3)$$

A weighting factor $P(\xi, \eta)$ is determined through the M -distribution which is assumed here to be proportional to $\exp(-\xi^2/2\xi_0^2)$ with ξ_0 as parameter to be adjusted because the most plausible mechanism giving rise to the

disalignment is a non-equatorial collision as discussed in Ref. 2, producing preferentially M_y ($= \bar{J} \sin \xi$) components.

Solid curves in Figs. 1 and 2 show the best fits for simultaneous fitting of Eqn. (2) to the measured in-plane and out-of-plane angular distributions of fission fragments. We fixed $11 \hbar$ for the value of K_0 in the fitting procedure. The resultant values of the best fit parameters are listed in Table 1. It turned out that the angular momenta of the amount of $31 \pm 3 \hbar$ and $26 \pm 3 \hbar$ are transferred in the present reaction when α -particles are emitted at 20° and 50° , respectively. If we assume that the angular momentum of the initial system is divided between α -particle and ^{10}B in proportion to their masses, the average entrance angular momentum ($\langle \ell \rangle$) responsible for α emission at 20° and 50° can be deduced to be $43 \pm 3 \hbar$ and $36 \pm 3 \hbar$, respectively. From the comparison of those values with the critical angular momentum (ℓ_{cr}) for complete fusion which is calculated to be $50 \hbar$ on the basis of the liquid-drop model,⁷⁾ we can conclude that the average ℓ -values in the entrance channel responsible for α emission are close to, but slightly smaller than ℓ_{cr} , being consistent that fast α -particles in the present reaction originate from the collisions with impact parameters ensuring enough overlap of projectile and target nuclei to fuse each other.

Table 1. Best fit parameters \bar{J} and ξ_0 together with the resultant values of alignment P_{zz} and average entrance angular momentum $\langle \ell \rangle$ for preequilibrium α emission. Errors estimated from the χ^2 -values are also given for \bar{J} .

Emission angle of α -particles	ξ_0 (degrees)	\bar{J} (\hbar)	P_{zz}	$\langle \ell \rangle$ (\hbar)
20°	62.1	31 ± 3	0.39	43 ± 4
50°	29.4	26 ± 3	0.69	36 ± 4

The disalignment of \bar{J} in the y - z plane was determined by the parameter ξ_0 . It is remarkable that for α emission at 20° , a large disalignment ($\xi_0 = 62.1^\circ$) was found compared with that ($\xi_0 = 29.4^\circ$) at 50° . The alignment parameter $P_{zz} = 3\langle M_z^2 \rangle / 2\langle J^2 \rangle - 1/2$ is also listed in Table 1, which is unity for fully aligned J and zero for isotropically oriented J . P_{zz} of 0.69 was obtained for α emission at 50° , which is rather close to the value of 0.6 – 0.8 obtained for deep inelastic reaction.²⁾ However, P_{zz} for α emission at 20° was 0.39, which is much smaller than the above values. It seems that the present data shows the large contribution of a non-equatorial collision to α emission at forward angle.

References

- 1) R. Vandenbosch and J. R. Huizenga: Nuclear Fission, Academic Press, New York and London (1973).
- 2) P. Dyer, R. J. Puigh, R. Vandenbosch, T. D. Thomas, M. S. Zisman, and L. Nunnolley: Nucl. Phys., A322, 205 (1979).
- 3) H. C. Britt and A. R. Quinton: Phys. Rev., 124, 877 (1961).
- 4) L. Westerberg, D. G. Sarantites, D. C. Hensley, R. A. Dayras, M. L. Halbert, and J. H. Barker: *ibid.*, C18, 796 (1978).
- 5) T. Nomura, H. Utsunomiya, T. Motobayashi, T. Inamura, and M. Yanokura: Phys. Rev. Lett., 40, 694 (1978); H. Utsunomiya, T. Nomura, T. Inamura, T. Sugitate, and T. Motobayashi: Nucl. Phys., A334, 127 (1980).
- 6) B. B. Back and S. Bjolnholm: Nucl. Phys., A302, 343 (1978).
- 7) R. Bass: *ibid.*, A231, 45 (1974).

4-6. Polarization of Preequilibrium Proton Emission in the $^{93}\text{Nb} + ^{14}\text{N}$ Reaction

| T. Sugitate, T. Nomura, M. Ishihara, Y. Gono,
H. Utsunomiya, K. Ieki, and S. Kohmoto

{ NUCLEAR REACTION $^{93}\text{Nb}(^{14}\text{N}, p)$, $E=95\text{MeV}$; measured $\rho(E, \theta)$,
spin polarization ($\theta=20^\circ$), double scattering method. }

Light particles such as p, d, t, and α emitted in heavy-ion reactions often exhibit forward-peaked angular distributions and continuous energy spectra enhanced at high-energy parts compared with those expected in compound nuclear reactions.¹⁾⁻³⁾ In our previous work³⁾ on ^{14}N -induced reactions at 6 – 8 MeV/amu, the energy spectra in question were well interpreted as those of preequilibrium (PE) emission from a locally heated nuclear system in the framework of the hot-spot model.^{3), 4)} We have measured for the first time spin polarization of protons emitted at 20° in the $^{93}\text{Nb} + ^{14}\text{N}$ reaction at 95 MeV by the double scattering method, in order to gain more insight into this phenomenon.

A 9 mg/cm² thick Nb foil was bombarded with 95 MeV ^{14}N -beam with a few hundred nA from the cyclotron. The beam energy at the centre of the target is about 88 MeV.

The polarimeter used in the present work is described elsewhere in this progress report. The left-right asymmetry was measured at 20° on both sides with respect to the beam direction and was deduced in the conventional manner using the geometrical average of the asymmetries obtained at 20° and 340° in order to cancel most possible false asymmetry to first order.⁵⁾ The effect of false asymmetry is estimated to be less than 2%.

We have also measured energy spectra of protons at various angles. Figure 1 shows angular distributions in the c.m. system as a function of proton energy. They are nearly symmetric with respect to 90° for low energy protons up to 10 MeV, but become more and more forward-peaked with the increase of proton energy.

Figure 2 (a) shows the energy spectra measured at $\theta_{\text{lab}} = 20^\circ$ and 156° corresponding to $\theta_{\text{cm}} = 22^\circ$ and 158° on the average. Protons emitted at $\theta_{\text{lab}} = 156^\circ$ are considered to originate mainly from a decay of compound nucleus. Then the difference between these two spectra is considered to represent an energy spectrum from the PE process of interest. This spectrum can be well fitted by the evaporation formula with temperature (T) of 3.5 MeV as shown by a smooth curve. The proportion of the PE component increases smoothly with the increase of proton energy, for instance, from 12 % at 7 MeV to 83 % at 20 MeV.

Figure 2 (b) shows the experimental polarization; they are 1.0 ± 3.8 , 3.5 ± 3.7 , 8.2 ± 3.4 , 11.0 ± 5.8 , and 18.6 ± 7.1 % for energy bins of 6.5 – 8.5, 9.2 – 10.9, 11.5 – 13.7, 13.7 – 16.4, and 16.4 – 20.5 MeV in the c.m. system, respectively. We follow the Madison convention for the sign of polarization.

This energy dependence is considered to originate mainly from the energy dependent proportion of the PE component mentioned above. Assuming that protons emitted in a compound reaction are unpolarized and the PE protons are polarized by +22 % independent of their energies, we obtain a solid curve shown in Fig. 2 (b) which agrees well with the experimental result.

Now we present a macroscopic explanation of the present result based on the hot-spot model. We first point out that if a total angular momentum of a highly excited nucleus is polarized, the intrinsic spin of nucleons emitted during its statistical decay is usually polarized in the same direction. To see this, we consider, for simplicity, a stretched downward transition by proton emission with kinetic energy E and total (orbital) angular momentum $j(\ell)$, for which the transmission coefficient is given by $T_\ell^j(E)$. Then, the polarization P of the evaporated protons can be given by

$$P = f_1 \times \left[\frac{\{T_{j-1/2}^j(E) - \frac{j}{j+1} T_{j+1/2}^j(E)\}}{\{T_{j-1/2}^j(E) + T_{j+1/2}^j(E)\}} \right],$$

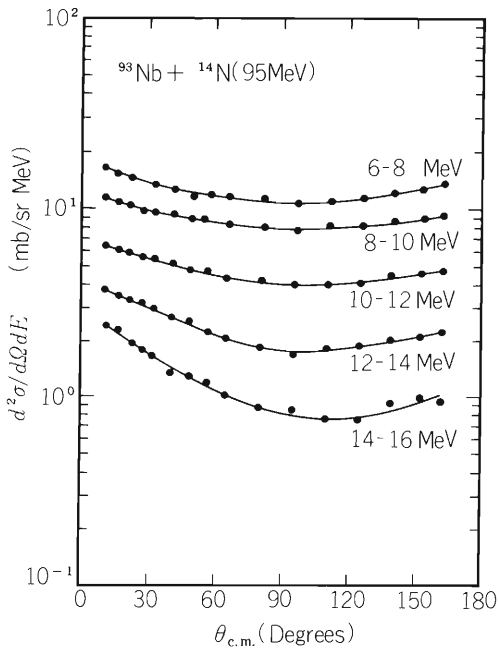


Fig. 1. The double differential cross sections of protons obtained for given c.m. energies are shown for the $^{93}\text{Nb} + ^{14}\text{N}(95\text{MeV})$ reaction at 95 MeV. Solid curves are to guide the eye.

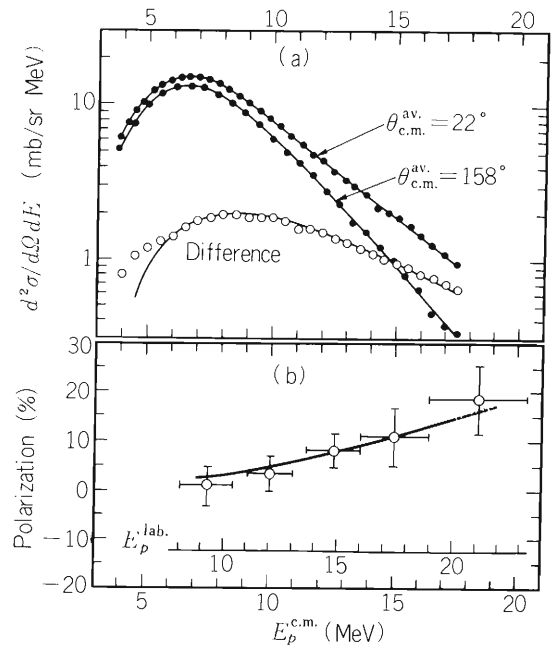


Fig. 2. Upper: Experimental energy spectra of protons obtained at $\theta_{\text{lab}} = 20^\circ$ and 156° , corresponding to $\theta_{\text{c.m.}} = 22^\circ$ and 158° on the average. Solid curves are to guide the eye. The difference between these two spectra is also shown, for which a solid curve given is the best fit by the evaporation formula with temperature of 3.5 MeV. Lower: The measured (circles) and estimated (solid curve) values of proton polarization. Horizontal lines for the experimental points show the size of energy bins. The given errors are only statistical. See the text for the estimated curve.

where f_1 is the initial polarization of the parent nucleus. Since the numerator within the bracket is usually positive, P has the same sign as f_1 . For the present reaction we have carried out more general statistical calculation, then we obtain $P = (0.2 - 0.3) \times f_1$.

Now we suppose a case in which a projectile is captured by a target nucleus in a nearly peripheral collision of which the impact parameters fall between those of deep-inelastic and compound reactions. We assume that local heating occurs around the contact region of the two nuclei and that a hot spot is finally created on the surface of this composite nucleus which is also rotating due to transfer of initial angular momenta. The relaxation time due to diffusion of heat estimated in Ref. 4 becomes 4×10^{-22} sec for a hot spot at $T = 3.5$ MeV on the surface of an $A \approx 100$ nucleus, while the present statistical calculation shows that the inverse of the evaporation probability of the hot spot is the same order of magnitude. We therefore postulate that protons of interest are evaporated from the hot spot, but not from the other cold part of the system. It is expected that the above emission is not isotropic, but occurs near the tangential direction on the average. Such evaporated protons must be polarized, as pointed out above, in the same direction as that of the rotation of the composite nucleus. The positive sign of the presently measured polarization thus indicates that the relevant PE proton emission takes place at negative angles as is the case for deep-inelastic reactions. This is reasonable

because the impact parameters involved are even smaller than those for deep-inelastic collisions.

Finally we note that no polarization is expected if the whole surface of the composite nucleus is heated and contributes to proton evaporation equally. The present result is therefore considered to be evidence for the hot-spot formation, as long as the relevant reaction mechanism can be described in terms of two-step processes, that is, formation of a highly excited nucleus and its statistical decay.

References

- 1) H.C. Britt and A.R. Quinton: *Phys. Rev.*, 124, 877 (1961).
- 2) T. Inamura, M. Ishihara, T. Fukuda, T. Shimoda, and K. Hiruta: *Phys. Lett.*, 68B, 51 (1977).
- 3) T. Nomura, H. Utsunomiya, T. Motobayashi, T. Inamura, and M. Yanokura: *Phys. Rev. Lett.*, 40, 694 (1978); H. Utsunomiya, T. Nomura, T. Inamura, T. Sugitate, and T. Motobayashi: *Nucl. Phys.*, A334, 127 (1980).
- 4) R. Weiner and M. Weström: *ibid.*, A286, 282 (1977).
- 5) G.G. Ohlsen: *Proc. 4th Intern. Symp. on Polarization Phenomena in Nuclear Reactions*, Zürich, p.287 (1975).

4-7. Spin Alignment in Heavy Ion Reaction

K. Ieki, M. Ishihara, T. Nomura, H. Utsunomiya,
T. Sugitate, S. Kohmoto, and Y. Gono

NUCLEAR REACTIONS $^{159}\text{Tb}(^{14}\text{N}, \text{HI}), E = 115 \text{ MeV}$; measured γ -coin;
in-plane and out-of-plane; deduced spin alignment.

The present study is concerned with spin alignment of the residual nucleus. We have measured angular distribution of γ -rays coincident with heavy ejectiles ($2 \leq Z \leq 7$) in $^{159}\text{Tb} + ^{14}\text{N}$ reaction.

A self supporting ^{159}Tb target of 4 mg/cm^2 in thickness was bombarded with $115 \text{ MeV } ^{14}\text{N}$ beam from the cyclotron. Emitted particles were detected with counter telescopes of $50\text{--}2000 \mu\text{m}$ Si detectors fixed at 40° from the beam direction. Coincident γ -rays were measured with a Ge(Li) detector at 11 angles in the reaction plane and at 11 angles out of reaction plane.

Typical angular distributions of γ -rays are shown in Fig. 1. Strong anisotropy is found not only in out-of-plane correlation, but also in in-plane correlation in every final channel. This fact indicates that spin vector is aligned in a complicated way, which is far different from isotropic or cylindrical distributions. To extract

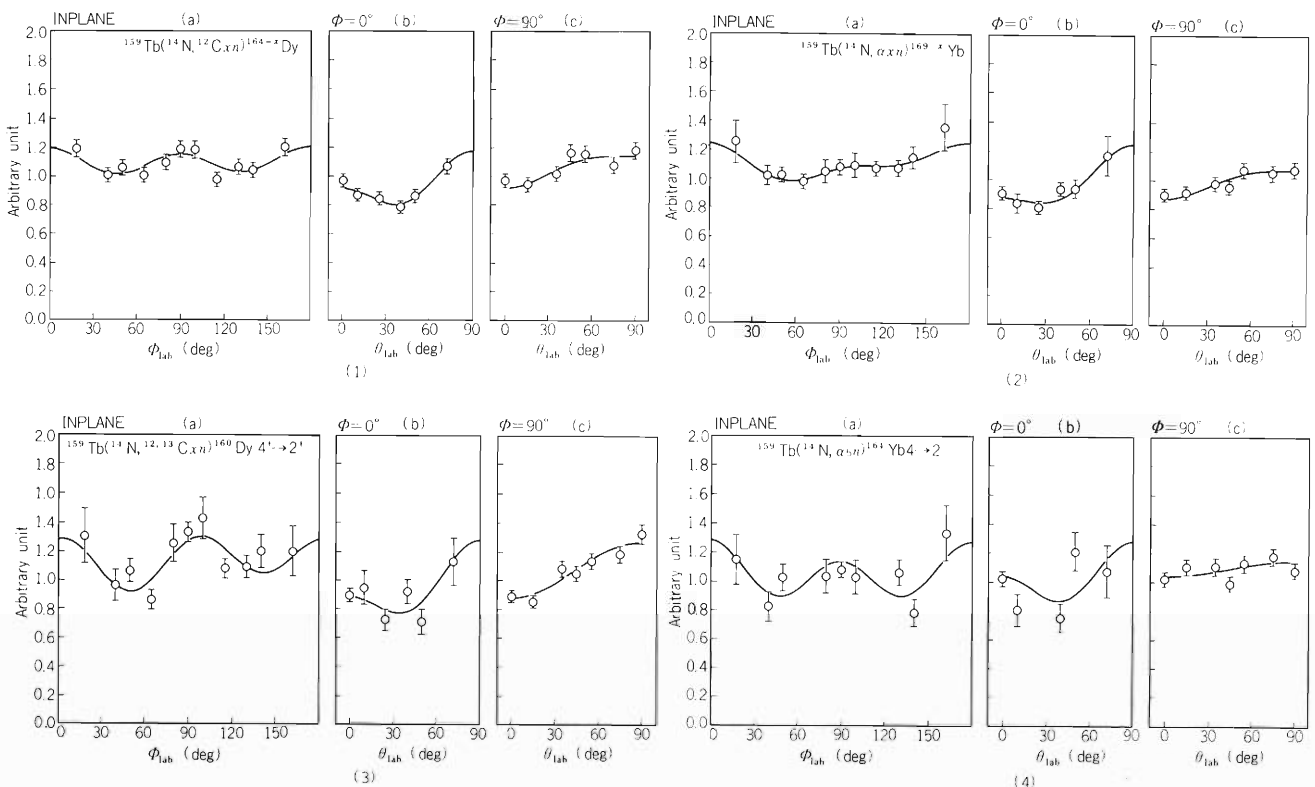


Fig. 1. Angular distributions of γ -rays. (a) is a distribution in the reaction plane. (b) is a distribution in the plane perpendicular to reaction plane and containing the beam axis. (c) is a distribution in the plane normal to the beam direction. Polar coordinate with z-axis normal to the reaction plane and x-axis to the beam direction is chosen in Lab. system. Yields are shown in arbitrary units. The curves are fits to the data (see text). Four reaction channels are shown:

- (1) an energy integrated γ -ray distribution coincident with C;
- (2) an energy integrated γ -ray distribution coincident with α ;
- (3) a γ -ray distribution of $^{160}\text{Dy } 4^+ \rightarrow 2^+$ transition coincident with C;
- (4) a γ -ray distribution of $^{164}\text{Yb } 4^+ \rightarrow 2^+$ transition coincident with α .

quantitative informations of spin alignment from γ -ray angular distributions, we performed following analysis.

With polar coordinate, angular distribution $W(\theta\phi)$ of γ -rays emitted from oriented states is expressed in general as

$$W(\theta\phi) \propto \sum_{\lambda q} (2\lambda+1)^{-1/2} A_{\lambda}(\gamma) \rho_{\lambda q} Y_{\lambda q}^*(\theta\phi), \quad (1)$$

where $\rho_{\lambda q}$ is statistical tensors of rank λ , which represent substate population of γ deexciting state and $Y_{\lambda q}^*$ are spherical harmonics. The angular distribution coefficient A_{λ} depends only on L, L', j_i, j_f , where L, L' are multiplicities of γ -ray and $j_i(j_f)$ is an angular momentum of initial(final) nuclear state. Eqn. (1) gives a relation between $W(\theta\phi)$ and spin alignment for a transition of given L, L', j_i, j_f . In the case of continuum γ -rays, however, it is rather difficult to specify j_i and j_f . In the present case, residual nuclei (i.e. Yb, Dy) are known to have good rotational properties, so that observed γ -rays of low energy (≤ 1.5 MeV) may be mostly attributed to stretched E2 transitions. In the case of $L = L', j_f = j_i - 2$, a transformation

$$\hat{\rho}_{\lambda q}(j_i) = \frac{\left\{ (2\lambda+1)(2j_i+\lambda+1)!(2j_i-\lambda)! \right\}^{-1/2}}{(2j_i)!} \rho_{\lambda q} \quad (2)$$

leads to

$$W(\theta\phi) \propto \sum_{\lambda q} A'_{\lambda} \hat{\rho}_{\lambda q}(j_i) Y_{\lambda q}^*(\theta\phi), \quad (3)$$

where A'_{λ} is independent of j_i . Note that j_i is only implicitly contained in Eqn. (3). We fitted γ -ray angular distributions to Eqn. (3) by least square method with $\hat{\rho}_{\lambda q}(j_i)$ as parameters. Using $\hat{\rho}_{\lambda q}(j_i)$ obtained, we further deduced a spin alignment parameter P_{zz} and its width σ defined by

$$P_{zz} = \frac{3}{2} \langle m^2 \rangle / j_i^2 - \frac{1}{2} \quad (4)$$

and

$$\sigma^2 = (\langle m^4 \rangle - \langle m^2 \rangle^2) / j_i^4, \quad (5)$$

where $\langle m^i \rangle$ is a i -th moment of magnetic substate m . P_{zz} characterizes spin alignment to z -axis and has a value between -0.5 and 1 , e.g. P_{zz} is positive for prolate alignment, negative for oblate alignment and zero for isotropic spin distribution. To investigate spatial spin distribution, we expressed P_{zz} and σ for following three different z -axes:

- (a) normal to reaction plane; (b) recoil direction; (c) normal to both (a) and (b) directions.

These three directions are orthogonal to each other, and a relation holds from the definition. The three dimensional distribution pattern of spin vectors may be characterized in a quantitative way in terms of these three P_{zz} 's. When the distribution of the spin vectors have axial symmetry with respect to one of the three axes, other two axes are equivalent and have the same P_{zz} values. For some typical cases, expected P_{zz} values are tabulated in Table 1: i) is the case for uniform spin distribution in the (a) – (c) plane, and ii) is the case for pure polarization with respect to (a) – axis.

$$P_{zz}(a) + P_{zz}(b) + P_{zz}(c) = 0 \quad (6)$$

Analyzed results are shown in Table 2. Errors from least square fit are smaller than 0.01 and omitted. Energy integrated γ -ray distributions are analyzed for different bins of particle energy. ‘‘Average’’ means weighted value with inclusive yields.

In every channel $P_{zz}(a)$ is positive, indicating an orientation favorable for (a)–axis. However, the size of $P_{zz}(a)$ is about $0.2 - 0.3$ and appreciably smaller than $P_{zz} = 1$ expected for pure polarization. In these cases the values of the ratio $R = W(\theta = 0^\circ) / W(\theta = 90^\circ)$ are $0.6 - 0.9$ and similar to those obtained for the $^{136}\text{Xe} + ^{197}\text{Au}$ reaction by Aguer et al.¹⁾ In Ref. 1 as well as in other works, $P_{zz}(a)$ was determined simply from the value of R by assuming axially symmetric Gaussian distribution of the spin vector with respect to (a)–axis. For instance, $P_{zz}(a) = 0.25$ corresponds to $R = 0.75$. We note that the value of R strongly depends on the direction angle ϕ so that such an analysis as in Ref. 1 may be sometimes misleading.

Table 1. P_{zz} value for typical cases.

	$P_{zz}(a)$	$P_{zz}(b)$	$P_{zz}(c)$
i)	0.25	-0.50	0.25
ii)	1.00	-0.50	-0.50

Table 2. Alignment parameter P_{zz} and its width σ .

Continuum γ -rays		P_{zz}			σ		
Emitted particle	Energy (MeV)	(a)	(b)	(c)	(a)	(b)	(c)
		^{12}C	80-90	0.20	-0.04	-0.16	0.26
	90-100	0.22	-0.12	-0.10	0.18	0.36	0.21
	Average	0.21	-0.07	-0.13	0.23	0.37	0.24
^{13}C	80-90	0.24	-0.14	-0.09	0.31	0.36	0.28
	90-100	0.23	-0.12	-0.11	0.22	0.36	0.32
	100-	0.24	-0.30	-0.06	0.19	0.21	0.31
	Average	0.24	-0.17	-0.09	0.23	0.32	0.31
α	20-25	0.21	-0.18	-0.03	0.26	0.34	0.28
	25-30	0.26	-0.17	-0.09	0.29	0.35	0.27
	30-35	0.34	-0.25	-0.09	0.28	0.29	0.31
	35-	0.36	-0.33	-0.33	0.22	0.19	0.29
	Average	0.27	-0.22	-0.06	0.27	0.31	0.28

Inspection of three P_{zz} 's may help to visualize the three dimensional pattern of spin distribution. In the case of α -particle channels, rather large negative values are obtained for $P_{zz}(b)$ indicating oblate spin alignment with respect to (b)-axis. Together with a relating large positive value of $P_{zz}(a)$, the spin orientation may be supposed to have roughly a sector shape distribution in (a) - (c) plane with direction (a) favored. In the case of C-channels, values of $P_{zz}(b)$ and $P_{zz}(c)$ are rather close to each other indicating a more symmetric spin distribution with respect to the (a)-axis. We also note that P_{zz} 's show a systematic dependence on Q-value. As the particle energy decreases, $P_{zz}(a)$ becomes smaller and $P_{zz}(b)$ larger towards positive. The latter results complies with the fact that (b) becomes larger with increasing inelasticity and may imply that the spin distribution becomes less confined in the (a) - (c) plane with increasing inelasticity of the reaction. This observation may be related to the fact that for larger negative Q-values the contact time of the colliding ions becomes longer so that the direction of transferred momentum may be more randomly distributed.

In the present preliminary analysis stretched E2 transitions were assumed for continuum γ -rays. It was shown that the spin vector distribution generally has a complicated pattern which does not have simple symmetries. The present analysis in terms of three P_{zz} 's may work as a simple method to represent such a distribution.

Reference

- 1) P. Aguer, R. P. Schmitt, G. J. Wozniak, D. Habs, R. M. Diamond, C. Ellegard, D. L. Hillis, C. C. Hsu, G. J. Mathews, L. G. Moretto, G. U. Rattazzi, C. P. Roulet, and F. S. Stephens: Phys. Rev. Lett., 43, 1778 (1979).

Y. Nagame, I. Kohno, M. Yanokura,
H. Kudo*, and H. Nakahara

(NUCLEAR REACTIONS $^{20}\text{Ne} + ^{50}\text{Cr}$, $E_{\text{lab}} = 146, 93 \text{ MeV}$)
measured charges $6 \leq Z \leq 20$, cross section, energy spectra,
angular distribution, charge distribution.

It has been predicted theoretically by Cohen et al.¹⁾ using the rotating liquid drop model that the large angular momenta involved in heavy ion reactions are expected to lower the fission barrier of rotating compound nuclei sufficiently to make fission a competing deexcitation process. For relatively light nuclear system, compound nuclear fission is predicted²⁾ to occur only at high angular momenta because the fission barrier, as calculated by rotating liquid drop model,¹⁾ decrease rapidly with increasing angular momentum. It is, however, difficult to distinguish fission from deeply inelastic process that involve both a large amount of mass transfer and an interaction time of the order of several rotations, resulting in a $1/\sin \theta$ angular distribution in the c.m. system. According to the rotating liquid drop model, the angular momentum dependence of fission barrier height varies with the fissility (Z^2/A), where Z and A are the atomic number and mass number of the fissioning nucleus. Therefore, we have been studying the systematic changes of the energy, angular and charge distributions of emitted particles as a function of the fissility and incident projectile energies. In the previous paper,³⁾ the isotopic dependence of the cross section for heavier products ($Z \geq 11$) was observed using the reaction system of 115 MeV $^{14}\text{N} + ^{58}\text{Ni}$ and $^{14}\text{N} + ^{64}\text{Ni}$.

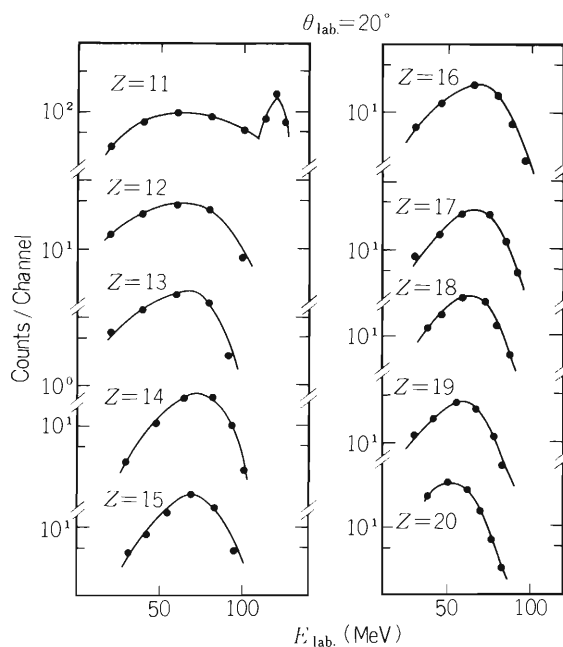


Fig. 1. The energy distributions of products ($Z \geq 11$) at $\theta_{\text{lab}} = 20^\circ$ in the reaction of 146 MeV $^{20}\text{Ne} + ^{50}\text{Cr}$.

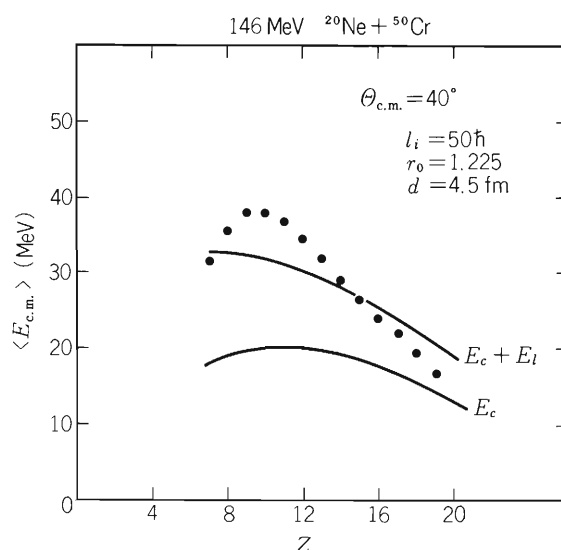


Fig. 2. The most probable kinetic energies as a function of the product charge for the system 146 MeV $^{20}\text{Ne} + ^{50}\text{Cr}$. Comparison with a result of calculation including the Coulomb (E_c) and centrifugal (E_l) components ($d = 4.5 \text{ fm}$).

* Tokyo Metropolitan University.

In this study, the bombarding energy dependence, i.e., angular momentum dependence has been investigated, especially for heavy products ($Z \geq 11$), with the $^{20}\text{Ne} + ^{50}\text{Cr}$ reaction system whose fissility ($Z^2/A \sim 16$) is close to the previous system. The critical angular momenta (ℓ_{cr}) for fusion calculated by Bass model⁴⁾ are 53h and 40h for the 146 MeV $^{20}\text{Ne} + ^{50}\text{Cr}$ system and 93 MeV $^{20}\text{Ne} + ^{50}\text{Cr}$ system, respectively. The liquid drop fission barrier at the ℓ_{cr} , calculated from Ref. 1 are 4 MeV and 17 MeV for 146 MeV system and 93 MeV system, respectively. From these values the fission cross section for 146 MeV $^{20}\text{Ne} + ^{50}\text{Cr}$ is expected to be larger than that for 93 MeV $^{20}\text{Ne} + ^{50}\text{Cr}$.

The experiments were performed at the cyclotron. An enriched self-supporting ^{50}Cr target of $500\mu\text{g}/\text{cm}^2$ thickness was bombarded with $^{20}\text{Ne}^{6+}$ ions at beam energies of 146 and 93 MeV. The reaction products were detected with ΔE -E counter telescope consisting of a gas proportional ΔE and a $300\mu\text{m}$ thick solid state E detector⁵⁾. The products with atomic numbers from 6 to 20 could be identified in the bombardment of ^{50}Cr by 146 MeV ^{20}Ne , and the energy spectra, angular and charge distributions of products were obtained.

Figure 1 shows the energy distributions at $\theta_{\text{lab}}=20^\circ$ for $Z \geq 11$. The single bell-shaped kinetic energy peaks in the region of the strongly damped collisions were observed for the products with $Z \geq 12$. The observed most probable kinetic energies at $\theta_{\text{c.m.}}=40^\circ$ were indicated by solid circles in Fig. 2 as a function of their atomic numbers. The kinetic energies calculated by Coulomb (E_C) energy and centrifugal force (E_ρ) which was obtained using the sticking model are shown by solid curves in Fig. 2. The good agreement for heavy products is obtained with $d=4.5\text{fm}$ and $\ell_i=50h$ ($\sim \ell_{\text{cr}}$), where d is the deformation factor and ℓ_i is the initial angular momentum. This large d is interpreted as representing a large deformation of the fragments at the scission point. The angular distributions for the products with $Z \geq 14$ show almost constant distributions in the c.m. system (Fig. 3). Thus these products ($Z \geq 14$) are considered to be either fusion-fission fragments or fragments emitted after interaction times that were longer than the time required for one rotation of the composite system. The charge distributions for various angles are shown in Fig. 4.

In 93 MeV $^{20}\text{Ne} + ^{50}\text{Cr}$ system, the contribution of strongly damped components or fusion-fission components could not be observed. It is considered that these results reflect some effects of angular momentum dependence.

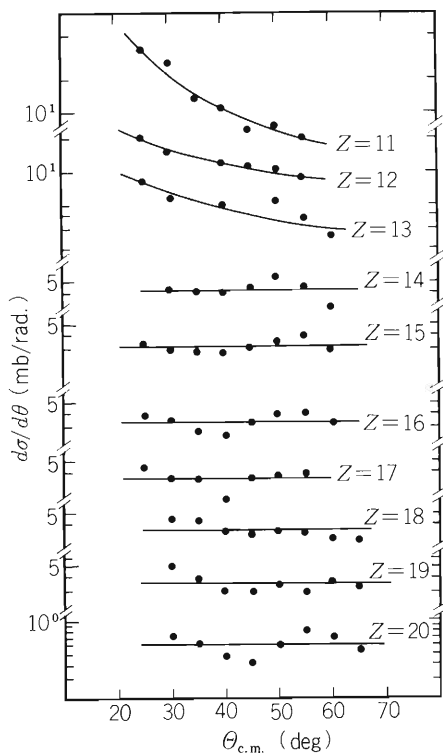


Fig. 3. The center-of-mass angular distributions for different charges produced in the reaction 146 MeV $^{20}\text{Ne} + ^{50}\text{Cr}$.

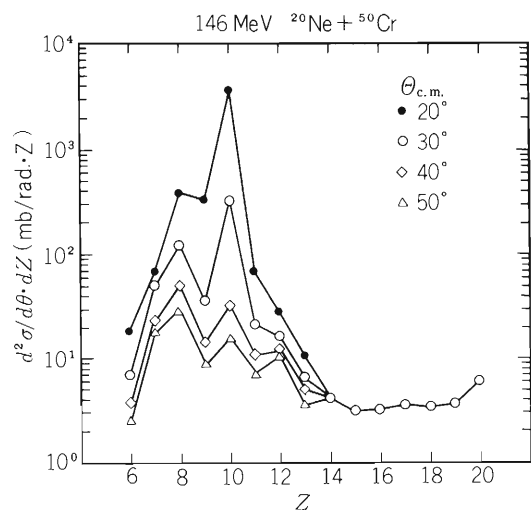


Fig. 4. The charge distribution at different center-of-mass angles for the system 146 MeV $^{20}\text{Ne} + ^{50}\text{Cr}$.

We are now studying the system of 120 MeV $^{20}\text{Ne} + ^{50}\text{Cr}$ reactions to investigate the angular momentum dependence in more detail.

References

- 1) S. Cohen, F. Plasil, and W.J. Swiatecki: *Ann. Phys.*, 82, 557 (1974).
- 2) F. Plasil and M. Blann: *Phys. Rev. C*, 11, 508 (1975).
- 3) M. Yanokura, H. Nakahara, and I. Kohno: *J. Phys. Soc. Japan*, 50, 369 (1981).
- 4) R. Bass: *Nucl. Phys.*, A231, 45 (1974).
- 5) M. Yanokura, I. Kohno, H. Nakahara, and K. Yamakoshi: *Oyo Buturi*, 49, 1095 (1980).

4-9. Recoil Range Distributions in the Reaction Induced by 115 MeV ^{14}N on ^{62}Ni

Y. Nagame, M. Watanabe,* H. Kudo,* H. Nakahara,
I. Kohno, and M. Yanokura

{ NUCLEAR REACTIONS $^{62}\text{Ni}(^{14}\text{N},x)$, $E=115$ MeV, measured
projected recoil ranges, measured cross sections. }

The nuclear reactions induced by 115 MeV ^{14}N ions on ^{62}Ni target have been investigated using recoil technique. The heavy products from fusion-evaporations and transfer reactions could be separated by radiochemical methods. The enriched ^{62}Ni target of self-supporting $900 \mu\text{g}/\text{cm}^2$ thick metallic foil was prepared by the electrodeposition method. The bombardments were performed with $^{14}\text{N}^{5+}$ ions accelerated in the cyclotron at the energy of 115 MeV for 10 to 15 h. The recoil ion ranges projected to the beam direction were measured by placing the target and a stack of $200 \mu\text{g}/\text{cm}^2$ thick Al catcher foils in front of a Faraday cup. For Co and Sc isotopes, the γ -ray spectrometries were performed after chemical separations, while other heavy products were directly measured with Ge(Li) detector.

The range distributions were obtained for each reaction products as shown in Figs. 1, 2. In Figs. 1, 2, the

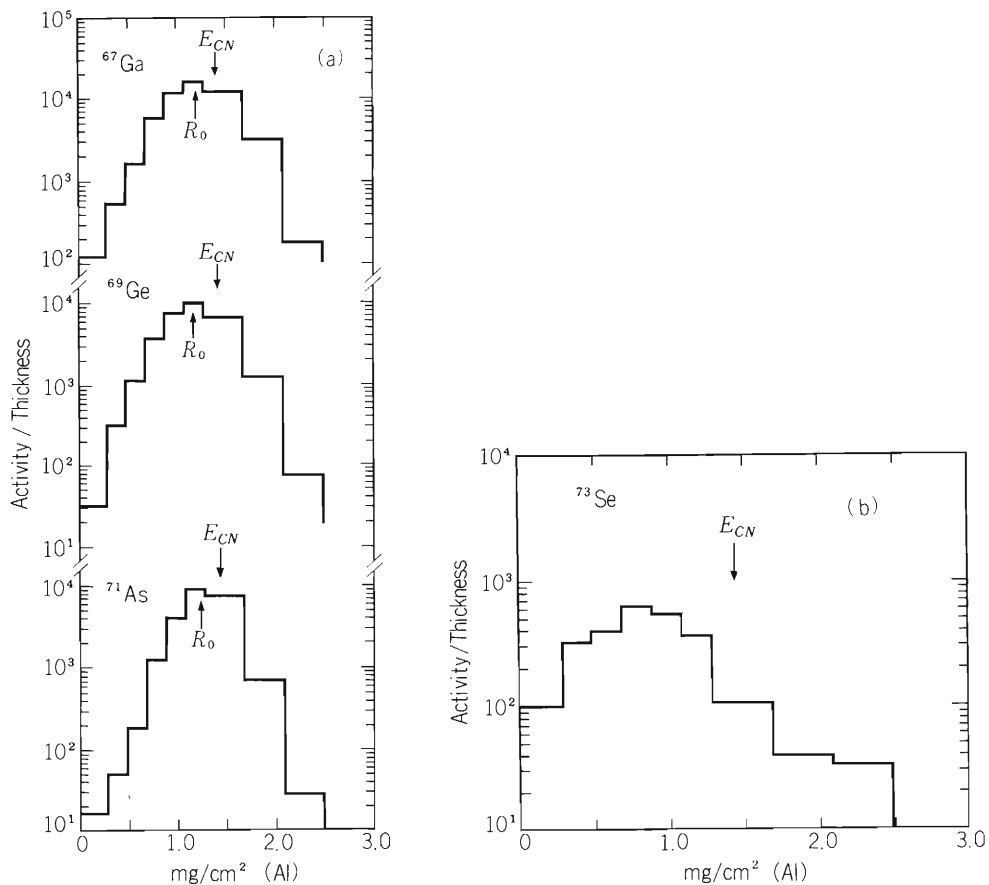


Fig. 1. Projected recoil range distributions of evaporation residue products: (a) ^{71}As , ^{69}Ge , and ^{67}Ga ; (b) ^{73}Se .

* Tokyo Metropolitan University.

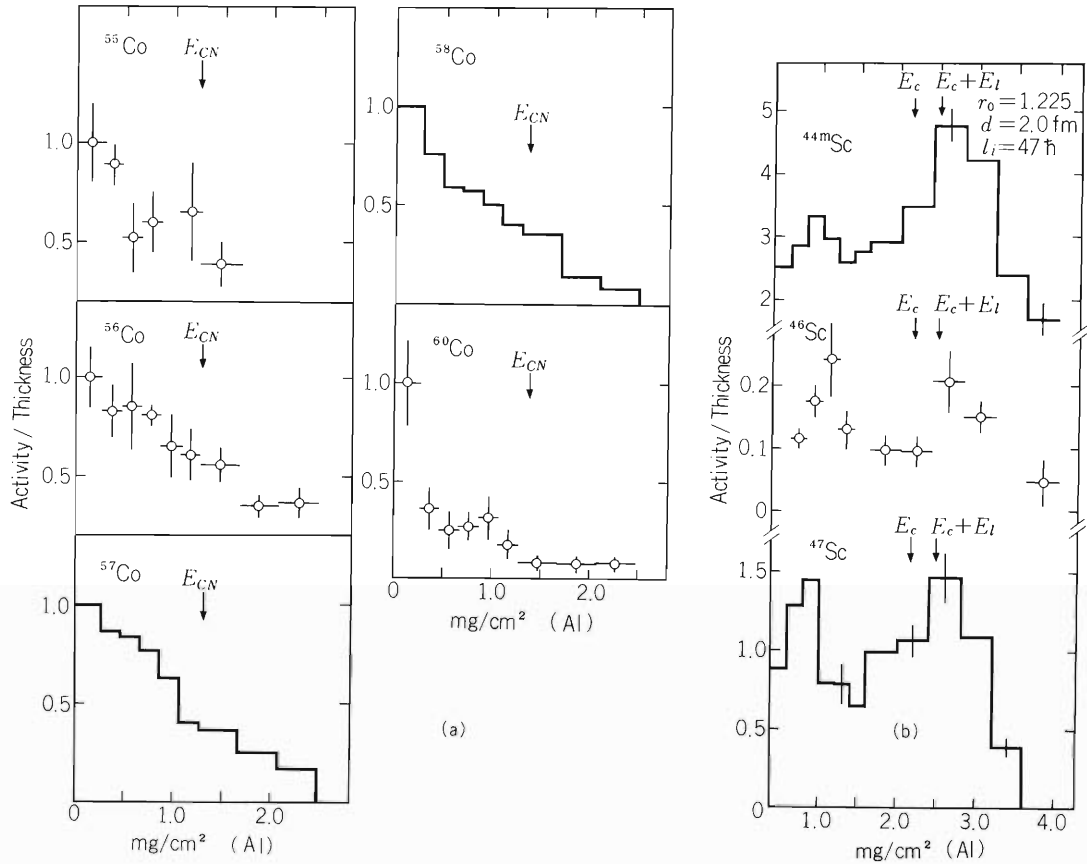


Fig. 2. Projected recoil range distributions of transfer reaction products: (a) Co isotopes; (b) Sc isotopes.

vertical arrows labeled E_{CN} indicate the range which would correspond to a full momentum transfer reaction, i.e., compound nucleus formation. The range-energy relationship is deduced using Northcliffe and Schilling tables.¹⁾ The arrows labeled R_0 designate the average range obtained in this experiment. The range distributions of the evaporation residue products collected in Fig. 1 (a) show typical Gaussian distribution and R_0 is close to E_{CN} . These results can be considered as an evidence for compound nucleus formation. On the other hand, the short mean range of ^{73}Se in Fig. 1 (b) can not be accounted for compound nucleus formation. This suggests that the pre-equilibrium particle emissions from composite system have occurred. The mean range of each Co isotope in Fig. 2 (a) is considerably shorter than that expected by full momentum transfer reaction. This includes the possibility of a predominant contribution from direct transfer reactions. The range distributions for Sc isotopes are shown in Fig. 2 (b). The arrows E_C and $E_C + E_l$ indicate the range which would correspond to Coulomb energy and Coulomb energy plus centrifugal energy, respectively. The parameters used for the calculations of the sticking model are also shown in Fig. 2 (b). The mean range of Sc isotopes is close to the range expected by $E_C + E_l$, and these Sc products are considered to be either fusion-fission fragments or strongly damped fragments. The peaks in the shorter ranges in Fig. 2 (b) are assumed to be the contribution from impurity in Al catcher foils. The cross sections for Co and Sc isotopes were obtained as shown in Fig. 3. The arrows labeled T and CN indicate the N/Z ratio which would correspond to the target and composite nucleus, respectively. The equilibration of N/Z ratio for Co and Sc isotopes were close to that of the composite nucleus. The Q_{gg} dependence of transfer reaction products (Co isotopes) is obtained except for ^{60}Co isotope as shown in Fig. 4. The nuclear temperature estimated by these isotope production was deduced to be 2.3 MeV from the following expression²⁾:

$$\sigma \propto \exp \left\{ (Q_{gg} + \Delta E_C) / T \right\} .$$

According to the statistical hypothesis concerning the Q_{gg} systematics, the production of ^{60}Co isotope is considered to be more direct transfer reaction than that of other Co isotopes.

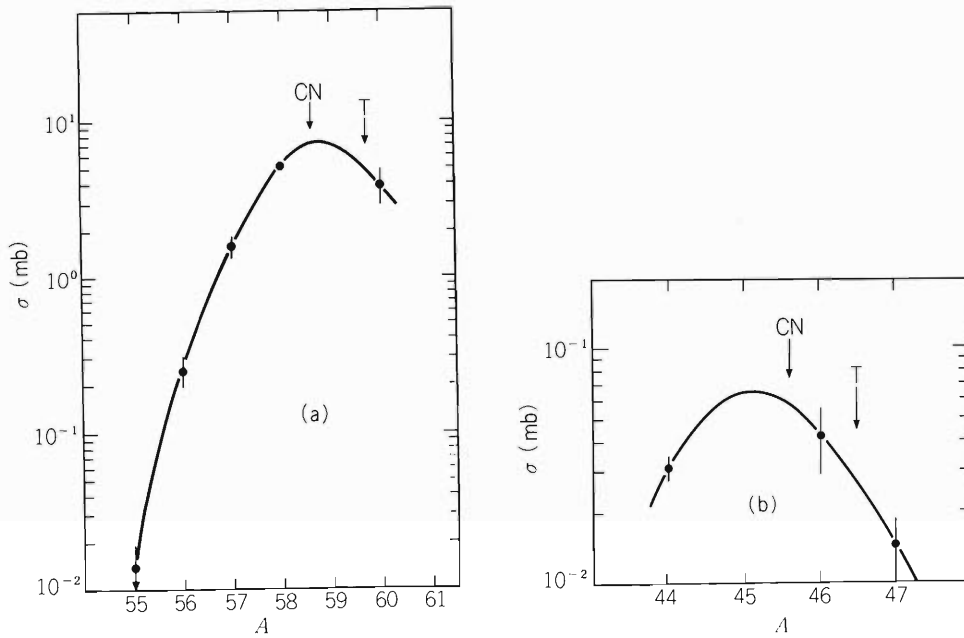


Fig. 3. Cross sections as a function of mass number: (a) Co isotopes; (b) Sc isotopes. Solid lines are drawn to guide the eye.

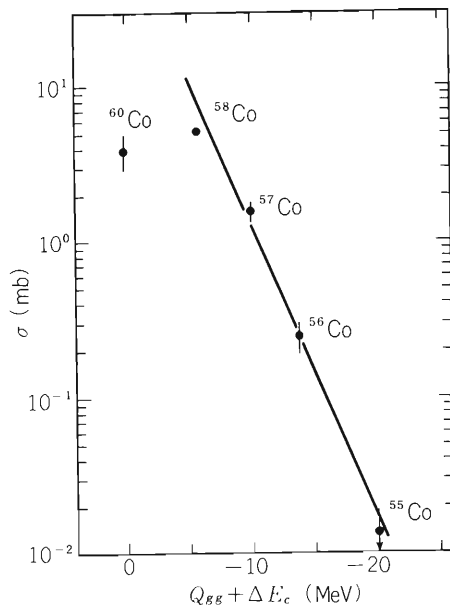


Fig. 4. The Q_{gg} dependence of Co isotopes. ΔE_c indicate the change of Coulomb interaction energy.

References

- 1) L. C. Northcliffe and R. F. Schilling: Nucl. Data Tables, A7, 233 (1970).
- 2) V. V. Volkov: Phys. Rep., 44, 93 (1978).

4-10. Correlation between the Fragment Mass and the Angular Anisotropy in the Proton-Induced Fission of ^{232}Th

H. Kudo,* Y. Nagame,* H. Nakahara,
I. Kohno, and M. Yanokura

NUCLEAR REACTION $^{232}\text{Th} (p, f)$; angular distribution,
excitation function two-mode hypothesis, K_0^2 , BCS model,
angular anisotropy.

The angular distributions of fission fragments were measured in the 15 MeV proton-induced fission of ^{232}Th . The details of the experimental procedure have already been reported.¹⁾ Angular anisotropies obtained for various masses are shown in Fig. 1. From this figure, it was found that the angular anisotropy is dependent on the fission fragment mass: the angular anisotropies of symmetrically divided fission fragments are smaller than those of asymmetrically divided fission fragments. Therefore, the mechanism of symmetric mass division is expected to be different from that of asymmetric mass division.

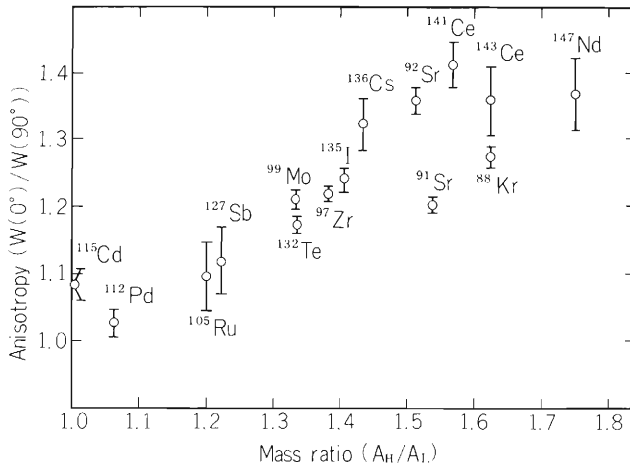


Fig. 1. Anisotropy in angular distributions of fission fragments from 15 MeV proton-induced fission of ^{232}Th vs mass ratio (mass of heavy fragment divided by mass of complementary light fragment).

In order to interpret the observed anisotropies, it is necessary to know the amount of contribution from each multiple chance fission, namely, (p, f), (p, nf), and (p, 2nf). For this purpose detailed excitation functions of fission products and neutron evaporation products were measured in the proton energy range of 8 ~ 22 MeV. It was found that the excitation functions of symmetrically divided fission fragments were apparently different from those of asymmetrically divided ones. This difference is shown in Fig. 2 as the ratio of the cross section of ^{115}Cd to that of ^{91}Sr . The excitation function of (p, xn) reactions and fission products are plotted in Fig. 3.

Both the anisotropy data and the excitation functions of fission fragments strongly suggest that asymmetric fission and symmetric fission proceed through different saddles. Therefore, for interpretation of these results, two-mode hypothesis was introduced. In the two-mode hypothesis the existence of two independent types of fission is assumed. For interpretation of the observed excitation functions the cross sections of the statistical evaporation and fission were calculated using the Alice code²⁾ which was modified by us to include the symmetric and asymmetric fission barriers and sub-barrier penetration terms. The results of this calculation are shown in Figs. 2 and 3 by solid lines, and used parameters and deduced quantities are tabulated in Table 1. The fission barrier heights for the asymmetric fission used in the calculation to give the best fit to the observed excitation functions are in good agreement with other reported data³⁾ and those for the symmetric fission are

* Tokyo Metropolitan University.

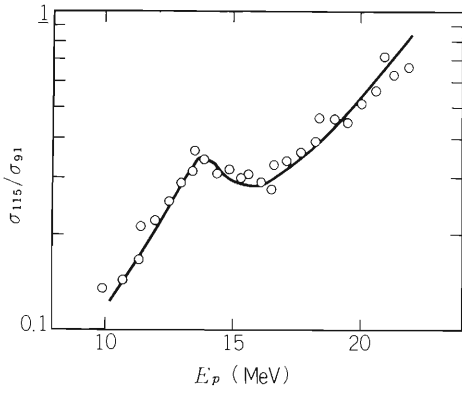


Fig. 2. Cross section ratio of ^{115}Cd to ^{91}Sr . Solid line is calculated with modified Alice code assuming the yield of ^{115}Cd in symmetric fission mode and the yield of ^{91}Sr in asymmetric fission mode are constant in this energy region.

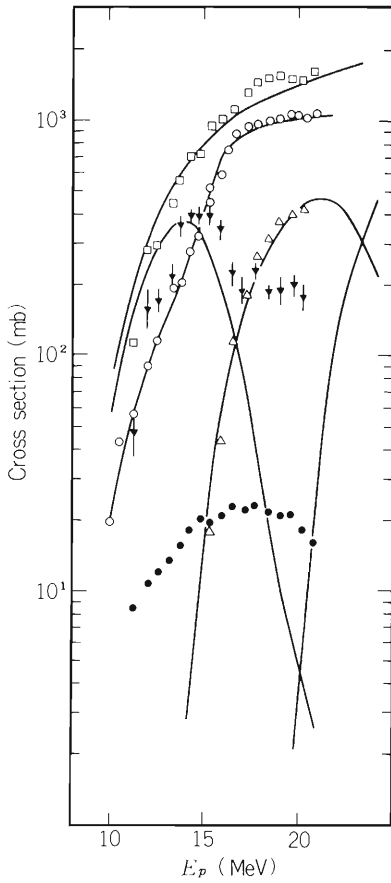


Fig. 3. Excitation functions of neutron evaporation products and fission. \circ : total fission; \bullet : $^{232}\text{Th}(p, n)^{232}\text{Pa}$; \blacktriangle : $^{232}\text{Th}(p, 2n)^{231}\text{Pa}$; \triangle : $^{232}\text{Th}(p, 3n)^{230}\text{Pa}$; \square : reaction cross section which was assumed to be the sum of cross sections of fission and evaporation process. Solid lines are the result of calculation with modified Alice code.

very close to the value for ^{232}Th predicted theoretically by Möller and Nix.⁴⁾ From this statistical calculation, the amount of contribution from each multiple chance fission and the effective excitation energies at the saddle points could be deduced as shown in Table 1.

The angular anisotropy of fission fragments is, according to Bohr's channel theory, related to the K quantum number of the saddle point configuration and given by the following equation at rather high excitation energies⁵⁾:

$$W(\theta) \propto \sum_{J=0}^{\infty} \frac{(2J+1)^2 T_J \exp \left\{ - \left(J + \frac{1}{2} \right)^2 \sin^2 \theta / 4K_0^2 \right\} J_0 \left\{ i \left(J + \frac{1}{2} \right)^2 \sin^2 \theta / 4K_0^2 \right\}}{\text{erf} \left\{ \left(J + \frac{1}{2} \right) / \left(2K_0^2 \right)^{1/2} \right\}}, \quad (1)$$

Table 1. Used parameters and deduced quantities in the calculation of proton-induced fission of ^{232}Th with modified Alice code.

B_f is fission barrier height; a_f and a_n are level density parameter at saddle point and ground state, respectively, and a_n was taken to be $A/8 \text{ (MeV)}^{-1}$ (A = mass number of fissioning nucleus). E_{ex} is excitation energy at saddle point and t is nuclear temperature at saddle point.

		B_f (MeV)	a_f/a_n	E_{ex} (MeV)*	t (MeV)*	Contribution to each mode of fission*
Asymmetric fission	(p, f)	5.9	1.02	14.3	0.69	0.39
	(p, nf)	6.2		7.5	0.50	0.05
	(p, 2nf)	6.0		2.1	0.27	0.56
Symmetric fission	(p, f)	8.8	1.15	11.4	0.58	0.98
	(p, nf)	8.7		5.0	0.39	0.02

* At $E_p = 15 \text{ MeV}$.

where J_0 is the zeroth order Bessel function and $\text{erf}(X)$ is the error function. K_0^2 is given by $t \cdot I_{\text{eff}}^2 / \hbar^2$, where t is nuclear temperature and I_{eff} is effective moment of inertia which is defined by

$$\frac{1}{I_{\text{eff}}} = \frac{1}{I_{\parallel}} + \frac{1}{I_{\perp}},$$

where I_{\perp} and I_{\parallel} are the moments of inertia around the axes perpendicular and parallel to the nuclear symmetry axis, respectively. J and T_J are the total angular momentum and the transmission coefficient, respectively.

However, for the nuclei of low excitation energy, the effect of nuclear pairing has to be taken into consideration (BCS model)⁶⁾ and the ordinary statistical argument of K_0^2 has to be modified accordingly. The moment of inertia of the nuclear superconductor is considerably smaller than that of rigid body⁷⁾. In the BCS model, K_0^2 is given by

$$K_0^2 = \frac{I_{\perp}}{I_{\perp} - A(t) I_{\parallel}^{\text{rigid}}} \cdot \frac{t_c I_{\parallel}^{\text{rigid}}}{\hbar^2} \cdot t \cdot A(t), \quad (2)$$

where $I_{\parallel}^{\text{rigid}}$ is the rigid body moment of inertia with respect to the symmetry axis, t_c is the critical temperature, t is nuclear temperature in unit of t_c , and $A(t)$ is the temperature-dependent integral. In the 15 MeV proton-induced fission of ^{232}Th , the excitation energy for the asymmetric third chance fission is expected to be only 2.1 MeV at the saddle point. Therefore, the pairing effect should be taken into account in the interpretation of the data. In the present case, t_c and $A(t)$ is estimated to be 0.431 and 0.336 MeV, respectively, for the fissioning nucleus ^{231}Pa from Ref. 7.

Using the results of calculation on the evaporation-fission competition including the two-mode hypothesis and Eqns. (1) and (2), angular anisotropy of the present system can be deduced theoretically. The result is tabulated in Table 2 together with the values of $A(t)$, I_{\perp}^{rigid} , $I_{\parallel}^{\text{rigid}}$ and K_0^2 . The angular anisotropies obtained are in good agreement with the observed data for the fragments produced by typical asymmetric and symmetric mass divisions (^{92}Sr , ^{141}Ce , ^{147}Nd , etc. for typical asymmetric mass division, ^{115}Cd , ^{112}Pd for typical symmetric mass division). The angular distributions of the fragments intermediate in the mass division can be considered to be mixtures of the angular distributions of asymmetric and symmetric fission modes.

It is concluded that, with the assumption of two saddle point configurations, one for symmetric fission and the other for asymmetric fission, the observed angular distributions of fission fragments could be reproduced

reasonably well. Therefore, it is suggested that the gross feature of the final mass division in fission process is already determined at saddle point configuration through which the nuclear collective motion would proceed.

Table 2. Theoretically predicted angular anisotropies in the 15 MeV proton-induced fission of ^{232}Th .

		A(t)	I_{\perp}^{rigid}	$I_{\parallel}^{\text{rigid}}$	K_0^2	W(0°)/W(90°)	$\left\{ \frac{W(0^\circ)}{W(90^\circ)} \right\}_{\text{sum}}$
Asymmetric fission	(p, f)	1	1.90	0.5675	71	1.05	1.30
	(p, nf)	1	1.89	0.5695	51	1.07	
	(p, 2nf)	0.336	1.88	0.5710	7	1.50	
Symmetric fission	(p, f)	1	1.90	0.5675	59	1.06	1.06
	(p, nf)	1	1.89	0.5695	40	1.08	

References

- 1) H. Kudo, H. Muramatsu, H. Nakahara, K. Miyano, I. Kohno, and M. Yanokura: IPCR Cyclotron Progr. Rep., 13, 24 (1979).
- 2) F. Plasil: ORNL Report, TM-6054 (1977).
- 3) B. B. Back, H. C. Britt, O. Hansen, B. Leoux, and J. D. Garrett: Phys. Rev. C, 10, 1948 (1974); R. Vandenbosch and G. T. Seaborg: Phys. Rev., 110, 507 (1958).
- 4) P. Möller and J. R. Nix: Nucl. Phys., A229, 269 (1974).
- 5) J. A. Wheeler: "Fast Neutron Physics", Wiley (Interscience), New York, Pt. II, p. 2051 (1963).
- 6) R. Vandenbosch, H. Warhanek, and J. R. Huizenga: Phys. Rev., 124, 846 (1961).
- 7) J. J. Griffin: *ibid.*, 132, 2204 (1963).

4-11. Friction Tensors for Ar + Au and Cu + Au

A. Iwamoto,* S. Yamaji, K. Harada,* and S. Yoshida

$\left\{ \begin{array}{l} \text{NUCLEAR REACTIONS} \quad \text{Microscopic calculation of friction tensors} \\ \text{for the systems Ar + Cu and Cu + Au: linear response theory:} \\ \text{two-center shell model.} \end{array} \right\}$

In Ref. 1 we have applied the linear response theory to the calculation of friction tensors for the system Ne + Al. In this calculation, use of the two-center shell model for the basic Hamiltonian was found to have a promising feature, namely, it could give us values of friction tensors systematically even for a very complicated configuration encountered in the heavy-ion reaction. These values were used later²⁾ in the equation-of-motion calculation and typical features of deep-inelastic collision were reproduced well. Although many works have been done for the microscopic calculation of friction tensors, there are only a few works which have calculated form factors properly. Thus we think it is useful to apply our model to heavier systems and analyze form factors of friction tensors.

In the calculation presented here, we changed the method of "subtraction" described in Ref. 1. This is because we intended to obtain friction tensors at surface region as accurate as possible. Another new point is that we included a new collective coordinate η , which describe the mass flow between two nuclei. As a result, we could also calculate friction tensors resulting from particle transfer.

We start from the expression of friction tensors given by linear response theory,

$$\gamma_{\mu\nu} = 4\pi\Gamma \sum_{jk} I_{jk} \frac{(e_k - e_j) \langle j | \hat{F}_\mu | k \rangle \langle k | \hat{F}_\nu | j \rangle}{\{(e_k - e_j)^2 + \Gamma^2\}^2} \quad (1)$$

where

$$I_{jk} = \frac{1}{1 + \exp\left(\frac{e_j - \lambda}{kT}\right)} \left\{ 1 - \frac{1}{1 + \exp\left(\frac{e_k - \lambda}{kT}\right)} \right\}. \quad (2)$$

Symbols used in these expressions are the same as in Ref. 1 and \hat{F}_μ stands for the generalized force corresponding to the coordinate μ . Single-particle energy e_j and wave function $|j\rangle$ are generated by the two-center Hamiltonian. As collective coordinates, we choose three kinds of coordinates: the distance R between two nuclei, the deformation δ of two nuclei (for simplicity, we assume the same deformation for both nuclei) and η which is given by $\eta = (A_1 - A_2) / (A_1 + A_2)$ where A_1 and A_2 are mass numbers of the two nuclei.

As was discussed in Ref. 1, there occurs a spurious term in Eqn. (1) when we calculate γ_{RR} , $\gamma_{R\delta}$, and $\gamma_{R\eta}$. It is connected to spurious excitation arising from the translational motion of each nucleus. In order to eliminate this contribution, we proceed as follows: when two nuclei are located with their surfaces touching each other or they are only a little distance apart (friction tensors for such configurations are most important and we concentrate ourselves to these configurations), we can classify the single-particle wave function according to whether it is localized to nucleus 1 or to 2. Correspondingly, matrix element $\langle k | \hat{F}_\mu | j \rangle$ appearing in Eqn. (1) is classified into three kinds: one where wave functions $|j\rangle$ and $\langle k|$ are localized to nucleus 1, one where $|j\rangle$ and $\langle k|$ are localized to nucleus 2 and one where $|j\rangle$ and $\langle k|$ are localized to different nuclei. Physically, the third one is related to particle transfer between two nuclei. We neglect it because the operator

* Japan Atomic Energy Research Institute.

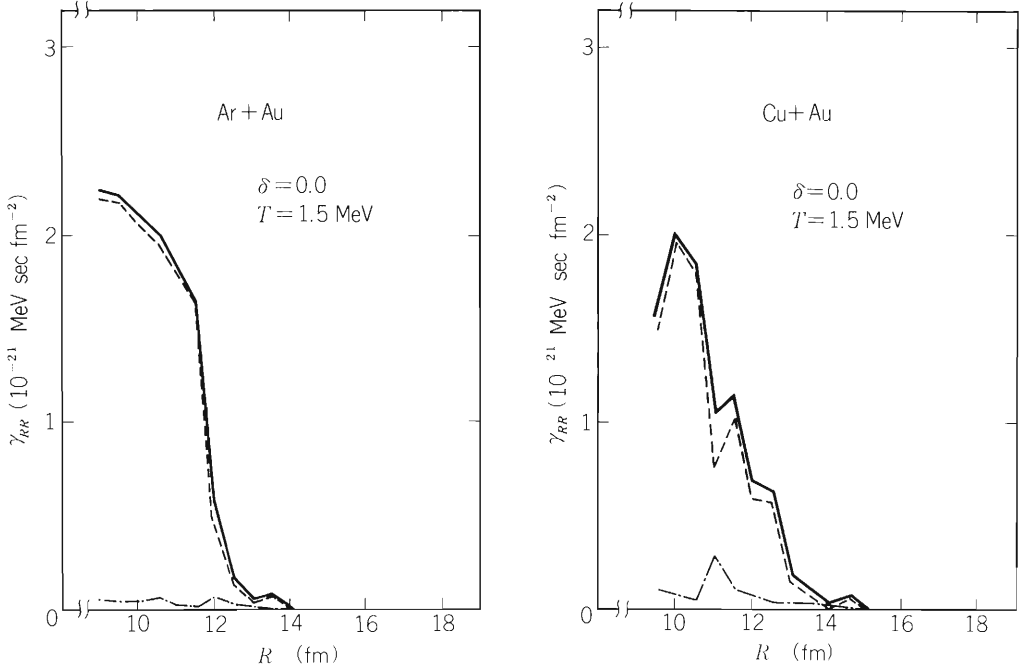


Fig. 1. Friction tensors γ_{RR} as a function of center separation R . Dashed lines are the contributions from heavy nucleus, the dot-and-dash lines are those from light nucleus and the solid lines are their sums. a) for Ar + Au system, b) for Cu + Au system.

\hat{F}_R has nothing to do with such process. Rather, the contribution from such process is accounted for by taking account of the η -motion in our model. The “subtraction” is carried out in our model in such a manner that the matrix element of the first kind is calculated in the rest frame of nucleus 1 and the matrix element of the second kind in the rest frame of nucleus 2. In this way, we calculate the excitation of nucleus 1 by the proximity of nucleus 2 and vice versa. In the calculation of friction tensors corresponding to η -motion, we adopt a similar method of subtraction. That is, we neglect the matrix element of the first and the second kinds and include only the third one. The details of this method will be published elsewhere.

In Fig. 1, we show the radial friction γ_{RR} calculated for systems Ar + Au and Cu + Au as function of center separation R . A contribution from heavy nucleus (Au) is shown by dashed lines, that from light nucleus

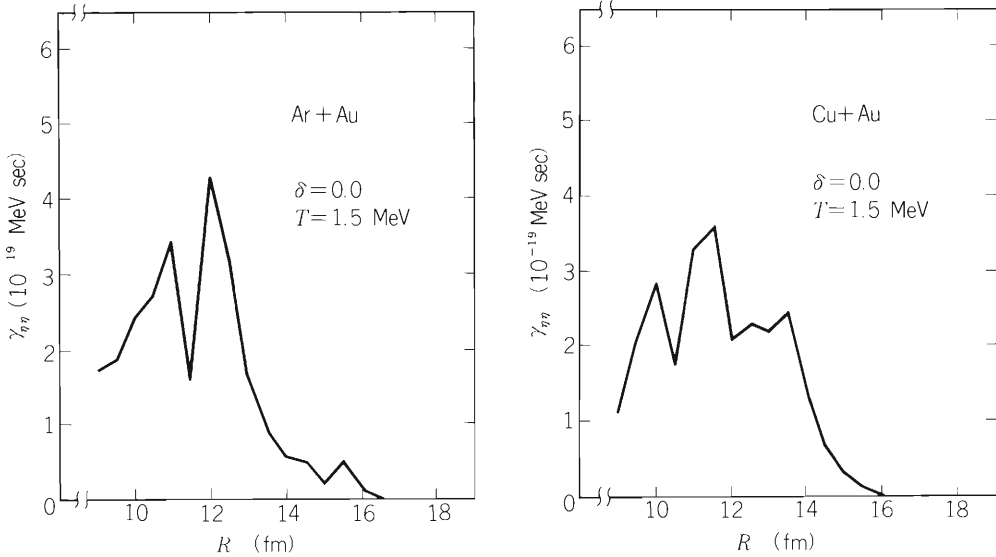


Fig. 2. Friction tensors $\gamma_{\eta\eta}$ as a function of center separation R . a) for Ar + Au system, b) for Cu + Au system.

(Ar, Cu) by dot-and-dash lines. We find that the contribution from heavy nucleus occupies the dominant part of the radial friction. It means that the intrinsic excitation of heavy nucleus is much larger than that of light nucleus. It seems that relative single-particle level densities near Fermi level plays a predominant role to allocate excitation energy to two nuclei. Comparing Fig. 1 (a) and 1 (b), we find that the absolute value of radial friction γ_{RR} is not very different for the two systems. Main difference is that effective diffuseness of γ_{RR} for Cu + Au is larger than that for Ar + Au. When we compare our results with that of proximity friction of Ref. 3, we find that, for Cu + Au system, they are very similar both in absolute value and in form factor. For Ar + Au system, however, our results have longer effective radius and shorter diffuseness. Although not shown in this figure, the radial friction calculated with the method of Ref. 1 are not very different from the present results. A difference is that the former has a little longer range.

In Fig. 2 we show the friction tensor $\gamma_{\eta\eta}$ for Ar + Au and Cu + Au systems. This is the first microscopic calculation of friction form factors corresponding to the mass flow between two nuclei. Just as was for γ_{RR} , the absolute values of $\gamma_{\eta\eta}$ are nearly the same for both system. A difference in the behavior is that $\gamma_{\eta\eta}$ has a surface-peaked form factors for both systems, while γ_{RR} shows rather volume type form factors. The range of $\gamma_{\eta\eta}$ is longer than that of γ_{RR} . Discussion on these points, together with that of the relation among γ_{RR} , $\gamma_{\eta\eta}$, and $\gamma_{R\eta}$ will be presented in the forthcoming paper.

References

- 1) K. Sato, A. Iwamoto, K. Harada, S. Yamaji, and S. Yoshida: *Z. Physik*, **A288**, 383 (1978).
- 2) K. Sato, S. Yamaji, K. Harada, and S. Yoshida: *ibid.*, **A290**, 149 (1979).
- 3) J. Randrup: *Ann. Phys.*, (N.Y.), **112**, 356 (1978).

4-12. Numerical Analysis of the $^{63}\text{Cu} + ^{197}\text{Au}$ Reaction Based on the Linear Response Theory

S. Yamaji, A. Iwamoto,* K. Harada,* and S. Yoshida

{ NUCLEAR REACTIONS Analysis for the $^{63}\text{Cu} + ^{197}\text{Au}$ reaction;
linear response theory; two-center shell model. }

On the basis of the linear response theory,¹⁾ a microscopic calculation of friction tensors $\gamma_{\mu\nu}$ ($\mu, \nu = R, \delta, \eta$) was performed for the systems $^{40}\text{Ar} + ^{197}\text{Au}$ and $^{63}\text{Cu} + ^{197}\text{Au}$,²⁾ using the two center model. The linear response theory seems to be more properly applied to those systems than to a light system such as $^{20}\text{Ne} + ^{28}\text{Si}$.³⁾ The distance R between the two nuclei, the deformation δ of each nucleus and the mass asymmetry η were taken as the collective variables in Ref. 2.

Neglecting the η -motion, we have solved the equations of motion with the calculated frictions for the reaction $^{63}\text{Cu} + ^{197}\text{Au}$ with full coupling terms, in which statistical fluctuations are also included. The mass tensors $m_{\mu\nu}$ in the equations of motion were approximated with hydrodynamical ones obtained by use of the Werner-Wheeler method. Yukawa-plus-exponential potential was taken as the nuclear potential in the same way as in Ref. 3. In the present calculation, the δ -motion is assumed to start when R reaches the distance of closest approach or the touching distance $R_1 + R_2$, where R_1 and R_2 are radii of the two nuclei. The potential for later process was calculated including the effects of the neck-formation and of the charge equilibration.

In addition to the radial-frictional force, tangential force F_t and rolling force F_r written in the form of $F_t = -C_t \gamma_{RR} (R / (R_1 + R_2))^2 \times (R_1 (\dot{\theta}_1 - \dot{\theta}_0) + R_2 (\dot{\theta}_2 - \dot{\theta}_0))$ and $F_r = -C_r \gamma_{RR} (R / (R_1 + R_2)) (\dot{\theta}_1 - \dot{\theta}_2)$, respectively, were included in the equations of motion, where θ_0 is the polar coordinate between the centers of two nuclei and θ_1 and θ_2 are the angles specifying the orientation of the two nuclei.

As the value of the parameter C_t , we took two values, 0.5 and 1.0. The former corresponds to the proximity friction⁴⁾ and the latter to Tsang's friction.⁵⁾

In γ -multiplicity (M_γ) measurement on 365 MeV $^{63}\text{Cu} + ^{197}\text{Au}$ reaction, a large amount of angular momentum transfer was observed in the quasi-fission process, but the evidence for a sticking behavior was not demonstrated because M_γ did not depend on mass asymmetry in the sticking case.⁶⁾

However, since our treatment is based on the axial symmetric two-center shell model, the system must possess the symmetric axis throughout the collision. Therefore, in spite of the incomplete achievement of the sticking condition, we require in our preliminary calculation that the sticking condition has been achieved when the deforming motion starts. In the calculation of the reaction $^{63}\text{Cu} + ^{197}\text{Au}$ with $E_{\text{lab}} = 365$ MeV and $\ell = 55 \hbar$, the coefficient C_r was taken as a parameter (zero corresponds to rolling). In Fig. 1, the quantities $R, \delta, \theta_1 - \theta_0, \theta_2 - \theta_0$ and $\Delta\ell$ for the case of $C_r = 20.0$ are shown as a function of time t , where $\Delta\ell$ is the angular momentum transfer. It can be seen that $\theta_1 - \theta_0$ and $\theta_2 - \theta_0$ are very small and that the calculated angular momentum transfer $\Delta\ell$ is nearly equal to $\Delta\ell^{\text{st}} = 22\hbar$ estimated by the relation in the sticking limit $\Delta\ell^{\text{st}} = \ell(I_1 + I_2) / (I_1 + I_2 + I_r)$, where I_1 and I_2 are the moments of inertias of the projectile and target nuclei and $I_r = \mu(R_1 + R_2)^2$, μ being the reduced mass. Therefore, Fig. 1 shows that the sticking motion is realized in the calculation for $C_r = 20.0$.

The result for the reaction $^{63}\text{Cu} + ^{197}\text{Au}$ with $E_{\text{lab}} = 365$ MeV is given in Fig. 2, which shows the deflection angle θ , its second moment $\chi_{\theta\theta}$, maximum deformation δ_{max} and energy loss E^* as a function of the initial angular momentum ℓ .

The appreciable difference appears only in the quantity $\chi_{\theta\theta}$ between the two cases, $C_t = 0.5$ and $C_t = 1.0$, which are plotted by the solid and dashed curves, respectively. However, this difference does not affect much

* Japan Atomic Energy Research Institute.

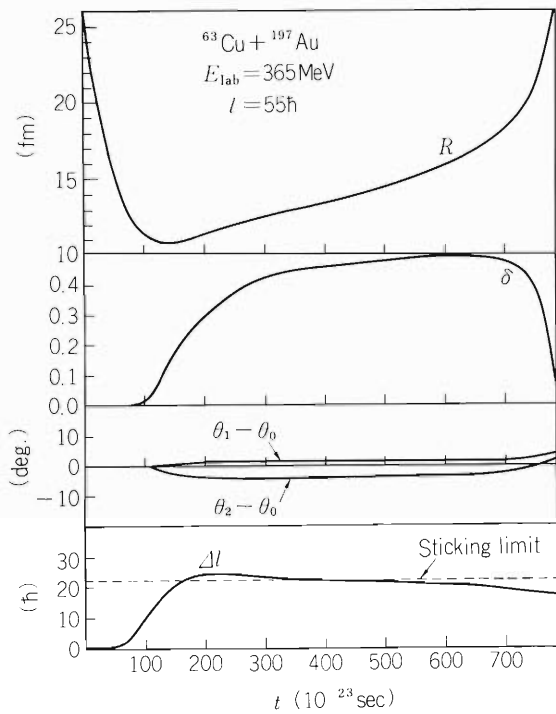
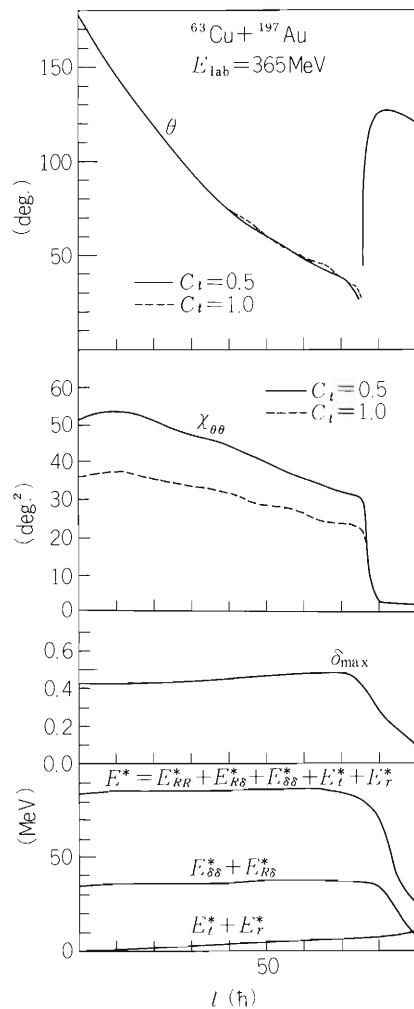


Fig. 1. The radial motion R , deforming motion δ , differences of angles $\theta_1 - \theta_0$, $\theta_2 - \theta_0$ and angular momentum transfer Δl as a function of time t for the reaction $^{63}\text{Cu} + ^{197}\text{Au}$ with $E_{\text{lab}} = 365 \text{ MeV}$ and l (initial angular momentum) = $55 \hbar$. The time t is set equal to zero at $R = 26 \text{ fm}$. The quantities $\theta_1 - \theta_2$ and $\theta_2 - \theta_0$ are normalized to zero at $\delta = 0.01$. The coefficient of the rolling friction C_r is taken to be 20.0. The quantities for $C_t = 0.5$ are shown, because the calculation of these quantities for $C_t = 0.5$ and 1.0 give nearly the same values.

Fig. 2. The deflection angle θ , its second moment $\chi_{\theta\theta}$, maximum value of the deformation δ_{max} and energy loss E^* as a function of the initial angular momentum l for the reaction $^{63}\text{Cu} + ^{197}\text{Au}$ with $E_{\text{lab}} = 365 \text{ MeV}$. The solid and dashed curves for θ and $\chi_{\theta\theta}$ correspond to the cases of $C_t = 0.5$ and $C_t = 1.0$, respectively. The quantities δ_{max} and E^* are shown only for $C_t = 0.5$, since there is not an appreciable difference between these quantities for $C_t = 0.5$ and $C_t = 1.0$.



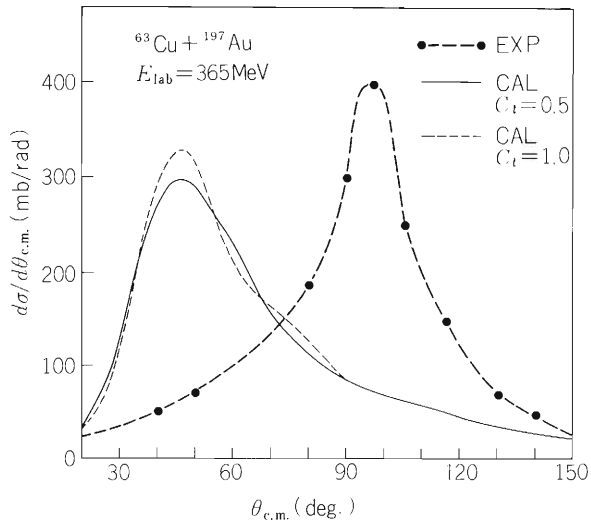


Fig. 3. Calculated angular distribution for the quasi-fission compared with the experimental result. The solid and dashed curves correspond to those calculated for the cases $C_t = 0.5$ and $C_t = 1.0$, respectively.

on the cross section (see Fig. 3).

It can be seen that the degree of freedom of the deformation plays an important role to explain the large energy loss in this heavy system $^{63}\text{Cu} + ^{197}\text{Au}$ as well as in the light system.³⁾ The experimental energy loss of about 80 MeV was well reproduced by the calculation including the energy loss due to the deforming motion whose magnitude is 35 MeV for $\ell \leq 75 \hbar$.

The cross section for the quasi-fission process can be obtained by integrating the Gaussian distribution function whose center is θ and whose width is $\chi_{\theta\theta}$ over the angular momentum ℓ from 0 to 75 \hbar . The calculated result is compared with the experimental one⁷⁾ in Fig. 3. The cross sections for $C_t = 0.5$ and $C_t = 1.0$ shown by the solid and dashed curves, respectively, are very similar to each other and the small difference between them was found to occur not from the difference between the second moments $\chi_{\theta\theta}$ for both cases but from the difference between the deflection angles θ for both cases. The orbits with the deformation degree of freedom stay longer in the region of internal attractive potential and are deflected more than those without deformation degree of freedom. Therefore, the fit to the experimental angular distribution becomes worse, as the peak position of the calculated cross section is shifted to the forward angle with the inclusion of the deformation degree of freedom. For the convenience of the calculation, the sticking motion was realized by using a large value of the rolling friction coefficient C_r . On the other hand, two nuclei do not completely stick as was revealed experimentally⁶⁾ but roll together. This rolling motion between two nuclei may suppress the evolution of the deformation, which yields a short collision time and large deflection angle. Therefore, the peak position of the calculated cross section will be shifted to backward angle and the fitting will be improved.

References

- 1) H. Hofmann and P. J. Siemens: Nucl. Phys., A275, 464 (1977).
- 2) A. Iwamoto, S. Yamaji, K. Harada, and S. Yoshida: IPCR Cyclotron Progr. Rep., 14, 44 (1980).
- 3) K. Sato, S. Yamaji, K. Harada, and S. Yoshida: Z. Physik, A290, 149 (1979).
- 4) J. Randrup: Annals of Physics, 112, 356 (1977).
- 5) C. F. Tsang: Physica Scripta., 10A, 90 (1974).
- 6) M. Lefort and C. Ngô: Ann. Phys., 3, 5 (1978).
- 7) C. Ngô and H. Hofmann: Z. Physik, A282, 83 (1977).

4-13. Semiclassical Treatment of the Direct Reactions Induced by Heavy Ions II

T. Kammuri and K. Matsuoka*

NUCLEAR REACTIONS Heavy-ion reactions; semiclassical theory of
one-and two-step transfer; energy spectra and polarizations

On the basis of the semiclassical theory of transfer reactions between heavy ions one can write the transfer form factor so as to show explicitly the effects of matching the linear and angular momenta before and after the transfer on the cross sections.¹⁾ In that paper we approximated the trajectory of relative motion to be a straight line, as was done by Brink.²⁾

Here we add formulas for the case in which two ions form a di-nuclear system temporarily. The incident ion is assumed to rotate around the target nucleus with an angular velocity Ω for a time interval τ . The form factor of the one-particle transfer process is given by

$$f_{if}^{(1)}(t) = N_{if}^{(1)} \exp\left\{-\frac{(R \Delta k / \sigma_1)^2}{2}\right\} \exp(-i\Omega \Delta L t), \quad (1)$$

and the transition amplitude is

$$C_{if}^{(1)} = (\pi / i\hbar) N_{if}^{(1)} \exp\left\{-\frac{(R \Delta k / \sigma_1)^2}{2}\right\} C^{(1)}(\vartheta), \quad (2)$$

where

$$C^{(1)}(\vartheta) = \sin \vartheta / \vartheta, \quad \vartheta = \phi \Delta L / 2, \quad \phi = \Omega \tau. \quad (3)$$

We follow the notations of Ref. 1, in which Δk and ΔL are the differences of the linear and angular momenta between the final and initial states respectively. The amplitude of the sequential transfer process becomes

$$C_{if}^{(2)} = (i\tau^2 / 2) (i\hbar)^{-2} \prod_{i=1}^2 N_i^{(1)} \times \exp\left\{-\frac{(R \Delta k_i / \sigma_{1i})^2}{2}\right\} C^{(2)}(\vartheta_1, \vartheta_2), \quad (4)$$

$$C^{(2)}(\vartheta_1, \vartheta_2) = \left\{ C^{(1)}(\vartheta_1 + \vartheta_2) - e^{i\vartheta_1} C^{(1)}(\vartheta_2) \right\} / \vartheta_1 \quad (5)$$

The differential cross sections of the one-and two-step transfer reactions are given by

$$\sigma^{(1)}(E_f, \theta) = \sum_{\lambda_1 \ell_2 \lambda_2} \sigma_{\lambda_1 \ell_2 \lambda_2}^{(1)}(E_f, \theta) \rho_n(E_f - E_i, \ell_2), \quad (6a)$$

$$\sigma^{(2)}(E_f, \theta) = \sum_{\substack{\lambda_1 \lambda_1' \ell_2 \lambda_2 \\ \ell_2' \lambda_2'}} \int dE_m \sigma_{\lambda_1 \lambda_1' \ell_2 \lambda_2 \ell_2' \lambda_2'}^{(1)}(E_f, E_m, \theta) \rho_m(E_m - E_i, \ell_2') \rho_n(E_f - E_m, \ell_2) \quad (6b)$$

respectively. Here $\sigma^{(i)}$'s ($i=1, 2$) in the right hand side are given by the product of the elastic scattering cross section with $|c^{(i)}|^2$, and $\rho_n(E^*, \ell_2)$ is the level density of the n -particle excitation of the final nucleus with the excitation energy E^* and spin ℓ_2

$$\rho_n(E^*, \ell_2) = \rho_0(2\ell_2 + 1) \exp(-\ell_2^2 / 2IT) (E^*)^{n-1} \quad (7)$$

* Osaka Institute of Technology.

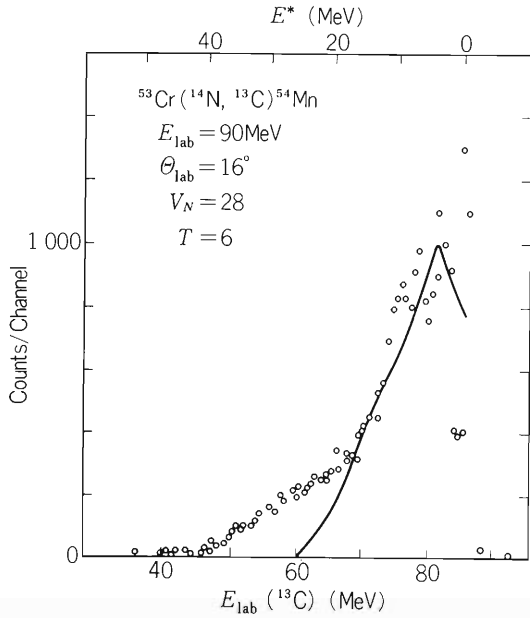


Fig. 1. Energy spectrum of ^{13}C emitted from the $^{53}\text{Cr}(^{14}\text{N}, ^{13}\text{C})^{54}\text{Mn}$ reaction at 90 MeV incident energy.

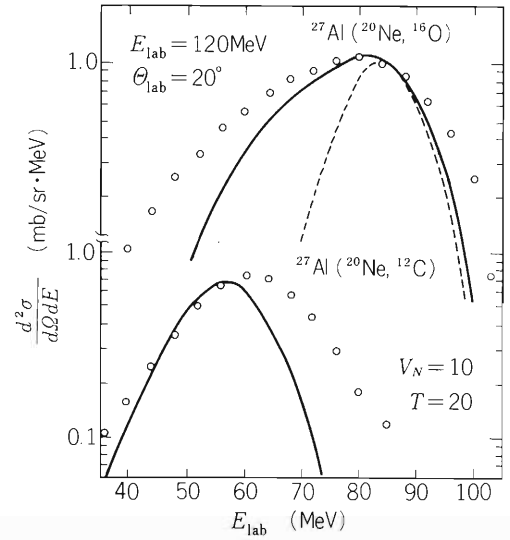


Fig. 2. Energy spectra of ^{16}O and ^{12}C emitted from the $^{27}\text{Al}(^{20}\text{Ne}, ^{16}\text{O})$ and $^{27}\text{Al}(^{20}\text{Ne}, ^{12}\text{C})$ at 120 MeV incident energy, respectively.

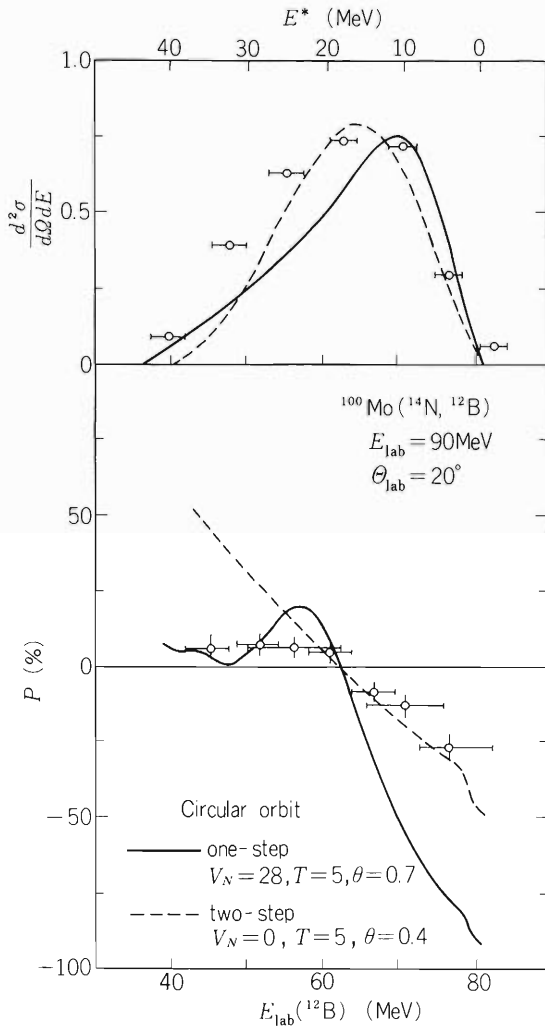


Fig. 3. Energy spectrum and polarization of ^{12}B from the $^{100}\text{Mo}(^{14}\text{N}, ^{12}\text{B})$ at 90 MeV incident energy.

Here the one-particle level density is assumed to be independent of E^* , and I is the moment of inertia of the relative motion between the cluster n and the core, and T is a parameter corresponding to the nuclear temperature. For small T the strong spin dependence of the level density shifts the peak of the energy spectrum to lower E^* as compared with that given by the matching condition.^{1),2)} The width becomes smaller correspondingly.

We firstly compare experimental results with the calculations done with the straight line trajectory. Figure 1 shows the energy spectrum of ^{13}C from the 90 MeV $^{14}\text{N} + ^{53}\text{Cr}$ reaction.³⁾ Here T is taken to be 6 MeV and the strength of the nuclear potential V_N equal to 28 MeV⁴⁾ is included in calculating the kinetic energies. Most of the calculated spectra of one-particle transfer reactions do not tend to zero for zero E^* . Figure 2 compares experimental ^{16}O and ^{12}C spectra from the 120 MeV $^{20}\text{Ne} + ^{27}\text{Al}$ reaction with calculations done by assuming α and 2α sequential transfers, respectively. We took T equal to 20 MeV and V_N was chosen to be 10 MeV. Solid curve in the ^{16}O spectrum shows cross sections summed over the transitions leading to three ^{16}O states having large spectroscopic factors for $^{20}\text{Ne}_{\text{g.s.}} \rightarrow ^{16}\text{O} + \alpha$, while in the dashed curve only the ^{16}O ground state is taken into account. We neglected the processes that populate excited states of ^{12}C as in Ref. 6.

The energy spectrum and polarization of ^{12}B in the $^{100}\text{Mo}(^{14}\text{N}, ^{12}\text{B})$ reaction at 90 MeV incident energy were analyzed by assuming the simultaneous transfer of two nucleons and the straight line trajectory.⁷⁾ Fit to the experimental polarization was good only at low E^* region. In Fig. 3. results of one-and two-step calculations under the assumption of the circular orbit are shown in solid and dashed curves, respectively. Values of (T, V_N, ϕ) in units of (MeV, MeV rad.) are (5, 28, 0.7) and (5, 0, 0.4) for one-and two-step calculations, respectively. Although there is a big difference in the adopted values of V_N , both calculations give equally good fit to the experimental results. Thus it is difficult to draw definite conclusions on the relative importance of the one-and two-step processes from the comparison of the theory with the experimental energy spectra and polarizations.

References

- 1) T. Kammuri, K. Matsuoka, and M. Sano: IPCR Cyclotron Progr. Rep., 13, 39 (1979).
- 2) D. M. Brink: Phys. Lett., 40B, 37 (1972).
- 3) T. Mikumo, I. Kohno, K. Katori, T. Motobayashi, S. Nakajima, M. Yoshie, and H. Kamitsubo: Phys. Rev. C, 14, 1458 (1976);
M. Yoshie and I. Kohno: Sci. Papers I.P.C.R., 69, 63 (1975).
- 4) P. J. Siemens, J. P. Bondorf, D. H. E. Gross, and F. Dickmann: Phys. Lett., 36B, 24 (1971).
- 5) J. B. Natowitz, M. N. Namboodiri, R. Eggers, P. Gonthier, K. Geoffroy, R. Hanus, C. Towsley, and K. Das: Nucl. Phys., A277, 477 (1977).
- 6) T. Udagawa, T. Tamura, and B. T. Kim: Phys. Lett., 82B, 349 (1979).
- 7) M. Ishihara, K. Tanaka, T. Kammuri, K. Matsuoka, and M. Sano: *ibid.*, 73B, 281 (1978).

4-14. Proton Inelastic Scattering to the
(1^+ , $T = 1$; 15.1 MeV) State in ^{12}C

M. Sano,* K. Yoro,** and T. Takemasa

{ NUCLEAR REACTIONS $^{12}\text{C}(p, p')^{12}\text{C}$, $E = 45.5$ and 155 MeV, 1^+ inelastic }
scattering, RPA calculation, DWBA analysis, pion condensate phase.

The problem of a pion condensate phase in atomic nuclei and nuclear matter is one of recent interest in nuclear physics.¹⁾ In particular, the possible appearance of precritical effect of the pion condensation in ordinary nuclei has been discussed in connection with excitations of low-lying particle-hole unnatural-parity states by inelastic electron²⁾ and proton scatterings.^{3),4)} If a nucleus is close to the threshold of the pion condensation, one may expect an enhancement of the differential cross sections at scattering angles corresponding to momentum transfer of $2 \sim 3m_\pi$. We have carried out analysis for the experimental data of (p, p') reactions to the 1^+ state in ^{12}C with respect to implications of precritical phenomena near pion condensation thresholds.

The nuclear interaction leading to pion condensation may be given by⁴⁾

$$V(q) = \frac{-1}{\epsilon(q)} \frac{f^2(q^2)}{4\pi} \left(\frac{\vec{\sigma}_1 \cdot \vec{q} \vec{\sigma}_2 \cdot \vec{q}}{q^2 + m_\pi^2} - g' \vec{\sigma}_1 \cdot \vec{\sigma}_2 \right) \vec{\Sigma}_1 \cdot \vec{\Sigma}_2, \quad (1)$$

where f^2 is the pion-nucleon vertex factor and $\epsilon(q)$ is a momentum-dependent polarization denominator associated with the virtual excitation of isobar-hole. The first term in the parenthesis is the free-pion exchange interaction, and the second term the Landau-Migdal interaction with a parameter g' .

The equation in the random phase approximation (RPA) with interaction (1) was solved for the 1^+ and 2^- states, taking into account of six single particle states: $0s_{1/2}$, $0p_{3/2}$, $0p_{1/2}$, $0d_{5/2}$, $1s_{1/2}$, and $0d_{3/2}$. The excitation energies calculated for various values of g' are presented in Table 1, and compared with the experimental

Table 1. Excitation energies of non-normal parity states in ^{12}C .

g'	$J^\pi=1^+, T=1$ E_X (MeV)	$J^\pi=1^+, T=0$ E_X (MeV)	$J^\pi=2^-, T=1$ E_X (MeV)
0.4	14.88	12.83	16.90
0.5	15.27	12.98	17.16
0.6	15.61	13.09	17.38
0.7	15.89	13.19	17.57
0.8	16.13	13.26	17.74
E_{ph}^0	11.77	11.77	15.62
E_{exp}	15.11	12.71	16.57

* Institute of Nuclear Study, University of Tokyo.

** Department of Physics, Osaka University.

values. A good agreement with the experiment is obtained for g' value of 0.4 to 0.8. However it should be noted that the results depend on the size of the configuration space and also on the values of unperturbed particle-hole energies.

In DWBA calculations, we took the general form for the interaction responsible for the inelastic scattering:

$$V(q) = \frac{-1}{\epsilon'(q)} \left\{ \frac{f^2(q^2)}{m_{\pi}^2} \frac{\vec{\sigma}_1 \cdot \vec{q} \vec{\sigma}_2 \cdot \vec{q}}{q^2 + m_{\pi}^2} - \frac{\alpha}{m_{\pi}^2} \vec{\sigma}_1 \cdot \vec{\sigma}_2 - \frac{\beta}{m_{\pi}^2} \frac{q^2}{q^2 + 4m_{\pi}^2} \right. \\ \left. \times S_{12}(\hat{q}) \right\} \vec{\Sigma}_1 \cdot \vec{\Sigma}_2, \quad (2)$$

where S_{12} is the tensor operator. The denominator $\epsilon'(q)$ is constructed from considerations of virtual intermediate isobar-hole and nucleon-hole excitations and is given by

$$\epsilon'(q) = 1 + \left\{ g' - \frac{q^2}{q^2 + m_{\pi}^2} \right\} \frac{f^2(q^2)}{m_{\pi}^2} \left\{ U_N(q) + 4U_{\Delta}(q) \right\}. \quad (3)$$

Here $U_N(q)$ and $U_{\Delta}(q)$ are nucleon and isobar Lindhard functions, respectively.⁴⁾ The interaction strength α and β are determined so as to fit the experimental cross section. The form factor is calculated using the RPA wave function in the $3\hbar\omega$ subspace.

The solid line in Fig. 1 shows the calculated result at $E_p = 155$ MeV with $g' = 0.8$, $\alpha = 0.4$, and $\beta = 0.3$.

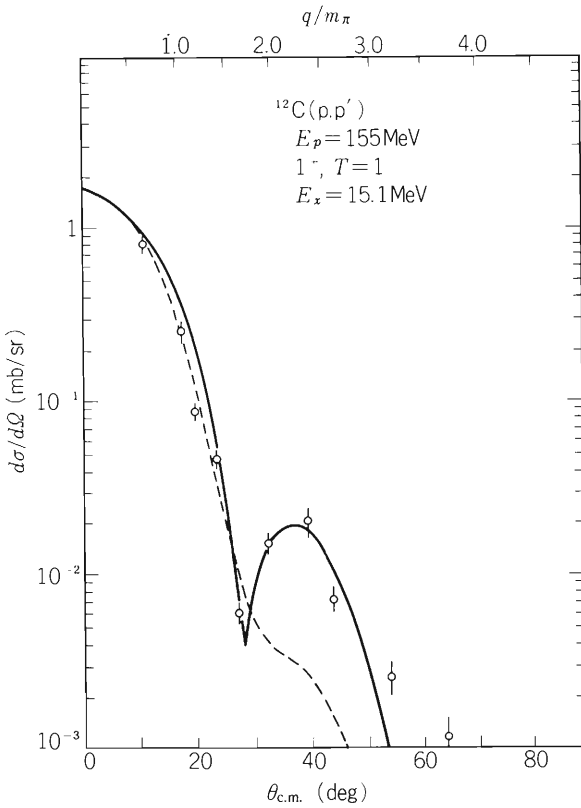


Fig. 1. Differential cross sections for 15.11 MeV transition in ^{12}C at $E_p = 155$ MeV. The solid curve corresponds to the theoretical prediction obtained with $g' = 0.8$, $\alpha = 0.4$, and $\beta = 0.3$. The dotted curve shows the calculated result of Buenerd.⁵⁾

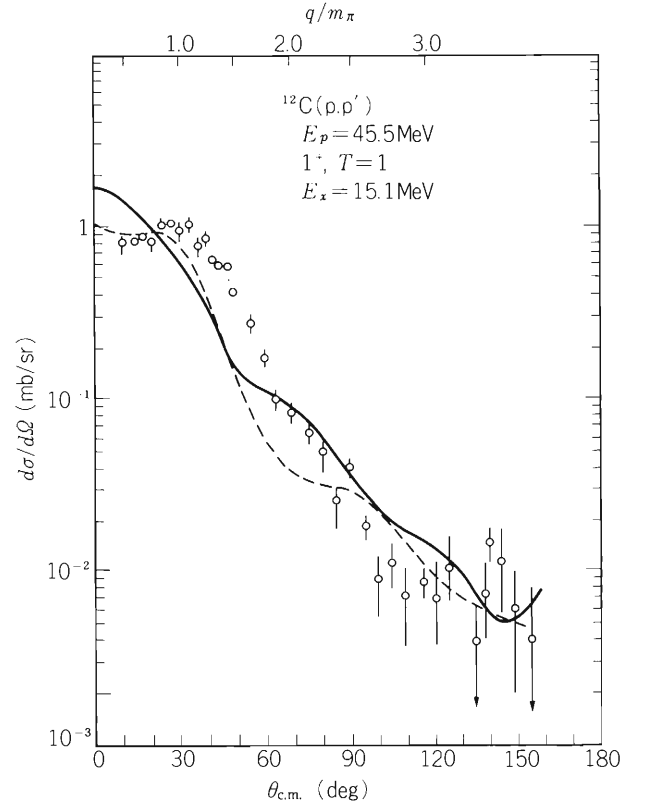


Fig. 2. Differential cross sections for 15.11 MeV transition in ^{12}C at $E_p = 45.5$ MeV. The solid curve corresponds to the theoretical prediction obtained with $g' = 0.8$, $\alpha = 0.5$, and $\beta = 0.3$. The dotted line shows the calculated result of Love and Parish.⁶⁾

The optical parameters are the same as those used in Ref. 5. It is seen that the calculation taking account of the nonnucleonic degrees of freedom correctly predicts the enhancement of the cross sections at $q \sim 2.5 m_\pi$ ($\theta_{\text{cm}} \sim 40^\circ$). This effect is attributed mainly to renormalization of the effective interaction; that is, the inverse of Eqn. (3) $\epsilon'(q)^{-1}$ has a bump at $q \sim (2-3)m_\pi$, and this leads to an enhancement in the cross section. For the sake of comparison, we present the result of the DWBA calculation performed by Buenerd⁵⁾ using the usual two-body interaction without the core polarization due to the isobar-hole and nucleon-hole excitations (dotted line in Fig. 1). As is seen, this conventional calculation reproduces well the data out to $q \sim 1.5 m_\pi$ ($\theta_{\text{cm}} \sim 25^\circ$), but fails to reproduce the peak at $q \sim 2.5 m_\pi$.

Figure 2 presents the DWBA cross sections at $E_p = 45.5$ MeV with $g' = 0.8$, $\alpha = 0.5$, and $\beta = 0.3$ (solid line), and the dotted line gives the conventional calculation performed by Love and Parish⁶⁾ without the core polarization. Experimentally, the sharp maximum of the differential cross section at $\theta_{\text{cm}} \sim 80 - 90^\circ$ corresponding to momentum transfer near the critical momentum for the pion condensation is not observed at 45.5 MeV. We see that the result reproduces fairly well the dependence of the second maximum of the cross section on incident energy. This indicates that disappearance of the second maximum of the cross section in low energy scattering is due to the effect of distortion on incoming and outgoing waves.

References

- 1) A. B. Migdal: *Rev. Mod. Phys.*, 50, 107 (1978) and references therein.
- 2) J. Delorme, M. Fricson, A. Figureau, and N. Giraud: *Phys. Lett.*, 89B, 327 (1980).
- 3) S. A. Fayans, E. E. Saperstein, and S. V. Tolokonnikov: *Nucl. Phys.*, A326, 463 (1979).
- 4) H. Toki and W. Weise: *Phys. Rev. Lett.*, 42, 1034 (1979).
- 5) M. Buenerd: *Phys. Rev. C*, 13, 444 (1976).
- 6) W. G. Love and L. J. Parish: *Nucl. Phys.*, A157, 625 (1970).

4-15. Perturbation Theory of Mass Transport in Nuclear Collision

K. Sato, N. Takigawa,* and S. Yoshida

$\left\{ \begin{array}{l} \text{NUCLEAR REACTION Heavy-ion reaction, mass transport coefficients,} \\ \text{perturbative expansion, dynamical effect.} \end{array} \right\}$

Gross features of the mass transport between two colliding heavy ions have been investigated by many authors.¹⁾ One needs, however, further study to understand various aspects of the mass transport phenomena. In this respect, microscopic theories are of particular interest.

As an example of the microscopic theories, Randrup has applied the time-dependent perturbation theory based on the nuclear mean field approximation and formulated the mass transport coefficients in terms of the single nucleon transfer matrix elements.²⁾ The expected change of the number of particles in nucleus 1 and the associated dispersion are given by

$$A - A_0 = \sum \rho_{2j} \left(\sum |t_{j \rightarrow i}|^2 \right) - \sum \rho_{1i} \left(\sum |t_{i \rightarrow j}|^2 \right), \quad (1)$$

$$\sigma_A^2 = \sum \left\{ (1 - \rho_{1i}) \rho_{2j} + \rho_{1i} (1 - \rho_{2j}) \right\} |t_{i \rightarrow j}|^2. \quad (2)$$

Here ρ_{1i} and ρ_{2j} are the occupation probabilities of the bound single particle states i in the nucleus 1 and j in the nucleus 2. The single nucleon transfer matrix element $t_{j \rightarrow i}$ in which $j \rightarrow i$ means the transfer of a nucleon from nucleus 2 to 1 is given by Eqns. (2.11) and (2.12) in Ref. 3. The matrix element $t_{i \rightarrow j}$ of a nucleon transfer from nucleus 1 to 2 is given by similar equations. Expressions (1) and (2), which are fairly simple, have been derived by disregarding the fact that the mass transport occurs between two nuclei which are in relative motion. Correspondingly, the transition matrices are estimated in the static approximation.

In treating the nucleon transfer between two nuclei which are in the relative motion, however, we should evaluate the transition matrix element analogously to finite range DWBA matrix element.⁴⁾ In Ref. 3, we have reported that such a matrix element of nucleon transfer is considerably influenced by the relative motion (Dynamical Effect). So far, however, it has not yet been clarified whether simple microscopic expressions like Eqns. (1) and (2) can be still obtained when the transfer matrix elements properly take account of the dynamical effect.

In this report we show that Eqns. (1) and (2) are still valid with a slight modification.

We follow the semi-classical theory of heavy ion reactions proposed by Dietrich and Hara.⁵⁾ In the theory, the direct sum of the whole bound single-particle states in nucleus 1 moving on a classical trajectory $\underline{R}(t)$ and of those in nucleus 2 at rest is used as a "working space". The creation and the annihilation operators of a nucleon thus depend on time. The non-orthogonality is taken into account by introducing the dual basis.

According to Ref. 5, the intrinsic states of the colliding nuclei approximately satisfy the following time-dependent Schrödinger equation:

$$i \frac{\partial}{\partial t} \Phi(t) = \left\{ \hat{H}_0(t) + \hat{V}(t, t) \right\} \Phi(t). \quad (3)$$

Here the operator \hat{H}_0 represents the sum of the intrinsic Hamiltonians of nuclei 1 and 2. The interaction \hat{V} reads as follows if we consider the mass transport only through the single nucleon transfer process:

$$\begin{aligned} \hat{V}(s, t) = & \sum \left\{ \tilde{\psi}_{1i} \left| U_1^{\text{ext}} + U^{\text{res}} \right| \psi_{2j} \right\} C_{1i}^+(t) \tilde{C}_{2j}(t) \\ & + \sum \left\{ \tilde{\psi}_{2j} \left| U_2^{\text{ext}} + m \ddot{\underline{R}}(s) (\underline{r} - \underline{R}(s)) + U^{\text{res}} \right| \psi_{1i} \right\} C_{2j}^+(t) \tilde{C}_{1i}(t), \end{aligned} \quad (4)$$

* Department of Physics, Tohoku University.

where ψ_{1i} is the moving single particle bound state wave function of nucleus 1 and is given by,

$$\tilde{\psi}_{1i} = \phi_{1i} \left(\underline{r} - \underline{R}(t) \right) e^{i(m\dot{\underline{R}}(t) \underline{r} - r(t))},$$

with

$$r(t) = \int_{-\infty}^t \left\{ \frac{m}{2} \dot{\underline{R}}^2(s) + m\ddot{\underline{R}}(s) \underline{R}(s) \right\} ds, \quad (5)$$

and $\tilde{\psi}_{1i}$ is its adjoint etc. The terms U_1^{ext} and U_2^{ext} are the potential due to nucleus 2 acting on a nucleon in nucleus 1 and the potential due to nucleus 1 on a nucleon in nucleus 2 respectively. The term U^{res} originates from the non-orthogonality of the basis and does not have simple physical meaning. The interaction $\hat{V}(t, t)$ contains both c-numbers and operators i.e. the creation and the annihilation operators. The first argument t indicates the time dependence of the c-numbers, while the second t refers to the time dependence of the operators. It is now of particular importance to remark that the derivative $\frac{\partial}{\partial t}$ in Eqn. (3) does not act on the creation and annihilation operators.⁵⁾

We can then easily move to the interaction representation,

$$\left. \begin{aligned} \Phi_I(t) &= e^{i\hat{H}_0(t)t} \Phi(t), \\ \hat{V}_I(s, t) &= e^{i\hat{H}_0(t)s} \hat{V}(s, t) e^{-i\hat{H}_0(t)s}, \end{aligned} \right\} \quad (6)$$

and we find the solution of Eqn. (3) in an iterative form,

$$|\Phi(t)\rangle = e^{-i\hat{H}_0(t)t} T \exp \left\{ -i \int_{t_0}^t e^{i\hat{H}_0(t)s} \hat{V}(s, t) e^{-i\hat{H}_0(t)s} ds \right\} |\psi_0(t)\rangle, \quad (7)$$

where T is the time ordering operator and $|\psi_0\rangle = \Pi C_m^+(t) |0\rangle$ is the Hartree-Fock ground state of the combined system. It is the solution of Eqn. (3) under no interaction and acceleration. The adjoint state of $|\Phi(t)\rangle$ is given by

$$|\tilde{\Phi}(t)\rangle = e^{i\hat{H}_0^+(t)t} T \exp \left\{ -i \int_{t_0}^t e^{i\hat{H}_0^+(t)s} \hat{V}^+(s, t) e^{-i\hat{H}_0^+(t)s} ds \right\} |\tilde{\psi}_0(t)\rangle, \quad (8)$$

where $|\tilde{\psi}_0\rangle = \Pi \tilde{C}_m^+(t) |0\rangle$. The tildes refer to the dual states.

The induced change in the number of particles of nucleus 1 during the time interval $t - t_0$ should be given by

$$A - A_0 = \langle \tilde{\Phi}(t) | \sum C_i^+(t) \tilde{C}_i(t) | \Phi(t) \rangle - \langle \tilde{\Phi}(t_0) | \sum C_i^+(t) \tilde{C}_i(t) | \Phi(t_0) \rangle, \quad (9)$$

where the argument t_0 in $\Phi(t_0)$ means that only the c-number part of $\Phi(t)$ is estimated at the time t_0 , while the creation and the annihilation operators are defined at t .

We now define the transfer operator $\hat{T}(t)$ by

$$\hat{T}(t) = \int_{t_0}^t e^{i\hat{H}_0(t)s} \hat{V}(s, t) e^{-i\hat{H}_0(t)s} ds, \quad (10)$$

We then divide it into two parts,

$$\hat{T}(t) = \hat{T}^{(+)}(t) + \hat{T}^{(-)}(t) = \sum t_{ji}(t) C_i^+(t) \tilde{C}_j(t) + \sum t_{ij}(t) C_j^+(t) \tilde{C}_i(t), \quad (11)$$

$$t_{ij}(t) = \int_{t_0}^t ds \langle \tilde{\psi}_{2j} | U_1^{\text{ext}} + m\ddot{\underline{R}}(s) (\underline{r} - \underline{R}(s)) + U^{\text{res}} | \psi_{1i} \rangle e^{-i(\epsilon_i - \epsilon_j)s}, \quad (12)$$

etc.

The first and the second parts of $\hat{T}(t)$ describe the transfer of a nucleon from the nucleus 1 to 2 and the opposite process respectively. We note that the nucleon transition matrix element $t_{ij}(t)$ defined by Eqn. (12) is essentially the same as that given by Eqn. (2,4) in Ref. 3, although the former is based on the Hartree-Fock theory and the latter on the shell model. The effect of the relative motion is naturally contained in the transition matrix element $t_{ij}(t)$. Approximately we replace $|\Phi(t)\rangle$ and $|\tilde{\Phi}(t)\rangle$ by the normalized wave functions of the first-order time-dependent perturbation theory. Then we find

$$A - A_0 \cong \langle \tilde{\psi}_0(t) | \{ \hat{T}^{(-)}(t), \hat{T}^{(+)}(t) \} | \psi_0(t) \rangle. \quad (13)$$

Similarly the fluctuation in the particle number of nucleus 1 at the time t is given by

$$\sigma_A^2 \cong \langle \tilde{\psi}_0(t) | \{ \hat{T}^{(-)}(t), \hat{T}^{(+)}(t) \} | \psi_0(t) \rangle. \quad (14)$$

If we take $t \rightarrow \infty$, the Hartree-Fock ground state of the combined system is simply given by the product of the ground state of each nucleus

$$\begin{aligned} \psi_0(t) &= |\psi_{01}(t)\rangle |\psi_{02}(t)\rangle \\ \tilde{\psi}_0(t) &= |\tilde{\psi}_{01}(t)\rangle |\tilde{\psi}_{02}(t)\rangle \end{aligned} \quad (15)$$

After a little manipulation, we finally arrive at

$$A - A_0 = \sum_{ji} t_{ji} t_{ij} n_j - \sum_{ji} t_{ji} t_{ij} n_i, \quad (16)$$

$$\sigma_A^2 = \sum_{ji} t_{ji} t_{ij} n_j (1 - n_i) + \sum_{ji} t_{ji} t_{ij} n_i (1 - n_j), \quad (17)$$

where n_i and n_j are the occupation probabilities of the bound single particle states i in the moving nucleus 1 and j in the nucleus 2 at rest respectively.

Comparing Eqns. (16) and (17) with Eqns. (1) and (2), we see that the simple microscopic expressions of the mass transport coefficients first obtained by Randrup in the static approximation still hold with slight modifications even when mass transport coefficients are extended to properly take into account the dynamical effect. The dynamical effect manifests itself mainly through the matrix elements of the nucleon transfer. The transition matrix element $t_{ij}(t)$, however, is not equal to the complex conjugate of $t_{ji}(t)$ any more in contrast with the static case considered by Randrup.

It is desired to study the dynamical effect due to the relative motion between two heavy ions on the mass transport coefficients by using Eqns. (16) and (17).

References

- 1) D.K. Scott: *Theoretical Methods in Medium-Energy and Heavy-Ion Physics*. (Ed. K.W. Mcvoy and W.A. Friedman), Plenum, p. 3 (1978) and references therein.
- 2) J. Randrup: *Nucl. Phys.*, A307, 319 (1978).
- 3) K. Sato, N. Takigawa, and S. Yoshida: *Deuxieme Colloque Franco-Japonais De Physique Nucleaire Avec Des Ions Lourds*, p. 385 (1979).
- 4) D.M. Brink: *Phys. Lett.*, 40B, 37 (1972); *Lectures at the Summer School at Les Houches* (1977); G.F. Bertsch and R. Schaeffer: *Nucl. Phys.*, A277, 509 (1977).
- 5) K. Dietrich and K. Hara: *ibid.*, A211, 349 (1973).

5. NUCLEAR PHYSICS

Nuclear Spectroscopy and Instrumentation

5-1. High Spin States in ^{158}Yb

A. Hashizume, T. Katou, Y. Tendow, and H. Kumagai

$\left[\begin{array}{l} \text{NUCLEAR REACTIONS } ^{142}\text{Nd}(^{20}\text{Ne}, 4n) E = 120 - 150 \text{ MeV}, \gamma\text{-}\gamma \text{ coin,} \\ ^{158}\text{Yb} \text{ deduced levels. Ge(Li) detectors, enriched target.} \end{array} \right]$

This study is one of a series of experiments on high spin states in Yb isotopes.¹⁾ The states in ^{158}Yb , highly neutron deficient nucleus, have been populated via the $^{142}\text{Nd}(^{20}\text{Ne}, 4n\gamma)$ reaction. A self-supporting ^{142}Nd target of isotopically enriched to 98 % was prepared by use of vacuum evaporation where $^{142}\text{Nd}_2\text{O}_3$ was reduced by thorium.

Excitation functions in the incident energy range of 120 to 150 MeV were studied. The main cascade γ -rays in yrast band were also observed via the $^{144}\text{Sm}(^{16}\text{O}, 2n\gamma)$ reaction in the energy range of 80 to 120 MeV. This reaction was used for the cross check of the residual nuclei to which the emitted γ -rays belong. The four fold coincidence spectra of $E_{\gamma_1} - E_{\gamma_2} - t - T$ have been measured, where E_{γ_1} and E_{γ_2} are the γ -ray energies, t is the relative time relation between the two γ -rays, and T shows the time from the bombardment by a natural bunched beam of the cyclotron.

The high spin states in ^{158}Yb have been studied by Beck et al.²⁾ and states up to 12^+ have been reported. Figure 1 shows a γ -ray spectrum which is a sum of 4 coincident spectra gated by the members of the ground state band from the 8^+ state. The γ -rays belonging to the transitions of $12^+ \rightarrow 10^+ \rightarrow 8^+ \rightarrow 6^+ \rightarrow 4^+ \rightarrow 2^+ \rightarrow 0^+$ are clearly observed in the figure. Besides these γ -rays, 649 and 682 keV γ -rays were detected. The 682 keV γ -ray is in coincidence with

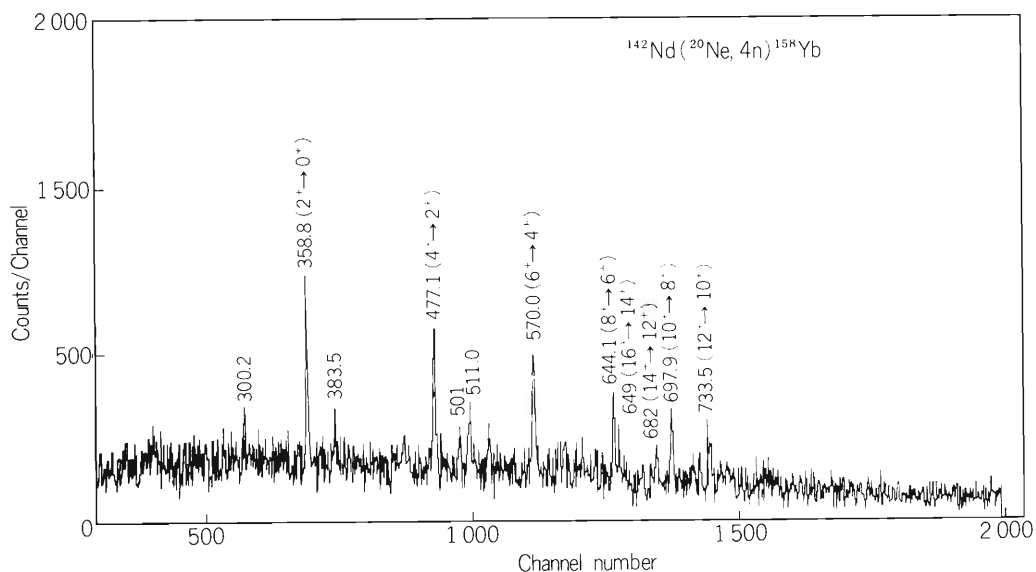
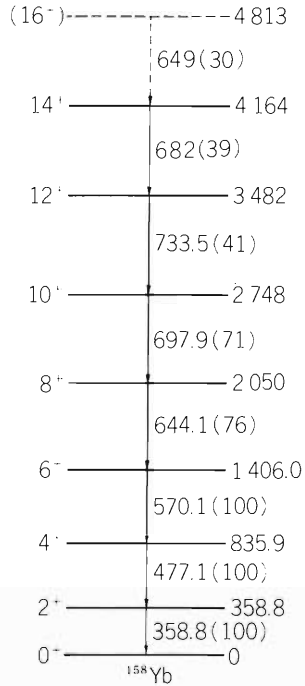
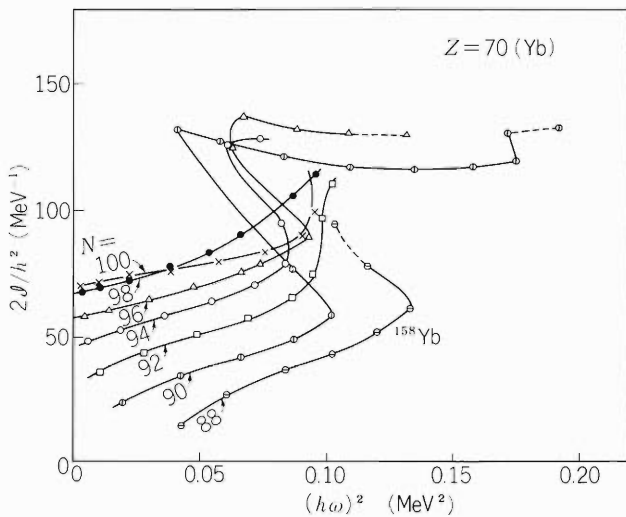
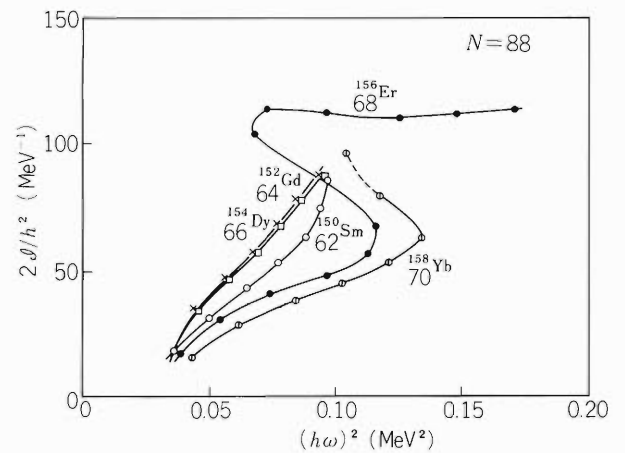


Fig. 1. A γ -ray spectrum which is a sum of 4 spectra obtained by $\gamma\text{-}\gamma$ coincidences gated by the cascade transitions from 10^+ to the ground state.

Fig. 2. High spin excited states in ^{158}Yb .Fig. 3. Moment of inertias of $Z = 70$ nuclei.Fig. 4. Moment of inertias of $N = 88$ nuclei.

all the γ -rays of the members of ground state band up to the 12^+ state and this is assigned to the transition of $14^+ \rightarrow 12^+$. The 649 keV γ -ray is a candidate of $16^+ - 14^+$ transition, however, the assignment is less certain because of statistics of each coincidence spectrum.

Figure 2 shows the ground state band of ^{158}Yb and Figs. 3 and 4 show the plots of angular frequency versus moment of inertia for the $Z = 70$ isotopes and the $N=88$ isotones. The nucleus ^{158}Yb preserves the same tendency of first deep backbending of ^{160}Yb and ^{156}Er .

References

- 1) A. Hashizume, T. Katou, Y. Tendow, and H. Kumagai: IPCR Cyclotron Progr. Rep., 11, 69 (1977); A. Hashizume, T. Katou, Y. Tendow, and H. Kumagai: *ibid.*, 12, 74 (1978).
- 2) F. A. Beck, E. Bozek, T. Byrski, C. Gehringer, J. C. Merdinger, Y. Schutz, J. Styczen, and J. P. Viven: *Phys. Rev. Lett.*, 42, 493 (1979).

5-2. Calculation of Widths of Hole Analog States

S. Yoshida* and S. Adachi*

(NUCLEAR STRUCTURE Calculation of hole analog states, $^{208}\text{Pb}(p, d)^{207}\text{Pb}$)

Hole analog states have been observed by neutron pick-up reactions with high energy-resolution. These states are often in continuum energy region and their widths are narrow. We have been working in this problem and obtained some results in the case of ^{207}Pb .

The hole analog states are the analog to the proton hole states and their widths result from mixing of the $T_{<}$ states by the Coulomb interaction. To calculate these widths the most convenient tool is the Green's function

$$G_{\beta\alpha}(\omega) = \langle \Phi_{\beta} | \frac{1}{\omega - H + i\delta} | \Phi_{\alpha} \rangle, \quad (1)$$

where ω is the excitation energy of the residual nucleus, and α indicates the neutron hole configuration. The final state β may be chosen to be a state decaying by emitting a proton.

To evaluate the Green's function, we first solve the Hartree Fock equation. The Hartree Fock Hamiltonian h is diagonalized by using harmonic oscillator basis. The resulting wave functions are all bound. A hole analog state is expressed as a superposition of configurations of type a and b shown in Fig. 1. The hole analog state with $T_{>}$ mixes with $T_{<}$ configurations, of which the most important ones are isovector monopole states with configurations shown by c in Fig. 1. The configuration space composed of these configurations is explicitly treated and it is called P-space. If the Hamiltonian H is diagonalized using these configurations we obtain discrete shell model states. To take into account the decay we have to introduce the Q-space which is defined by $1 - P = Q$. The most important configurations in the Q-space are continuum states and more complicated states which are shown by d and e respectively in Fig. 1. The continuum state must be constructed to be orthogonal to bound states.

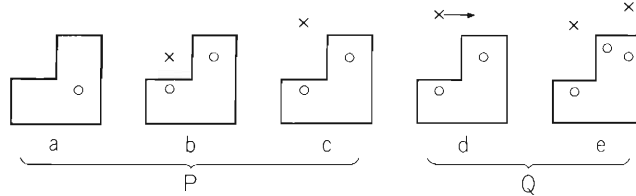


Fig. 1. Configurations used in calculations.

The Green's function is evaluated as,

$$Q \frac{1}{\omega - H + i\delta} P = Q \frac{1}{\omega - QHQ + i\delta} QHP \frac{1}{\omega - \mathcal{H}_p} P, \quad (2)$$

where

$$\mathcal{H}_p = PHP + PHQ \frac{1}{\omega - QHQ + i\delta} QHP \longrightarrow PHP + PHQ \frac{1}{\omega - h + i\delta} QHP. \quad (3)$$

In the above equations, the arrow indicates the approximate form which will be used in the following.

Broadening of the levels comes from decay into the Q-space in the effective Hamiltonian given by Eqn. (3).

There are two important contributions: one is that from the configuration shown by d in Fig. 1 whose space is denoted by $Q\uparrow$, while the other is from 2p-3h configuration shown by e in Fig. 1, whose space is called $Q\downarrow$. Therefore the effective Hamiltonian (3) becomes

$$\begin{aligned} \langle \alpha | \mathcal{H}_p | \beta \rangle = & \langle \alpha | H | \beta \rangle + \int \langle \alpha | h | q \rangle \frac{\rho(\epsilon_q)}{\epsilon - \epsilon_q + i\delta} \langle q | h | \beta \rangle d\epsilon_q \\ & + \sum_{\gamma} \langle \alpha | H | \gamma \rangle \frac{Q}{\omega - \epsilon_{\gamma} + i\delta} \langle \gamma | H | \beta \rangle . \end{aligned} \quad (4)$$

In the second term of the right hand side of the above equation H's are approximated by h's, q denotes configuration in the $Q\uparrow$ space, and $\rho(\epsilon_q)$ is the level density.

The matrix of the effective interaction given by Eqn. (4) is symmetric and complex so it may be diagonalized by a complex orthogonal transformation T:

$$\begin{aligned} (T \mathcal{H}_p T^{-1})_{st} &= (\epsilon_s - \frac{i}{2} \Gamma_s) \delta_{st} \\ TT^T &= 1. \end{aligned} \quad (5)$$

The total width Γ_s is evaluated as

$$\Gamma_s = -2\pi \text{Im} \left(\sum_{\alpha\beta} T_{s\alpha} \langle \alpha | \mathcal{H}_p | \beta \rangle T_{s\beta} \right) . \quad (6)$$

The escape width appears in the Green's function in Q-space in the expression (2) and has the following form:

$$\Gamma_{sq}^{\uparrow} = 2\pi\rho(\omega) \left| \sum_{\alpha} T_{s\alpha} \langle \alpha | h | q_{\omega} \rangle \right|^2 . \quad (7)$$

In a similar way the spreading width which expresses decay into Q space is given by

$$\Gamma_s^{\downarrow} = 2 \sum_{\gamma} \left| \sum_{\alpha} T_{s\alpha} \langle \alpha | H | \gamma \rangle \right|^2 \frac{\delta}{(\omega - \epsilon_{\gamma})^2 + \delta^2} , \quad (8)$$

where γ is restricted to 2p-3h configurations. Thus the total width Γ_s is given by

$$\Gamma_s = (\sum_q \Gamma_{sq}^{\uparrow} + \Gamma_s^{\downarrow}) / N_s , \quad (9)$$

where

$$N_s = \sum_{\alpha} |T_{s\alpha}|^2 \geq 1. \quad (10)$$

In the following, some numerical results for ^{207}Pb analog states are presented. In the calculation we used Skyrme III interaction in solving Hartree Fock problem. When we diagonalize the Hartree Fock Hamiltonian h, harmonic oscillator wave functions whose size parameter is fixed to 0.1688 fm^{-2} are used. The number of basis which is denoted by N_{sp} is chosen from numbers between 10 and 20, while the dimension of the Q-space N_{ph} is chosen from numbers between 44 and 86 which corresponds respectively to $\Delta n=2$ and 4. In evaluating the matrix elements given by Eqn. (4) the real part of the last two terms of r.h.s. is neglected. The results are shown in Table 1 together with experimental data. The excitation energies E_s are measured from the ground state of ^{208}Pb . In the case of $N_{sp}=14$ and $N_{ph}=44$, the level is split into two. As seen from the table, the escape widths seem to be more or less the same except for the case $N_{sp}=20$ and $N_{ph}=44$, while the spreading widths change little from case to case. As for the total width in the case of $J^{\pi}=1/2^{-}$, the theoretical value is a little smaller than experimental values, while in the case of $J^{\pi}=11/2^{-}$ they are of comparable magnitude.

Table 1. Comparison between calculated and experimental results for ^{207}Pb hole analog state.

J^π	N_{sp}	N_{ph}	E_s (MeV)	Γ_s^\uparrow (keV)	Γ_s^\downarrow	Γ_s	E_s (Exp)	Γ_s (Exp)
$1/2^-$	10	44	25.48	40			26.66	350±60
		86	25.40	30				
	20	14	44			50 ± 115		
		44	25.65	221	150			
		65	25.54	57	160			
		86	25.51	63	155	230		
$11/2^-$	20	44	27.95		155		29.94	225±40
		86	27.87	68				

5-3. A Double Scattering Proton Polarimeter

T. Sugitate, T. Nomura, M. Ishihara, Y. Gono,
H. Utsunomiya, K. Ieki, and S. Kohmoto

NUCLEAR INSTRUMENT Proton polarimeter, double scattering method,
second target carbon, second scattering angle 45° ; measured and calculated
analyzing powers.

A double scattering proton polarimeter using a carbon foil as an analyzing target was constructed for the purpose of measuring spin polarization of protons emitted in heavy-ion reactions. These protons often have continuous energy spectra¹⁾ and the polarization of such protons is considered to be less than about 20 % from our preliminary work. Special care was, therefore, taken of the following points.

- 1) Possible backgrounds originating from γ -rays, neutrons and electrons must be negligible, because we cannot subtract them from an observed energy spectrum.
- 2) It is necessary to distinguish elastic from inelastic scatterings in the analyzer.
- 3) High analyzing powers are essential to suppress the effect of possible false asymmetry originating from anisotropic angular distribution of protons and geometrical unbalances of the polarimeter.
- 4) Good efficiencies are required, since the yield of protons is not very large.

Figure 1 shows a schematic view of the present polarimeter used for the $^{93}\text{Nb}(^{14}\text{N}, p)$ reaction at 95 MeV. A 9 mg/cm^2 thick Nb target (T) with a $35 \mu\text{m}$ Au backing (Au) was bombarded with ^{14}N -ions from the cyclotron. The backing is thick enough to stop the beam, protecting the ΔE_1 counter from the elastically scattered ^{14}N -ions. Protons emitted from the target pass through the Au backing, an aluminium energy degrader (D) and the ΔE_1 counter. Then they are scattered by the carbon analyzer (A) of 34 mg/cm^2 thickness. The scattered

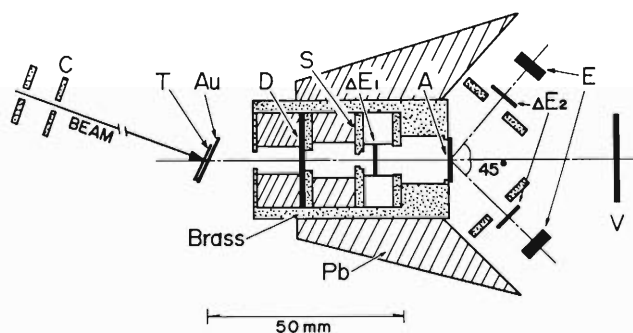


Fig. 1. Schematic view of the present polarimeter. C: Beam collimator, T: Target, Au: Au backing, D: Energy degrader, S: Entrance slit, ΔE_1 : $50\text{mm}^2 - 50\mu\text{m}$ Si detector, A: Carbon analyzer, ΔE_2 : $50\text{mm}^2 - 50\mu\text{m}$ Si detector, E: $50\text{mm}^2 - 2000\mu\text{m}$ Si detector, V: $60\mu\text{m}$ Si detector.

protons are detected and particle-identified by asymmetry counters which are counter telescopes consisting of $50\ \mu\text{m}$ (ΔE_2) and $2000\ \mu\text{m}$ (E) Si detectors. They are placed at 45° on both sides with respect to the emitted protons. Yield of protons from the Au backing is less than a few percents in the case of Nb target. Thus the effect on polarization from these protons is negligible. With the help of the veto counter (V) accidental coincidences between ΔE_1 and $\Delta E_2 - E$ detectors were found to be less than 0.1 %. The solid angles of the ΔE_1 and the asymmetry counters are 6.7 and 50 msr, respectively. Lead blocks are placed in order to protect the asymmetry counters from γ -rays produced in the target.

Pulse heights of the ΔE_1 counter work for rough particle-identification and ensure that incoming particles into the analyzer are really protons, so that we can eliminate reactions occurring in the analyzer. We can also distinguish inelastic from elastic scatterings, because the proton energies measured with the counter telescopes are quite different from each other for the same pulse heights of the ΔE_1 counter. However, this discrimination becomes difficult for high-energy protons, limiting the applicable energy range to less than around 20 MeV.

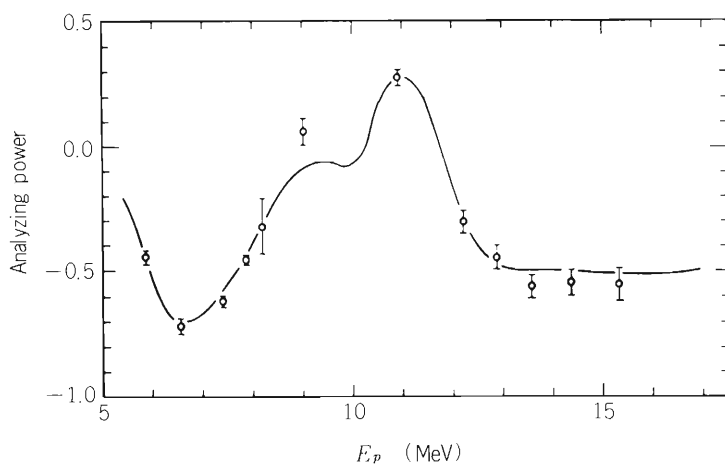


Fig. 2. Experimental and calculated effective analyzing powers of the present polarimeter given as a function of proton energy incident on the carbon analyzer.

Figure 2 shows effective analyzing powers of the present polarimeter estimated from the known polarizations and cross sections of proton elastic scatterings with carbon given in the literature.²⁾ They were experimentally checked by measuring the double scattering of proton beam using a carbon target at various energies available from the cyclotron. Agreement between experiment and calculation is satisfactory for the present purpose. Since the analyzing powers are small between 8.5 – 12 MeV, we used energy ranges of 5.5 – 8.5 and 12 – 17 MeV for the actual analysis. The analyzing powers in these two energy regions are -0.54 and -0.46 on the average with efficiencies of 1.3 and 0.7×10^{-5} , respectively. Proton energies incident on the carbon analyzer could be changed through an energy degrader inserted between the target and the ΔE_1 counter as shown in Fig. 1.

A measurement of polarization in the case of the $^{93}\text{Nb} + ^{14}\text{N}$ reaction at 95 MeV is reported elsewhere in this progress report.

References

- 1) T. Nomura, H. Utsunomiya, T. Motobayashi, T. Inamura, and M. Yanokura: Phys. Rev. Lett., 40, 694 (1978); H. Utsunomiya, T. Nomura, T. Inamura, T. Sugitate, and T. Motobayashi: Nucl. Phys., A334, 127 (1980).
- 2) S. J. Moss and W. Haerberli: *ibid.*, 72, 417 (1965); G. E. Terrell, M. F. Jahns, M. R. Kostoff, and E. M. Bernstein: Phys. Rev., 173, 931 (1968); H. O. Meyer, W. G. Weitkamp, J. S. Dunham, T. A. Trainor, and M. P. Baker: Nucl. Phys., A269, 269 (1976).

6. ATOMIC AND SOLID-STATE PHYSICS

6-1. X-Rays Following Multiple Inner-Shell Ionization (5)

Y. Awaya, T. Tonuma, Y. Tendow, H. Kumagai,
 T. Katou, K. Izumo, A. Hashizume, A. Hitachi,
 M. Nishida, A. Yagishita, and T. Hamada

The spectra of Ta, Au, and Pb $M\alpha$ and $M\beta$ X-rays induced by 84 MeV N ions were measured by using a crystal spectrometer.^{1), 2)} A flat crystal of EDDT(020) was used for measurement of Ta M X-rays and that of Ge(111) for Au and Pb. The detection of X-rays was made by using a side window gas-flow type proportional counter with a 1 μm polypropylene window. The

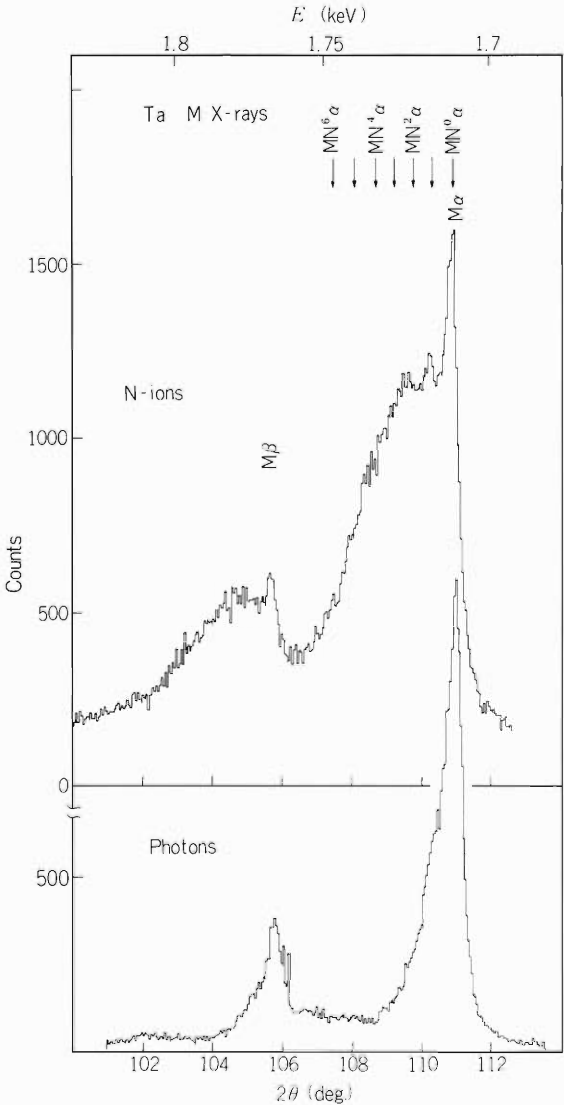


Fig. 1. Ta M X-ray spectra obtained by 84 MeV N-ion and photon excitation.

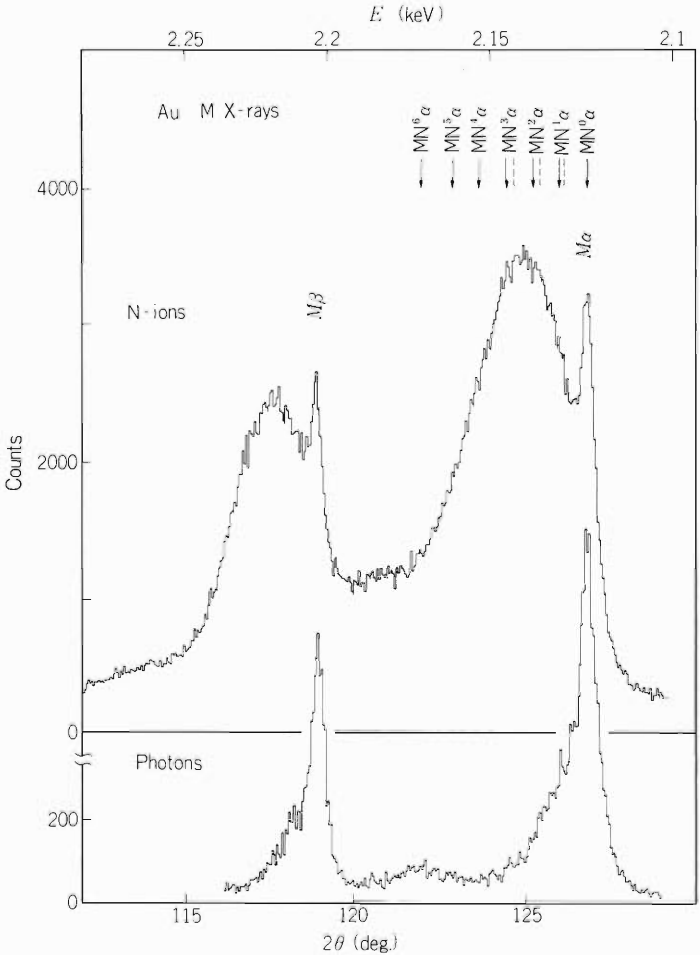


Fig. 2. Au M X-ray spectra obtained by 84 MeV N-ion and photon excitation.

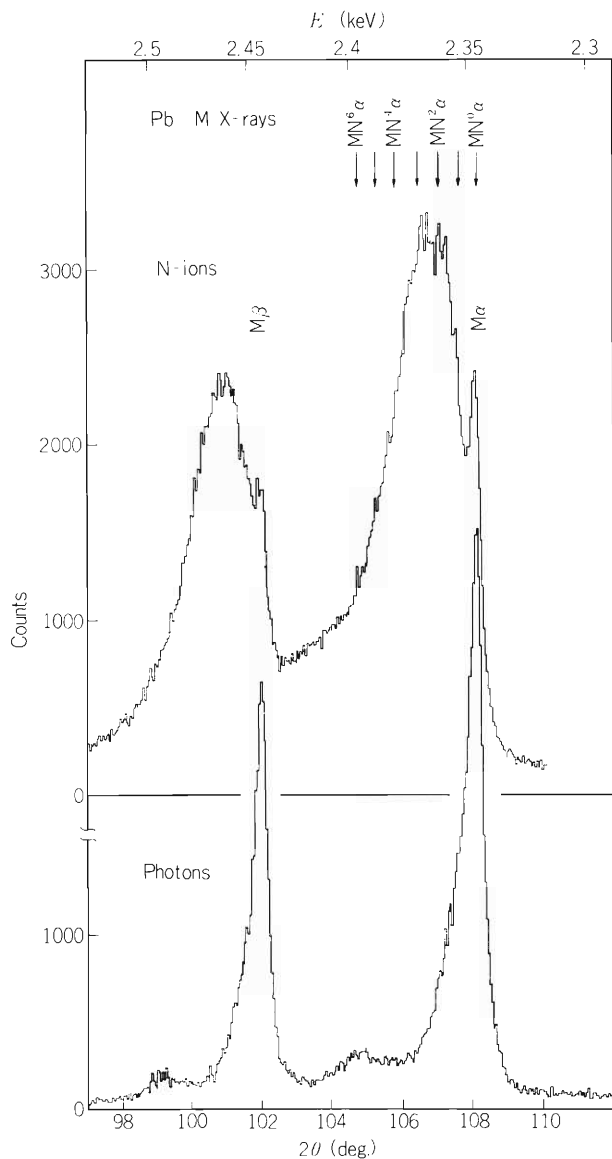


Fig. 3. Pb M X-ray spectra obtained by 84 MeV N-ion and photon excitation.

targets were self-supporting metallic foils with the thickness in the range of 2.2 to 2.8 mg/cm². They were placed at 60° with respect to the beams. The estimated energy loss of the incident ions in the target was less than 3.5 MeV. The integrated beam current was kept constant at each angle and the spectrometer was controlled automatically.

The spectra of N-ion-excited $M\alpha$ and $M\beta$ X-rays of Ta, Au, and Pb are shown in Figs. 1 to 3 in comparison with those of photon-excited ones. The arrows in the figure denote the position of MN^n satellite lines, which correspond to the initial configuration of single M-shell and n N-shell vacancies, estimated by the Hartree-Fock-Slater calculation by assuming the N-vacancies being in N_3 - (4d-) shell.

This may be the first case of the measurement of heavy-ion induced M X-ray spectrum by the crystal spectrometer. In contrast with previously reported KL^n and LM^n satellites,^{3) - 6)} the MN^n satellite lines are not resolved in energy, except for the MN^0 line of each element and the MN^1 line of Ta. The main reason may be that there are much more sub-shells in N orbit than L or M orbits. In Fig. 2, the broken lines show the estimated positions of MN^n satellites by assuming the vacancies being in N_2 - (4p-) shell in order to see the effect of different configuration. In the actual case, vacancy-configuration will be more complex and multiplets will be formed. Additional ionization of O-shell electrons would broaden each peak also.

The analysis of the data is in progress.

References

- 1) Y. Awaya, Y. Tendow, H. Kumagai, M. Akiba, T. Katou, and T. Hamada: IPCR Cyclotron Progr. Rep., 9, 79 (1975).
- 2) H. Kumagai, Y. Awaya, Y. Tendow, T. Katou, and M. Akiba: Reports I.P.C.R., (in Japanese), 53, 153 (1977).
- 3) Y. Awaya, M. Akiba, T. Katou, H. Kumagai, Y. Tendow, K. Izumo, T. Takahashi, A. Hashizume, M. Okano, and T. Hamada: Phys. Letters, 61A, 111 (1977).
- 4) Y. Awaya, T. Katou, H. Kumagai, T. Tonuma, Y. Tendow, K. Izumo, A. Hashizume, T. Takahashi, and T. Hamada: *ibid.*, 75A, 478 (1980).
- 5) Y. Awaya: Electronic and Atomic Collisions, North-Holland, p. 325 (1980).
- 6) Y. Awaya, T. Katou, H. Kumagai, T. Tonuma, Y. Tendow, K. Izumo, T. Takahashi, A. Hashizume, and T. Hamada: IPCR Cyclotron Progr. Rep., 13, 73 (1979).

6-2. A Target Chamber for X-Ray-Angular-Distribution Measurement

Y. Awaya, I. Takeshita, Y. Tendow,
and T. Katou

A target chamber has been designed and constructed for the use in experiments mainly on the angular distribution of X-rays. A sectional view of the chamber is shown in Fig. 1, where the left and right parts with respect to the a-a' line show different sections. The chamber is 30 cm in inner diameter and 15 cm in depth. The wall of the chamber is made of stainless steel and the upper and the lower lids and other parts that may be irradiated by stray beams are made of aluminum.

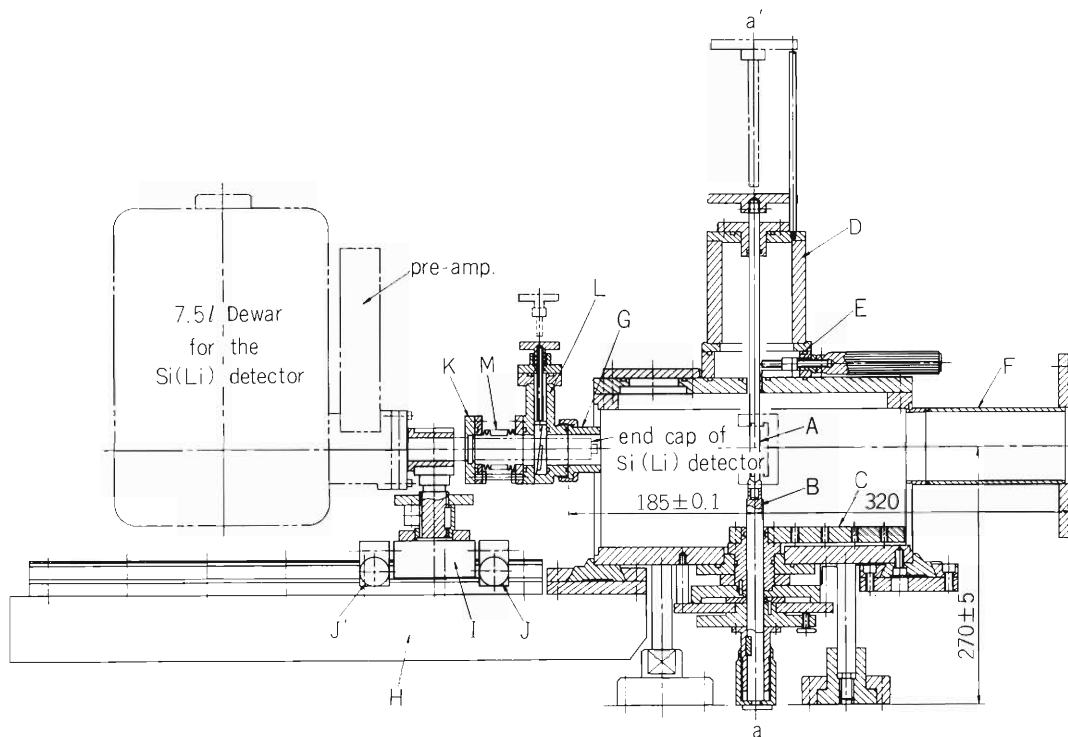


Fig. 1. Sectional view of the chamber. A: target holder, B: target-holer support, C: turn arm, D: target box, E: gate valve, F: port for beam transportation, G: port for X-ray measurement, H: turn arm, I: sliding saddle, J and J': stoppers, K: flange with O-ring, L: compact-type gate valve, M: bellow-duct.

The chamber contains a target holder A, a target holder support B, which defines the position and the angle of the target with respect to the beam, and a turn arm C. The height and angle of B and the angle of C are adjustable without opening the vacuum system. The target is changed without breaking the vacuum by lifting up the target holder by hands into the box D, which is connected with the upper lid through a gate valve E. On the wall, there are two ports F for the beam transportation, the one is connected to the beam duct from the cyclotron and the other

to a Faraday cup. Besides, there are thirteen ports G for measurement of X-rays. These are positioned at 25° , 45° , 70° , 90° , 110° , 135° , 155° , -30° , -60° , -90° , -120° , and -150° with respect to the beam. The surface of the flange-joints of these ports is finished up accurately so that the distance from the center of target to the center of every flange joint is made equal, i.e. 185 ± 0.1 mm.

There is another tern arm H, which holds a Si(Li) X-ray detector and moves in air around the target. The detector moves back-and-forth on the arm by sliding saddle I whose position is defined by two stoppers J and J". We usually use the Si(Li) detector designed for a microanalyser. The end-cap-pipe of the detector mounts a flange K which is connected to the port G through a gate valve L and a bellow-duct M. The compact-type gate valve L is specially designed by one of the authors (I. T.). The pipe slides in the flange K through greased O-ring. Thus, the angle of the detector with respect to the beam is changed and the detector is set at a desired distance from the target without breaking the vacuum. When the energy of X-rays to be measured is so high that their attenuation is negligible, L and M are removed and the every port of G is covered with a $50 \mu\text{m}$ Be foil.

There are three apertures on the upper lid and four on the wall at level lower than G. They are used for various purposes, e.g., for viewing the beam position by a television camera, as an inlet for the electronic signals or providing bias voltages, an inlet of gases for the gas-target cell and so forth. A photograph of the chamber is shown in Fig. 2.

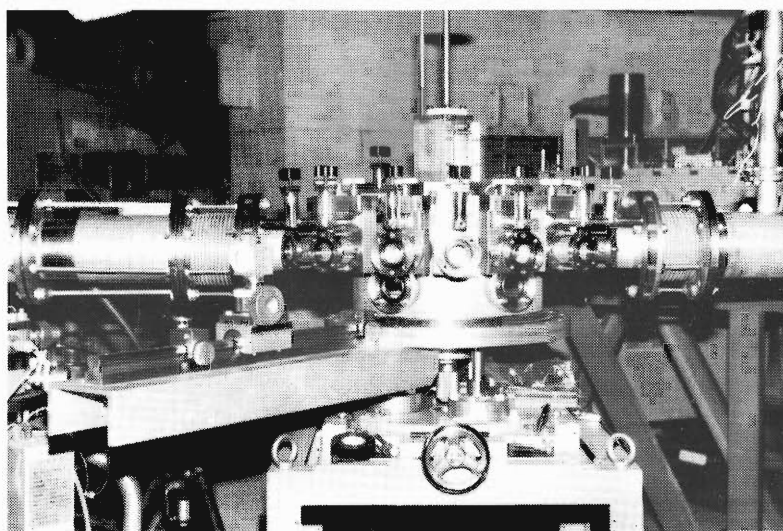


Fig. 2. Photograph of the chamber.

6-3. Kr $K\beta/K\alpha$ X-Ray Intensity Ratio by 6 MeV/amu Ion Bombardment

T. Tonuma, Y. Awaya, T. Kambara, H. Kumagai,
M. Kase, I. Kohno, A. Yagishita, and K. Izumo

Measurement of Kr $K\beta/K\alpha$ intensity ratio was made by 6 MeV/amu ion bombardment as a function of Kr gas pressure. We used ion beams of He, Li, B, C, N, O, and Ne from the cyclotron. K X-ray of Kr was detected with a Si(Li) detector.

The experimental apparatus, the condition of the measurement and a part of the experimental data have been reported.^{1),2)}

Figure 1 shows Kr $K\beta/K\alpha$ intensity ratios as a function of Kr gas pressure. The value of Kr $K\beta/K\alpha$ ratio induced by He ion bombardment increases slightly with gas pressure. The value for Li ion bombardment seems almost independent of gas pressure. On the other hand, the values for B, C, N, O, and Ne ion bombardment decrease with increasing gas pressure and the values decrease more rapidly for larger Z_1 of incident particles.

The values of $K\beta/K\alpha$ ratio without self-absorption, that are obtained by extrapolation of the curves to gas pressure of zero,²⁾ increase with Z_1 .

The gas pressure dependence of $K\beta/K\alpha$ ratio gives information about the multiple inner shell ionization.²⁾ On the assumptions that the value of fluorescence yield for each $K\beta$ satellite is the same and that the ionization cross section of single K-shell and n L-shell electrons is given by the binomial distribution formula, the average number of L-shell vacancies \bar{n}_L can be derived from the data. We estimated the effect of rearrangement on the $K\beta/K\alpha$ ratios in the simplest form. The transition of M-shell electrons to L-shell vacancies give the largest contribution to the effect. We took the rearrangement coefficient, f , as $\Gamma_L/\Gamma_{\text{total}}$ and obtained the results of \bar{n}_L values from the

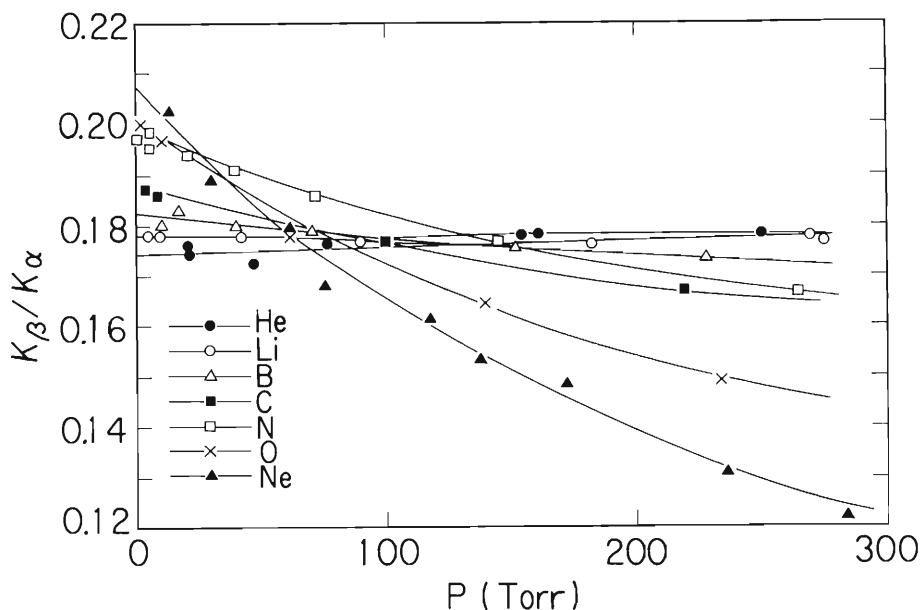


Fig. 1. Kr $K\beta/K\alpha$ intensity ratios induced by 6 MeV/amu ion bombardment as a function of Kr gas pressure.

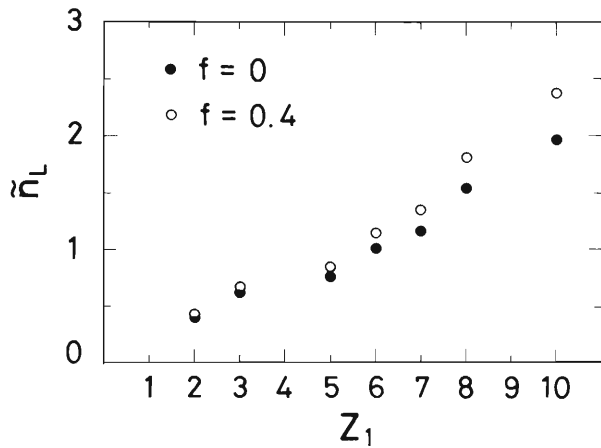


Fig. 2. The average number of L-shell vacancies \bar{n}_L versus atomic number of the incident particle Z_1 .

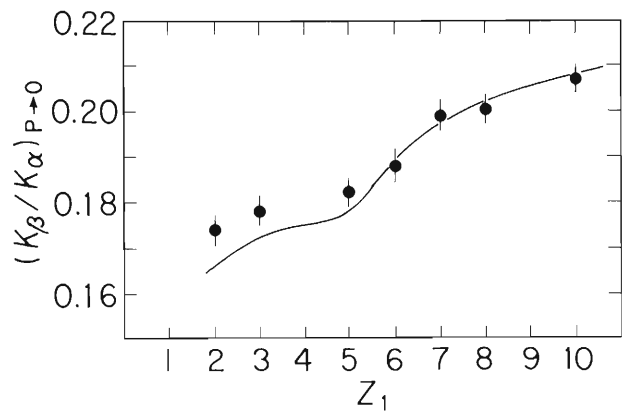


Fig. 3. Kr $K\beta/K\alpha$ intensity ratios without self-absorption as a function of Z_1 . Solid circles show the experimental results and solid line shows the calculated ones.

gas pressure dependence assuming f equal to 0.4 as shown in Fig. 2, where Γ_L and Γ_{total} are the decay rate of M-shell electrons to L-shell vacancies and the total decay rates, respectively. In the figure the solid circles show the results without the rearrangement effect and the open circles show the results with the effect. It is found that the effect is larger for larger Z_1 .

In Fig. 3 the full circles show the Kr $K\beta/K\alpha$ ratio without self-absorption as a function of Z_1 . The Z_1 -dependence of the ratios was estimated by use of \bar{n}_L values obtained from gas pressure dependence. We also assume that the ionization probability of an M-shell electron is proportional to Z_1^2 and the ionization of 3d-electrons precedes that of 3p-electrons. The solid line in the figure shows the calculated results for $f = 0.4$ as a smooth curve for convenience.

References

- 1) T. Tonuma, Y. Awaya, T. Kambara, H. Kumagai, and I. Kohno: IPCR Cyclotron Progr. Rep., 12, 84 (1978).
- 2) T. Tonuma, Y. Awaya, T. Kambara, H. Kumagai, M. Kase, and I. Kohno: *ibid.*, 13, 84 (1979).

6-4. Chemical Effect in Cu L X-ray Satellite Spectra

M. Uda and K. Maeda

Chemical effect appeared in intensity distributions of Cu L X-ray satellite spectra has been described in the last issue of IPCR Cyclotron Progr. Rep.¹⁾ X-ray transition energies of the satellites have also been calculated in the above mentioned report by use of the Hartree-Fock-Slater method whose computer program was written by Herman-Skillman.²⁾ The calculated transition energies agreed with the observed ones. A quantitative explanation of the satellite intensity distributions can not, however, be given by the above calculation. In this report an index to the solution of this problem will be given.

In the direct Coulomb ionization process, an initial electron vacancy distribution y_n of one and n vacancies in the L and M shells, respectively can be expressed by a binomial one,

$$y_n = {}_{18}C_n P_M^n (1 - P_M)^{18-n}, \quad (1)$$

where P_M is an ionization probability of the M shell at zero impact parameter. y_n is to be independent of chemical environment, or an ionization cross section of the M shell should be determined only by the relation between the incident energy and species of the projectile, and the species of the target atom.³⁾ Change in the intensity distributions of Cu L X-ray satellite spectra can then be explained by electron transfer, via a valence band, from surrounding atoms to the atom of interest prior to L X-ray emission. Let us define a probability of the transfer from a L^1M^n state to a L^1M^{n-1} state as $f_{n,n-1}$. Such a one electron transfer process occurs successively. Therefore, each of relative intensities of the L X-ray satellites y_n^X is written as

$$y_n^X = (\omega_n / \tilde{\omega}) (1 - f_{n,n-1}) (y_n + f_{n+1,n} y_{n+1} + f_{n+2,n+1} f_{n+1,n} y_{n+2} + \dots), \quad (2)$$

where ω_n and $\tilde{\omega}$ are a fluorescence yield of the L^1M^n state and a mean fluorescence yield, respectively. For the diagram line we get

$$y_0^X = (\omega_0 / \tilde{\omega}) (y_0 + f_{1,0} y_1 + f_{2,1} f_{1,0} y_2 + \dots). \quad (3)$$

If n is small, as in the case of Cu L X-ray spectra induced by 84 MeV N^{4+} , we may write $f_{n,n+1} \equiv f$. Then Eqns. (2) and (3) are simplified as

$$y_n^X = (\omega_n / \tilde{\omega}) (1 - f) (y_n + f y_{n+1} + f^2 y_{n+2} + \dots), \quad (4)$$

and

$$y_0^X = (\omega_0 / \tilde{\omega}) (y_0 + f y_1 + f^2 y_2 + \dots). \quad (5)$$

For the multiply ionized state $L_3^1 M^n$ induced by 84 MeV N^{4+} , we can estimate P_M of Cu to be 0.094 by the extrapolation of P_M data⁴⁾ obtained from Y, Mo, Sn, and Ag. From the P_M value thus determined we get the initial vacancy distribution in the Cu M shell, y_n , which is depicted in Fig. 1.

f is defined as

$$f = \Gamma_V / (\Gamma_L + \Gamma_V) , \quad (6)$$

where Γ_L and Γ_V are widths of the L shell of Cu and the valence band for Cu bearing compounds. As the widths of inner shells are less sensitive than the width of an outer shell to the change in chemical environment, we use the same theoretical value of Γ_L (Ref. 5) for all the Cu bearing compounds. For the first transition elements, the width of the valence band can be represented by that of $3d_{3/2,5/2}$ or $M_{4,5}$. Then the valence band width of CuF_2 ^{3),6)} may be replaced by the width of F 2p of this compound. y_n^X changes with f . Such a feature can be seen in Fig. 2. Using Eqn. (6) we get f for CuF_2 to be $45.4 \times 10^{-4} / (256 + 45.4) \times 10^{-4} = 0.15$.

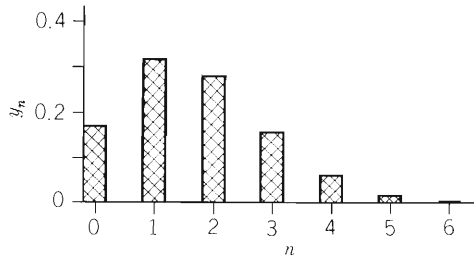


Fig. 1. An M shell vacancy distribution of Cu with $P_M = 0.094$. The distribution is expressed by the binomial one. A vacancy configuration is given by $L^1 M^n$.

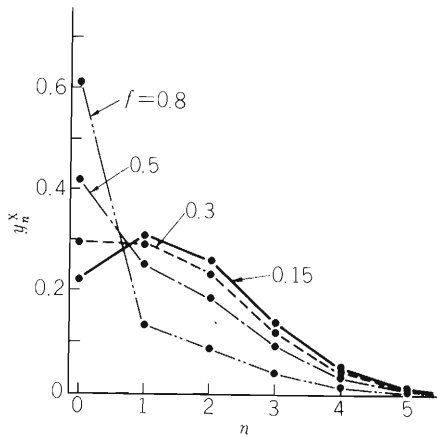


Fig. 2. An emitted Cu L X-ray intensity distribution as a function of the number of vacancies in the M shell, n . A parameter f is assumed to be from 0.15 to 0.8.

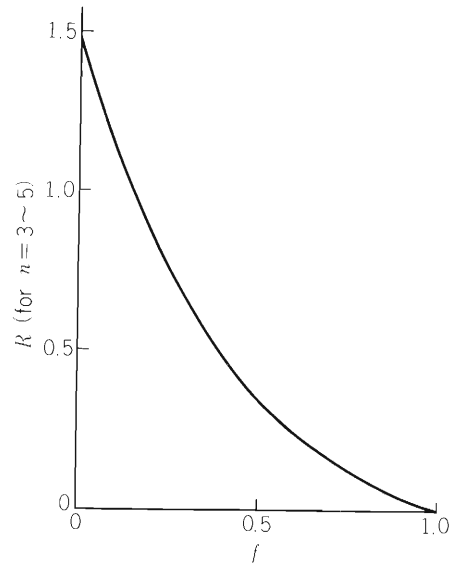


Fig. 3. R versus f curves for $n = 3 - 5$. See the text for the meaning of R and f .

If we use CuF_2 as a reference compound, we can simplify the relative intensity relation as

$$\frac{y_n^X(f) / y_n^X(f=0.15)}{y_0^X(f) / y_0^X(f=0.15)} \equiv R , \quad (7)$$

which includes one parameter f alone. The relation between R and f can now be drawn by putting an appropriate f value into Eqn. (7), as shown in Fig. 3. Then from the observed value of R we can determine the f value associated with the compound of interest. For more exact evaluation of R the emitted X-ray intensity should be corrected by taking the self absorption into account. Such a correction is now in progress.

References

- 1) M. Uda, K. Maeda, H. Endo, Y. Sasa, and M. Kobayashi: IPCR Cyclotron Progr. Rep., 13, 86 (1979).
- 2) F. Herman and S. Skillman: "Atomic Structure Calculations", Prentice Hall Inc., Englewood Cliffs, New Jersey (1963).
- 3) M. Uda, H. Endo, K. Maeda, Y. Awaya, M. Kobayashi, Y. Sasa, H. Kumagai, and T. Tonuma: Phys. Rev. Lett., 42, 1257 (1979).
- 4) Y. Awaya, K. Izumo, T. Tonuma, T. Katou, Y. Tendow, H. Kumagai, T. Takahashi, A. Hashizume, and T. Hamada: IPCR Cyclotron Progr. Rep., 13, 76 (1979).
- 5) E. J. McGuire: Phys. Rev. A, 3, 587 (1971).
- 6) H. Endo, M. Uda, and K. Maeda: *ibid.*, 22, 1436 (1980).

6-5. Energy Straggling of C Ions in Metal Foils and Foil Non-Uniformity Effect

T. Takahashi, Y. Awaya, T. Tonuma, H. Kumagai,
K. Izumo, A. Hitachi, M. Nishida, and A. Hashizume

Recently, Sofield, Cowern, and Freeman¹⁾ pointed out that the departure of our experimental energy straggling of C ions^{2),3)} from the Bethe-Livingston theory may be ascribed to non-uniformity of the foil. According to Sofield et al., square of the apparent energy straggling due to foil non-uniformity is given by

$$\eta_f^2 = 2^2 (2 \ell n 2) (\sigma_f / \Delta x)^2 (\Delta E)^2, \quad (1)$$

where σ_f is the thickness fluctuation (standard deviation), Δx the mean thickness of the foil and ΔE the mean energy loss in the foil.

Using the experimentally observed straggling (fwhm) η_{exp} and the theoretical value from the Bethe-Livingston theory, η_{BL} , we calculated the ratio R^c/R^{He} in Ref. 2, to evaluate the “true” straggling for C ions in foils of unsatisfactory uniformity. Here, R^c is $\eta_{\text{exp}}/\eta_{\text{BL}}$ for C ions and R^{He} is the ratio for He ions (details are explained in Ref. 2). We admit that the ratio is inadequate as a measure for deviation from the Bethe-Livingston theory, because R^c/R^{He} cannot cancel the foil non-uniformity effect.

However, it should be noted that the value of $(\sigma_f/\Delta x)^2$ derived from the relation¹⁾

$$\eta_f^2 = \eta_{\text{exp}}^2 - \eta_{\text{BL}}^2 \quad (2)$$

should be equal for both C ions and He ions, if Sofield’s concept is valid. According to our experiment, $(\sigma_f/\Delta x)^2$ obtained from C ions is $(6.7 \pm 1.2) \times 10^{-4}$, whereas $(\sigma_f/\Delta x)^2$ obtained from He ions is $(-4.8 \pm 6.6) \times 10^{-4}$ for Ag foils. For the other foils $(\sigma_f/\Delta x)^2$ is always larger for C ions than for He ions as shown in Table 1. The difference is not within the limit of error except

Table 1. Values of $(\sigma_f/\Delta x)^2$ derived from Eqns (1) and (2).

Foils	$(\sigma_f/\Delta x)^2$ obtained from the experiment of ~ 7 MeV/nucleon He ions	$(\sigma_f/\Delta x)^2$ obtained from the experiment of ~ 7 MeV/nucleon C ions
Al	$(0 \pm 5.4) \times 10^{-4}$	$(3.0 \pm 0.7) \times 10^{-4}$ *
Ag	$(-4.8 \pm 6.6) \times 10^{-4}$	$(6.7 \pm 1.2) \times 10^{-4}$
Au	$(2.9 \pm 0.4) \times 10^{-3}$	$(4.0 \pm 0.6) \times 10^{-3}$
Pb	$(8.5 \pm 1.5) \times 10^{-3}$	$(12.9 \pm 1.5) \times 10^{-3}$

* This value was obtained from the experiment using C ions of 5.31 MeV/nucleon.

for the Al foil. Therefore, it would be reasonable to consider that the difference between $(\sigma_f/\Delta x)^2$ for C ions and that for He ions is small but still exists.

The reason for the discrepancy shown in Table 1 might be explained by charge exchange because of the small difference. Accordingly, it should be reserved to conclude that the carbon ions of 5 -- 7 MeV/nucleon are fully stripped, as has been claimed by Sofield et al.

References

- 1) C.J. Sofield, N.E.B. Cowern, and J.M. Freeman: Nucl. Instr. and Meth., 174, 611 (1980).
- 2) T. Takahashi, Y. Awaya, T. Tonuma, H. Kumagai, K. Izumo, A. Hashizume, S. Uchiyama, and A. Hitachi: *ibid.*, 166, 587 (1979).
- 3) T. Takahashi, Y. Awaya, A. Hashizume, K. Izumo, H. Kumagai, T. Tonuma, and S. Uchiyama: IPCR Cyclotron Progr. Rep., 12, 92 (1978).

6-6. Helium Embrittlement in Precipitation-hardenable Alloys

H. Shiraishi, H. Shinno,* N. Yamamoto,* H. Yoshida*,
H. Kamitsubo, I. Kohno, and T. Shikata

It is well known that iron base austenitic alloys of high nickel (25 – 45 %) content have excellent low swelling characteristic. However, several experimental data suggest that these materials in a precipitation-hardened state have higher sensitivity to neutron irradiation embrittlement than 316 or similar 300 series stainless steels. From the standpoint of a reactor structural design, high strength and high ductility are desirable for reactor operation at high temperature, but, in general, high strength reduces the ductility. This trend is substantially strengthened in the irradiated state. The neutron irradiation embrittlement at temperature higher than $0.5 T_m$ (T_m : melting point) is strongly correlated with the so-called helium embrittlement. In the present study, the embrittlement of helium injected materials was determined as a function of the tensile strength. The strength was widely varied by various types of pre-injection and post-injection treatments. The present work aimed to find out such a treatment which will give a good combination of strength and ductility.

Results of chemical analysis of the samples used are presented in Table 1. 7817 and 7818 are γ' Ni₃ (Ti, Al) and γ'' Ni₃Nb precipitation-hardenable alloys, respectively. The specimens for tensile test were fabricated in National Research Institute for Metals. The dimension of gauge section was 10 mm long, 4 mm wide, and 0.2 mm thick. The conditions of solution treatments and helium preinjection treatments are given in Table 2.

Table 1. Chemical composition of used samples. (wt.%)

	C	Ni	Cr	Mo	Ti	Al	Nb	Si	Mn	B
7817	0.021	40.2	14.6	3.19	2.01	0.87		0.47	0.19	0.0049
7818	0.024	39.9	14.7	3.03	0.31		2.96	0.48	0.19	0.0048

The specimens were deformed by the tensile test machine before the helium injection. Helium was injected at constant high temperature (650°C), using the cyclotron. Conditions of helium injection and post-injection treatment are also given in Table 2. The helium concentration amounted to 5 to 10 atomic ppm. The tensile test was conducted at 650°C in vacuum of 3×10^{-4} Pa with a strain rate of 5×10^{-4} /s. Conditions for six kinds of treatments done before helium injection are presented in Table 2. Solution treatment and 10 % pre-strain treatment followed by two kinds of aging treatments resulted in the highest precipitation strengthening and the state of slightly overaged condition, respectively. These conditions were decided from the result of preceding experiment on the aging response of 7817 alloy. 7818 alloy was not precipitation-hardened so much as 7817 alloy by these pre-injection treatments.

The result of the tensile test is shown in Table 2. 7817 alloy hardened by γ' -precipitation has a higher sensitivity to the helium embrittlement than 7818 alloy hardened by γ'' -precipitation. In 7817 alloy, overaging improved the ductility and the combination of 10 % pre-strain and overaging gave the best combination of strength and ductility. In 7818 alloy, the decrease of total elongation in the solution treated and aged condition was very small. The 10 % pre-strain seemed to have deleterious effect on ductility in this case. The post-injection anneal recovered the ductility in 7817 alloy, but the reversed effect was observed in 7818 alloy. These complex behaviours of the helium embrittlement of alloys precipitation-hardened by intermetallic compound are seen to be dependent on the aging process and their inherent tensile strength, as illustrated in Fig. 1. The tensile strength was varied in a wide range by various pre- and post-injection treatments. Figure 1 shows that the degree of helium embrittlement is mainly determined by the alloy strength, regardless of the alloy

* National Research Institute for Metals.

Table 2. Mechanical properties of helium injected 7817 and 7818 alloys (Fe-40Ni-15Cr).

Test temp.: 650°C, Strain rate: 5×10^{-4} /sec

Sample No.	Pre-injection treatment	He conc. (at. ppm)	Injec. temp. (°C)	Post-injection treatment	0.2% proof stress (Mpa)	Tensile strength (Mpa)	Uniform elonga. (%)	Total elonga. (%)
7817	ST 1000°C, 30min	{ 5	650		410	701	3.3	3.3
		{ 0			281	624	35.2	43.7
	ST + 700°C, 300h	{ 5	650		770	870	1.8	1.8
		{ 0			709	865	5.2	26.6
	ST + 750°C, 300h	{ 5	650	750°C, 700h	625	732	5.7	5.7
		{ 0			624	775	7.5	35.3
		{ 10	650		449	632	12.3	15.3
		{ 0			no experiment			
	10% PS	{ 5	650		574	776	1.9	2.2
		{ 0			455	686	22.0	33.2
	10% PS + 700°C, 30h	{ 5	650	700°C, 988h	841	907	1.2	1.2
		{ 0			818	928	4.5	24.4
		{ 10	650		545	698	8.0	8.2
		{ 0			no experiment			
	10% PS + 700°C, 300h	{ 5	650	700°C, 700h	825	910	5.6	7.0
		{ 0			759	825	7.3	24.4
{ 10		650	522		686	8.2	9.6	
{ 0			no experiment					
7818	ST 1100°C, 30min	{ 5	650	650°C, 1000h	194	475	27.4	31.4
		{ 0			174	482	31.5	39.2
		{ 10	650		470	602	7.3	14.5
		{ 0			no experiment			
	ST + 700°C, 300h	{ 5	650		243	531	19.3	32.5
		{ 0			223	479	23.7	33.0
	ST + 750°C, 300h	{ 5	650		224	528	18.3	38.3
		{ 0			234	488	17.7	43.1
	10% PS	{ 5	650		342	518	17.1	17.9
		{ 0			347	514	19.2	28.1
	10% PS + 700°C, 30h	{ 5	650		287	497	21.0	23.2
		{ 0			498	648	12.6	29.3
	10% PS + 700°C, 300h	{ 5	650		312	499	12.5	15.2
		{ 0			473	615	11.5	23.9
	ST + 750°C, 300h + 650°C, 300h	{ 10	650		234	516	22.0	39.8
		{ 0			250	521	22.3	43.3
ST + 700°C, 300h + 650°C, 300h	{ 10	650		287	570	22.6	34.9	
	{ 0			329	577	29.3	37.3	

ST: Solution treatment; PS: Pre-strained

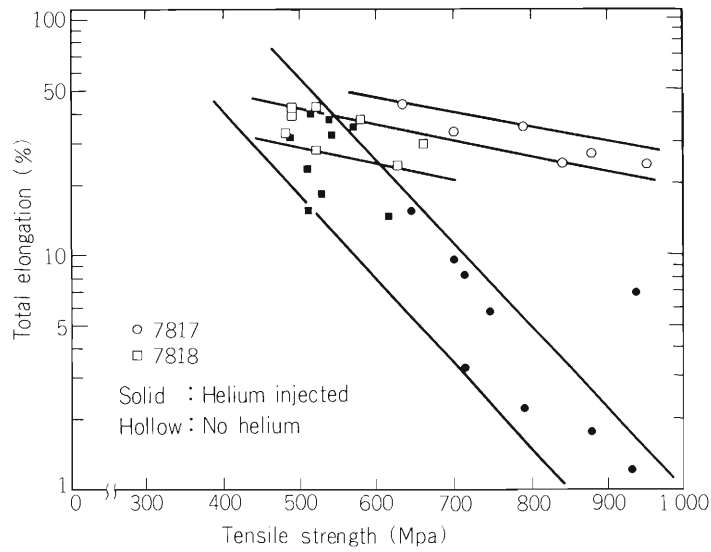


Fig. 1. Relationship between total elongation and tensile strength of helium injected Fe-Ni-Cr austenitic alloys. He conc.: 5 – 10 atomic ppm; Test temp.: 650°C; Strain rate: 5×10^{-4} /s

type, except for one example of 7818 alloy which was 10 % pre-strained and aged at 700°C for 300 h. At the stress level of 500 Mpa, the helium embrittlement was suppressed almost perfectly. The total elongation of 5 % can be ensured at the tensile strength of 650 Mpa. The result of the pre-injection treatment (10 % pre-strain + 700°C, 300 h) in 7817 alloy is unusual and the reason or the mechanism for the improvement should be investigated more carefully before arriving at any conclusion, but makes one to expect further improvement in the total elongation at such a high strength level.

6-7. Backward Secondary Electron Emission from Al, Cu, Ag, and Au Targets under High Energy N^{7+} and N^{4+} Ion Bombardments

A. Koyama, T. Shikata, and H. Sakairi

In the last volume we reported on total backward secondary electron emission (BSEE) yields under proton bombardments, $\gamma(p)$, for Al, Cu, Ag, and Au targets in the incident energy range from 5 to 12 MeV.¹⁾

In that report it was shown that $\gamma(p)$ is in proportion to the specific electronic energy loss (SEEL) of protons, S_p , in target materials, and that the ratio $\gamma(p)/S_p$ is independent of proton incident energy.

In the present report we study BSEE yields for N^{7+} and N^{4+} ion bombardments. The apparatus and experimental procedures are the same as those in the previous report.

Ions N^{4+} are directly accelerated by the cyclotron. On the other hand, ions N^{7+} are produced by passing N^{4+} ions through a 6 μm aluminum foil. Ions N^{7+} are separated and guided to the target by a magnetic analyser. The distance between the aluminum foil and the target is about 8 m.

Figure 1 shows the total BSEE yields from Al, Cu, Ag, and Au targets for N^{7+} and N^{4+} ion bombardments, $\gamma(N^{7+})$ and $\gamma(N^{4+})$, at an incident energy of 6.8 MeV/amu. Values of $49\gamma(p)$ and $16\gamma(p)$ for this incident energy are also shown for reference.

According to Oda and Lyman, forward SEE yields for various projectiles with the same velocity are proportional to the square of the effective charge numbers Z_{eff} of the projectiles.²⁾ The effective charge number of a N^{7+} ion is nearly equal to 7 at this incident energy.³⁾ The charge number of N^{7+} within the secondary electron escape depth will therefore be 7 at this energy. However, values of $\gamma(N^{7+})$ are smaller than those of $49\gamma(p)$ for all these target materials. Further

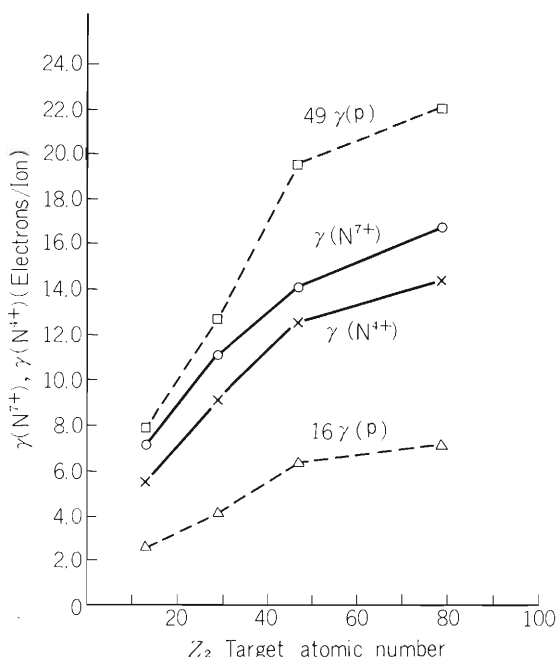


Fig. 1. Total backward secondary electron emission ratios under N^{7+} and N^{4+} ion bombardments for Al, Cu, Ag, and Au target materials. Incident energy is 6.8 MeV/amu. Squares and triangles show values of 49 and 16 times those of $\gamma(p)$, respectively. The values of $\gamma(p)$ were taken from Ref. 1.

experiments are necessary to elucidate the departure of the BSEE yield from the proportionality to Z_{eff}^2 .

According to electron loss cross sections of N^{4+} ions in the energy region concerned here, the charge number of N^{4+} ions is not increased so much and nearly equal to 4 within the secondary electron escape depth.⁴⁾ However $\gamma(N^{4+})$ is about twice as large as $16\gamma(p)$, though it is of course smaller than $\gamma(N^{7+})$.

This will be explained as follows: the charge number of a N^{4+} ion will appear to be 4 for a target electron when it is far from the N^{4+} ion, where the charge of the nitrogen nucleus is screened by the remained three electrons of the N^{4+} ion. But the charge number of the N^{4+} ion will appear to be 7 for a target electron which is nearer to the nitrogen nucleus than all the three electrons. Therefore $\gamma(N^{4+})$ will have a value between those of $\gamma(N^{7+})$ and $16\gamma(p)$.

References

- 1) A. Koyama, T. Shikata, and H. Sakairi: IPCR Cyclotron Progr. Rep., 13, 94 (1979);
A. Koyama, T. Shikata, and H. Sakairi: Japan. J. Appl. Phys., 20, 65 (1981).
- 2) N. Oda and J.T. Lyman: Radiat. Res., Suppl., 7, 20 (1967).
- 3) P.G. Roll and F.E. Steigert: Nucl. Phys., 17, 54 (1960).
- 4) T. Tonuma, Y. Miyazawa, F. Yoshida, T. Karasawa, T. Takahashi, and S. Konno: J. Phys. Soc. Japan, 34, 148 (1973).

6-8. Measurements of the Compton Profile and Angular Correlation of Positron Annihilation Radiations in Amorphous $\text{Mg}_{70}\text{Zn}_{30}$

N. Shiotani, N. Sakai, T. Okada,
H. Sekizawa, and T. Mizoguchi

A study was made on the electron momentum distribution in amorphous $\text{Mg}_{70}\text{Zn}_{30}$ alloy by measurements of the Compton profile and angular correlation of positron annihilation radiations.

Amorphous $\text{Mg}_{70}\text{Zn}_{30}$ ribbons were prepared by melt spinning method. The thickness and the width of the ribbon were about $50\ \mu\text{m}$ and $2\ \text{mm}$, respectively. The ribbons of $20\ \text{mm}$ in length were put side by side and stacked one over another to form a specimen of $20\ \text{mm}$ in length, by $20\ \text{mm}$ in width, and $0.6\ \text{mm}$ in thickness for the positron annihilation experiment and that of $20\ \text{mm}$ in length, by $20\ \text{mm}$ in width, and by $1.0\ \text{mm}$ in thickness in an envelope of Mylar sheet of $0.01\ \text{mm}$ in thickness for the Compton profile measurement. The Compton profile was measured using $59.54\ \text{keV}$ γ rays from ^{241}Am source of $300\ \text{mCi}$ and a pure Ge detector. The specimen was kept at room temperature in vacuum. The scattering angle was chosen to be 150 degrees. The overall momentum resolution was 0.66 atomic units (a.u.) in full width at half maximum. The multichannel pulse height analyzer with a built-in digital stabilizer was used. Two γ rays of $59.4\ \text{keV}$ from ^{241}Am and $23.8\ \text{keV}$ from $^{119\text{m}}\text{Sn}$ were used as the standard peaks. The accumulated counts at the peak of the Compton profile were about 1×10^4 .

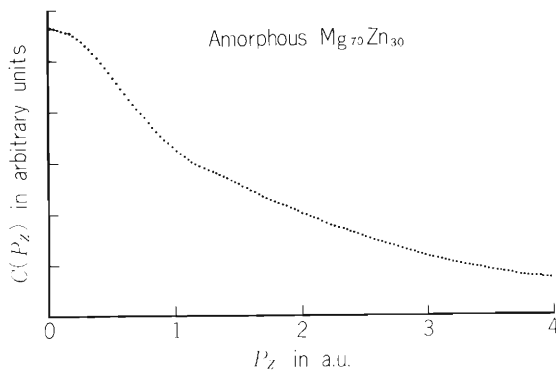


Fig. 1. The Compton profile $C(p_z)$ of the amorphous $\text{Mg}_{70}\text{Zn}_{30}$ alloy measured at $300\ \text{K}$. The corrections were made of the back ground, the detector efficiency, the self-absorption and the long tail effect.

The measured Compton profile $C(p_z)$ of the amorphous $\text{Mg}_{70}\text{Zn}_{30}$ is shown in Fig. 1. Corrections were made of the backgrounds, the effect of the energy-dependent efficiency of the detector, the self-absorption in the specimen and so-called "long tail" effect. The effect of multiple scattering is not corrected. The observed profile consists of a parabolic valence electron part and a broad core electron part. Due to the low momentum resolution, a break at the Fermi momentum is smeared and hard to be seen. However, the parabolic part of the observed profile of the amorphous $\text{Mg}_{70}\text{Zn}_{30}$ alloy is very much similar in shape to that of a pure magnesium single crystal measured with the same experimental conditions.¹⁾ This fact strongly indicates that the bulk of the valence electrons in amorphous $\text{Mg}_{70}\text{Zn}_{30}$ alloy behaves like free-electrons.

The angular correlations of positron annihilation radiations were measured using a parallel slit system. The geometrical angular resolution was measured to be 0.61 milliradians or 0.084 a.u. in the momentum resolution. The angular correlation curves were measured at $80\ \text{K}$ and $300\ \text{K}$. The specimen was kept in vacuum at both temperatures. The accumulated coincident counts were over 5×10^4 at the central portion of the angular correlation curves. The observed angular correlation curves $N(p_z)$ and their slope $|\Delta N(p_z)/\Delta p_z|$ are shown in Figs. 2 and 3. Owing to much better momentum resolution in the angular correlation measurement than in the Compton profile measurement, it is clearly seen that the angular correlation curves consist of the parabolic main part and the broad tail with much smaller intensity. There is a definite break at the Fermi momentum on each curve. Comparing the observed angular correlation curves of the amorphous $\text{Mg}_{70}\text{Zn}_{30}$ alloy with that of a pure

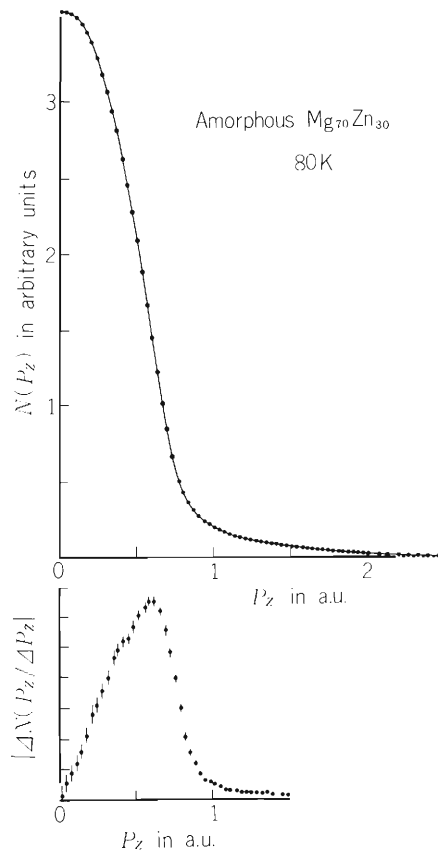


Fig. 2. The angular correlation curve $N(p_z)$ of the amorphous $Mg_{70}Zn_{30}$ alloy measured at 80 K and its slopes.

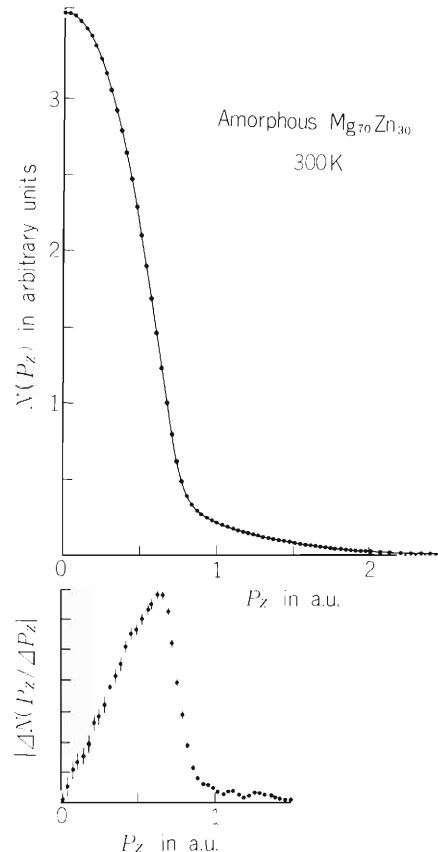


Fig. 3. The angular correlation curve $N(p_z)$ of the amorphous $Mg_{70}Zn_{30}$ alloy measured at 300 K and its slopes.

Mg single crystal measured with the same experimental conditions,²⁾ we find the following facts: 1) the break at the Fermi momentum is very much smeared in the amorphous alloys, and 2) the momentum-dependent enhancement effect which appears in the case of simple metals as characteristic bulge of the main parabolic part is not seen in the amorphous alloys. Short mean free path of the electrons and the positrons due to the randomness of the lattice potentials would cause in general smearing of the break, but little is known quantitatively. On the other hand it has been known from studies of crystalline simple metals and alloys that a heavy smearing of the break occurs when a positron is trapped by vacancy type defects³⁾ or localized in a region where an attractive potential for the positron is formed by inhomogeneity of constituents.⁴⁾ The momentum-dependent enhancement effect which appeared as the bulge of the parabolic part is characteristic for the special case of a positron freely moving in an electron gas. If the positron is not free to move, the enhancement effect may appear in a different way. Thus the two experimental findings mentioned above strongly imply that the positron is not free to move in the amorphous $Mg_{70}Zn_{30}$ alloy. The positrons are localized most probably in low density diluted regions inherently contained in amorphous structures.

References

- 1) N. Sakai and H. Sekizawa: to be published.
- 2) N. Shiotani, T. Okada, H. Sekizawa, and S. Wakoh: J. Phys. Soc. Japan, 50, (1981) in press.
- 3) J. H. Kusmiss and J. W. Swanson: Phys. Lett., 27A, 517 (1968).
- 4) P. Kubica, B. T. A. McKee, A. T. Stewart, and M. J. Stott: Phys. Rev. B, 11, 11 (1975).

6-9. ^{119}Sn Emission Mössbauer Study of ^{119}Sb Adsorbed on $\alpha\text{-Fe}_2\text{O}_3$

T. Okada, H. Sekizawa, F. Ambe, and S. Ambe

A study was made on the electronic states of dilute tin ions on the surface of hematite ($\alpha\text{-Fe}_2\text{O}_3$) by means of ^{119}Sn Mössbauer emission spectroscopy. The ^{119}Sn source is realized by utilizing the EC decay of ^{119}Sb (Fig. 1) adsorbed on the surface. Hematite is a corundum type iron oxide with a rhombohedral symmetry $R\bar{3}C$. Below 260K, which is called Morin transition temperature, hematite is antiferromagnetic, while it becomes weakly ferromagnetic above 260K by slight canting of the antiferromagnetic sublattices. The Néel temperature T_N of hematite is 950K.

Radioactive ^{119m}Te was produced by bombarding a tin plate with 40 MeV α -particles from the cyclotron. The nuclide was chemically separated from the solution containing the dissolved target. ^{119}Sb arising from the ^{119m}Te was repeatedly separated in a carrier-free state. Then, hematite powder was dispersed in a slightly acidic aqueous solution containing the $^{119}\text{Sb}^{5+}$ ions. The resultant suspension was stirred in order to let the hematite adsorb the ^{119}Sb ions on the surface. The hematite powder was filtered and dried in vacuum at room temperature and this is called specimen (A). Then, a number of powder specimens were subjected to two hour heat-treatments in air at various temperatures so as to diffuse ^{119}Sb ions into the specimens; the heat treatments were done at 200°C (B), 420°C (C), 500°C (D), and 700°C (E). Another specimen (F) was obtained by coprecipitating $^{119}\text{Sb(V)}$ and Fe^{3+} from an aqueous solution with subsequent calcination in air at 700°C for two hours.

Mössbauer emission spectra of ^{119}Sn (resulting from the EC decay of ^{119}Sb) were taken against a BaSnO_3 absorber at room and liquid nitrogen temperatures.

The spectra for the specimens (A) to (F) are shown in Fig. 2. From the values of isomer shifts, it is certain that the valence states of tin ions resulting from $^{119}\text{Sb}^{5+}$ are Sn^{4+} in all the specimens. Even in the "as adsorbed" specimen (A), there can be seen a remarkable broadening of the emission line. We attribute it to magnetic interaction on the tin ions from the magnetically ordered hematite matrix through the supertransferred hyperfine interaction mechanism. The average hyperfine magnetic field increases by heat-treatment as can be seen for (B)–(E). The

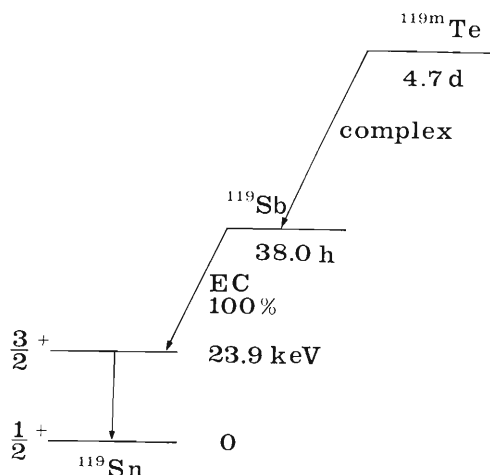


Fig. 1. Decay scheme of ^{119m}Te and ^{119}Sb .

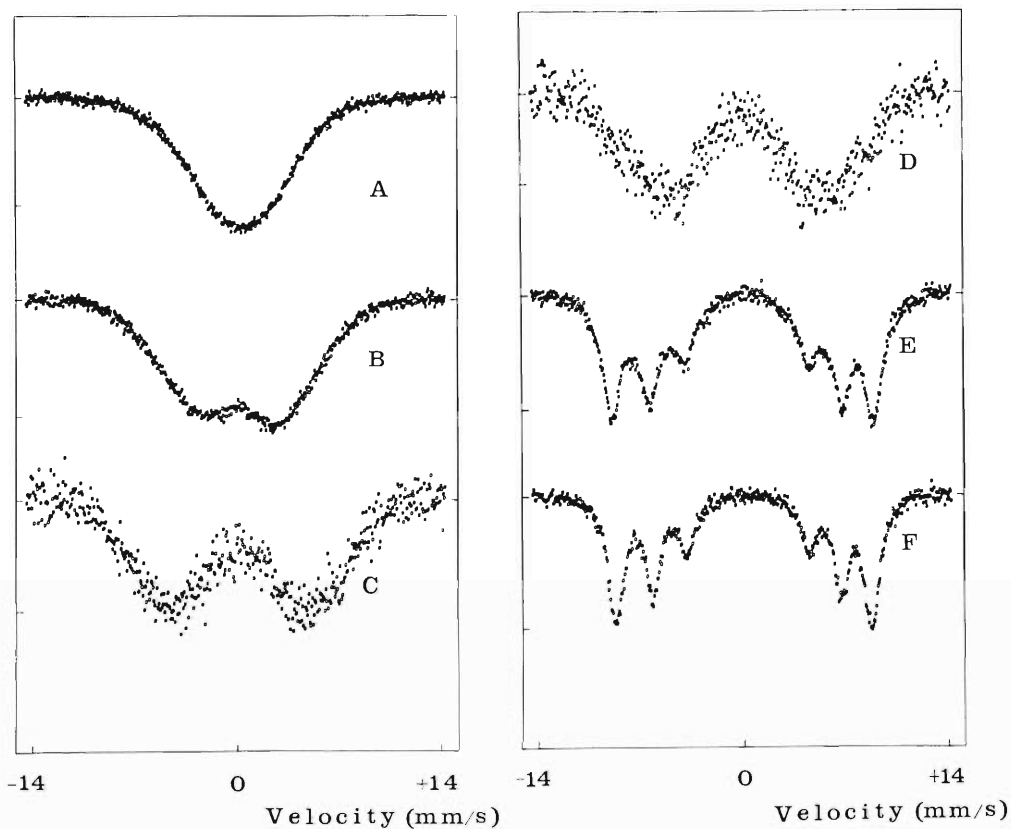


Fig. 2. Mössbauer emission spectra of ^{119}Sb adsorbed on hematite. (A): "as adsorbed". (B) – (E): after two hour heat-treatment at 200°C (B), 420°C (C), 500°C (D), and 700°C (E). (F): coprecipitated and calcined for two hours at 700°C .

spectrum of (E) is almost equal to that of (F), which means that after two hour heat-treatment at 700°C the adsorbed $^{119}\text{Sb}^{5+}$ ions diffuse into the matrix deep enough to feel the same supertransferred hyperfine magnetic field as the coprecipitated ions. The fact that no diamagnetic component exists in spectrum (A) is especially interesting. It means that all the adsorbed $^{119}\text{Sb}^{5+}$ ions are bound to Fe^{3+} ions of the matrix through O^{2-} without forming three-dimensional clusters.

The detailed report of the investigation in progress will be published elsewhere.

6-10. X-Rays Induced by Collisions between 110 MeV

Ne Ions and Gases

T. Kambara, Y. Awaya, A. Hitachi,
M. Kase, I. Kohno, and T. Tonuma

X-rays from 5.5 MeV/amu highly ionized Ne-ion bombardment on gases of atomic number $Z_T \leq 10$ were studied. Most of the observed X-rays are from the radiative electron capture (REC) and the electronic transitions in the projectile ions. A Si(Li) detector was used in most of the measurements, and a crystal spectrometer was used only in high resolution measurements of X-rays emitted from the projectile ions. The target gases were H_2 , He, CH_4 , N_2 , O_2 and Ne whose pressure ranged from 0.5 to 300 Torr.

Ne-ions of 120 MeV from the cyclotron were led to the gas target cell. The gas pressure was monitored by an α -tron gauge. The beam energy at the center of the cell was reduced by about 10 MeV. Such reduction is caused by the energy loss in the beam entrance window (7 μm thick Al foil) and the target gas. The charge state of the ions in the cell is considered to be in equilibrium: about 80% of the ions are $10+$ (bare), about 20% are $9+$ (H-like) and a few percents are $8+$ (He-like).¹⁾ Emitted X-rays passed through a 4 μm thick Mylar foil window and were detected by either the Si(Li) detector or the crystal spectrometer. The Si(Li) detector was placed at 90° to the incident beam direction and the crystal spectrometer at about 116° . The resolution of the Si(Li) detector was about 270 eV (FWHM) at 6.4 keV. A TAP crystal ($2d = 25.69 \text{ \AA}$) and a gas flow proportional counter were used in the spectrometer, the resolution of which was about 7 eV (FWHM) at 1.25 keV (Mg K X-ray).

Figure 1 shows an X-ray spectrum measured by the Si(Li) detector when the target was N_2 gas at about 20 Torr. Two peaks appearing close together at about 1.0 and 1.2 keV correspond to the K X-rays from the projectile ions. The broad peak near 4 keV corresponds to the REC X-rays. Figure 2 shows high resolution spectra of K X-rays from the projectile measured by the crystal spectrometer when the target was N_2 gas at about 50 Torr. It was found that the peaks at 1.0 and 1.2 keV observed by the Si(Li) detector originated in the one electron transitions in the hydrogen-like Ne^{9+} ions: the 1.0 keV peak was from the $2p-1s$ transition and the 1.2 keV peak is a superposition of the lines from the $np-1s$ ($n=3, 4, 5, 6$) transitions. The measured X-ray energy values, after the correction for the Lorentz transformation, agree with the calculated ones from the Dirac equation within 0.5%.

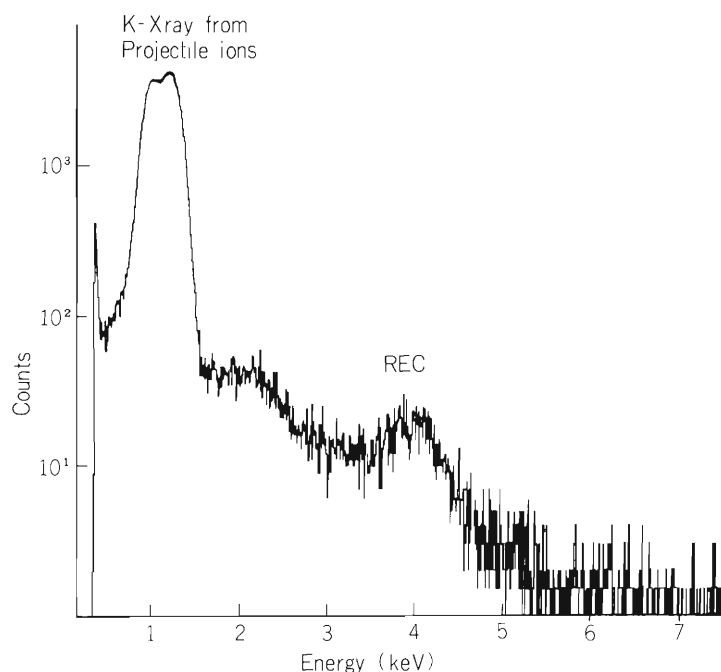


Fig. 1. Spectrum of X-rays from Ne-ion bombardment on 20 Torr N_2 gas, measured by the Si(Li) detector.

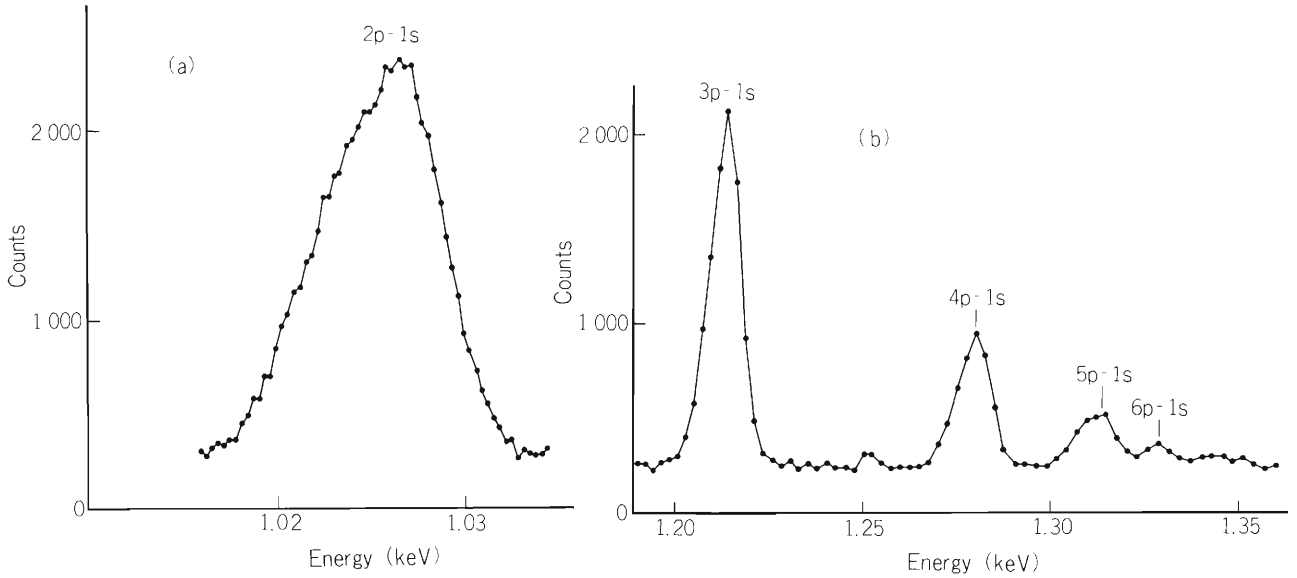


Fig. 2. High resolution K X-ray spectrum from Ne-ions incident on 50 Torr N_2 gas, measured by the crystal spectrometer.

The profile of the REC spectra reflects the electron momentum distribution in the target. We have calculated the peak positions and widths by the impulse approximation²⁾ with the approximate wave function given by Slater³⁾ for the target electrons. In the calculation, we assumed that 1) incident ions are 10^+ , 2) target gas is of atomic particles and 3) only the outermost shell electrons of the target are captured. The REC cross section is given by the impulse approximation as follows:

$$\frac{d^2\sigma}{dE_X d\Omega_X} = \int d^3p_i \left(\frac{d\sigma}{d\Omega} f \right)_{\vec{p}_0, \vec{p}_i} \left| \phi(\vec{p}_i) \right|^2 \delta(E_i - E_f),$$

where $d\Omega_X$ is the solid angle, E_X is the energy of the REC X-ray quanta, $\vec{p}_0 = m\vec{v}_0$ with ion velocity v_0 and electron mass m , \vec{p}_i is the momentum of the target electron to be captured and $\frac{d\sigma}{d\Omega} f$ is the capture cross section of free electrons by the incident ions. The δ -function guarantees energy conservation and $|\phi(\vec{p}_i)|^2$ is the momentum distribution of the target electrons. The approximate wave function of Slater gives the momentum distribution as follows:

$$\left| \phi(\vec{p}_i) \right|^2 = 8 p_s^5 / \pi^2 \left(p_i^2 + p_s^2 \right)^4,$$

where $p_s = Z_{sc} m e^2 / \hbar n^*$ with screened nuclear charge Z_{sc} and effective principal quantum number n^* . Values of n^* and Z_{sc} are listed in Table 1. Table 1 lists also T_s , the average kinetic energy which is equal to $p_s^2 / 2m$.

Table 1. The values of the effective principal quantum number (n^*), screened nuclear charge (Z_{sc}), and average kinetic energy of the target electrons ($T_s = p_s^2 / 2m$).

	H ₂	He	CH ₄	N ₂	O ₂	Ne
n^*	1	1	2	2	2	2
Z_{sc}	1	1.7	3.25	3.9	4.55	5.85
T_s (eV)	13.6	39.3	35.9	51.9	70.4	117

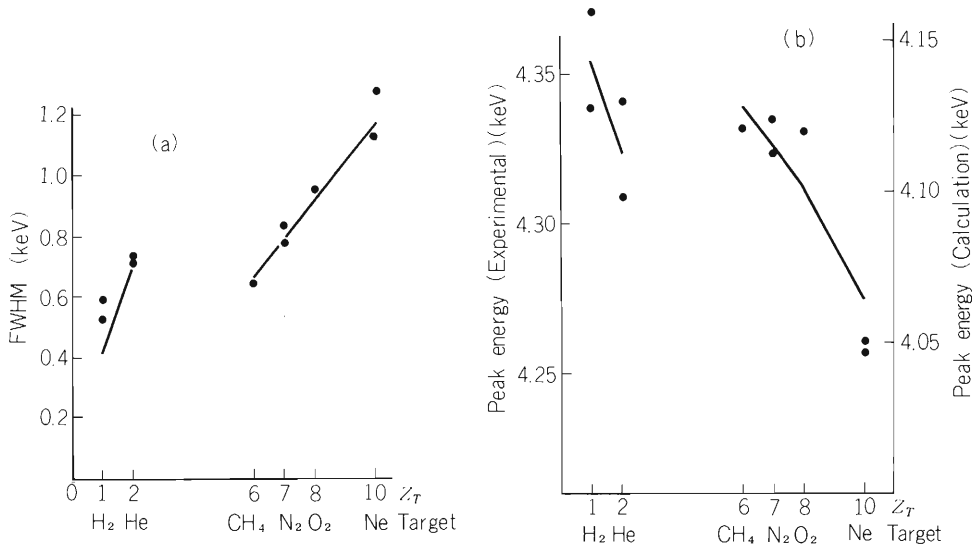


Fig. 3. Dependence of REC peak on the target. (a) width, (b) position. The solid lines show the calculated values and the dots are from the least squares fitting of the experimental data.

The results of the calculation is shown in Fig. 3 with the experimental data. The experimental values of the peak widths and positions were derived from the observed spectra by the least squares fitting. Values of peak width lie on two lines in the figure, which correspond to $n=1$ shell for H₂ and He, and $n=2$ shell for CH₄, N₂, O₂ and Ne. The agreement between the experimental data and the result of the calculation is good. On the other hand, the experimental peak positions were reproduced by the calculation as far as their relative values are concerned. The reasons for it may be considered as follows: 1) we neglected the contribution from Ne⁹⁺ which may shift the peak to lower energy; 2) the REC peaks are broad and there is some uncertainty in defining the peak position by the least squares fitting; 3) the beam energy at the center of the cell may be lower than that estimated.

Further experiments and analyses, such as the measurement of the angular distribution of REC X-rays, are now in progress.

References

- 1) J. B. Marion and F. C. Young: "Nuclear Reaction Analysis Graphs and Tables", North Holland, p.45 (1968).
- 2) M. Kleber and D. H. Jakubassa: Nucl. Phys., A252, 152 (1975).
- 3) J. C. Slater: "Quantum Theory of Atomic Structure", McGraw-Hill, New York, 1, 369 (1960).

7. RADIOCHEMISTRY AND NUCLEAR CHEMISTRY

7-1. Chemical Separation of ^{18}F in the ^3He Activation Analysis of Oxygen

T. Nozaki and Y. Terai

We have found an excellent method of separating ^{18}F in the charged particle activation analysis of oxygen by the $^{16}\text{O}(^3\text{He}, \text{p})^{18}\text{F}$ reaction. This oxygen analysis has been regarded as useful for many years in the science and industry related to high-purity substances. Relatively small number of matrices, however, have been analysed by this method, principally because of the following reasons: 1) the accessibility of ^3He bombardment has been rather limited, and 2) ^{18}F in the bombarded sample should usually be separated from various positron emitters formed simultaneously by difficult and tedious procedures. We made considerable efforts to set up a manual for the chemical separation of fluorine from each matrix using the distillation of fluorine as the principal step. Although this distillation is often used in quantitative analysis, it cannot be regarded as the best method when used in activation analysis. A notable time of careful operation is needed for it, and the ^{18}F in the distillate should be converted into a chemical form suitable for counting and carrier-recovery measurement.

Our present method makes use of the following properties of KBF_4 : 1) it can be precipitated and recrystallized from strong acid solution, because its solubility is 2.6 g/l at 20°C and 38 g/l at 100°C in water and is nearly the same in 1 : 3 HCl and 1 : 3 HNO_3 , 2) scavenging with $\text{Zn}(\text{OH})_2$ is possible in its recrystallization from water; it is completely inert to both oxidation and reduction, and thus the oxidation states of impurities can be changed in its recrystallization.

The ^{18}F separation in the KBF_4 method consists of the following four steps.

- 1) Dissolution of the sample after the surface-contamination removal in an acid mixture containing 100 – 150 mmol of HF carrier in a closed polyethylene bottle.
- 2) Addition of H_3BO_3 (2 – 3g) and 3 M KCl (20 ml) to the solution; its heating and cooling; filtration of the resultant KBF_4 precipitate; and washing with a KCl solution.
- 3) Dissolution of the KBF_4 in hot water (50 – 70 ml) containing ZnCl_2 (1 mmol) or another reagent for the scavenging; precipitation of the scavengers and its removal by filtration; acidification of the filtrate and its cooling to precipitate KBF_4 , and filtration of the precipitate and its washing with CH_3COOK solution and ethanol.
- 4) Radioactivity measurement and carrier recovery measurement by weighing after drying. The scavenging can often be omitted for a matrix containing over 1 ppm oxygen or giving no markedly high positron activity from itself.

This method can be applied to almost all matrices. The time required for the process is usually less than one hour and sometimes under 30 min. The carrier recovery is 40 – 80 %. This KBF_4 process demonstrates its superiority to the distillation-involving process especially in the analysis of Ge, GaAs, and Zn, from which volatile radioactivity of ^{73}Se , 76 , ^{77}Br and radio-germanium, respectively, are formed. Since, KBF_4 contains as much as 60.4 % of fluorine and since it is of rather low density, the self-absorption of positron annihilation radiation is very

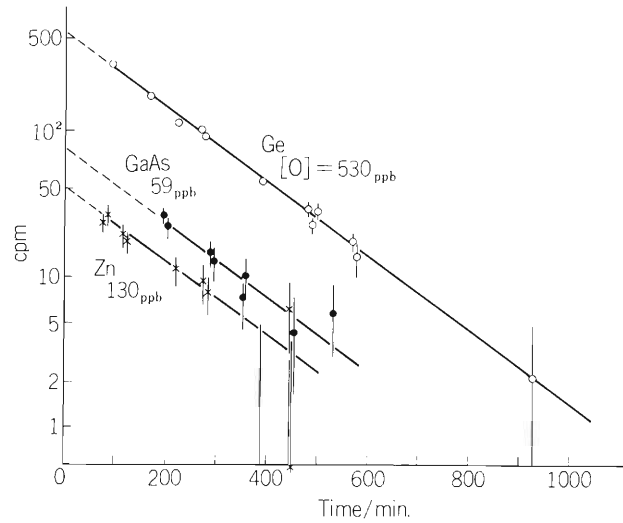


Fig. 1. Decay curves of ^{18}F for various metal matrices (Ge, GaAs, and Zn).

small even when a large amount of fluorine is added as carrier. Decay curves actually observed are shown in Fig. 1. Down to 1 ppb of oxygen can be shown to be thus determined, when an improved coincidence counting apparatus with a much lower background than our present counter is used.

An ultra-compact cyclotron has recently been developed for the production of radioisotopes of low atomic numbers for medical use. A similar machine is going to be used for activation analysis, giving much more chance of ^3He bombardment than at present.

7-2. Recoil Range of ^{18}F Formed by Various Reactions

T. Nozaki, M. Iwamoto, and K. Usami

Measurement of the distribution of forward recoil range of ^{18}F formed by various reactions was continued by the same technique as described previously.¹⁾ The distribution curves for the $^{18}\text{O}(p, n)^{18}\text{F}$ and $^{20}\text{Ne}(d, \alpha)^{18}\text{F}$ were newly obtained, and a slight correction was found to be necessary in the curve for the $^{20}\text{Ne}(^3\text{He}, \alpha p)^{18}\text{F}$ reaction. The result is shown in Fig. 1.

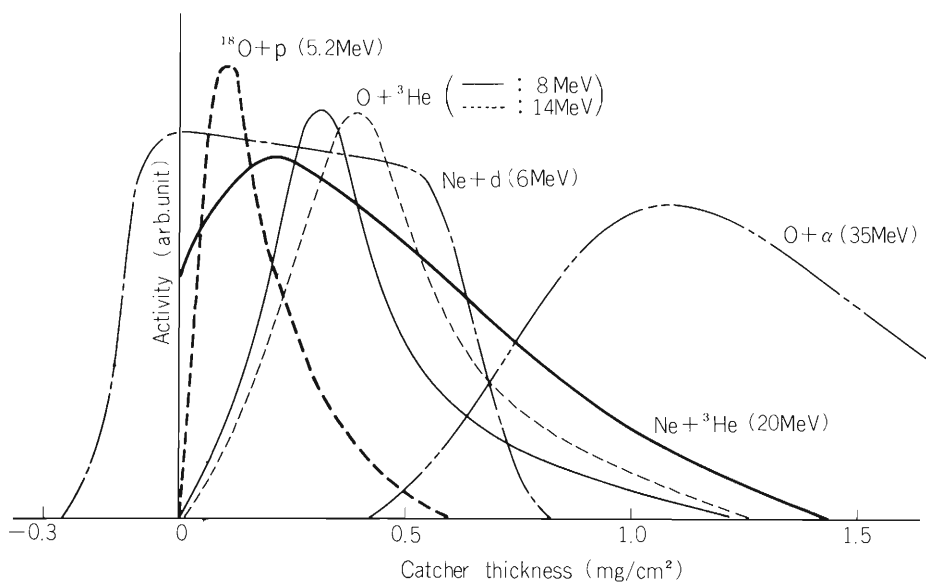


Fig. 1. Distribution of forward recoil range of ^{18}F in Si formed by various reactions.

(): incident energy

Reference

- 1) T. Nozaki, M. Iwamoto, K. Usami, K. Mukai, and A. Hiraiwa: IPCR Cyclotron Progr. Rep., 13, 106 (1979).

7-3. Heat Treatment Behavior of Oxygen in Silicon as Measured by Charged Particle Activation

T. Nozaki and Y. Itoh

By the use of activation analysis with the $^{16}\text{O}(^3\text{He}, p)^{18}\text{F}$ reaction, a method has been developed for the measurement of oxygen depth profile in silicon up to a few hundred micrometers from the surface. This measurement now attracts great interest in the research and industry relating to semiconductor silicon. A device was set up for the activation of oxygen with an equal probability along the depth in the measurement portion of the sample. Then, silicon wafers of known oxygen concentrations were heat-treated under various conditions and the resultant oxygen profiles were measured. Infrared spectrophotometry was also used to know the change of the physical state of oxygen.

The device is shown in Fig. 1. The activation of oxygen with an equal probability is effected by an absorber assembly rotating in the ^3He beam path. The absorber assembly consists of several aluminum foils set in a frame, with their thicknesses and widths being suitably selected from the excitation functions for the activation reaction and the energy loss curve for ^3He particle in aluminum. Some fluctuation, however, is inevitable in the oxygen activation along the depth, as is illustrated in Fig. 2. This curve was obtained by the bombardment of stacked Mylar foils and used as a standard in the oxygen profiling. Silicon sample after heat treatment and bombardment was etched stepwise with HF-HNO_3 , and ^{18}F activities in the resultant etching solutions were measured by $\text{Ge}(\text{Li})$ detector together with the decay curves. The thickness

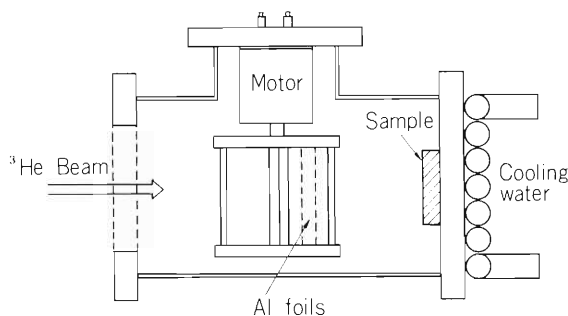


Fig. 1. Device for the activation of oxygen in an equal probability along the depth.

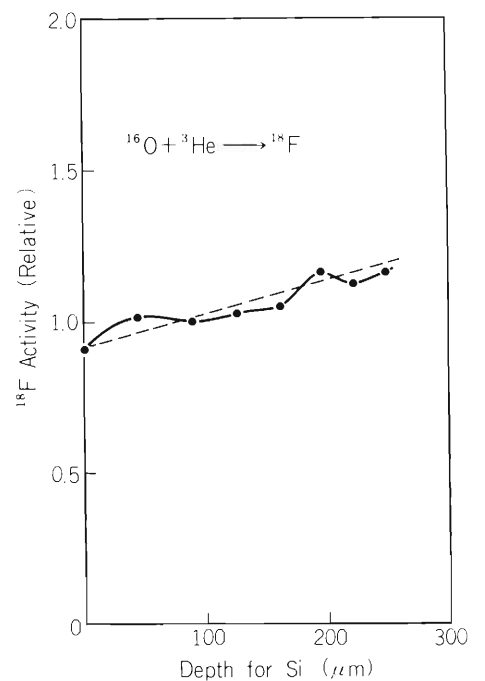


Fig. 2. Calibration curve.

removed in each etching was known from the decrease of the wafer thickness measured by a dial gauge. The oxygen distribution along the depth was thus obtained as a histogram.

Oxygen distributions in silicon wafers before and after heat treatment in argon are shown in Fig. 3. Initial oxygen concentrations of the samples were 11 wt. ppm and 9 wt. ppm for sample A and H, respectively. The temperature and duration of heat treatment were 1250°C and 100 h. With heat treatment in nitrogen, no remarkable change was observed in oxygen distribution. With heat treatment in oxygen, the resultant distribution curve was found to vary according to the initial oxygen concentration in the sample. More detailed study is now in progress.

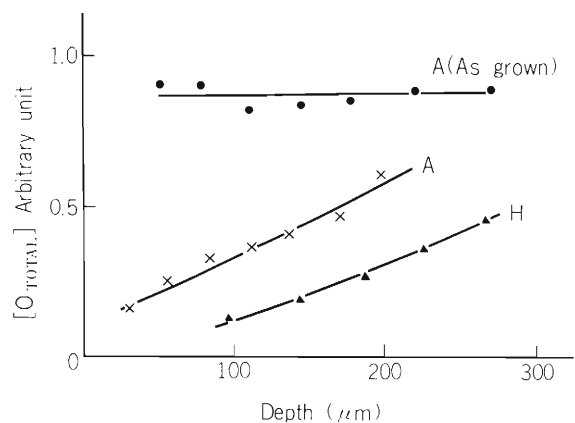


Fig. 3. Oxygen distribution after heat treatment in argon (1250°C, 100h).

7-4. Isomer Shift of ^{119}Sn in Binary Compounds of the Elements from Indium to Iodine

F. Ambe and S. Ambe

We reported Mössbauer emission spectra of defect ^{119}Sn atoms in binary compounds of typical elements in the 5th period of the periodic table.^{1)–4)} The spectra were obtained on ^{119}Sb - and $^{119\text{m}}\text{Te}$ -labeled sources prepared by radiochemical procedures. The method has a great advantage over the ion-implantation⁵⁾ in that the sources obtained are free from local damage of the matrix induced by the energetic incident ion and are also free from local disturbance of the lattice due to “bringing-in” of an extra atom.

The results accumulated so far in our laboratory have led to a systematics of isomer shift for the defect and normal ^{119}Sn in the binary compounds, combined with the data of absorption measurements.^{3),6)} As seen in Fig. 1, the isomer shift of ^{119}Sn shows a clear tendency to increase with increase of the atomic number of the nearest neighbor atoms. The observed correlation indicates that more electronegative neighbor atoms increase s-electron density at the ^{119}Sn nucleus,

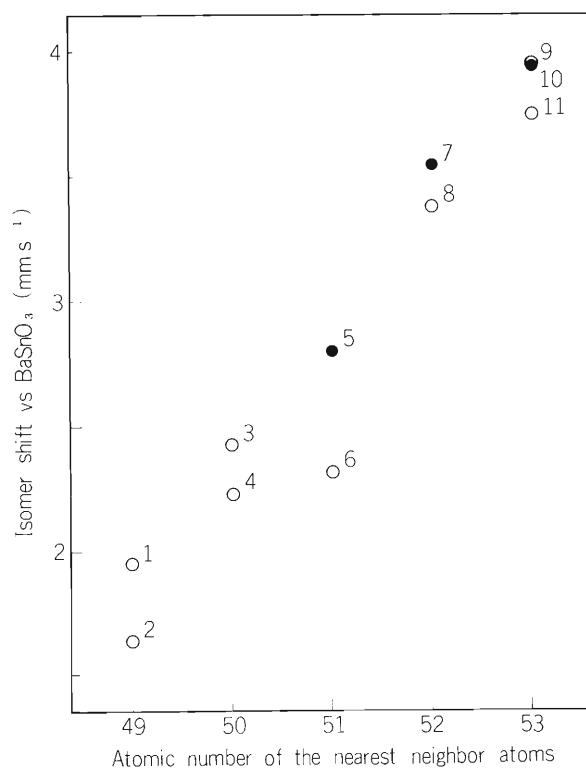


Fig. 1. Isomer shift of defect and normal ^{119}Sn in binary compounds of the elements from indium to iodine. Open circles refer to defect ^{119}Sn in emission measurements and closed ones to normal ^{119}Sn in absorption measurements.
 1. In^{119}Sb , 2. $\text{In}_2^{119\text{m}}\text{Te}_3$, 3. Sn^{119}Sb , 4. $\text{Sn}^{119\text{m}}\text{Te}$,
 5. SnSb , 6. $\text{Sb}_2^{119\text{m}}\text{Te}_3$, 7. SnTe , 8. $^{119}\text{Sb}_2\text{Te}_3$,
 9. $^{119}\text{SbI}_3$, 10. SnI_2 , 11. $^{119\text{m}}\text{TeI}_4$.

suggesting domination of p-character in the tin-ligand bonds. The systematics can be said to be rather remarkable in view of the variety of structures and types of bonding involved in the binary compounds.

The investigation is now being extended to compounds of cadmium and silver.

References

- 1) F. Ambe, S. Ambe, H. Shoji, and N. Saito: J. Chem. Phys., 60, 3773 (1974).
- 2) F. Ambe and S. Ambe: Bull. Chem. Soc. Japan, 47, 2875 (1974).
- 3) F. Ambe and S. Ambe: J. Chem. Phys., 73, 2029 (1980).
- 4) F. Ambe and S. Ambe: IPCR Cyclotron Progr. Rep., 13, 112 (1979).
- 5) G. Weyer, J. W. Petersen, S. Damgaard, and H. L. Nielsen: Phys. Rev. Lett., 44, 155 (1980).
- 6) N. N. Greenwood and A. Timnick: J. Chem. Soc. A, 1971, 676.

7-5. A Mössbauer Emission Study of Defect ^{119}Sn Atoms in Proton- and α -Irradiated SnSe

S. Ambe and F. Ambe

We are studying the chemical states of dilute impurity ^{119}Sn atoms in metals and semiconductors by Mössbauer emission spectroscopy using cyclotron-produced ^{119}Sb and $^{119\text{m}}\text{Te}$ as the source nuclides.^{1), 2)} Previously we reported the results on defect ^{119}Sn arising from the EC decays of $^{119\text{m}}\text{Te}$ doped radiochemically into Se metal and SnSe.³⁾ This year the final states of recoil ^{119}Sb and $^{119\text{m}}\text{Te}$ atoms produced in p- and α -irradiated SnSe have been studied.

Tin isotopes enriched in ^{120}Sn (for p-irradiation) or ^{117}Sn (for α -irradiation) were used for preparation of SnSe samples in order to minimize the resonant self-absorption of γ -rays in the sources. A stoichiometric mixture of ^{120}Sn or ^{117}Sn and Se metals was fused under Ar to prepare $^{120}\text{SnSe}$ and $^{117}\text{SnSe}$. Powder of the SnSe samples was irradiated on an aluminum plate cooled with water by 16 MeV protons or 38 MeV α -particles. Mössbauer emission spectra of the irradiated samples were measured against a BaSnO_3 absorber at 78 K. Measurement of the α -irradiated $^{117}\text{SnSe}$ was performed after a radioactive equilibrium had been attained between $^{119\text{m}}\text{Te}$ and its daughter ^{119}Sb .

The emission spectrum of p-irradiated $^{120}\text{SnSe}$ (Fig. 1) was essentially the same as the absorption spectrum of normal SnSe. This indicates that the ^{119}Sn atoms arising from ^{119}Sb are located in the Sn site of SnSe. Since the recoil energy associated with the EC decay of ^{119}Sb is much smaller than the displacement energy in solid, the ^{119}Sn atoms arising from ^{119}Sb remain in the original position of ^{119}Sb after the decay.¹⁾ It is concluded, therefore, that the energetic

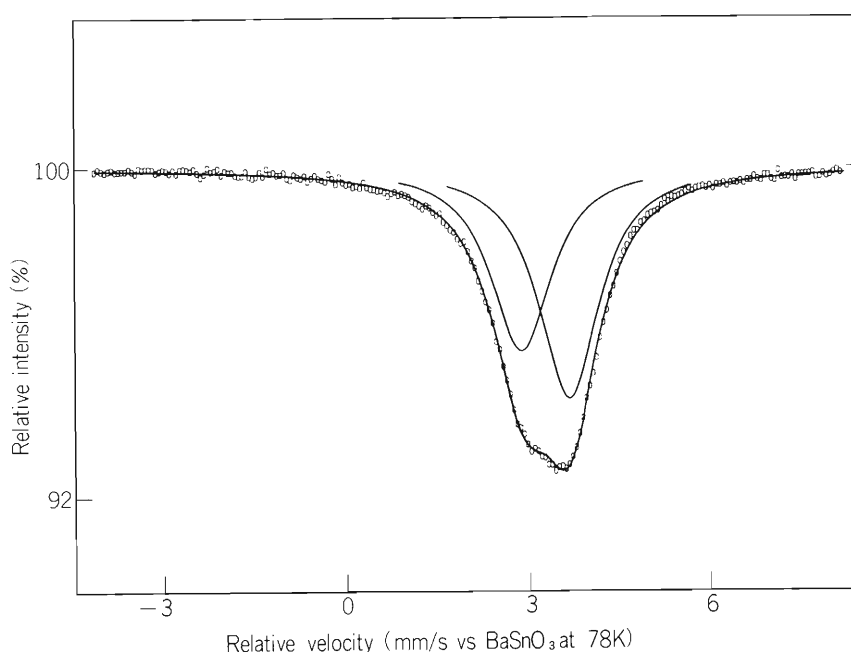


Fig. 1. ^{119}Sn -Mössbauer emission spectrum of p-irradiated $^{120}\text{SnSe}$.

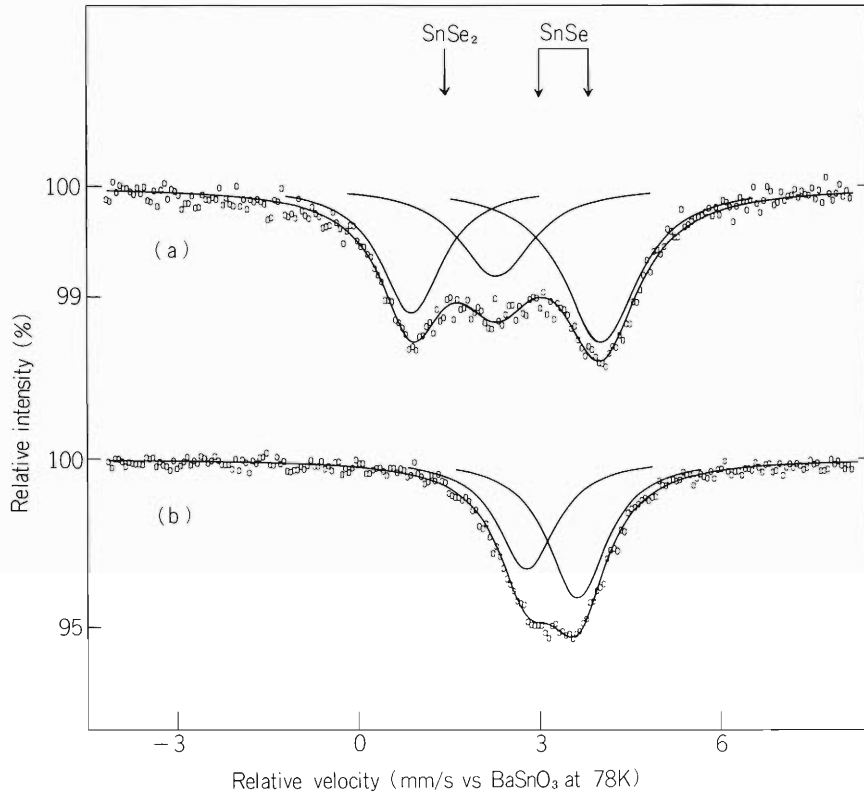


Fig. 2. ^{119}Sn -Mössbauer emission spectra of α -irradiated $^{117}\text{SnSe}$ (a) before and (b) after 1 h annealing at 600°C . The arrows show the absorption lines of normal SnSe and SnSe_2 .

recoil ^{119}Sb atoms produced by the $^{120}\text{Sn}(p, 2n)^{119}\text{Sb}$ reaction were stabilized in scarcely perturbed Sn site of the SnSe matrix.

As shown in Fig. 2(a), α -irradiated $^{117}\text{SnSe}$ gave a complex emission spectrum completely different from both the absorption spectrum of SnSe and the emission spectrum of the radiochemically prepared $\text{SnSe}(^{119\text{m}}\text{Te})$ source.³⁾ It was decomposable into three Lorentzian lines (designated hereafter as L1–L3 from the left to the right). The emission lines could be hardly assigned on the basis of isomer shifts for the absorption lines of SnSe ⁴⁾ and SnSe_2 .⁵⁾ A drastic change in the position and the relative intensity of each line was observed by thermal annealing of the samples after irradiation. With the elevation of annealing temperature, the relative intensity of the L2 and L3 peaks increased in parallel and, at the same time, the two peaks moved closer to each other, the center of the two peaks remaining almost unchanged. The peaks gave finally the quadrupole doublet of ^{119}Sn in the normal Sn site of SnSe after 1 h annealing at 600°C (Fig. 2(b)). From these observations, the lines L2 and L3 in Fig. 2(a) are ascribed to a quadrupole doublet of ^{119}Sn in Sn site of SnSe with an unusual distortion in the Se ligand configuration. The line L1 became smaller by thermal annealing, disappearing completely after 1 h annealing at 600°C . The line is assigned to an ionic tetravalent tin in a defect structure. It is interesting to note that the chemical state of $^{119\text{m}}\text{Te}$ produced by the α -reaction in SnSe is much different from that of $^{119\text{m}}\text{Te}$ introduced radiochemically into the same matrix, even after thorough annealing.

References

- 1) F. Ambe, S. Ambe, H. Shoji, and N. Saito: J. Chem. Phys., 60, 3773 (1974).
- 2) F. Ambe and S. Ambe: *ibid.*, 73, 2029 (1980).
- 3) S. Ambe and F. Ambe: IPCR Cyclotron Progr. Rep., 13, 109 (1979).
- 4) V. Fano and I. Ortalli: J. Chem. Phys., 61, 5017 (1974).
- 5) L. N. Vasile'v: Izv. Akad. Nauk. SSSR. Neorg. Mater., 13, 1752 (1977).

8. RADIATION CHEMISTRY AND RADIATION BIOLOGY

8-1. Inactivation of Ribonuclease A in Solution by N-Ion Beam

Y. Hattori and F. Yatagai

Work aiming at the characterization of the damage on biological substances by high-LET particles has been continued. In order to reveal detailed nature of radiation inactivation of enzyme, heat sensitivity of ribonuclease (RNase) A (EC 2.7.7.16) solution irradiated with N-ion beam has been studied. The irradiation was carried out using the biological irradiation apparatus described previously.¹⁾ The accelerated N-ion beam emerged through the vacuum window of 20 μm Al foil. Samples of aqueous solution of RNase A (crystalline preparation of Sigma Chemical Co. $5 \times 10^{-6}\text{M}$) were irradiated in the glass vessel²⁾ through its Mylar film window at room temperature in the presence of air under agitation. N-ion beam energy at the position of Mylar film was 4.6 MeV/amu.

Irradiated RNase solutions were subjected to the assay of residual activity according to the method of Anfinsen et al.,³⁾ before and after heating at 60°C for 15 min. RNase A is heat-stable and the activity loss of unirradiated sample solution by this heat treatment was found to be less than 10% of the initial activity. The activity loss by heating increased for the irradiated enzyme solution, showing the formation of heat-unstable molecules by the irradiation.

Figure 1 shows logarithmic plot of the residual activities of the irradiated enzyme solutions after the heat treatment versus those before the heating. Positive correlation is seen between the above-mentioned two indices of inactivation (coefficient of correlation: 0.76). The data indicate that the increase in inactivation of RNase A molecules by N-ion beam is accompanied with the increase in rate of latently damaged molecules which are unstable against the heating.

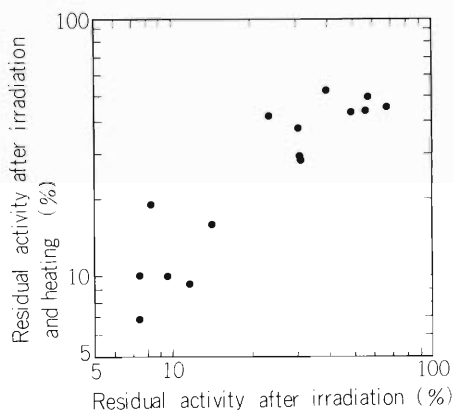


Fig. 1. Logarithmic plot of the residual activities of N-ion irradiated RNase A solutions after heating of 60°C for 15 min versus those before heating. RNase A: $5 \times 10^{-6}\text{M}$. Abscissa: residual activity before the heat treatment expressed as per cent of the unirradiated sample; ordinate: residual activity after the heat treatment (irradiation + heating) expressed as per cent of each irradiated sample before the heating. Data from three experiments.

References

- 1) F. Yatagai and A. Matsuyama: *IPCR Cyclotron Progr. Rep.*, **13**, 118 (1979).
- 2) Y. Hattori, F. Yatagai, and A. Matsuyama: *ibid.*, p.120.
- 3) C. B. Anfinsen, R. R. Redfield, W. L. Choate, J. Page, and W. R. Carroll: *J. Biol. Chem.*, **207**, 201 (1954).

8-2. Inactivation of Cultured Normal Human Fibroblasts, IMR-90, Cells with Nitrogen Ions Accelerated in the Cyclotron

I. Kaneko, T. Ohno, K. Nakano, and F. Yatagai

Irradiation with high charged particles is supposed to be advantageous in therapy of solid tumors since it is characterized by an improved depth-dose distribution, efficient relative biological effectiveness, reduction in oxygen enhancement and reduced occurrence of sublethal damage repair. Although many investigations have been made on cell inactivation with high-LET radiations, it is still obscure whether normal human cells have any ability to recover from potentially lethal damage (PLD) after irradiation with high LET particles.

Most of the radiation inactivation experiments have been performed with established cultured mammalian cells. Radiobiological studies with diploid cells are frustrated by the low cloning efficiency of the cells in normal culture media and variation in the cloning efficiency with factors such as cell density. "Feeder cell" technique was used to improve and standardize the cloning efficiency of diploid fibroblasts derived from normal human tissue.

Normal human lung fibroblasts, IMR-90 cells, were maintained as described previously¹⁾ in the medium TOM-H, an improved MEM for human cell culture, containing 10 % fetal bovine serum (FBS). The cells at 28–32 population doubling level were used throughout the experiments. Two to three days before the irradiation, the cells were seeded onto a cover glass of 15 mm diameter that was fixed with silicon grease in small glass petri dish of 20 mm diameter. Ten to twenty thousand cells suspended in 0.2 ml medium were quietly delivered onto the cover glass. For experiments to examine potentially lethal damage repair, ten thousand cells in 0.2 ml medium were delivered onto the cover glass. The dish was incubated in a humidified CO₂-incubator until the day of irradiation. HeLa S3 cells grown in MEM containing 10 % FBS were once washed with Ca⁺⁺ and Mg⁺⁺ free Dulbecco's phosphate buffered saline, trypsinized and kept as a suspension in an ice bath. This suspension was irradiated to a dose of 5500 rad with ⁶⁰Co γ -rays at a dose rate of 99 rad per minute to serve as feeder cells. Although HeLa cells have smaller potential for supporting colony formation of IMR-90 cells than normal fibroblasts, the use of HeLa cells made it easier to discriminate the smallest IMR-90 colonies (50 cells per aggregate) from the back ground feeders.

After irradiation with N-ion beams or ⁶⁰Co γ -rays, the cells were kept in an ice bath before replating. One hundred and fifty to three thousand IMR-90 cells were mixed with thirty thousand inactivated HeLa cells and seeded into a 6 cm plastic dish with 10 ml of TOM-H containing 10 % FBS. The cells were cultured for two weeks. The maximum inoculation of irradiated IMR-90 cells was restricted to three thousand cells per dish to avoid additional feeding effects by IMR-90 cells themselves.

Chinese hamster V-79 cells were cultured and irradiated as above. However, no feeder cells were used for their colony formation. MEM containing 10 % FBS was used for culture of Chinese hamster V-79 cells.

Cells cultured on the cover glass were washed with Dulbecco's phosphate buffered saline (PBS⁺). The cell layer was covered with a polycarbonate film (5 μ m in thickness) wetted with

PBS⁺ to minimize the effect of δ -rays generated during the N-ion irradiation. The small dish with the cover glass was then wrapped with sterilized polycarbonate film (6 μ m in thickness) to keep moisture and sterility. Cell-handling procedure for the irradiation was similar to that described previously²⁾ except the usage of a cover glass of 15 mm diameter. A new apparatus was used to irradiate the cells with the beam elastically scattered at some angle by a scattering foil.³⁾

The survival curve of IMR-90 cells was exponential throughout the dose range for the irradiation with N-ion accelerated in the cyclotron (4.6 MeV/amu at the sample). The small shoulder region was obtained by calculation of the linear regression of the whole data obtained from repeated experiments. However, this region was 95 % confidence limit of the regression line. D_0 , D_q , and the extrapolation number were 109 rad, 14 rad, and 1.1, respectively.

When the confluent monolayer of IMR-90 cells was irradiated and incubated before replating, cell damage increased for two hours after the N-ion irradiation and then it recovered to the level just after the irradiation. This pattern of recovery was also observed in Chinese hamster V-79 cells and apparently different from the known pattern of the recovery from potentially lethal damage after the γ -ray irradiation.

References

- 1) T. Ohno: *Mech. Age. Dev.*, 11, 179 (1973).
- 2) Y. Yamawaki, F. Yatagai, I. Kaneko, K. Sakamoto, S. Okada, and A. Matsuyama: *IPCR Cyclotron Progr. Rep.*, 10, 36 (1976).
- 3) F. Yatagai and A. Matsuyama: *ibid.*, 13, 118 (1979).

9. RADIATION MONITORING

9-1. Routine Monitoring

M. Koyama, K. Igarashi, I. Usuba
S. Fujita, and I. Sakamoto

Results of routine radiation monitoring carried out on the cyclotron from April 1979 to March 1980 are described.

No remarkable change in leakage radiation and residual activities was observed during this period. Some aspects of the leakage radiation are described in the following report.

(1) Surface and air contamination

The surface contamination has been kept below 10^{-6} $\mu\text{Ci}/\text{cm}^2$ on the floor of cyclotron room and the underground passage, and below 10^{-7} $\mu\text{Ci}/\text{cm}^2$ in the experimental areas, hot laboratory and chemical laboratories. The contamination was wiped off twice a year, and immediately after this decontamination, the contamination on the floor of cyclotron room and the underground passage had been reduced to a value below 10^{-7} $\mu\text{Ci}/\text{cm}^2$.

When the accelerating chamber was opened, slight contamination of the air in the cyclotron room was observed. The value of radioactivity concentration (beta-gamma) was 10^{-12} $\mu\text{Ci}/\text{cm}^3$.

(2) Drainage

The radioactive concentration of the drain water from the cyclotron building was found to be of the order of 10^{-6} – 10^{-7} $\mu\text{Ci}/\text{cm}^3$. The total quantity of activities in the aqueous effluents in

Table 1. Annual exposure dose received by the cyclotron workers from April 1979 to March 1980.

Workers	Number of persons			Collective dose (man-mrem)
	Dose undetectable	10-100 (mrem)	101-300 (mrem)	
Operators		6	1	370
Nuclear physicists	5	6		130
Accelerator physicists	9	4		590
Physicists in other fields	15	5	1	320
Nuclear chemists	2	4	2	880
Radiation chemists	2			
Biological chemists	7			
Health physicists	2			
			Total	2290

Average annual dose per person: 31.4 mrem .

Maximum individual annual dose: 420 mrem .

this period was about $60 \mu\text{Ci}$, and the radioactive nuclides found by the γ -ray spectrometry were mainly ^{65}Zn , ^{57}Co , ^{58}Co and ^{75}Se .

(3) Personnel monitoring

The external exposure dose to personnel was measured with γ -ray and neutron film badges. The dose received during the present period by all the cyclotron workers is shown in Table 1. The collective γ -ray dose to all workers was 2290 man-mrem, while those owing to thermal and fast neutron exposures were too small to be detected. The collective dose to the cyclotron workers is about 90 % of the value in the preceding period.

In this period the dose to the cyclotron operators was 370 man-mrem, which was 16.2 % of the dose of cyclotron workers, and the maximum individual annual dose was 120 mrem.

9-2. Leakage-Radiation Measurement at the Underground Passage

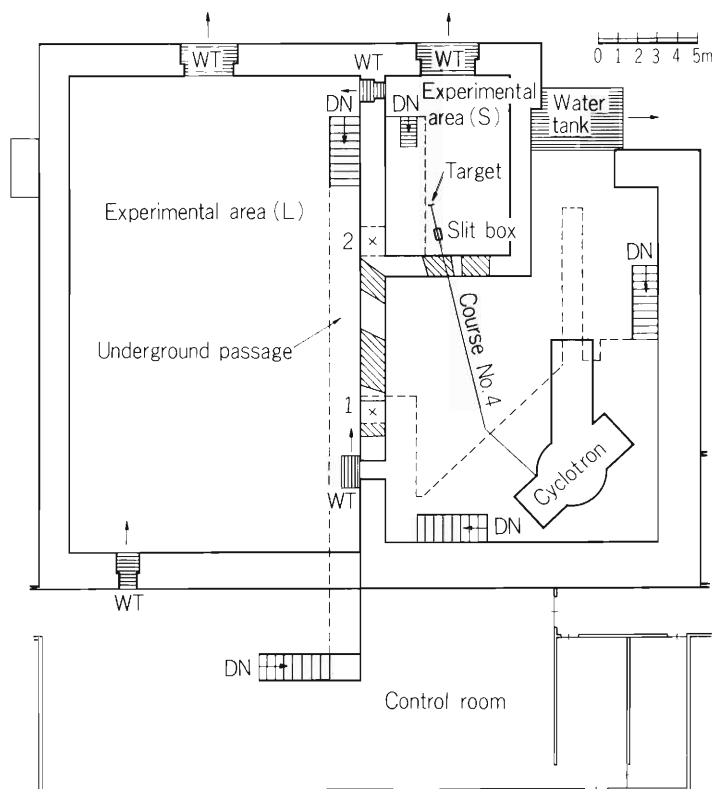
I. Sakamoto

Leakage radiation during operation of the cyclotron at the underground passage of the cyclotron building was measured. Leakage dose received from April 1979 to March 1980 by γ -ray and neutron film badges which were left at the underground passage, is shown in Table 1. The machine time allotted for deuteron acceleration was 8 h in March.

Table 1. Leakage radiation dose (in mrem) at the underground passage from April 1979 to March 1980.

Radiation	Point of observation*	
	1	2
γ -rays (mrem)	1870	810
Thermal neutrons (mrem)	500	220
Fast neutrons (mrem)	510	580
Total (mrem)	2880	1610

* See the figure shown below.



As to the dose values at point No. 2 measured every month, the maximum dose of 760 mrem was observed in October. In this case, the values of gamma dose, thermal neutron dose and fast neutron dose were 420 mrem, 110 mrem and 230 mrem, respectively.

The increase of fast neutron was observed at point No. 2 in April, October and February. The total fast neutron dose measured in the three months was 480 mrem, which was 82.7 % of the total dose in this period. As a result of investigation, it was concluded that the fast neutron dose was due to the 22 MeV α -particle bombardment on a brass slit at about 100 nA in case of irradiation experiment in the beam course No. 4.

10. HEAVY ION LINEAR ACCELERATOR PROJECT

10-1. Status of RILAC

M. Odera

Almost all of the hardwares of RILAC were installed before the end of March 1980. Some beam diagnostic elements and the circuits necessary for automatic control of the high power radio-frequency amplifiers are behind the schedule. It is expected that the latter will be completed and become operational before the end of 1980. Since minimum number of the diagnostic probes were already set in the beam line and any exacting demand for beam quality has not been put forward to date, installation of the remaining probes can be postponed until next year.

Meanwhile, acceleration test by the first cavity was made. Beams were obtained easily. Setting and sensing of the parameters of the beam transport system through the central control console aided by a computer were tried and found fast and reliable in so far as control of the quadrupole and dipole magnets are concerned. Remote control of the radio-frequency amplifiers will be started early next year.

Subjects of experiments for initial few years have been decided in 1979. Members in charge of each subject and the committee of users are arranging the experimental sites and preparing the instruments. As the central unit for on-line data acquisition and processing, a minicomputer Perkin-Elmer Model-3220 was purchased and installed in March 1980. Its word-length is 32 bit. Its memory capacity is 768 kB in IC and is supplemented by two disk memories of 80 MB each and a magnetic tape of 1600 bpi. A grazing incidence spectrometer for beam foil spectroscopy was installed in April. A high-vacuum chamber of the high resolution Auger electron spectrometer was carried in at August. Tuning and test of the electron spectrometer are in progress. Other apparatuses will be carried in between Dec. 1980 and Mar. of 1981. Those instruments and electronics most of which are NIM modules are connected with the on-line computer via CAMAC system. The interface circuits necessary were designed by a member of the user's group and fabrication is being made by a factory.

The experimental apparatuses which will be installed at each end of nine beam-lines in three vaults are listed below. The designations of the beam-lines can be found in the figure in p.129 of this progress report.

- A-1: A scattering chamber of 1 m diameter for the experiments on nuclear physics.
- A-2: A crystal spectrometer for the X-ray measurements.
- B-1: A scattering chamber for the experiments on atomic physics.
- B-2: A 2.2 m grazing incidence spectrometer and a vacuum chamber equipped with a movable target holder for beam-foil spectroscopy.
- C: A scattering chamber for the irradiation of metals.
- D-1: A magnet and a goniometer for the measurements of magnetic moments. A scattering chamber for the particle- γ coincidence experiments.

- D-2: An electron spectrometer for measurements of the electron emission from metal-surfaces.
- E-1: An irradiation chamber for the study of the radiation biology.
- E-2: A high-resolution Auger electron spectrometer.

T. Kambara, S. Takeda, and M. Odera

1. Status of hardware

The greater part of the control system including the minicomputer (HP-1000) was installed in November 1979.¹⁾ Some control devices, such as off-line control panels for the ion source and a panel for on-line fine tuning of analog parameters, were added to the control console in 1980. The latter panel has three sets of shaft encoders and gas discharge character displays which are linked to the computer via a microprocessor. Figure 1 shows the layout of the console.

During last year, the CPU, mass storage (magnetic tape and disc) and CRT terminals have worked well with few failures, but the control and measurement interface (HP2240A/41A) and the serial data link have failed more frequently. In most cases of failure, we replaced the circuit board concerned and the system recovered normal operation.

At present, more than 40 magnet power supplies distributed in the linac vault are linked to the computer. The magnet currents are remotely controlled by reference voltage signals (set-points) which are proportional to the desired currents and are supplied from digital-to-analog converters (DAC's) in the data stations. The control and data processing of beam emittance and profile monitors are tested using the computer.

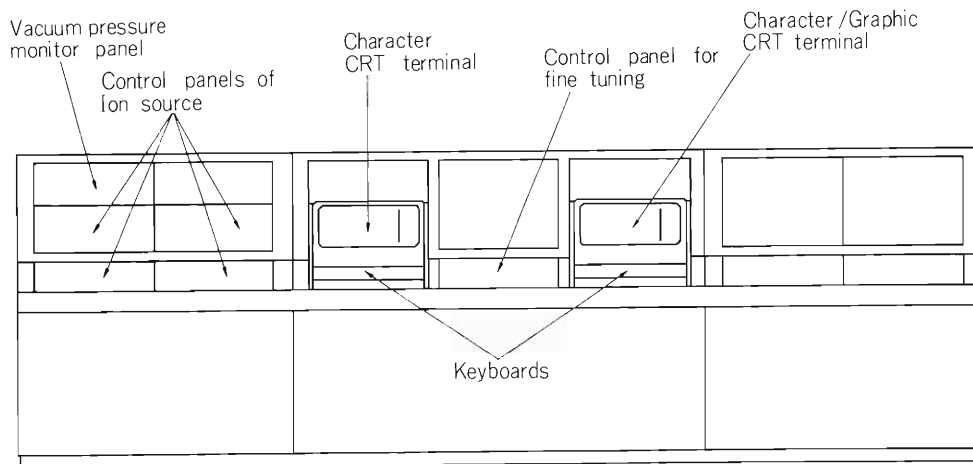


Fig. 1. Front view of the control console.

2. Software development

The programs for the operation and test are developed and executed under the RTE-IV operating system. Some programs for the beam monitors are written in Assembler, while all others are written in FORTRAN. The operation of the magnet power supplies is done as described below.

(1) Start of operation

We use one of the two CRT terminals in the console for the operation. When the program is started, the computer checks the serial data link and the HP2240A/41A's and then asks us the name, mass, charge and acceleration conditions of the ion. When we input these parameters from the keyboard, the computer calculates and stores predicted values of the magnet currents, then it is ready for display and control.

(2) Display of parameters

Because there are many parameters to be displayed and controlled, they are divided into groups called

pages. Up to nine parameters can be put in a page in any combination. We select any page by inputting the page number from the keyboard. On the CRT screen, a table is displayed which contain the name, status informations and numerals such as predicted values from the calculation, present set-point values and measured values of the parameters in the page. The numerals are displayed in the engineering units. We can update the informations on the CRT by pressing the RETURN key. The response time including the measurement, data transfer, conversion and display is about 2 seconds at maximum. Most of the time is spent in the data transfer on the serial data link. Figure 2 shows an example of the table displayed.

```

NAME OF ION=AR      Z=18      MASS= 40      CHARGE= 3
M/Q=13.33      FREQ.=      .0000MHZ
                                PRESET      SCAN      PREV
                                PRINT      INDEX      NEXT
PAGE 10:  INJECTOR PARAMETERS.                                TIME 12: 0:25

```

NAME UNIT	INJ. KV	DQ1-1 A	DQ1-2 A	BM1 A	BM2 A	TQ1-1 A	TQ1-2 A	SL1	SL2
STATUS	OK OF	OK ON	OK ON	OK ON	OK ON	OK ON	OK ON		
CALC.	500.00	57.97	51.44	117.41	116.27	51.44	44.09		
PRESET	.00	57.96	51.35	117.40	116.26	51.37	44.00		
MEAS.	-1.00	58.03	51.52	117.35	116.54	51.39	45.38		
NO. INPUT	*	2 57.97	3 51.44	4 117.41	5 116.27	6 51.44	7 44.09	*	*

OK? OK

Fig. 2. Example of table displayed on CRT screen.

(3) Control

We can change the magnet currents as listed below:

i) We can set all the set-points in the page to the predicted values from the calculation, or set them to zero as long as they are controllable from the computer. Only we have to do is to press a few of the eight programmable keys on the keyboard.

ii) We can select any parameter in the page separately and input the set-point with the numerical keys on the keyboard.

iii) We can select up to three parameters and change their set-points almost continuously by turning the shaft encoders on the panel for fine tuning. The panel is set between the two CRT terminals. This method is useful in finding the best beam transport condition starting from the calculated values as the first approximation.

In any case, the computer checks whether the input values are within certain limits, converts them to the output values to the DAC's and sends them to the data stations. Because the magnet currents are changed stepwise and rather slowly, it takes about 6 min to set all the magnet currents to the specific calculated values.

3. Improvement and expansion plans

The circuits and the wiring for the on-line control of the RF system have been ordered to the contractor and will be completed by the end of 1980. We will connect one of the data stations in the linac vault with the computer by an optical fiber HP-IB link, instead of the present serial data link. We expect to improve the data transfer rate in this way.

Figure 3 is a block diagram of the control system after the above modification is done.

We are planning to monitor other parameters such as vacuum pressure or beam current outputs from slits and stoppers by the computer. Monitoring of these parameters will be necessary in future for closed loop operation of the linac.

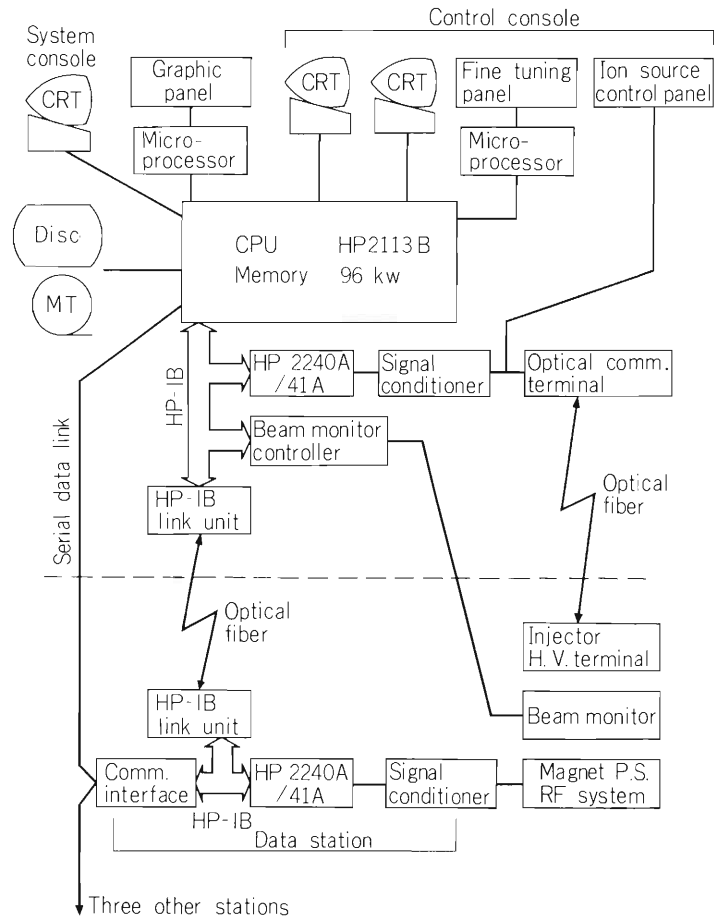


Fig. 3. Block diagram of the control system after the modification mentioned in the text.

Reference

- 1) T. Kambara, S. Takeda, and M. Odera: IPCR Cyclotron Progr. Rep., 13, 134 (1979).

10-3. Design of ECR Ion Source

M. Yanokura and M. Odera

Development of an electron-cyclotron resonance (ECR) ion source has been started to get multiply charged ions. For this type of ion source, there is no need of arc and heater power supplies on the high voltage platform. There is no problem of electrode corrosion due to arcs, since there is neither cathode nor anode which may cause discharge. Therefore, the ECR ion source has inherently a long life, and can be operated in CW mode. On the other hand, the ECR ion source requires high magnetic field and micro-wave power.

As the first step of development, a single stage ECR ion source was designed. A schematic cross section of the ECR ion source is shown in Fig. 1. A pair of solenoidal coils has been constructed. Each coil consists of 112 turn hollow-conductors. A soft-iron return yoke was incorporated to save the electrical power for coils and to decrease the leakage of magnetic flux. Measured axial magnetic fields are shown in Fig. 2. Currents of the coils are given in amperes. When the same current is fed to two coils, mirror ratio or maximum to minimum fields ratio is about 1.78. Maximum field was increased by about 50 % by incorporating the return yoke. Strength of the magnetic field was found to be proportional to the coil current up to 100 A. The magnetic field of 877 gauss is required as the resonance field at 2.45 GHz. The current of 140 A is obtained to get this field strength by the extrapolation of the data mentioned above. In this case, the current density in the conductors is 1.9 A/mm^2 and the power dissipation becomes 460 W per coil.

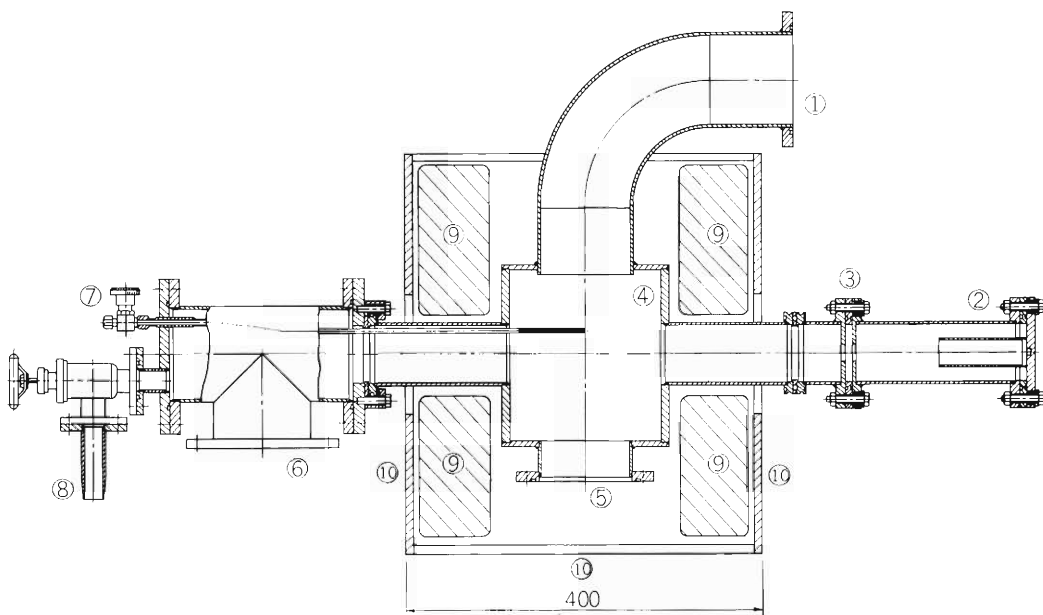


Fig. 1 ECR ion source test-stand.

1. wave guide, 2. faraday cup, 3. extraction electrode, 4. ECR cavity,
5. flange, 6. pumping port, 7. gas inlet, 8. pumping port. 9. coils,
10. return yoke.

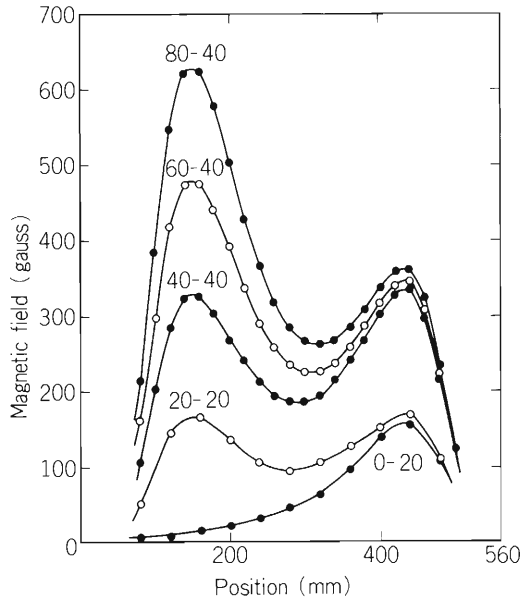


Fig. 2. Axial magnetic field of the test ion source. Numerals are coil currents in Ampere.

A cavity for ECR plasma containment is under construction. Total length of the ECR ion source test-stand is about 1200 mm. Dimension of the cavity is 206 mm in diameter and 200 mm in length. A diffusion pump of 1500 ℓ /sec is used to evacuate the cavity. The gas pressure is estimated to be less than 10^{-4} Torr when the source is operating. Micro-wave power is fed to the cavity through a vacuum window at the exit of a wave guide power feeder. The whole vacuum components including the cavity are made of stainless steel.

10-4. System for Beam Monitoring with Beam Slit and Stopper

M. Kase, I. Yokoyama, and M. Hemmi

About 30 sets of beam slit (SL) and beam stopper (BS) devices are installed along the beam line of the linac. Beam current signals from these devices give a rough estimation of beam intensity and profile. The indication of these information on the control desk panel is often required for the machine operation.

Figure 1 shows the beam monitoring system using the SL and BS apparatuses.

Slit sizes of the SL devices, in general, are manually adjusted. However, horizontal slit widths can be remotely adjusted for some SL instruments which are installed in the low energy beam line between the injector and the first cavity. More compact and simpler SL instruments (used as beam baffles), whose slit sizes are fixed, are installed in each space between the acceleration cavities.

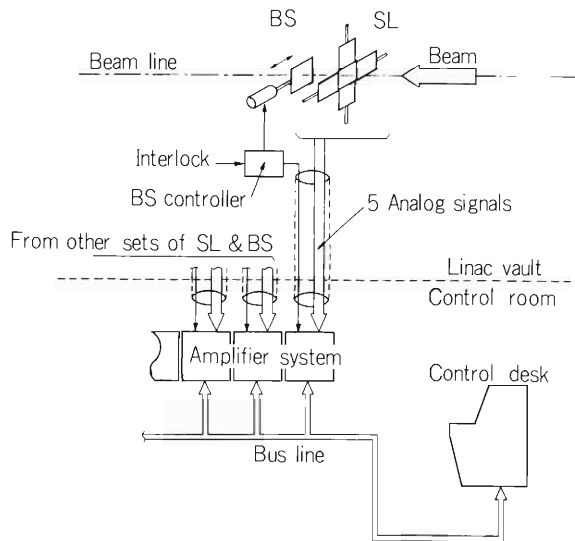


Fig. 1. Block diagram of beam monitoring system using beam slits (SL) and beam stoppers (BS).

The BS device is typically set up with the SL system in one vacuum chamber, called slit box. Copper plates of the BS devices are plunged into or pulled out from the beam course swiftly by pneumatic cylinders which can be remotely driven by BS controllers. Some BS controllers are connected with the interlock network in order to protect persons or instruments from operator's mishandling.

Five analog signals of beam currents from one set of SL and BS are led to the amplifier system mounted in a rack in the control room through five coaxial cables bounded in a wire braid tube together with some control lines. By dc amplifier the current signals are linearly converted to low-impedance voltage signals, whose magnitudes are always kept between 0.1 to 1.0 V for any beam intensity from 1 nA to 100 μ A by automatic gain control circuits. The beam currents at all SL devices are separately indicated on the analog meters together with meter-full-scale values. At the amplifier system, in addition, one can drive any BS devices and the beam current at the BS is also read in the same way.

Four SL signals, one BS signal and some digital signals can be sent from the amplifier system

to the control desk via bus lines. If an operator pushes the button on the control desk panel corresponding to the SL instrument which he wants to monitor, then the beam currents at the selected SL are indicated on the analog meters on the panel together with meter-full-scale values and the corresponding SL address. And it also becomes possible for the operator at the control desk to control and read the BS device installed just behind the selected SL instrument.

10-5. Acceleration Test of the First Cavity

M. Kase, M. Yanokura, Y. Chiba, and T. Tonuma

The beam acceleration test by the first cavity was started in the spring of 1980. It has been confirmed that N^+ ions were successfully accelerated. In this report, we give a summary of the acceleration test.

The N^+ ions, which were produced in an axially extracting PIG ion source¹⁾ and accelerated by the injector dc voltage, V_{inj} , were introduced into the first cavity. The ions were then accelerated by the rf acceleration voltage across drift tube gaps, V_{rf} . The conditions of acceleration are listed in Table 1. In order to examine the beam acceleration, it is necessary to

Table 1. Conditions of acceleration.

Ions	N^+
Injector voltage, V_{inj}	310 kV
Beam current at the entrance to the first cavity	200 nA (dc beam)
Acceleration frequency	20 MHz
Acceleration voltage, V_{rf}	128 kV (peak value)

measure the beam energy. However it was not available to measure the beam energy after the first cavity by a magnetic field or directly by an SSD in the beam path. So we employed an indirect method: to know the beam energy from the energy spectrum of the beam scattered by a thin Au target. The arrangement of the apparatus and the block diagram of the electronic circuits are shown in Fig. 1. The Au target $20 \mu\text{g}/\text{cm}^2$ in thickness was prepared by the vacuum evaporation on a polycarbonate film. The energy calibration was performed by means of the interpolation using 500 keV and 1 MeV nitrogen ions from the injector and 5.48 MeV alpha particles from ^{241}Am .

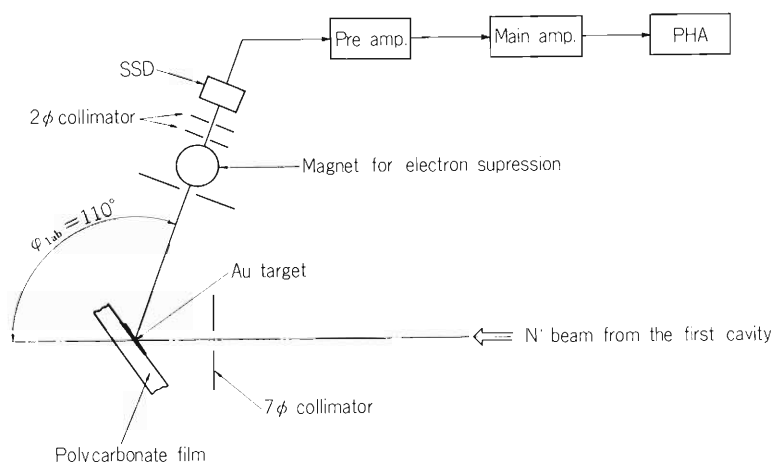


Fig. 1. Arrangement of the apparatus and block diagram of electronic circuits.

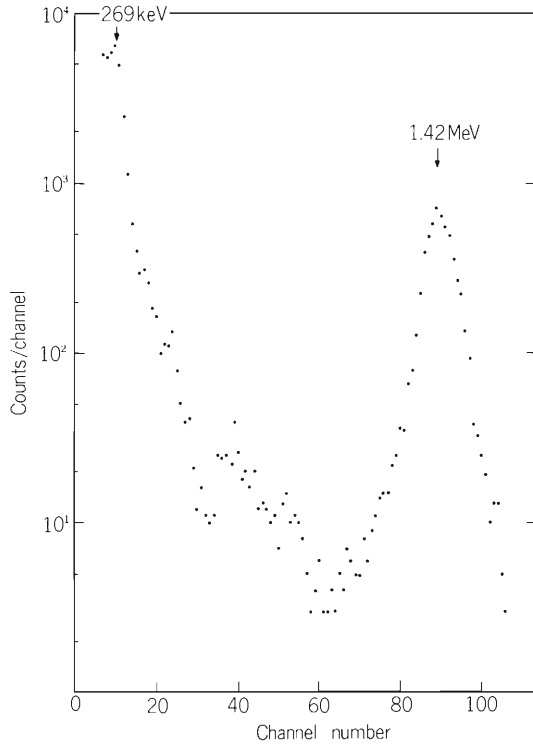


Fig. 2. Pulse height distribution for nitrogen ions scattered by a Au target at the scattering angle of 110° in the laboratory system.

Table 2. Observed and calculated values of the beam energy and its spread.

	observed value	calculated value
E_{mp}	1.8 MeV	1.86 MeV
ΔE	82 keV (fwhm)	112 keV (full width)
$\Delta E/E_{mp}$	4.5 %	6 %

Figure 2 shows a typical example of the pulse height distribution for the scattered nitrogen ions. We can see a peak at 1.42 MeV due to the ions accelerated by the first cavity. The most probable energy of the accelerated N^+ ions, E_{mp} , is determined by considering the kinematics of N-Au elastic scattering and the peak displacement caused by the energy loss in the Au target. Furthermore, the energy spread, ΔE , can be obtained by subtracting the contributions of the target energy loss and its straggling from the observed peak width. These values are summarized in Table 2 together with the values calculated in the way described in Ref. 2. The agreement between observation and calculation are satisfactory if the errors in the measurement and the simplifications made in the calculation are taken into account. The beam intensity of N^+ ions irradiating the Au target can be estimated from the peak yield using the Rutherford formula. Consequently, the beam current of N^+ ions sufficiently accelerated by the first cavity is evaluated to be 4×10^{-9} A on the assumption that it is a uniform beam of 30 mm diameter. The ratio of the accelerated beam current to that injected into the first cavity is about 0.02. The transport efficiency of the first cavity for dc beam has an upper limit of about 0.2 which is estimated from the phase acceptance of the cavity. The obtained value, however, is much smaller than this limit. The difference may be due mainly to the insufficient adjustment of magnetic fields of the triplet quadrupole magnet set in front of the cavity and each quadrupole magnet inside the drift tube.

A better adjustment of the magnetic fields and use of a beam buncher will improve this ratio.

As seen from Fig. 2, there is another peak in the lower energy region. It is supposed that this peak corresponds to 310 keV neutral nitrogen atoms produced in the beam path between the second deflecting magnet (BM2) and the first cavity through the electron capture reaction of nitrogen ions with residual gas.

By changing the acceleration frequency from 20 MHz to 24 MHz, we obtained 2.6 MeV for the N^+ ions. In this case, V_{inj} was 460 kV and V_{rf} was 162 kV (peak value). No difficulty was met in changing the parameters. The measurement of the beam energy was made for this parameter set with the same arrangement as shown in Fig. 1.

References

- 1) S. Nakajima: IPCR Cyclotron Progr. Rep., 12, 141 (1978).
- 2) T. Tonuma, F. Yoshida, and M. Odera: Reports I.P.C.R. (in Japanese), 51, 53 (1975).

Y. Chiba

The IPCR heavy ion linear accelerator includes six pairs of main resonators and power amplifiers; they are required to be continuously tunable from 17 to 45 MHz.^{1), 2)}

An RF control unit is provided for each pair. Figure 1 shows a block diagram of the unit. All functions of the unit are controlled by the control processor of the accelerator control system.³⁾ The power amplifier coupled with the main resonator is shown schematically in Fig. 1 of another report in this volume.²⁾ It has seven adjustable devices (①~⑦ in Fig. 1) for tuning and six terminals (a – f in Fig. 1) to supply RF sample signals to the control unit.

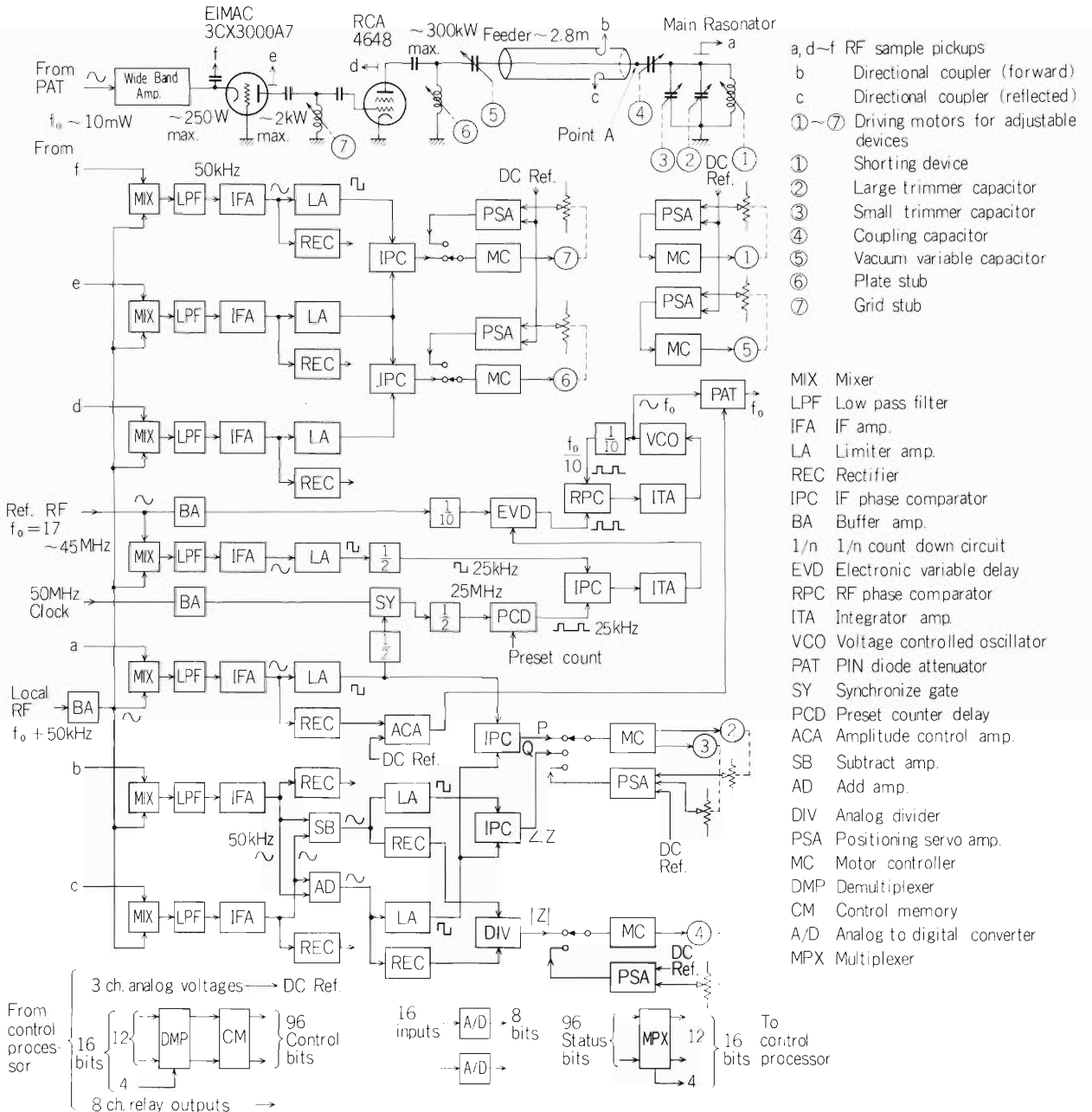


Fig. 1. Block diagram of RF control unit.

1) RF processing

Six RF samples from the pickups and the directional couplers and an RF reference signal are mixed with signals generated by a local oscillator and are converted into intermediate frequency (IF) signals of 50 KHz. The RF reference is distributed to each RF control unit from a synthesizer through lines of equal electrical length. A definite phase relationship between the units is established in this way. The local frequency signal is also distributed from a common source. After amplification, a part of the IF signal is rectified to give an amplitude output, and the other is converted into a square wave keeping phase information in its rising and falling edges. A pair of square waves is applied to a phase comparator to obtain an output proportional to their phase difference.

The IF signals from the two directional couplers are added to or subtracted from each other and converted into IF signals proportional to voltage and current on the feeder at the front end: point A in Fig. 1. They are applied to a phase comparator and, after being rectified, to an analog divider. Their outputs represent angle and magnitude of impedance Z: input impedance of the resonator seen from the front end of the feeder.

2) Auto-tuning feed back loops and positioning servo loops

There are four auto-tuning feed back loops, loop A to D; one of them, loop B, may be better called auto-impedance matching rather than auto-tuning loop. The tuning scheme of each loop is described by itemizing in the following: item 1 is the aim of the loop; item 2 describes a variable used to detect tuning error of the loop; item 3 gives the value which the variable takes at the exact tuning point; item 4 are the names of adjustable devices of the loop. Each loop is composed to keep the variable to the value specified in item 3 by trimming the adjustable device.

Loop A. 1) Tuning of the main resonator. Two schemes, P and Q, are selectable; scheme P responds to wider deviation of tuning but the value mentioned above has a slight frequency dependence. 2P) Phase difference between RF voltage in the main resonator and that of the front end of the feeder. 3P) A value slightly less than 90 deg. 2Q) Angle of the impedance Z. 3Q) 0 deg. 4) The small and large trimmer capacitors.

Loop B. 1) Impedance matching between the main resonator and the feeder. 2) Magnitude of the impedance Z. 3) 60 Ω . 4) The coupling capacitor.

Loop C. 1) Tuning of the plate circuit of the 4648. 2) Phase difference between plate RF voltages of the 4648 and the 3CX3000. 3) 180 deg. 4) The plate stub.

Loop D. 1) Tuning of the grid circuit of the 4648. 2) Phase difference between plate and cathode RF voltages of the 3CX3000. 3) 0 deg. 4) The grid stub.

All auto-tuning loops are locked out unless RF level in the main resonator is normal.

Loop A and B interfere with each other and loop C. For avoiding excursions of the loops caused by the interferences, loop B is activated only when loop A stays in the neighborhood of the tuning point. Similarly, loop C is interlocked to loop A and B.

An adjustable device is preset to a given position by the servo loop comparing reference voltage with the output of the position potentiometer. Two reference voltages are used. One assigns the positions of three and another four devices. Selection of run or halt and selection of the servo loop or the auto-tuning loop are decided for each device independently according to the commands from the control processor. The shorting device for coarse tuning of the main resonator and the variable vacuum capacitor for adjustment of plate load resistance of the 4648 have the servo loops only.

3) Phase and amplitude regulation

After the square wave from the resonator is delayed by preset counts of 25 MHz clock, its phase is compared with that from the RF reference. The output of phase comparator controls an electronic variable delay, inserted into the loop of a phase locked oscillator locked to the RF reference, so as to keep the output null. Thus the RF phase of the main resonator is fixed at any position ranging ± 180 deg. or more against the reference by changing the preset counts; a count corresponds 0.72 deg.

An RF amplitude stabilization loop compares the amplitude output from the main resonator with a reference voltage and drives a PIN diode attenuator controlling the input RF level of the power amplifier. This loop also includes a pulser to enable breakthrough of multipactoring by pulse RF excitation and protection circuits for the final tube.

The expected stabilities are $\sim 1 \times 10^{-4}$ for amplitude and less than ± 0.5 deg. for phase.

For initial tuning at an operating frequency, the control unit searches rapid growth of RF voltage in the main resonator by moving the trimmer capacitors around preset positions together with pulse RF excitation.

4) Computer control

The control processor sends following control informations to each RF control unit: Three channels of analog voltage, 0 – 10 V at 10 or 14 bits resolution; eight relay contact outputs; parallel 16 bits of TTL logic.

Two channels of analog voltage are used for the reference of positioning and one for the reference of the RF amplitude in the main resonator.

Four relay outputs turn on and off four groups of the power supplies. Next one makes resetting the overload protection, and another one controls the tap changer of the plate power supply of the final tube.

The 16 bits parallel data are used as four bits address, including one spare bit, and 12 bits control data. They are stored in 8 words control memory of 12 bits length; total number of control bits is 96. Each bit of the memory is assigned to a proper control function. For example, preset counts defining the RF phase occupies ten bits.

The maximum 96 bits of status informations in the RF system are transformed into 8 channels of 12 bits length by a multiplexer. A word of 16 bits length formed by joining 4 bits channel address, including one extra bit, to 12 bits data is transmitted to the control processor. In the 96 bits, outputs of two 8 bits A/D converters each having 16 analog channels are included for analog informations.

For maintenance aim, it is possible to operate all the functions of the control unit from the local panel of it instead of the control processor.

A simplified version of the RF control unit is used for the buncher and the chopper.

References

- 1) M. Odera: IPCR Cyclotron Progr. Rep., 7, 140 (1973).
- 2) T. Kubo and Y. Chiba: *ibid.*, 14, 123 (1980).
- 3) T. Kambara, M. Odera, and S. Takeda: *ibid.*, 12, 131 (1978); 13, 134 (1979).

10-7. Measurement for Characteristics of RILAC RF System and Excitation Test of Resonators

T. Kubo and Y. Chiba

Master oscillator and power amplifier (MOPA) method is applied to the radio-frequency (RF) system of the variable frequency linac (RILAC).¹⁾ The frequency range is from 17 to 45 MHz. A schematic diagram of the system is shown in Fig. 1. It consists of one master oscillator and six power amplifier chains with control circuits²⁾ which are separately coupled to each resonator by coaxial feeders. Each power amplifier chain has a solid state amplifier as the first stage, a grounded-grid triode (EIMAC-3CX3000A7) as the second stage and a grounded-cathode tetrode (RCA-4648) as the final stage. The resonator is of a $\lambda/4$ mode coaxial type³⁾ and has three movable tuning devices. A shorting plate is used for coarse tuning and two capacitive trimmers for fine tuning. The feeder is capacitively coupled to the resonator with a disk forming the tip of feeder (coupling capacitor disk). For getting the impedance matching between the resonator and the feeder, the coupling capacitance is adjustable by changing the insertion depth of the disk into the resonator. The plate- and grid-circuits of the RCA-4648 are tuned by two coaxial stubs of variable length which are indicated as PSTUB and GSTUB in Fig. 1, respectively. A variable vacuum capacitor (VVC) can vary the load impedance seen by the RCA-4648.

The greater part of the RF system was installed in 1979, except the control circuits which would be used for the automatic operation.²⁾ In 1980, we have started to measure electrical

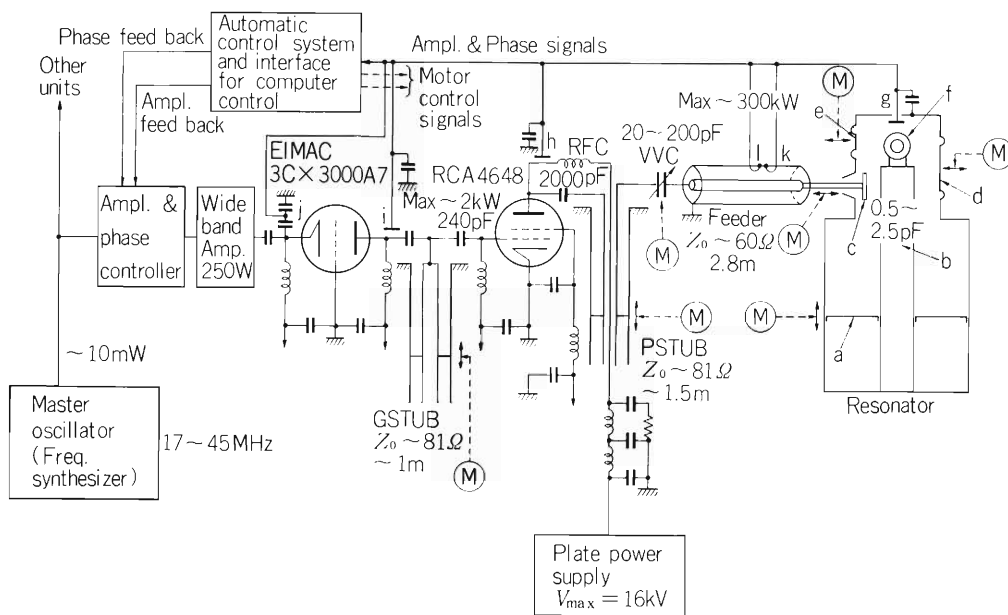


Fig. 1. Schematic diagram of the RILAC RF system. a) Shorting plate, b) Stem, c) Coupling capacitor disk, d) Large capacitive trimmer, e) Small capacitive trimmer, f) Drift tube, g) – j) Voltage pick-ups, k) Directional coupler (forward), l) Directional coupler (reflected), (M) Drive Motor.

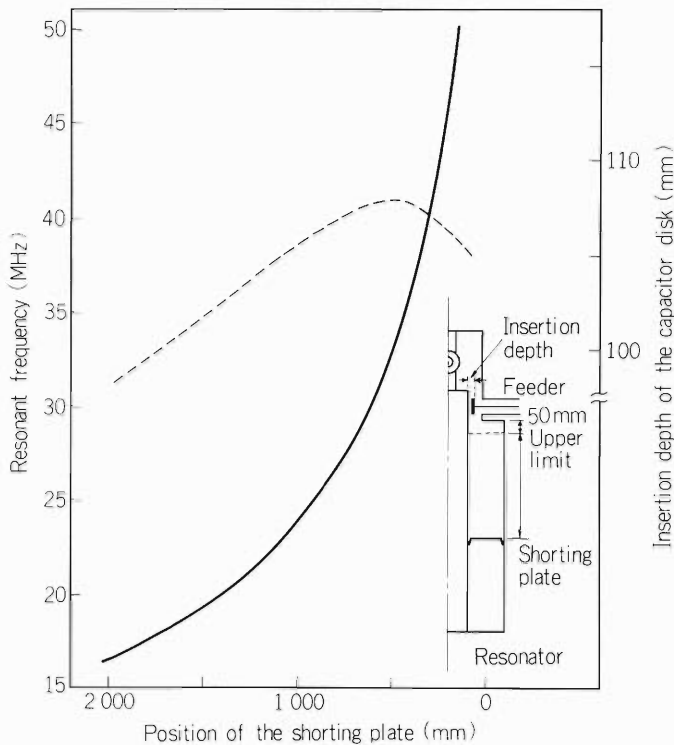


Fig. 2. Characteristics of the resonator. This figure is of the No. 4 unit. The solid line shows the resonant frequency and the dashed line the optimum insertion depth of the capacitor disk. The position of the shorting plate is measured from the upper limit as illustrated in this figure. Two fine tuning devices are fixed at the center of the moving ranges.

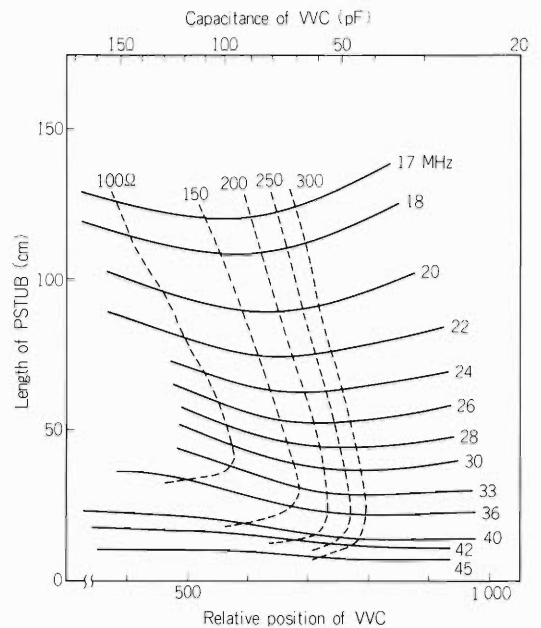


Fig. 3. Characteristics of the plate-circuit of the RCA-4648. This figure is of the No. 5 unit. Solid lines show the resonant frequencies and dashed lines the load impedances.

characteristics of the RF system and to excite the resonators by the manual operation in order to confirm the performance.

Before operating the system at high RF levels, the measurements were carried out with respect to the following items:

- 1) The relation between the resonant frequency and the position of the shorting plate.
- 2) The optimum insertion depth of the coupling capacitor disk. The results for the above two items are shown in Fig. 2. The resonant frequency and the optimum depth were determined by searching for the condition that the input impedance of the resonator looked through the coupling capacitor is equal to the characteristic impedance of feeder (60Ω). Under this condition, the resonance and the impedance matching between the resonator and the feeder are attained at the same time.

- 3) The load impedance of the RCA-4648 and the optimum length of PSTUB to satisfy the tuning. The load impedance and the resonant frequency for the plate-circuit of the RCA-4648 are shown in Fig. 3 as functions of the capacitance of VVC and the length of PSTUB. In this measurement, the feeder was replaced by a dummy load of 60Ω to simulate the ideal impedance matching between the resonator and the feeder.

- 4) The optimum length of GSTUB to satisfy the tuning. The result is shown in Fig. 4.

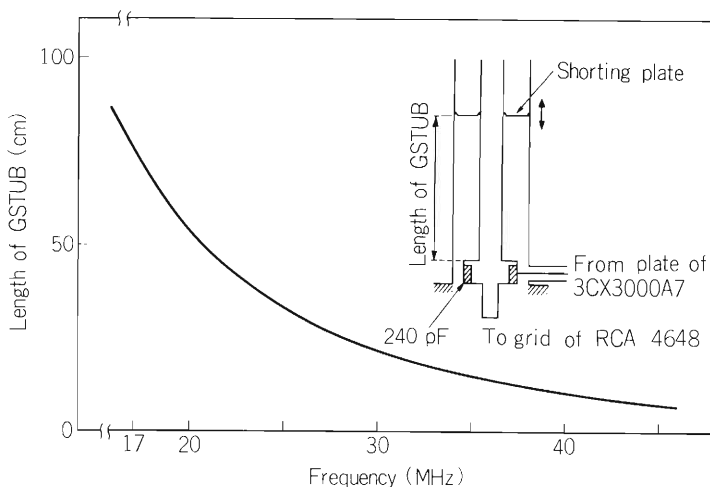


Fig. 4. Characteristics of the grid-circuit of the RCA-4648. This figure is of the No. 5 unit. The length of GSTUB is measured as illustrated in this figure.

5) The calibrations for voltage pick-ups. The voltage pick-ups are of a capacitive divider type (see g ~ j in Fig. 1) and work as amplitude and phase detectors. The calibrations were performed by comparing with the output voltages of standard probes. Their frequency characteristics were found to be almost flat.

In these measurements, an RF vector voltage meter and an RF current probe were used.

Using these data, we have manually operated the power amplifiers at frequencies ranging from 17 to 30 MHz. The accelerating voltages which were generated in the resonators were measured by the voltage pick-ups. The energy spectra of the bremsstrahlung X-rays from the resonators were taken at the same time. The calibrations for the voltage pick-ups were checked by these energy spectra. The maximum voltages described in the specifications⁴⁾ have been achieved for the No. 5 (280 kV) and No. 6 (300 kV) resonators. However, the operation became somewhat unstable near the maximum voltages by sparkings which occurred in the resonators. Conditionings were necessary to get the stable operation at high accelerating voltages. Multipactoring phenomena which occurred in the resonators could be overcome by overcoupling the amplifiers to the resonators and by pulsing the amplifier driving signals until normal RF fields were attained in the resonators.

These data obtained will be used for the automatic operation with the control circuits. The measurement and excitation test for remaining units are in progress.

References

- 1) Y. Chiba: IPCR Cyclotron Progr. Rep., 13, 143 (1979).
- 2) Y. Chiba: *ibid.*, 14, 120 (1980).
- 3) Y. Chiba: *ibid.*, 10, 144 (1976).
- 4) Y. Chiba: *ibid.*, 13, 141 (1979).

10-8. Magnets for Beam Transport System

M. Hemmi, Y. Miyazawa, and M. Odera

A design of the beam transport system was described in a previous IPCR Cyclotron Progr. Rep.¹⁾ This report is confined to the results of measurements of the five dipole magnets installed.

At the beginning of 1980, the magnets were installed in the target area as shown in Fig. 1. Beams accelerated by the linac are deflected into five directions by the switching magnet (SW). Each beam channel has two target stations except channel-C. Channel-C may be used, in future, as a part of the beam transport line leading to the SSC which is under construction. A vertically bending magnet (VM) in channel-E deflects beam to the target station in the lower floor vault (Target area III).

Table 1 shows characteristics of the magnets. Maximum magnetic rigidity of ions which the SW magnet can deflect is 3700 kG-cm for the beam deflection angles of $\pm 30^\circ$. The maximum momentum of beams that can be bent by the analysing magnets (BA) in the channels A and B is limited by the magnetic rigidity of 2200 kG-cm. For the VM magnet it is 1400 kG-cm. Therefore, it is necessary to use a charge stripper in front of the BA and VM magnets in order to deflect all kinds of the beams accelerated by the linac. Rigidity of the beam can be 3000 kG-cm.

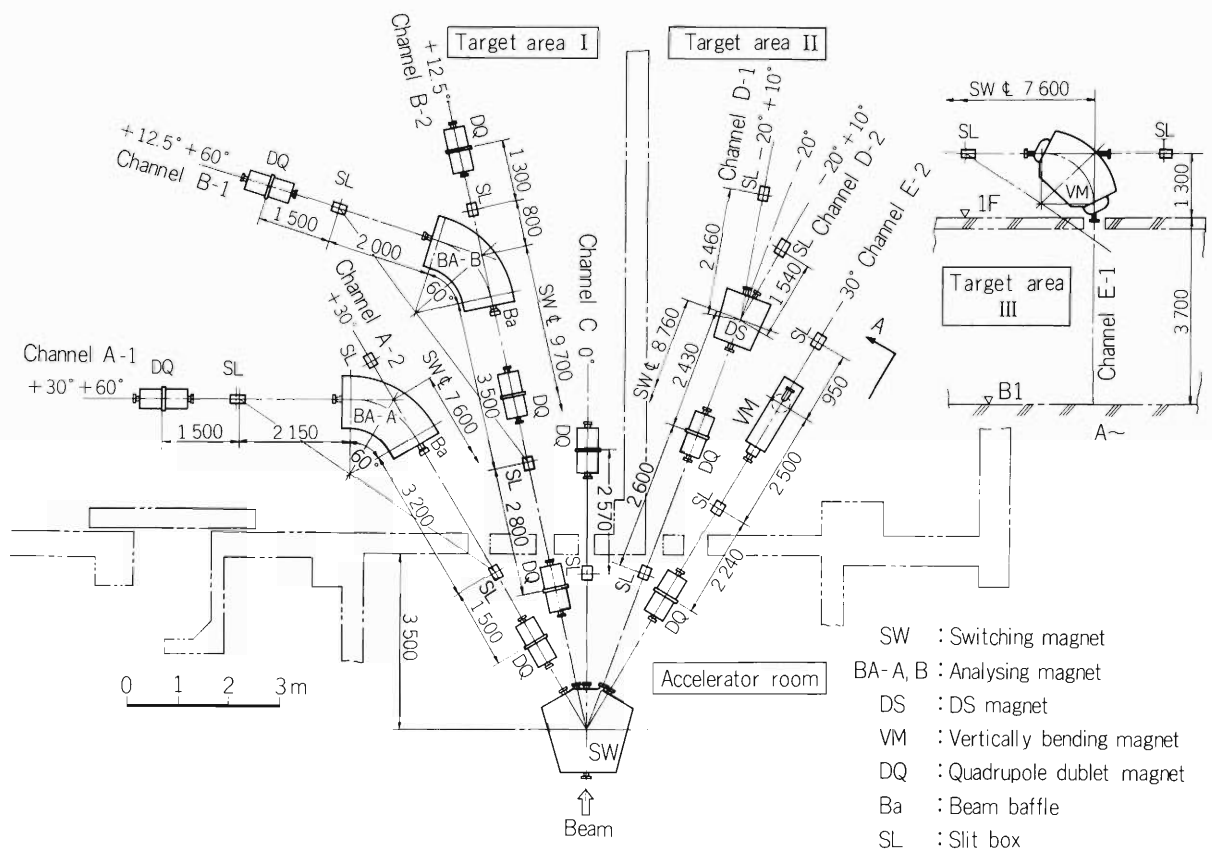


Fig. 1. Layout of beam transport magnets.

Table 1. Characteristics of the magnets.

		SW	BA-A -B	VM	DS
Pole gap	(cm)	5	5	5	5
Pole face area (S_p)	(cm ²)	6056	4340	3769	2043
Cross-sectional area of yoke (S_y)	(cm ²)	8000	6400	4080	2226
Ratio of S_y/S_p		1.32	1.47	1.08	1.09
Return path length of flux	(cm)	228	159	150	138
Number of turns		300	300	300	420
Cross-sectional area of conductor	(mm ²)	$0.8^t \times 86 = 68.8$	$0.8^t \times 85 = 68$	$0.8^t \times 85 = 68$	$0.55^t \times 85 = 46.8$
Coil current	(A)	200	200	200	80
Current density	(A/mm ²)	2.91	2.94	2.94	1.71
Angles of beam deflection	(deg.)	0, 12.5, 30 -20, -30	0, 60	0, 90	-10, +10
Slant angle of pole boundary	(deg.)	0	0	26.5	0
Radius of curvature	(cm)	250 ($\pm 30^\circ$)	150	100	400
Maximum field of magnet	(kG)	14.3	15.1	14.1	8.2
Amperere-turn	(AT)	6×10^4	6×10^4	6×10^4	3.1×10^4
Magnetic rigidity	(kG-cm)	3575	2265	1410	3280

Figure 2 shows excitation curves of the magnets. There is no indication of saturation in the return yokes of DS (the small angle deflection switching) and BA magnets, but a small saturation effect is seen in the case of the VM and SW magnets. The pole edge of VM magnet is rotated so that normal to the edge face makes an angle of 26.5° with respect to the beam axis to obtain stigmatic focusing effect.

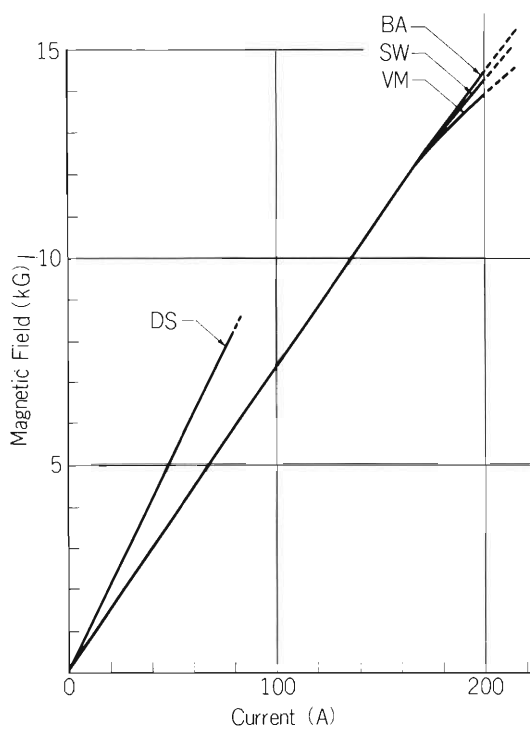


Fig. 2. Excitation curves of various magnets.

Figure 3 shows various fringing-field distributions of the magnets. The pole corners are shaped so that the magnetic field inside the iron is almost homogeneous. The relative distribution of the fringing field of each magnet was found to be constant within the range of the applied excitation current, showing the effect of the pole corner profile. The pole gap field were also measured and no effects of corner saturation were seen.

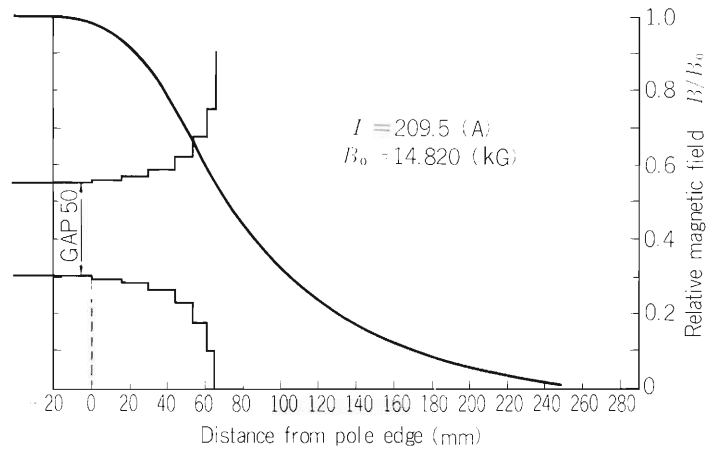


Fig. 3. (a) Fringing field curve measured for SW magnet.

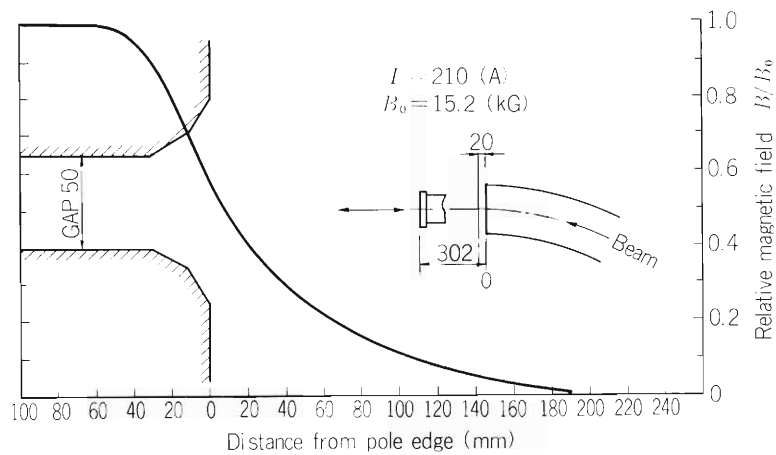


Fig. 3. (b) Fringing field curve measured for DS, VM, and BA magnets.

Reference

- 1) M. Hemmi, Y. Miyazawa, M. Odera, and T. Tonuma: IPCR Cyclotron Progr. Rep. 12, 138 (1978).

10-9. Vacuum System of the Beam Transport Lines

Y. Miyazawa and M. Hemmi

The vacuum system of the beam transport lines can be divided into six blocks: Those for the five channels and one for the chamber of switching magnet. Figure 1 shows the layout of the vacuum equipment along the beam transport lines. Each beam channel is provided with a turbo-molecular pump (TMP) and a triode sputter ion-pump (IP) having pumping speed of 140 ℓ /sec and 120 ℓ /sec for air, respectively. The chamber of the switching magnet to which the five channels are joined is provided with a turbo-molecular pump having pumping speed of 450 ℓ /sec. The vacuum elements for the beam lines are joined with each other by the European vacuum standard (PNEUROP) NW63 flanges and pipes. A vacuum gate valve is provided at the end of each channel separating the vacuum chambers for experiments from the beam line. It is pneumatically operated and can be opened only when the pressure in the chamber is below 5×10^{-6} Torr.

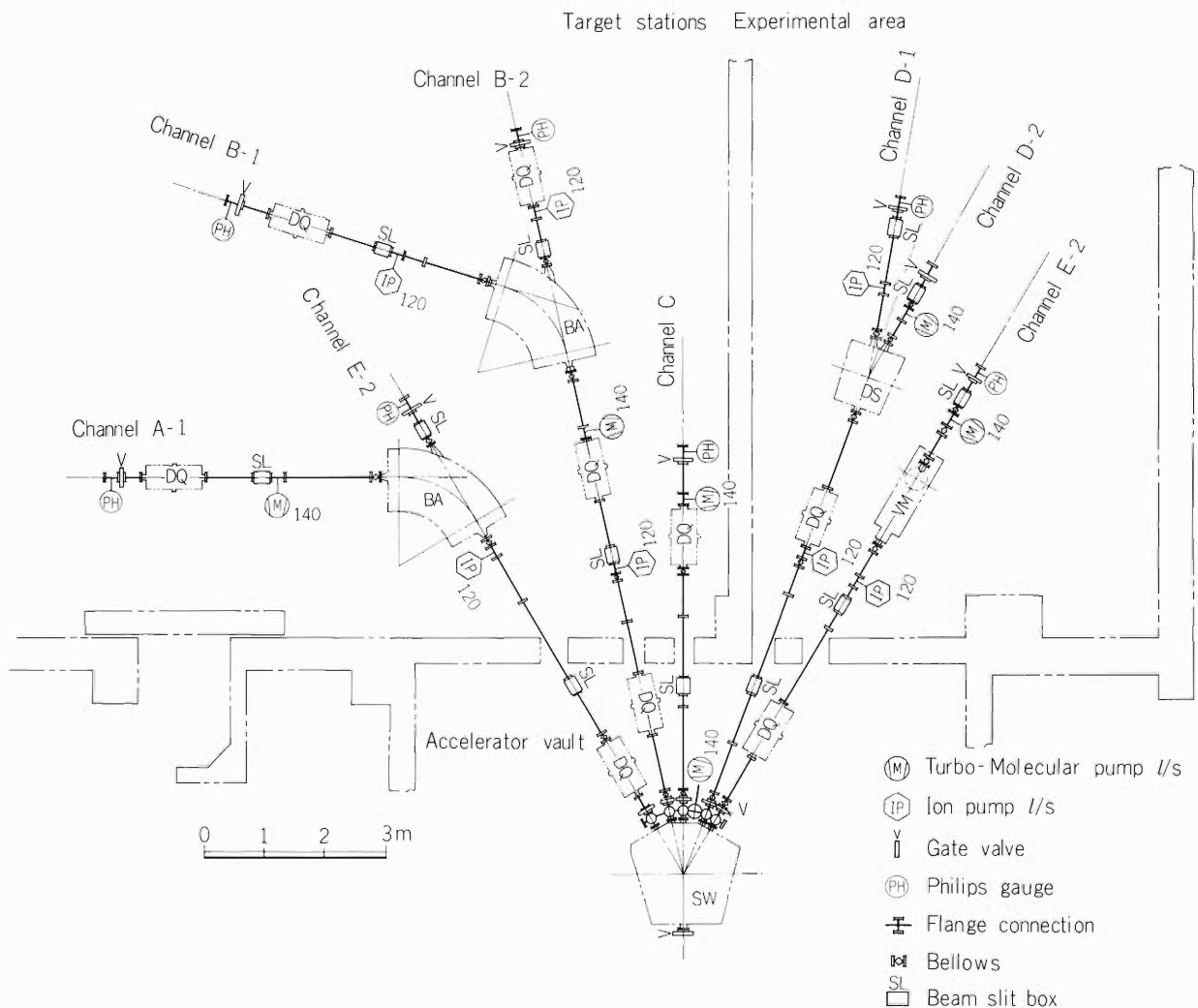


Fig. 1. Vacuum system of the beam transport lines.

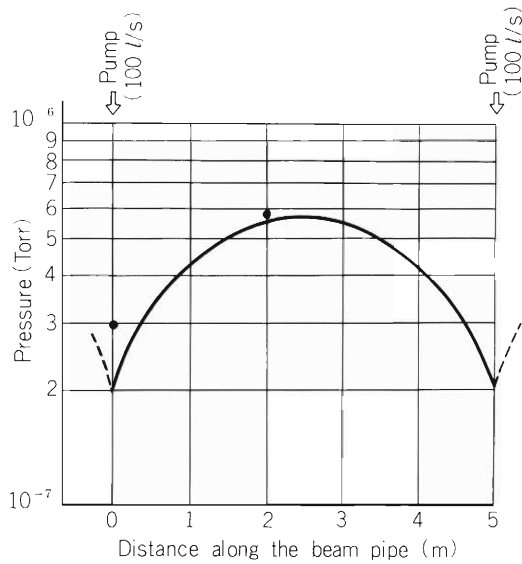


Fig. 2. Vacuum pressure distribution between pump stations: Solid line was calculated assuming a degassing rate of 4×10^{-9} Torr·ℓ/ sec·cm² from the surface of the stainless steel pipes. Closed points are measured values at channel-C.

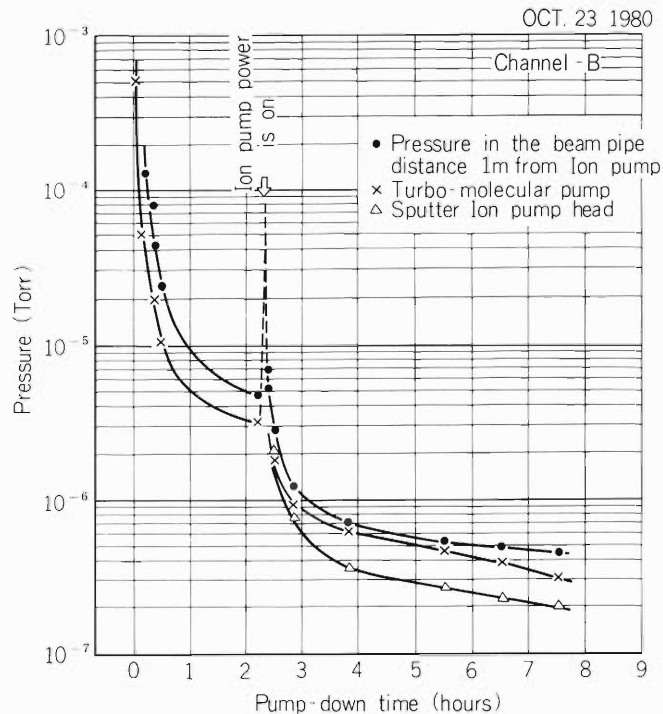


Fig. 3. Typical pump down curve of channel-B.

Roughing of the beam pipe can be done directly through each turbo-molecular pump by a forepump (340 ℓ/min). When the pressure at the outlet of the turbo-pump falls below 1 Torr, the turbo-pump can be run to block forepump oil vapor from passing backward through the turbo-pump into the connected system. The power of the sputter ion-pump is supplied when the turbo inlet pressure reaches 5×10^{-6} Torr.

To avoid the beam loss due to the charge exchange reactions between heavy ions and residual gas molecules, the required mean pressure in the beam pipe should be below 1×10^{-6} Torr. Therefore, turbo pumps or sputter ion pumps were needed to be distributed along the beam line at every 5 meters. The vacuum obtainable at the pump inlet is 1×10^{-7} Torr without baking

treatment. The pressure at half way between pumps rises to a value three times of that at the pump head. Figure 2 shows the pressure distribution along the beam line calculated assuming the outgassing rate of 4×10^{-9} Torr $\cdot\ell$ /sec $\cdot\text{cm}^2$. The outgassing rate in the channel-A obtained by a pressure rise test is about 1×10^{-10} Torr $\cdot\ell$ /sec $\cdot\text{cm}^2$. Figure 3 shows a typical pump down curve measured for channel-B. The required pressure of 1×10^{-6} Torr can be reached within 3 h from the start of evacuation from atmospheric pressure. At present the vacuum system is operating satisfactorily. To improve ultimate pressure further, we are preparing metal gaskets to replace the organic seals in near future.

10-10. Heavy Ion Source for the Linac

M. Kase and Y. Miyazawa

The linac requires heavy ions with a charge to mass ratio of $1/27 < q/m < 1/4$ from its ion source. In order to produce such ions, a PIG source of a radially extracting type has been designed¹⁾ and installed in the 500 kV terminal of the injector.

A cross sectional view of the ion source for gas-ion production is shown in Fig. 1. The anode is made of water cooled copper. The beam exit slit in a replaceable molybdenum plate is 2 mm \times 10 mm in size. The anode bore is 8 mm in diameter and the distance between the cathode and the anti-cathode is 100 mm. The cathode, which is a tungsten rod with a diameter of 10 mm, is heated by the bombardment of electrons from a 0.8 mm ϕ tungsten filament. The filament current of 36 A is supplied by a 19 kHz self-oscillator. The electron bombardment power required to burn the arc discharge is about 600 W (800 V \times 0.75 A). The anti-cathode is a molybdenum rod with a diameter of 12 mm.

The ion source is set in a 150 mm gap of magnetic poles. The magnetic field can be varied up to 7.2 kG. Typical gas flow rate is 0.5 ml/min. The vacuum pressure around the ion source during the operation is maintained less than 1.5×10^{-5} Torr by means of two turbo-molecular pumps with pumping speeds of 450 and 3000 ℓ /sec.

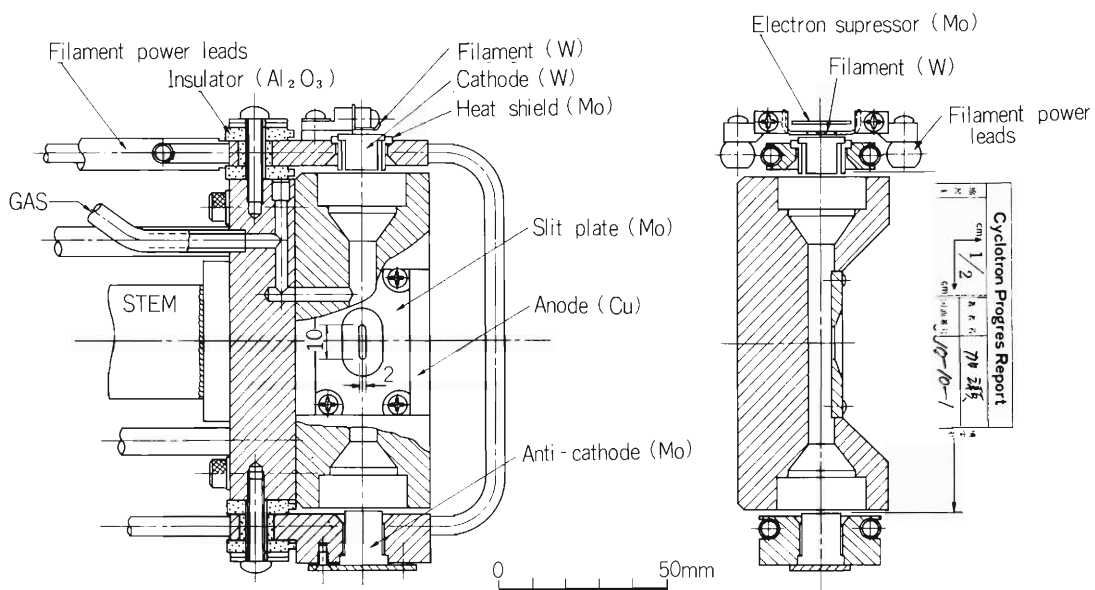


Fig. 1. Cross sectional view of the PIG source for gas ions.

Figure 2 shows schematically the beam extraction arrangement. The puller, which is mounted on the extractor facing the anode slit, has a slit of 10 mm \times 14 mm in size. The relative position of the extractor to the ion source can be remotely adjusted. The extractor is biased at 0 \sim -30 kV against the anode which is at the potential of the injector terminal.

The extracted beam is bent through an angle of 120° in the magnetic field to give beam analysis and horizontal focussing. The pole edge of magnet is rotated so that normal to the edge face makes an angle of 30° with respect to the beam axis to obtain vertical focussing.¹⁾ In addition, the beam is focussed with an einzel lens.

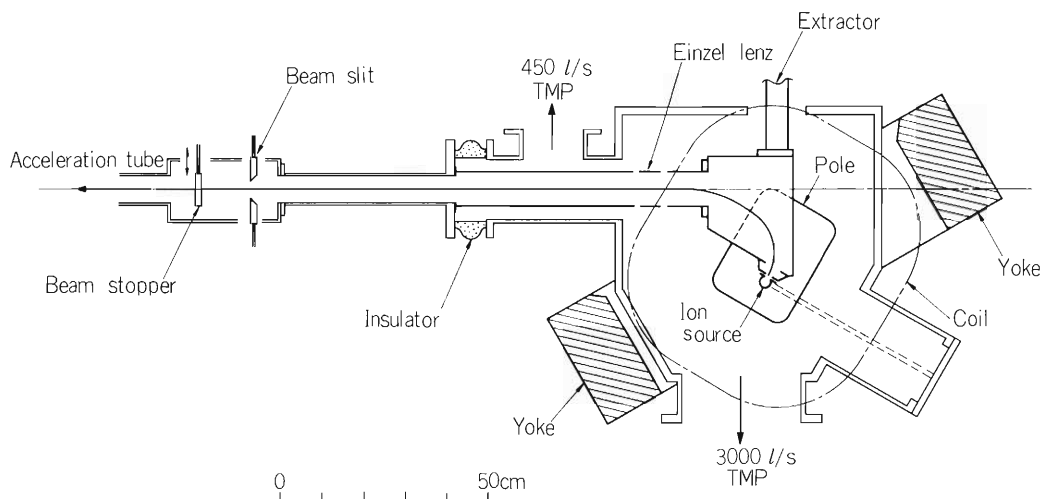


Fig. 2. Plane view of beam extraction arrangement in the injector terminal.

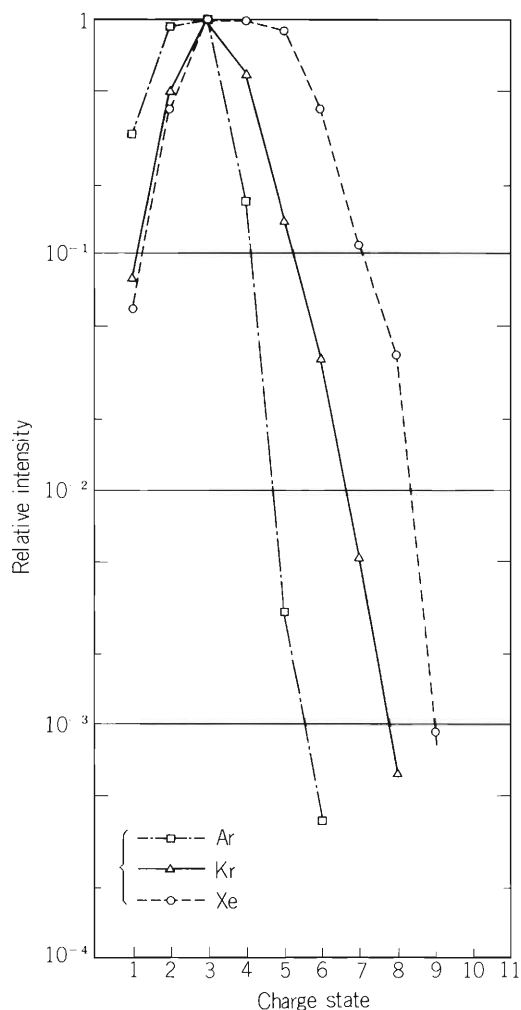


Fig. 3. Charge state distributions of Ar, Kr, and Xe ions obtained with the PIG source. The arc conditions are $350 \text{ V} \times 1.6 \text{ A}$ for Ar ions, $250 \text{ V} \times 4.5 \text{ A}$ for Kr ions, and $270 \text{ V} \times 2.9 \text{ A}$ for Xe ions. The maximum beam currents are $40 \mu\text{A}$ for Ar^{3+} , $5.6 \mu\text{A}$ for Kr^{3+} , and $2.9 \mu\text{A}$ for Xe^{5+} .

The ion beam passing through a beam slit of 10 mm × 10 mm in size are measured with a beam stopper. Figure 3 shows the typical data of the charge distributions given by the ion source with a dc arc operation. These are obtained for the magnetic field of 5.2 kG by scanning the extraction voltage.

In order to increase the yields of higher charge-state ions, it is necessary to improve the vacuum around the ion source and employ a pulsed arc operation. For metal ions, the PIG source with a sputtering electrode in the anode wall is being built.

Reference

- 1) Y. Miyazawa, M. Yanokura, M. Hemmi, F. Yoshida, M. Kase, and M. Odera: IPCR Cyclotron Progr. Rep., 13, 151 (1979).

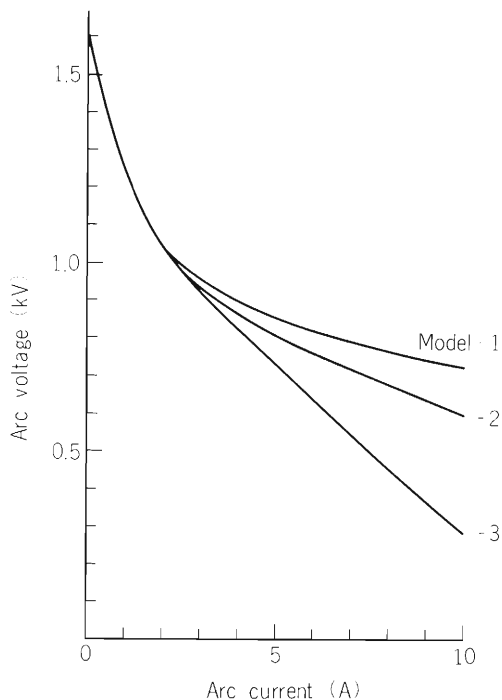


Fig. 2. Characteristics of the arc power supply.

the arc power supply is shown in Fig. 2. For the present ion source we use the operation mode-1. In this mode, the output resistance of the arc power supply is 25Ω at the arc current above 8 A. It is planned to pulse the arc current to get highly charged ions in the future. Mode-2 or -3 will be used in this case.

The extraction potential is provided by a 30 kV DC power supply. The current capacity is 40 mA. When heavier ions are extracted, however, we often observe the extraction current to become larger than 40 mA. It is caused by increase of electron emission from the surface of the extractor bombarded by ions.

Half of the extraction voltage is applied to the center electrode of the einzel lens in order to focus the divergent beam extracted from the ion source.

The magnetic field of 4 to 7.2 kG is required to produce and analyse all kinds of ions. The coils of this magnet were made by copper-tapes with the edge cooling, called tape coil, to

Table 1. Ratings of the power supplies for the ion source.

	Filament	Electron bombardment	Arc	Sputtering source	Extraction	Magnet
Wave form	HF	DC	DC	DC	DC	DC
Voltage	10 V (rms)	-1.3 kV	-1.5 kV	-1.5 kV	-30 kV	80 V
Current	70 A (rms)	1.5 A	10 A	1 A	40 mA	150 A
Regulation	-	-	a)	-	Voltage	Current
Ripple (at full load)	-	<1 %	<1 %	<1 %	<3 V	1×10^{-4} b)
Electrical isolation	5 kV DC	5 kV DC	GND c)	GND c)	GND c)	GND c)

a) See Fig. 2.

b) Current stability.

c) GND means that one of the output terminals is connected to the chassis.

reduce the power consumption of the magnet. The maximum input to the primary of the magnet power supply is 20 kVA. This power consumption corresponds to one third of the total power possible to use on the H.V. terminal. Power supplies on the H.V. terminal are controlled at the control desk through photo-coupler devices. The devices are connected by a fiber light-guide 15 m long.

Table 1 summarizes the specifications of the power supplies.

10-12. Multi-Wire Beam Emittance Monitor and Beam Profile Monitor

M. Saito, I. Yokoyama, M. Kase,
T. Kambara, and M. Odera

Two new beam diagnostic systems, one for profile measurement and the other for emittance measurement, were fabricated and tested in the beam line of the linac. Each system is composed of multi-wire beam probes, driving system for the probes, and electric circuits for control, data acquisition and data transfer which are linked to the computer of the control system (HP-1000).¹⁾ The computer sends instructions to the systems, receives measured data from them, and processes the obtained data numerically. The result is shown on a graphic CRT terminal of the computer. Such on-line digital measurement system will be useful in future for closed-loop operation of the linac.

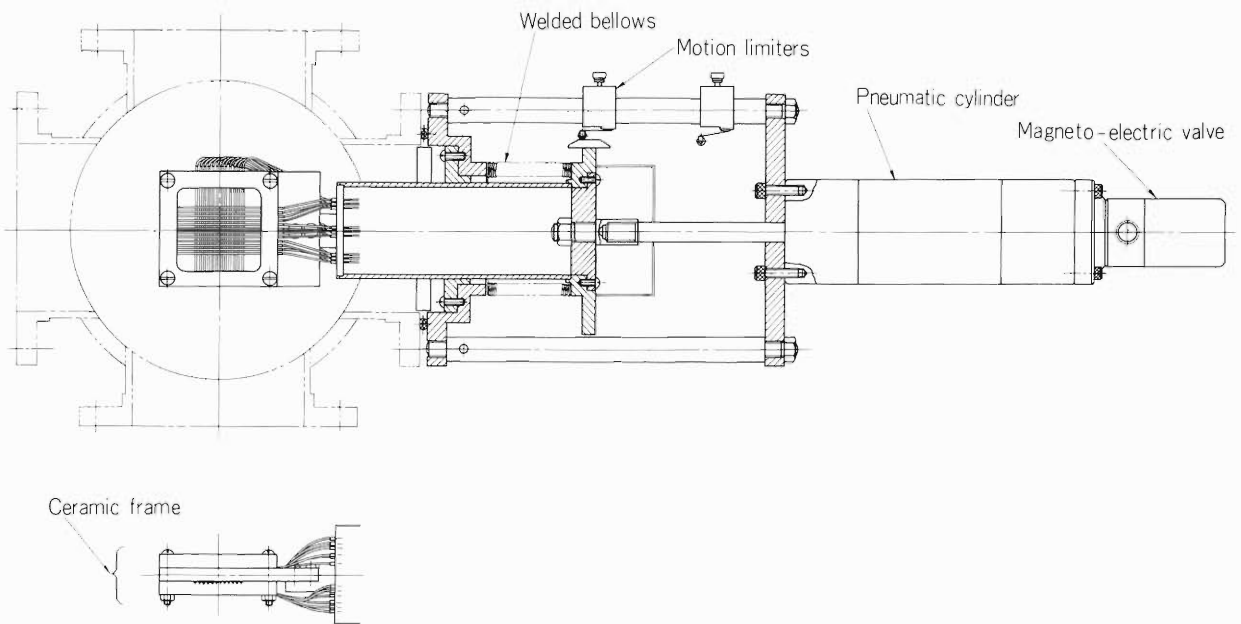


Fig. 1. Beam profile monitor probe and pneumatic cylinder.

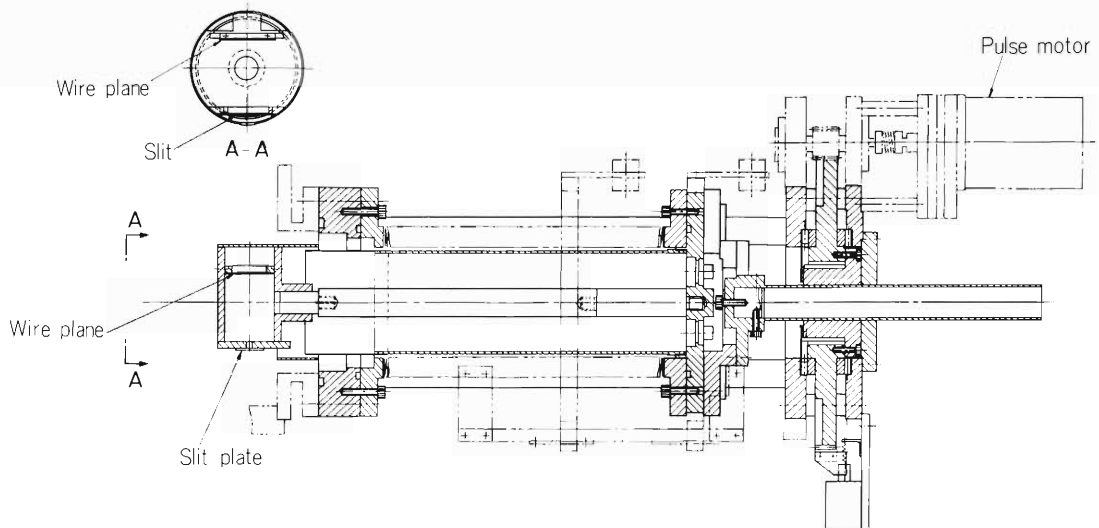


Fig. 2. Beam emittance monitor probe and pulse motor.

1. Probes

Figure 1 shows the profile monitor probe. It has a 12×12 wire net and each wire is connected to an amplifier separately. The probe is driven by a pneumatic cylinder for fast insertion into and extraction from the beam path. Beam profiles in x- and y- directions are taken simultaneously when it is inserted into the beam path.

The emittance monitor has two probes, one for x- direction and the other for y- direction. Figure 2 shows the probe. The probe has a multi-wire beam current sensor and a 0.2 mm wide slit in front of it. A plane containing each wire and the slit defines an angle to the beam axis. The probe moves across the beam stepwise and at each position of step, it measures the beam currents emerging from the slit to different angles by the multi-wire sensor. At present, one step is 2 mm and each x- and y- sweep consists of 20 steps. The probes are driven by pulse motors, because precise positioning of the probes is needed in the measurement.

2. Control and data acquisition system

(1) General

The control and data acquisition systems for the two types of monitors are almost the same except the driving systems of the probes. Each system has a local unit near the beam line and a central unit in the control room, connected together by a bit serial data line. The central unit is linked to the control computer via the HP IB IEEE standard 488-1978 "Digital Interface for Programmable Instrumentation". The local unit performs the actuation of the probes, measurement and digitization of the beam currents and transfer of the data to the central unit, according to the instruction from the central unit. The central unit receives the data from the local unit, stores them temporarily in its memory and sends them to the control computer. It also accepts instructions from the computer, translates and sends them to the local unit. Each unit has a microprocessor Intel 8080 to perform these functions. Figure 3 shows a block diagram of the system.

(2) Local unit

The local unit has a 12 bit ADC (analog-to-digital converter) section and a control circuit. The former is enclosed in a shielding box separated from the latter to ensure good S/N ratio in measuring weak currents. It is composed of 30 pre-amplifiers with high input impedance, paired with sample-hold circuits, a multiplexer and the ADC. Variation of gain of the amplifiers is checked by supplying reference signals to each input through relays.

For the emittance monitor, a power supply for the pulse motors and an x- and y- channel switching circuit are also included in the local unit. They are contained in a separated chassis from the other parts which are sensitive to electric noises.

(3) Example of emittance measurement

The central unit is in HLT (stand by) status when it is waiting for an instruction from the computer. The

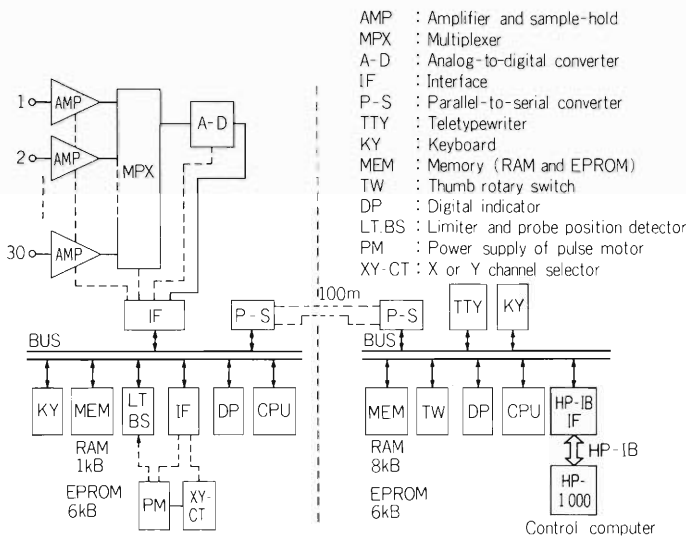


Fig. 3. Block diagram of the monitor data acquisition system.

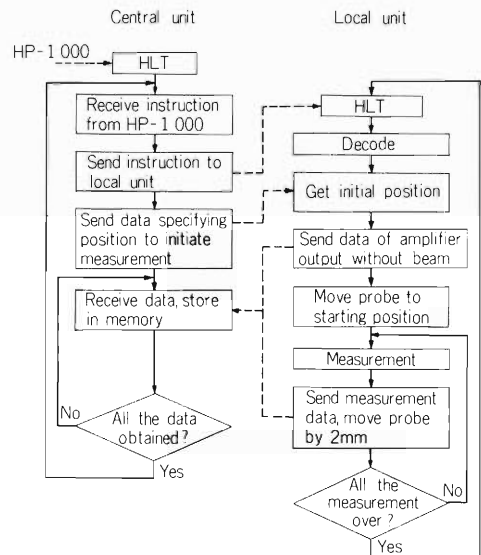


Fig. 4. Flow chart of execution steps for the case of the instruction "XO". Paths of transfer of signals between central and local units are indicated by dotted lines.

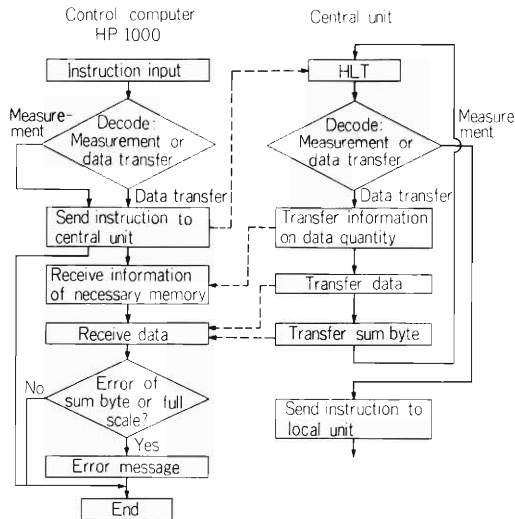


Fig. 5. Flow chart of execution steps for an instruction to transfer the measured data to the control computer.

unit accepts instructions related to the execution of measurements and the data transfer from the unit to the computer. There are 12 instructions for the measurements and 10 for the data transfer, each of which consists of two ASCII characters. More details will be described elsewhere.²⁾ An example of emittance measurement is shown below: When the central unit receives the instruction "XO" which requires measurement of emittance in x-direction, it translates the instruction code and sends it to the local unit. The local unit reads the instruction and sends a ready status sign back to the central unit. The central unit reads it and sends to the local unit, information to specify the probe position from where the measurement starts. The coordinate of the position has been manually set on the panel of the central unit. Then the local unit makes a measurement, without beam current, to see the deviation of the amplifier outputs from null, sends the data to the central unit and drives the probe to the position of the first measurement. After the first measurement, the local unit moves the probe by a distance of 2 mm and sends the first data to the central unit if it is ready to accept them. After the data transfer process, the central unit sends a non-busy sign to the local unit and waits for following data. The local unit becomes ready for the next measurement when the probe arrives at the next position.

In this way the measurements are repeated and after the completion of the 20th measurement, the local unit sends a sign of completion, draws the probe from the beam path back to the initial stand-by position and takes the HLT status. The central unit stores the data from the local unit in its memory sequentially and when it receives the final data, it lights a lamp indicating that it is ready for next instruction from the computer and goes back to the HLT status. Execution of the "XO" instruction is thus finished. Figure 4 shows the transaction process between the local and the central unit.

Other instructions are executed in a similar manner. When any error in data transfer or delay of response of more than 10 seconds is observed, execution of the instruction is interrupted, the probe goes back to the stand-by position and error indication lights are lit on the panels of both units. The data transfer process is checked by comparing the sums of corresponding bytes in memories of both units.

All the procedures of the measurement of beam profile are similar to that of emittance, except that the measuring process is simpler and needs much shorter time.

(4) Data transfer to the control computer

When one of the instructions for data transfer is issued by the computer, the code is sent to the central unit via the HP-IB. The central unit reads the instruction and transfer the contents of the memory to the computer. Errors in the data transfer process is checked by the method mentioned above. The sum byte of the content of the memory of the central unit are sent to the computer after the completion of the transfer of the measured data. The central unit then goes back to the HLT status again. Figure 5 shows the transaction process between the central unit and the computer.

The computer transforms the format of the data, checks the sum bytes and checks if the obtained data are within certain limits. If any error is found, a warning is given to the operator. The result of the numerical processing of the obtained data is shown in the form of contour diagram or a graph on the screen of the graphic CRT terminal (HP2648A).

10-13. A 100 cm Scattering Chamber

I. Kohno, M. Yanokura, Y. Gono, and I. Takeshita

A scattering chamber has been designed for universal use in the experiments on nuclear scatterings and reactions by the heavy-ion linac. A cross-sectional view of the scattering chamber is shown in Fig. 1. The chamber is 100 cm in inner diameter and 45 cm in inner depth, and its main parts are made of stainless steel. The whole scattering chamber can be moved horizontally and vertically for the initial installation. The side wall has 8 windows of 100 mm in inner diameter. The movable parts of this scattering chamber are listed in Table 1. Shafts of the turn table and the turn arms are of pipe structure. Each of them is supported independently by a greaseless ball bearing which is fixed to a solid frame. With this system it

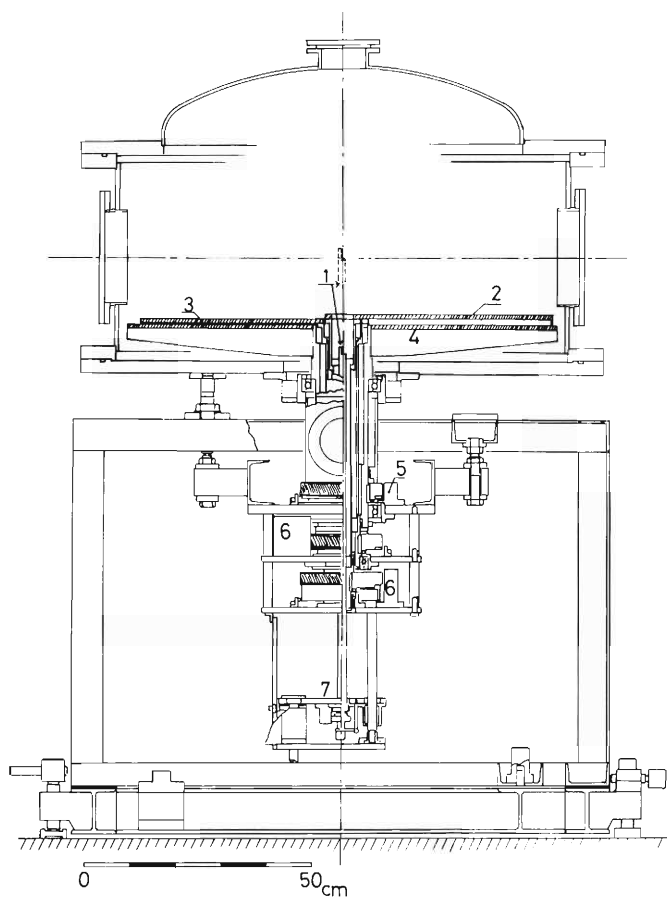


Fig. 1. Cross sectional view of the scattering chamber. 1, Target holder, 2, Turn arm, 3, Turn arm, 4, Turn table, 5, Electric motor to move turn table, 6, Electric motors to move turn arms, 7, Electric motor to move target holder.

Table 1 Movable parts of the scattering chamber.

Turn table 1	rotation in all angles with accuracy of setting	$\pm 0.05^\circ$
Turn arm 2	" "	$\pm 0.05^\circ$
Target holder 1	" "	$\pm 0.5^\circ$
	vertical motion 180 mm with accuracy of setting	± 0.5 mm
Adjustment: by remotely controlled electric motors		
Indication of their position: by digital indicators and optical detectors		

is possible to rotate them independently and to keep them free from the influence of distortion of the chamber. Special care is paid to make the scattering chamber vacuum to be free from oil. Teflon rings are used to reduce the gas flow from the rotation systems to the chamber. This allows to apply a differential pumping of these two parts and to introduce the rotation system without grease. Two turbo-molecular pumps of pumping speeds 1500 ℓ/sec and 120 ℓ/sec are prepared for the scattering chamber and the shaft parts of the rotation systems, respectively.

10-14. Design of an Electron Spectrometer

A. Yagishita and T. Nakamura

Auger, autoionization, and secondary electrons are ejected from an atom or molecule when a fast charged particle is incident on it. Much information on both atomic structures and dynamic excitation mechanisms is obtainable by electron detection. Thus, several works on electron-spectroscopic studies by high-energy ion-atom collisions have been reported. There is little data, however, on the studies by highly-stripped-ion impacts at energies lower than 500 keV. Data on collisions between atoms and heavy ions, which have mass numbers larger than 36, at energies higher than 100 MeV are also scarce. To investigate these fields of ion-atom collisions, therefore, we started the construction of an electron spectrometer in the linac laboratory at the beginning of 1980.

Our design concerning the heart of the spectrometer, the energy-dispersing element, mostly has followed the idea developed by Kuyatt and Simpson¹⁾ for the use of an electrostatic energy filter of hemispherical shape. On the other hand, in the design of electron-optical lenses to accelerate, decelerate, transport, and focus an electron-beam from an interaction region to a detector, we have utilized electrostatic lenses of two or three apertures. The electron-optical properties of them such as focal lengths, principal plane positions, and spherical aberration coefficients had been calculated in Refs. 2 and 3.

Figure 1 shows the schematic drawing of the spectrometer with an electron gun. Figure 2 shows the photograph of it. They are all placed in a vacuum chamber, in which the magnetic fields are reduced by double-layer μ -metal shieldings. Apertures defining the size of the electron-beam and electron-optical lenses were fabricated from molybdenum. Hemispherical electrodes, shielding cylinders of the lenses, and X-Y deflectors were made from stainless steel.

Some characteristics of the spectrometer are shortly described below. The radial distance of outgoing electrons (x_2) from a mean orbit radius R_0 is given as a function of that for incoming electrons (x_1), of electron energy E , and of the incident angle α of the electrons with respect to the mean orbit. This relation may be

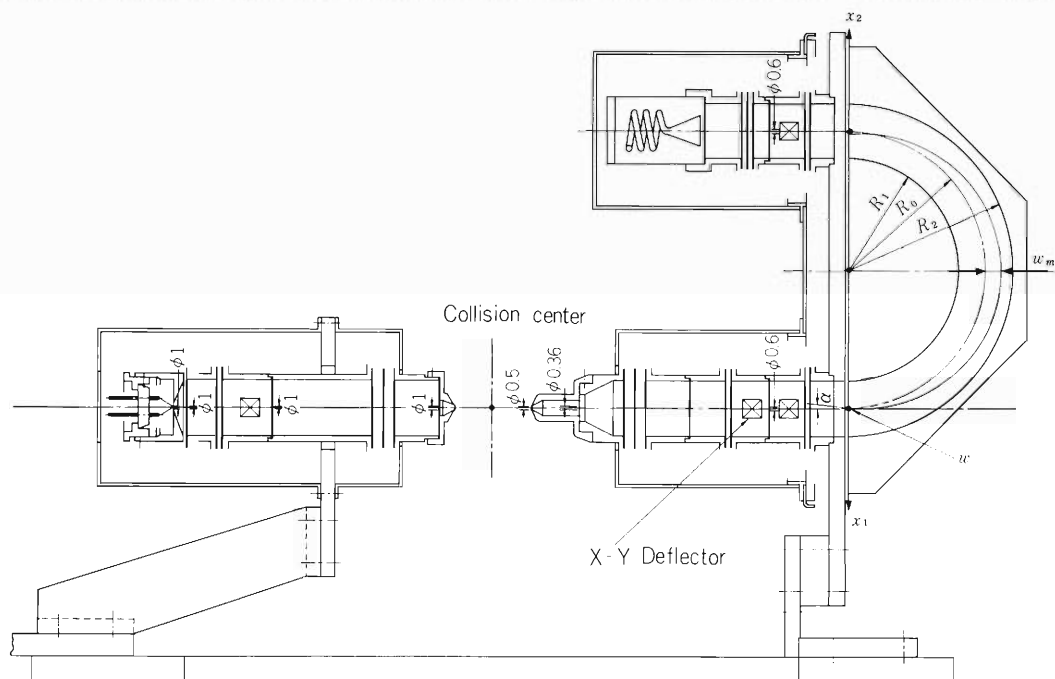


Fig. 1. A schematic drawing of the electron spectrometer.

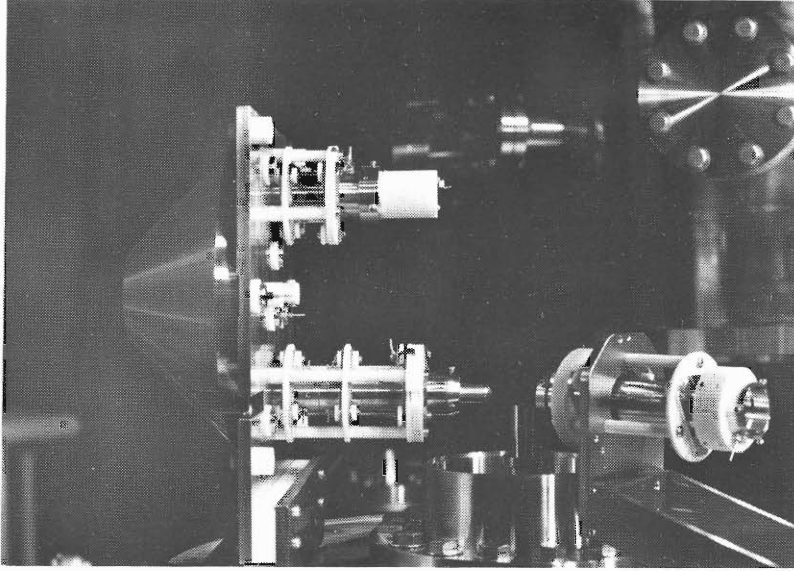


Fig. 2. A photograph of the electron spectrometer.

written as¹⁾

$$X_2 / R_0 = -x_1 / R_0 + 2(\Delta E / E_0) - 2\alpha^2, \quad (1)$$

where E_0 is a mean energy and $\Delta E = E - E_0$. Postulating that entrance and exit slits are of equal width w and that the term α^2 of Eqn. (1) is neglected, the transmission of electrons through the hemispherical electrodes would be given by a triangular figure as a function of E . FWHM (full width at half maximum) $\Delta E_{1/2}$ of the triangle is given by

$$\Delta E_{1/2} / E_0 = W / 2 R_0. \quad (2)$$

Addition of the α^2 term of Eqn. (1) has the effect of changing the shape of the transmission function. To reduce the tailing of the line shape, we have chosen

$$\alpha^2 = W / 4 R_0. \quad (3)$$

Using Eqns. (1), (2), and (3) the base width ΔE_b of the transmission function is given by

$$\Delta E_b / E_0 = 2.5 \Delta E_{1/2} / E_0. \quad (4)$$

The maximum deviation w_m of the electron-beam from the mean orbital radius R_0 may be written as¹⁾

$$\frac{w_m}{R_0} = \frac{\Delta E_b}{E_0} + \left\{ \alpha^2 + \left(\frac{W}{2R_0} + \frac{\Delta E_b}{E_0} \right)^2 \right\}^{1/2}. \quad (5)$$

In order to transmit the whole divergent electron-beam, we have chosen a gap $\Delta G = 20\text{mm}$ between the hemispherical electrodes.

When electrons having the energy E_0 in electron-volt travel on the circle of radius R_0 , the potential difference V in volt between the electrodes is given by¹⁾

$$V = E_0 / e \left\{ (R_2 / R_1) - (R_1 / R_2) \right\}, \quad (6)$$

where R_1 is the radius of the inner hemisphere, R_2 of the outer hemisphere, and e the electron charge in Coulomb.

The design parameters of the hemispherical deflector are easily calculated by Eqns. (2) – (6). They are listed in Table 1 together with the predicted energy resolution for $E_0 = 2, 20,$ and 50 eV.

Detailed description of the spectrometer, including the electrostatic lens system, voltage control unit, and data acquisition system, will be presented with some experimental data in a literature.

Table 1. Parameters of the hemispherical deflector.

Parameters	Calculated values		
$\Delta E_{1/2} / E_0$		0.01	
$\Delta E_b / E_0$		0.025	
α^2		0.0707	
w_m / R_0		0.104	
$w_m / \Delta G$		0.260	
E_0 (eV)	2	20	50
$\Delta E_{1/2}$ (eV)	0.02	0.20	0.50
ΔE_b (eV)	0.05	0.50	1.25
V (Volt)	1.67	16.7	41.7

Mean radius $R_0 = 50$ mm. Entrance and exit virtual aperture $w = 1.0$ mm.

References

- 1) C. E. Kuyatt and J. A. Simpson: Rev. Sci. Inst., 38, 103 (1967).
- 2) F. H. Read: J. Phys. E, 3, 127 (1970).
- 3) E. Harting and F. H. Read: Electrostatic Lenses, Elsevier Sci. Pub. Co., Amsterdam (1976).

T. Shikata and A. Koyama

An electron spectrometer for the study of the energy and the angular distribution of electrons ejected from metal surface by fast ion impact is now under construction.

In order to measure the electrons ejected in various directions from 0 to 180° with respect to the incident ion beam direction, slots must be provided in the electrodes of the analyzer to allow the ion beam to pass through. Such an arrangement, however, cause the lowering of the resolution of the analyzer. To avoid such lowering, we used energy filters with a slotted parallel plate type analyzer, employing the principle of the energy analyzer used in the "DUPONT 650 ELECTRON SPECTROMETER".

A schematic drawing of the analyzer is shown in Fig. 1. The trajectory of the electrons is shown by dotted line. The electron beam is first retarded to match the energy of the parallel plate type analyzer which plays a role of a narrow band-pass filter. The deflected electrons pass through a quadrupole lens which aligns the beam, and enter into the low-pass filter. The reflected low energy electrons again pass through the quadrupole lens and enter into the high-pass filter via a deflector. The transmitted high energy part of the electrons is

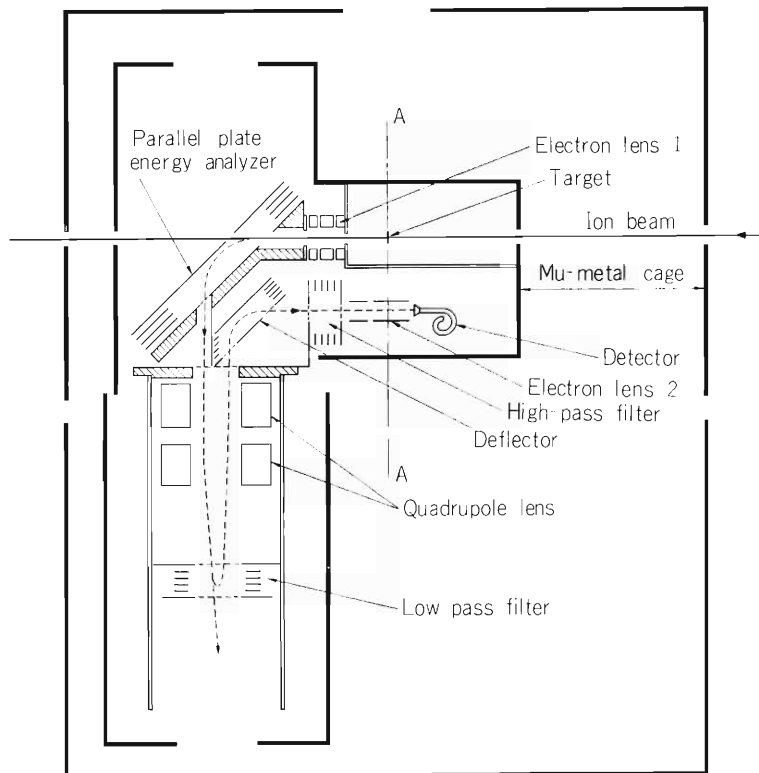


Fig. 1. Schematic drawing of the analyzer.

accelerated and is collected in the detector. If we set the band width formed by both filters narrow, the improvement of the resolution is attained. Energy spectra of electrons will be obtained by scanning the retardation potential applied on the electron lens 1.

The instrument can be rotated around the axis A-A passing through the beam spot on the surface of the target.

Magnetic shielding is carried out using double mu-metal cages.

Data acquisition system is also in preparation.

10-16. Design of an Apparatus for RILAC-Beam Irradiation of Biological Samples

F. Yatagai and S. Kitayama

An apparatus was designed to study various effects of high-LET radiations on biological materials. One example to be studied is the biological effects observed with the increase of high energy secondary electrons (δ -rays) accompanied by an increase of atomic number of incident heavy particles. The method is to irradiate samples by the elastically scattered beam at a certain angle with respect to the beam axis (Fig. 1). This method has already been applied for the irradiation at the IPCR cyclotron. The biological sample mounted on a holder faces the vacuum window and can be rotated for the uniform irradiation, because the relative intensity of scattered beam decreases with increasing scattering angle.

An attempt was made to improve the irradiation system used at the IPCR cyclotron. The most important improvement is to place two independent slit boxes between the bending magnet and the scattering foil for better beam-collimation (Fig. 1). Moreover, the center of the plate, which contains four sample-holders arranged in a circle, can be adjusted to coincide with the beam axis for the irradiation of each sample at the same dose rate.

It is expected from many points of view that this irradiation system will provide an accurate dosimetry and a uniform irradiation.

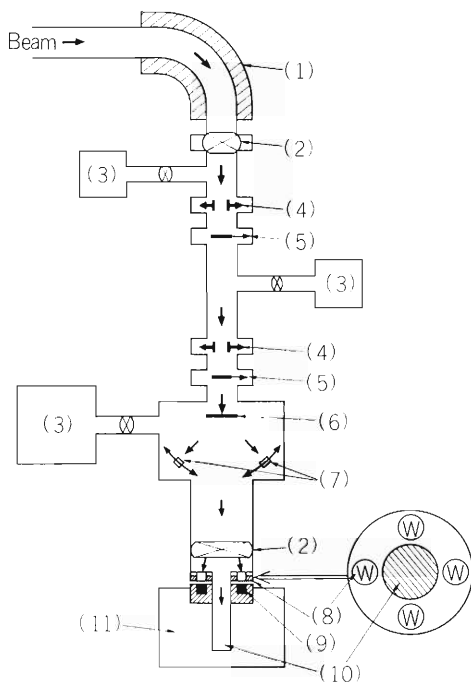


Fig. 1. Scheme of the apparatus for RILAC-beam irradiation of biological samples. (1) Bending magnet, (2) Beam shutter, (3) Turbo molecular pump, (4) Slit box, (5) Beam stopper, (6) Scattering foil, (7) Solid state detector, (8) Vacuum window, (9) Sample holder, (10) Faraday cup, (11) Thermostat.

Reference

- 1) F. Yatagai and A. Matsuyama: IPCR Cyclotron Progr. Rep., 13, 118 (1979).

10-17. Beam-Foil Spectroscopy

K. Ando and K. Mori

Radiative transition probability is one of the most important atomic parameters. A unique experimental method of deriving the transition probability is to measure the radiative mean lives of the upper excited electronic states of the emission multiplets produced in the “beam-foil” source. Recent interest on beam-foil spectroscopy is in the study of highly ionized heavy ions. The foil excitation technique can be used efficiently on heavy ion beams accelerated by linear accelerators. In case of the IPCR heavy ion linear accelerator, multiply-ionized heavy ions are expected for use on beam-foil spectroscopy. On the other hand, atomic wavefunctions can now be calculated with sufficient accuracy to enable theoretical computations of radiative transition probabilities to be made. The theoretical estimates are based mainly on either self-consistent field (SCF) calculations, including configuration interaction (CI) if necessary, or Coulomb approximation. Computational techniques are recently in so highly advanced stage that the complicated calculations for SCF plus CI are practicable. Therefore, the sophisticated calculations, such as multi-configuration relativistic Hartree-Fock (MCRHF) SCF, including Lamb shift, give us the *ab initio* theoretical oscillator strengths and transition probabilities for heavy ions. Several convenient computational codes are now available.¹⁾ Therefore, it is important to obtain accurate experimental data of transition probabilities in order to compare with the theoretical ones deduced from the advanced wavefunctions.

Preparation for beam-foil experiments on highly ionized ions from the heavy ion linear accelerator at IPCR has been almost completed. The experiment of beam-foil spectroscopy is

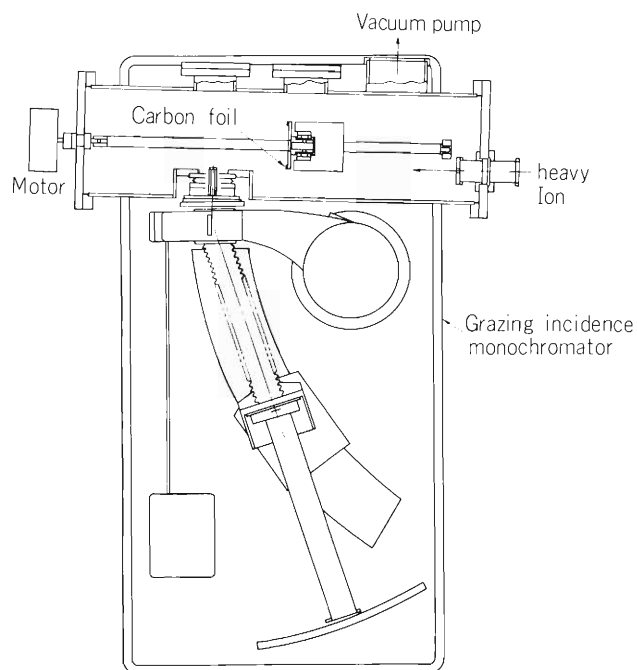


Fig. 1. Schematic drawing of beam foil experiment.

to be performed as illustrated in a schematic drawing of Fig. 1. The accelerated ion beams transmit through a carbon foil, being further stripped and excited. Spectral emission of the excited ion decays along the travelling path. Decay time of the emission, thus life time of the excited state, can be measured through the displacement distance from the foil. In the present case, the relative distance between the foil and the monochromator entrance slit, which observes the emitting ion, is changed by moving the foil continuously upstream from the slit. The maximum movable distance is 500 mm, and the accuracy of determination of the foil position is within $\pm 25 \mu\text{m}$. The target chamber accommodating the above mechanism is evacuated by a turbomolecular pump of 500 ℓ/sec . Spectra from the emitting ions are observed by a 2-m NIKON McPHERSON (Model 247) grazing incidence monochromator. Highly ionized high Z ions have so large transition probabilities for the resonance transition that the lifetimes of the resonance upper states are too short to be observable by the usual experimental setup. We attempted to redesign the entrance slit assembly of the monochromator in order to observe the ion beam as close as possible. Thus, the distance between the entrance slit and the ion beam become about 5 mm, which corresponds to the space resolution along the beam of 0.06 mm, enabling the lifetime even smaller than 0.1 nsec to be measured.

Reference

- 1) For example, G.E. Bromage: Report AL-R-3 Appleton Laboratory, England (1978).

10-18. Multichannel Detection in Normal-Incidence Vacuum Ultraviolet Region

M. Hara and K. Mori

Recently a microchannel plate (MCP) is used as a position sensitive detector array for one or two dimensional image dissection.¹⁾ A multichannel detector system with microchannel plates has been constructed and used for polychromatic observation of vuv emission spectra of laboratory plasmas by single photon counting method. As is shown in Fig. 1, a set of cascaded microchannel plates is used as one dimensional detector array. Photoelectrons produced by an incident photon at the surface of MCP are multiplied, and the multiplied pulse charges are collected by multiwire anode. Each wire is connected with the neighbors by resistances (510Ω) and both end wires are fed to charge sensitive pre-amplifiers. The charges arriving at the particular wire of the collector are divided by the resistance network into two charges q_a and q_b which are inversely proportional to the resistances. One can determine the position of the incident photon by the simple calculation $q_a/(q_a + q_b)$ and the data are stored in PHA. We get better spatial resolution than the interval between wires by this charge division method in which the center of gravity of charges is calculated.²⁾ The MCP used in this work is that of Hamamatsu TV F1158-13 type whose channel diameter and channel pitch are 20.0 and $24.5 \mu\text{m}$, respectively.

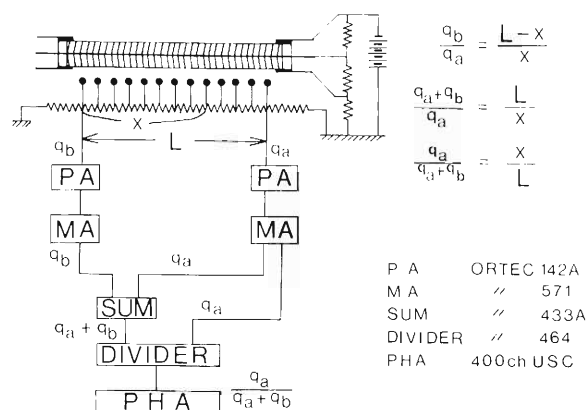


Fig. 1. Schematic diagram of position analyzer electronics.

This was operated at 0.94 kV for the first MCP and 1.17 kV for the second one to reduce noise pulses keeping high gain. Multiwire anode is made of $60 - 75$ parallel $40 \mu\text{m}\phi$ stainless steel wires fixed to the epoxy-glass frame with epoxy resin using a winding machine which consists of revolving cylinder and feeding screw. The anode is 10 mm in length and 9 mm in width with $150 \mu\text{m}$ interval or $12 - 15 \text{ mm}$ in width with $200 \mu\text{m}$ interval. Linearity and resolution of this system were checked by feeding the noise pulses of ordinary secondary electron multiplier tube to each wire. Spatial resolutions of $70 - 80 \mu\text{m}$ ($200 \mu\text{m}$ interval anode) and $50 - 60 \mu\text{m}$ ($150 \mu\text{m}$ interval anode) were obtained.

For this application, this detector system is set at the focal plane of normal incidence spectrometer, as is shown in Fig. 2. This spectrometer has a grating of $1200 \ell/\text{mm}$ and a

reciprocal dispersion of 5.5 \AA/mm which is almost independent of wavelength. Each channel of MCP has such a long dead time (some tens of msec) that a light source is set at a distance 30 cm apart from the entrance slit of the spectrometer in order to decrease the flux density at the surface of MCP. As the light source we used an ordinary glow discharge tube made of quartz capillary. Pressure in the light source can be varied from 0.01 to 0.2 Torr. Voltage and current of the discharge are 500 – 600 V (depending on gases and pressure) and 200 mA (stabilized), respectively. Neon doublet at 735.9 \AA and 743.7 \AA , argon resonance doublet at 1048.2 \AA and 1066.7 \AA , and hydrogen Lyman α at 1015.7 \AA were detected with good S/N ratio. The spectra obtained showed the FWHM of 0.5 \AA (wavelength) or $90 \mu\text{m}$ (spatial resolution) in case of $200 \mu\text{m}$ interval anode and 0.33 \AA or $60 \mu\text{m}$ in case of $150 \mu\text{m}$ interval anode. We get better wavelength resolution and S/N ratio by measuring vuv emission at higher spectral orders, because the dispersion becomes larger and MCP itself has little sensitivity in visible region. We measured the profile of the HeI 584.3 \AA resonance line at the 5th order by varying the source pressure. Typical spectra obtained with $150 \mu\text{m}$ interval anode are illustrated in Fig. 3. The lower

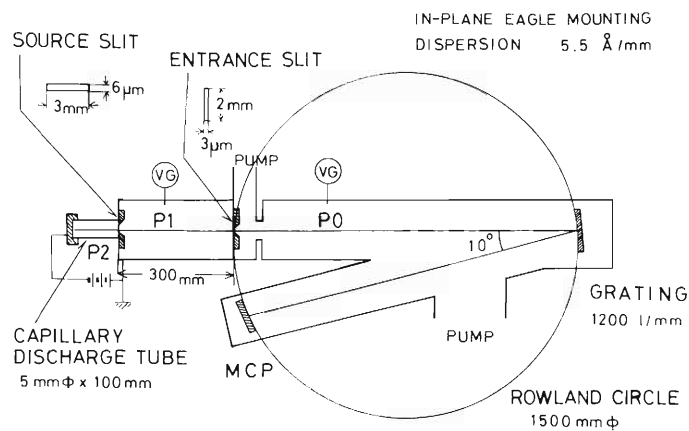


Fig. 2. Schematic views of normal incidence spectrometer.

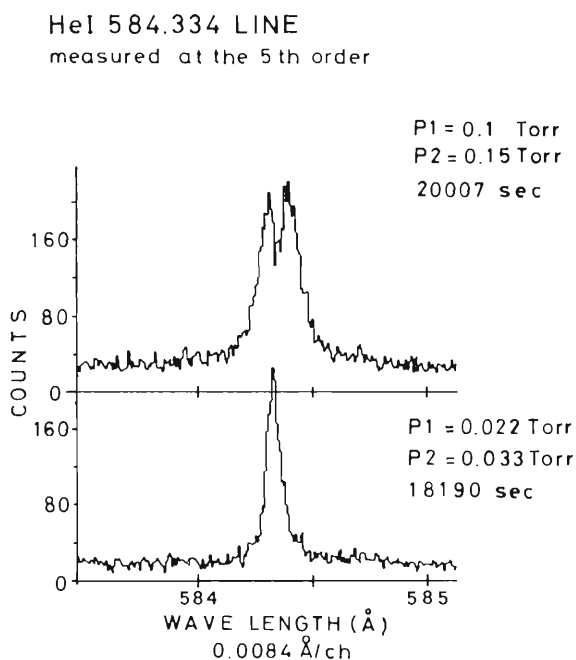


Fig. 3. Typical spectra of HeI 584.334 \AA line obtained with this detector system.

spectrum measured at lower pressure showed FWHM of 0.066 \AA (wave-length) or 60 \mu m . On the other hand, the upper spectrum clearly shows spectral broadening and dip. The dip of this spectrum is due to the resonance absorption through the path between the light source slit and the entrance slit. Taking account of the plasma parameters of this glow discharge, natural broadening and pressure broadening (Stark and resonance broadening) can be neglected compared with Doppler broadening. Even if the resonance absorption and detector width are taken into account, the broadening of the upper spectrum cannot be explained without recognizing that the neutral helium at the excited states has Doppler temperature of several electron volts.

References

- 1) J. G. Timothy and R. L. Bybee: *Appl. Opt.*, 14, 1632 (1975); G. Knapp: *Rev. Sci. Instrum.*, 49, 982 (1978).
- 2) R. Gott, W. Parkes, and K. A. Pounds: *IEEE Trans. Nucl. Sci.*, NS-17, 367 (1970).

10-19. Spherical Target Chamber for Heavy-Ion Implantation

M. Iwaki and F. Ambe

A versatile target chamber for implantation and other irradiation experiments has been designed, constructed and installed at the end of beam line C of the heavy-ion linac, as shown in Fig. 1.

The main part of the chamber is a spherical SUS304 vessel with an inner diameter of 315 mm and is equipped with ports for incident beam, target drive mechanism, target setting, vacuum pump, and so on.

The beam from the linac is introduced into the chamber through two pairs of slit plates, which can be independently moved in the horizontal and vertical directions by remote control. Each plate is connected to a BNC standard connector for monitoring the ion beam current. Between the slits and the chamber is a beam shutter which can be also operated from the control room.

The target holder can be moved in the vertical direction (± 20 mm max.) and rotated around the vertical axis ($\pm 45^\circ$ max.) by servo and pulse motor drives respectively. During irradiation the movements can be repeated at a speed selectable within a definite range. Combination of the two kinds of movements can be also selected. The drive mechanism is used to position the

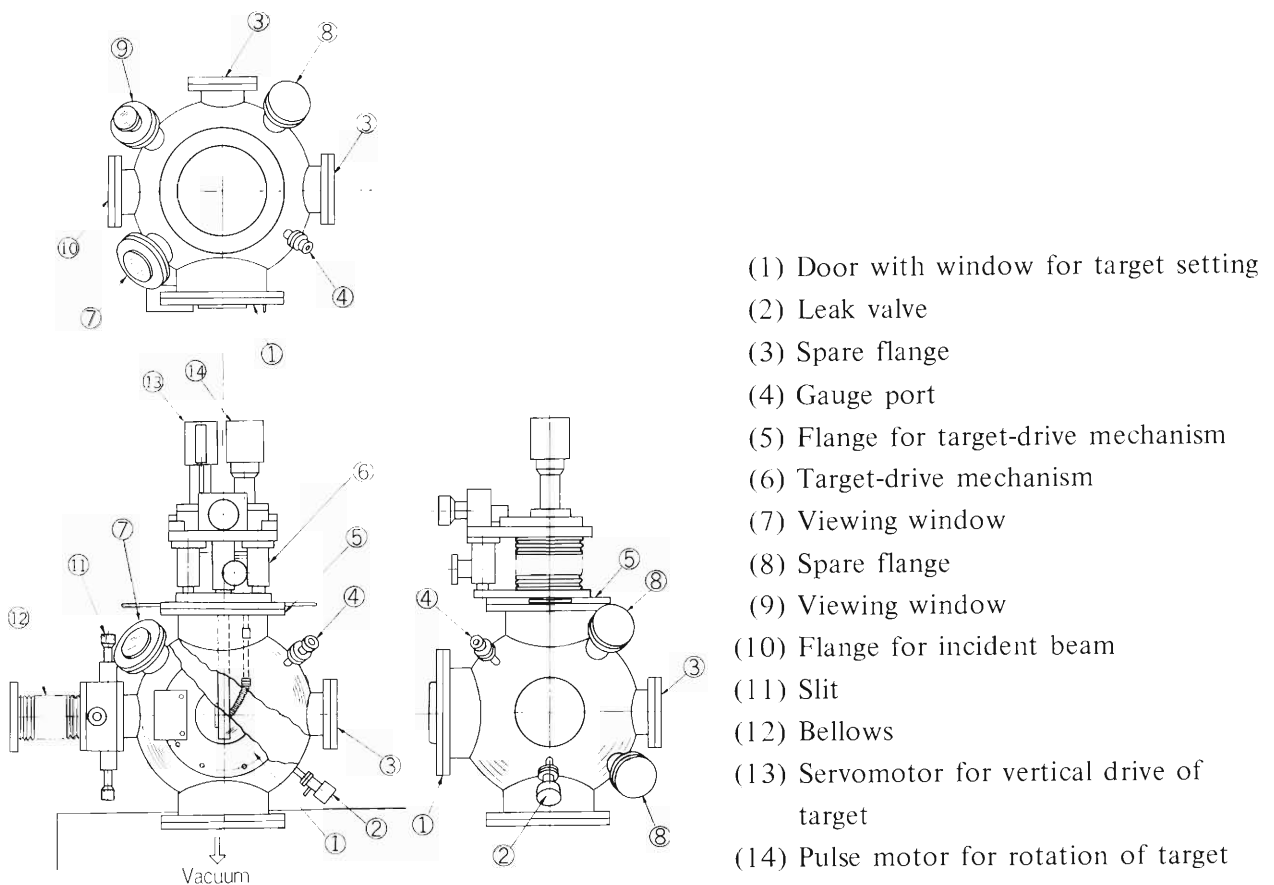


Fig. 1. Sketches of the chamber.

target, to disperse the heat generated in the target by irradiation, or to ensure uniformity of the ion beam across the substrate area. The target holder can be cooled with water or liquid nitrogen, which is introduced into the holder through a pair of mini-bellows. The holder is insulated from the chamber in order to indicate the beam current on the remote panel.

The evacuating system consists of a 250 ℓ/s turbo-molecular pump and a 244 ℓ/min rotary pump. All the vacuum valves are driven by compressed air. The whole system is protected from accidents due to a mistake in operation. Throughout the system Viton O-rings and metal sheets are used as seals.

The chamber is to be utilized in heavy-ion implantation of materials such as steel and semiconductors and also in a wide variety of irradiation experiments.

10-20. On-line Data Processing System at RILAC

H. Kumagai and T. Wada

PERKIN ELMER model 3220 super mini-computer system has been introduced for on-line data taking and data processing.

In March 1980, the initial system was installed in a counting room at RILAC. It includes P-E 3220 central processor with bootstrap loader, memory error logger, floating point processor and 512k byte ECC MOS memory, a 9-track magnetic tape unit of 1600 BPI, an 80M byte cartridge disk, two cassette magnetic tape units, two CRT terminals, a DEC writer, a line printer, a digital plotter, and a CAMAC crate.

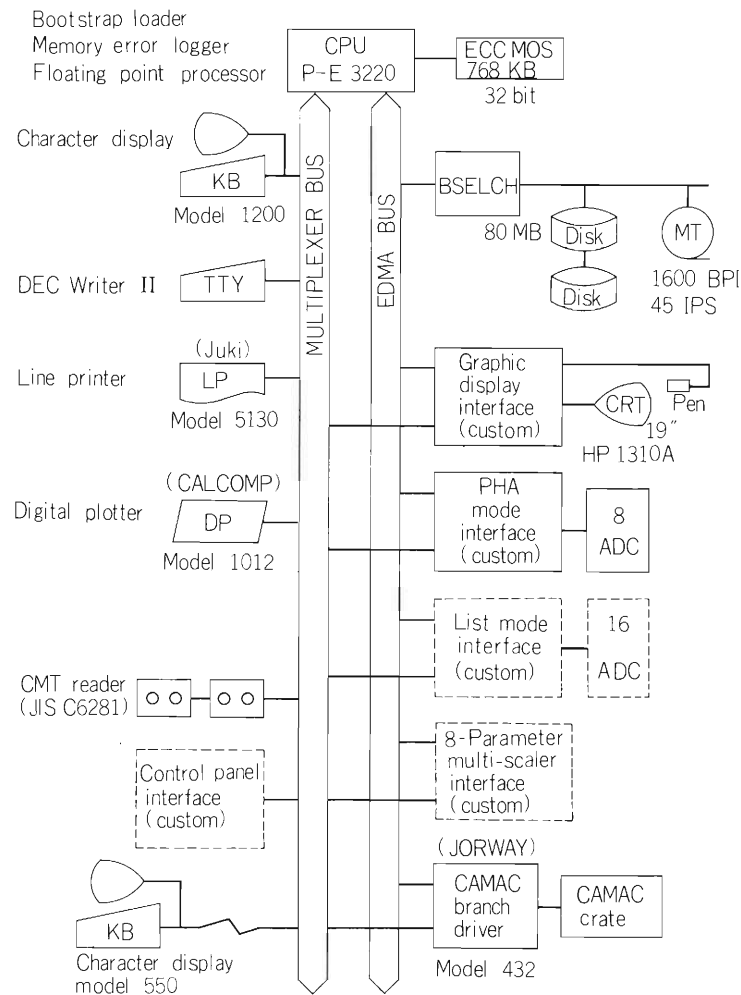


Fig. 1. Configuration of data processing system. The interfaces enclosed by dashed lines will be installed in April of 1981. The abbreviations are, ECC for error check and correction, DRAM for dynamic random access memory and EDMA for extended direct memory access unit.

Additional 256k byte memory, an 80M byte cartridge disk, a graphic display interface, a 19 inch CRT, a PHA mode interface and eight NIM-ADCs were installed in September 1980.

The present configuration of the system is shown in Fig. 1.

The specification of P-E 3220 computer are as follows:

Processor		
General registers	8 sets of 16, 32 bit g.r.	
Floating point registers	8 sets of 32 bit f.p.r.	
	8 sets of 64 bit f.p.r.	
User instruction	200 (48 floating point)	
Execution time (Reg. to Reg.)		
	Add	0.45 μ s
	Multiply	7.85 μ s
	Add (f.p. 64 bit)	1.25 μ s
	Multiply (f.p. 64 bit)	1.85 μ s
	Divide (f.p. 64 bit)	7.05 μ s
Addressing	Direct to 4M byte	
	Relative to ± 16 k byte	
Arithmetic	2's complement	
Main Memory		
Type	16k byte DRAM (TMS 4116-15)	
Word Length	32 bit + ECC (7 bit)	
Size	Up to 4M byte	
Access time	500ns	
	340ns effective with cache	
I/O		
Devices	1023	
Priority	4 interrupt levels	
EDMA	7 ports, 8M byte/sec	
Operating System		
	OS/32	
Languages		
	CAL (common assembly language)	
	CAL MACRO	
	FORTRAN-7	
	COBOL	
	BASIC-2	

The abbreviations are, ECC for error check and correction, DRAM for dynamic random access memory and EDMA for extended direct memory access unit.

The specifications of custom made interface are as follows:

For the increment (PHA) mode interface:

- (1) maximum 8 ADC's with 13 bits are connected;
- (2) the data from ADC's are stored in FILO (first in last out) memory of 64 words;

- (3) the contents of main memory corresponding to the data of FIFO are read, modified and stored through DMA channel;
- (4) a X-tal oscillator (1 MHz) is prepared to measure true time or live time of each ADC;

For graphic display interface:

- (1) a buffer memory of 60k bytes is included;
- (2) 16 sets of register are prepared to store the DMA commands;
- (3) the display modes are X-Y and T-Y;
- (4) the change of Y scale including a logarithmic scale is performed by hardware;
- (5) maximum 4 spectra can be overlaped and shifted independently in Y direction;
- (6) the display areas in the main memory are selected by 37 toggle switches;
- (7) the position of each marker is determined by thumb switches or a light pen.

The CAMAC system is prepared for the control of other experimental devices.

10-21. Beam Sharing System between Linac and Separated-Sector Cyclotron

M. Sasagase

The possibility of placing a beam sharing system between the linac and the separated-sector cyclotron (SSC) was examined. This beam sharing system should be set up between the 6th tank and the switching magnet of the linac. Within the variety and the energy regions of ions accelerated by the linac, the beam sharing should be possible and furthermore the beam transport system must be achromatic especially for the injection to the SSC. The analysis of the beam transport optics showed that such a beam sharing system satisfying these requirements is feasible.

The calculation of the beam transport optics was carried out within the first-order formulation using the program TRANSPORT¹⁾ in the cases of $^{238}\text{U}^{10+}$ (200 MeV) and $^{20}\text{Ne}^{4+}$ (80 MeV) beams. Hereafter, the incident beam is assumed to be U^{10+} ions.

The arrangement of the beam sharing system is shown in Fig. 1. U^{10+} ions accelerated by the linac are partially stripped of their electrons by a stripper foil at S_0 . Unstripped U^{10+} ions are guided to the switching magnet (SW) through bending magnets BM1, BM2, and BM3. U^{40+} ions are selected by a slit at S_2 to be guided to the SSC. Parameters of each element are listed in Table 1.

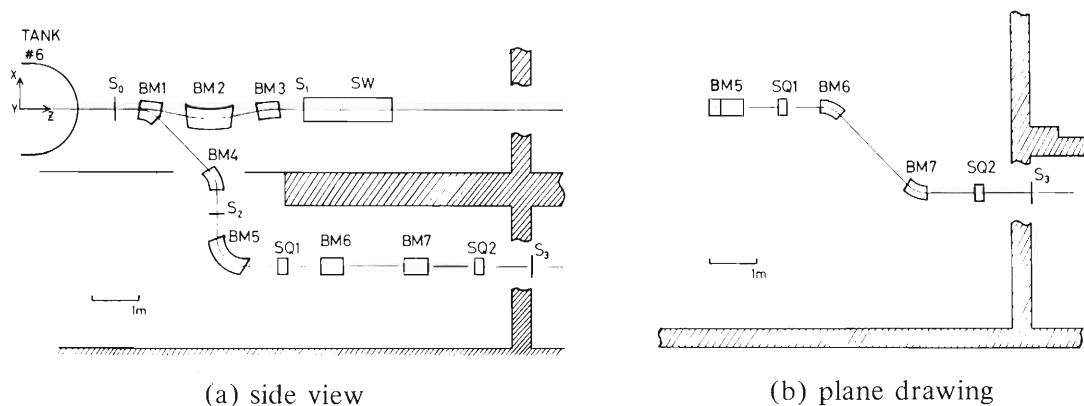


Fig. 1. Arrangement of the beam sharing system.

The feature of the initial beam at S_0 is assumed as follows: (1) the half-width of the envelope is 5 mm and the angular divergence is 5 mrad both horizontally and vertically, and (2) the half-width of the momentum spread is 0.075 %. Achromatic transport from S_0 to S_3 is possible. The beam envelopes are exhibited in Fig. 2. The trajectories of U^{40+} ions are well separated from those of U^{39+} ions, as shown in Fig. 3. In the calculation of optics, care was taken so that the half-width of the beam envelope does not exceed 2 cm. However, for the transport of U^{10+} ions to the SW, the half-width of the beam envelope somewhat exceeds this limitation at the exit of the SW. A more parallel incident beam, for example, a beam with the half-width of the envelope of 8 mm and its divergence of 3 mrad, is desirable to avoid this difficulty.

Table 1. Characteristics of transport elements.

Bending magnets

Element	Angle of bend (deg)	Radius (cm)	Magnetic field (kG)	$\beta_1^a)$	$\beta_2^b)$
BM1	45 (11.5 ^{c)})	60 (240 ^{c)})	13.09 ^{d)}	8.2	0.3(0 ^{c)})
BM2	23 ^{c)}	240 ^{c)}	13.09 ^{d)}	14.8	14.8
BM3	11.5 ^{c)}	240 ^{c)}	13.09 ^{d)}	0	8.2
BM4	45	60	13.09 ^{d)}	9.8	0
BM5	90	60	13.09 ^{d)}	10.6	29.0
BM6	45	60	13.09 ^{d)}	0	0
BM7	45	60	13.09 ^{d)}	31.4	-11.5

Singlet quadrupole magnets

Element	Length (cm)	Radius (cm)	Magnetic field (kG)
SQ1	20	3.81	2.33 ^{e)}
SQ2	20	3.81	0.74 ^{e)}

- a) angle of pole-face rotation at the entrance
- b) angle of pole-face rotation at the exit
- c) in the case of $^{238}\text{U}^{10+}$ (200 MeV)
- d) in the case of $^{238}\text{U}^{40(10)+}$ (200 MeV)
- e) in the case of $^{238}\text{U}^{40+}$ (200 MeV)

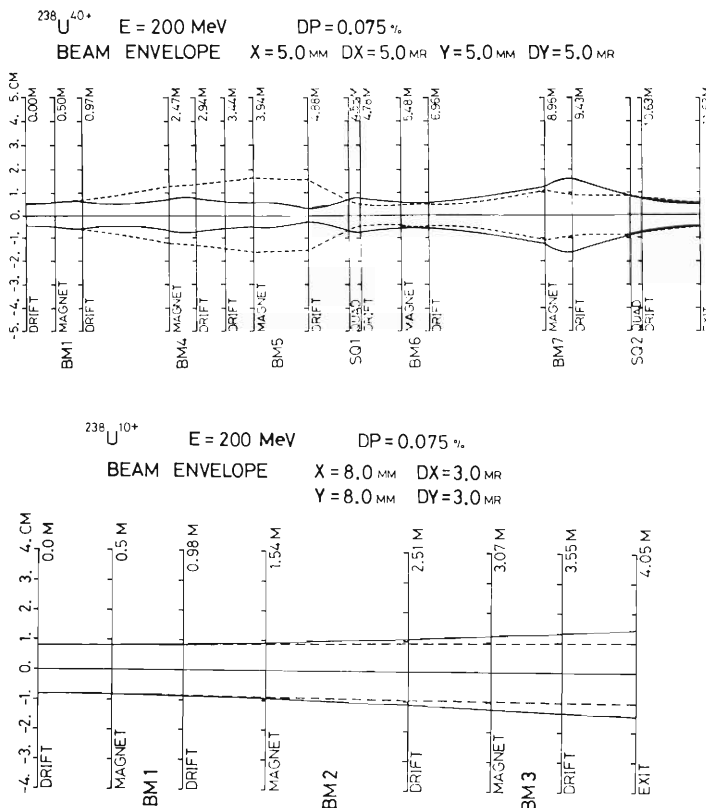


Fig. 2. Beam envelopes in the vertical (x) plane (solid lines) and the horizontal (y) plane (dashed lines).

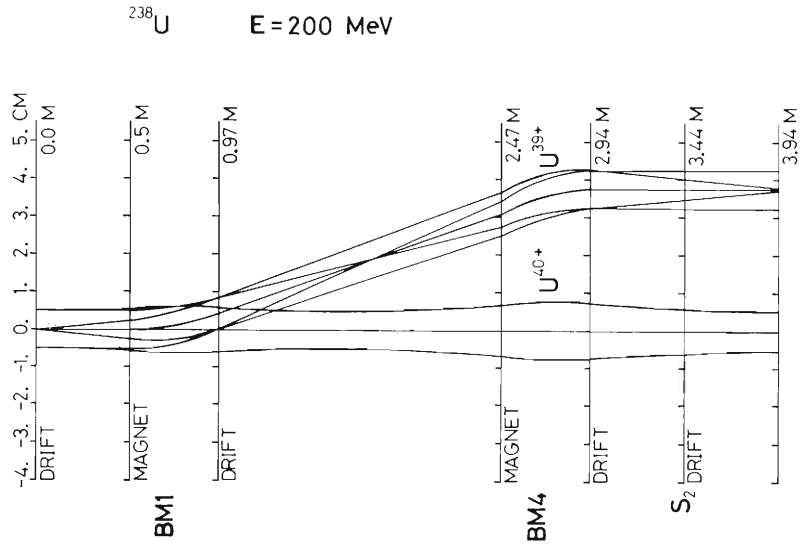


Fig. 3. Single rays for $^{238}\text{U}^{39+}$ and $^{238}\text{U}^{40+}$ ions at the charge selection part.

When Ne^{4+} ions are used as the incident beam, Ne^{4+} and Ne^{10+} ions are guided to the SW and the SSC, respectively. The central trajectory of Ne^{4+} ions differs from that of U^{10+} ions. So the magnetic field of the BM2 must be adjusted to return the trajectory to the initial beam axis.

Reference

- 1) K. L. Brown, F. Rothacker, D. C. Carey, and Ch. Iselin: SLAC-91 (1974).

11. SEPARATED-SECTOR CYCLOTRON PROJECT

11-1. Status of the Separated-Sector Cyclotron in IPCR (Riken)

H. Kamitsubo

Construction of an accelerator complex composed of a separated-sector cyclotron (SSC) and two injectors was proposed in 1972 to extend the studies in various research fields by energetic ion beams in IPCR. The first part of this proposal was accepted in 1974 and the variable-frequency heavy-ion linac (Rilac) was installed in 1980. The second part of the proposal has been funded this year. The final design works are now in progress.

Construction of the big accelerator complex is a major part of the IPCR Accelerator Science Project which aims to develop the accelerator-assisted studies in the various research fields such as nuclear and atomic physics, solid state physics, nuclear and radiation chemistry and radiation biology. Accordingly the SSC as well as the Rilac should be able to accelerate not only light ions but also heavy ions in the energy range as wide as possible. The SSC is also required to provide a beam of good quality and of enough intensity.

The design goal of the SSC was thus fixed to achieve the maximum beam energies of 130 MeV/u for fully stripped light heavy-ions and 14 MeV/u for very heavy ions such as uranium. Those for other kinds of ions will lie in the range between these two values. We expect that protons will be accelerated up to 200 MeV. Energy variability should be realized down to 10 MeV/u for most kinds of ions. High resolution beams of protons, deuterons and α particles will be required for the study of nuclear physics and therefore the beam quality has to be as high as possible.

Table 1 Examples of some operating parameters at maximum energies in the proposed accelerator complex.

LINAC						SSC							
Beam	Charge (q_1)	m/q_1	Accelerating RF freq. (MHz)	RF voltage (MV)	Energy per nucleon (MeV/u)	Charge (q_2)	m/q_2	B_{inj} (Wb/m ²)	B_{max} (Wb/m ²)	Orbit freq. (MHz)	Accelerating RF freq. (MHz)	h number	Energy per nucleon (MeV/u)
⁴⁰ Ar	8+	5	44	20	3.8	15+	2.7	1.45	1.55	4.8	43.3	9	66.6
⁸⁴ Kr	9+	9	33	20	2.2	24+	3.5	1.45	1.5	3.67	33	9	36.8
¹³² Xe	9+	15	26	20	1.36	30+	4.4	1.43	1.46	2.88	26	9	22.3
²³⁸ U	10+	24	20.4	20.4	0.84	37+	6.4	1.55	1.57	2.14	19.4	9	12.1
						40+	5.9	1.52	1.54	2.27	20.4	9	13.6

Cyclotron ($\bar{R}_{ext} = 0.893$ m)

Beam	Charge	Orbit freq. (MHz)	RF freq. (MHz)	B_{ext} (Wb/m ²)	Energy per nucleon (MeV/u)	Charge	m/q_2	B_{inj} (Wb/m ²)	B_{max} (Wb/m ²)	Orbit freq. (MHz)	Accelerating RF freq. (MHz)	h number	Energy per nucleon (MeV/u)
P	1+	7.37	22.1	0.485	9	1+	1	0.838	0.994	7.37	44.2(29.5)	6(4)	184
³ He	2+	7.37	22.1	0.727	9	2+	1.5	1.26	1.49	7.37	44.2(29.5)	6(4)	184
¹² C	4+	6.51	19.6	1.28	7	6+	2	1.48	1.67	6.5	39.1(26.0)	6(4)	134.6

The accelerator complex consists of the SSC and two injectors, one being the Rilac and the other a cyclotron of $k = 90$. Examples of operating parameters at the maximum energies for several kinds of ions are listed in Table 1. The beam from the Rilac will be injected into the SSC after it passes through a charge stripping foil. Matching condition of the resonance structure of the beam between the Rilac and the SSC gives a limitation on the RF system of the SSC: width of the accelerating electrode (Δ) at the injection radius should be equal to the length of the last drift tube of the Rilac and also the RF frequency should be exactly the same for both accelerators.

The Rilac accelerates ions in the fundamental mode, that is, with a harmonic number of 1 over the frequency range of 17 – 45 MHz. The harmonic number, h , of the SSC was determined to be 9 from the matching condition with the Rilac and the maximum field strength of the sector magnets. The injection radius is 0.89 m in this case. The above value of h is different from that reported previously. This is because we decided to reduce the maximum field strength of the sectors from energy saving point of view. The maximum value of B_{inj} was reduced from 1.7 to 1.55 T and the injection radius was increased from 0.79 to 0.89 m.

The matching condition between the SSC and the injector cyclotron has to be taken into account, too. The simplest combination of the parameters is that the extraction radius of the injector is equal to the mean injection radius of the SSC and the ratio of the harmonic numbers is an integer. Since the injection cyclotron will be operated in the orbit frequency range of 2.7 – 7.5 MHz, $h = 3$ and 6 are favourable values for the injector and the SSC, respectively.

The beam from the Rilac should be transported by about 60 m to the SSC. The beam transport system is designed to bring the beams without any loss and also to match the beam quality to the acceptance of the SSC. Two RF bunchers will be installed to get the phase focus at the injection point of the SSC.

In the early stage of the design work, a horizontal injection was extensively studied. It became clear that stray field of the sector magnets is not so small that the injection orbit varies considerably depending on the ions and their energies. In that case a quadrupole doublet and steering magnets of large aperture will be necessary to inject all kinds of ions correctly. New methods of the injection were, therefore, looked for and finally a canted injection was adopted.

The SSC has four sectors of 50° with straight edges. The sector magnet and 30 trim coils yield the required isochronous field of 1.67 T at maximum. The focusing properties have been extensively calculated with computer codes developed by N. Nakanishi and by A. Goto, independently, by using measured field distribution for a pair of a quarter scale model magnets.

Ions are accelerated by 20° delta-shaped electrodes located at the opposite valley spaces between the sectors. The RF frequency range of the RF system is chosen to be 17 – 45 MHz as mentioned above. RF electric field distribution and quality factors were measured for a half scale model cavity. The effective accelerating voltage for the cyclotron injected beam will be $2/3$ of that for the Rilac injected beam.

The beams from the injectors are brought slantingly into the SSC through the valley and bent by 45° onto the median plane in the central region. Then they are inflected by 100° with a bending magnet and enter the magnetic inflection channel between two pole tips of the first sector magnet. The second magnetic channel and an electrostatic inflector bring the beams onto the first equilibrium orbit.

Detailed design studies of the vacuum chamber, RF resonators and other components are now in progress. Recently the sector magnets were ordered to Sumitomo Heavy Industry Co.

11-2. Design of the Sector Magnet for the SSC

S. Motonaga, H. Takebe, T. Wada,
Y. Obana, J. Fujita, and Y. Ikegami

The separated-sector cyclotron (SSC) projected at IPCR has been designed as a post accelerator for the variable-frequency heavy-ion linac and the conventional AVF cyclotron. The main characteristics of this SSC are described in this report by H. Kamitsubo. A number of possible technical realizations were considered, one of these being operation with the harmonic number of 9 in place of 8 in order to reduce the maximum field of the magnet and to obtain wide space in the central region of the SSC. The maximum magnetic field was reduced from 17.5 to 15.5 kG and the injection radius was increased from 79 to 89 cm. The geometrical size and the major design parameters of the sector magnet had been fixed. Remaining problem for the final design of the magnet is mechanical design of the trim coil system and the design of the vacuum chamber connecting the magnet chamber and RF resonating chamber in narrow central space of the SSC.

General

The profiles of the magnetic field should provide the isochronism, focusing and orbital stability for the beam in a wide range of energy and particles. In order to get desired field profile in the range of 7 to 15.5 kG, measurements of the magnetic field have been carried out using a 1/4 scale model of the sector magnet. The final parameters of the sector magnets were determined from the results of the analysis of the magnetic properties and computation of beam dynamics based on the above measurements. Table 1 lists the design parameters of the sector magnets. The main magnet system of the SSC consists of four sector magnets with sector angle of 50° , gap distance of 8 cm and maximum magnetic field of 15.5 kG. The maximum magnetomotive force was estimated to be 1.35×10^5 ampere turns for the maximum field of 15.5 kG. The maximum power consumption of the main coils is estimated to be 520 kW. Each sector magnet is about 5.7 m long and its weight is 540 tons. The shape and geometrical size of the sector magnet is shown in Fig. 1.

Poles and yokes

The pole tip contour and pole edge profiles are shown in Fig. 2. The pole edge profile except the inner part is approximated by a B-constant profile so that the effective angle of the sector magnet does not change in the range of magnetic field to be used. This was confirmed by the analysis of the magnetic field computed by TRIM

Table 1. Design parameters of SSC magnets.

Number of Sector Magnet	4
Sector angle	50°
Gap width	8 cm
Injection mean radius	89.3 cm
Extraction mean radius	356 cm
Height of magnet	5.63 m
Overall diameter	12.8 m
Total weight	2160 ton
(540 ton/one sector magnet)	
Maximum magnetic field (excitation)	15.5 kG
Maximum ampere turns	1.35×10^5 A.T
Maximum current	1160 A
Current stability	0.002 %
Maximum power	520 kW
Number of trim coils	30 pairs \times 4
Maximum current	500 A
Total trim coil power	280 kW

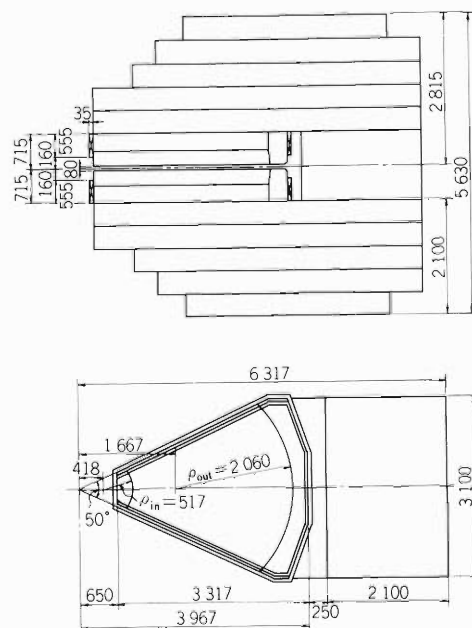


Fig. 1. Geometrical lay-out of the sector magnet.

code and the measured field of the model magnet. The effective angle obtained from model measurements agrees with the designed value of 50° within 1.0° . However, this profile can not be used at inner edges of the pole pieces as shown in Fig. 2, because the usable range of the magnetic field in the radial direction will be reduced by the B-constant profile. Radial dimension along the central line of the pole tip is 3317mm. In the radial direction the pole tips extend 3.5 gaps toward the center from the first equilibrium orbit and 3.0 gaps outward beyond the extraction equilibrium orbit. The gap spacers and the components necessary for the injection and extraction will be inserted in these extended areas.

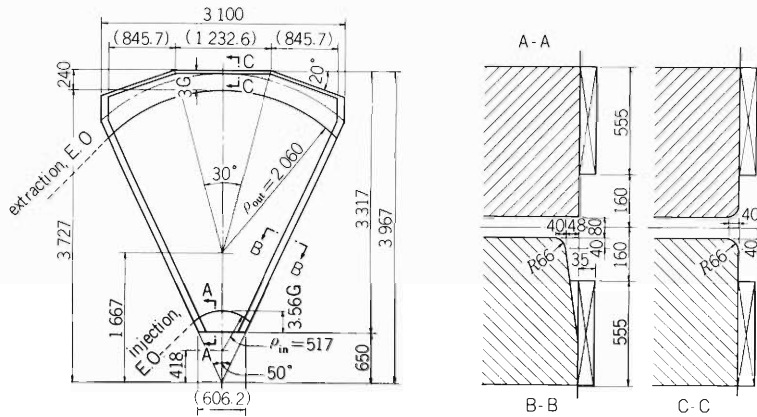


Fig. 2. Pole tip contour of the sector magnet.

The upper and lower yokes will be divided into four or five slabs for convenience of the construction and transportation. Cross-sectional area of each Yoke is equal to that of the pole base. The maximum field and the field profile of the sector magnet strongly depend on the iron material. Very homogeneously forged steel with carbon content of 0.02 – 0.01% were specified for the pole and rolled steel of 0.08 – 0.1 % carbon content for the yoke of each magnet. Two poles of each sector magnet should be prepared from a single ingot. Table 2 shows specification of the steel. The specified mechanical tolerances of the alignment for the construction are 0.1 mm and 0.05 mm for coaxial and parallel alignment, respectively, of the poles without magnetic field.

Table 2. Specified chemical composition of the low carbon steel (weight percent).

	C	Si	Mn	P	S	Cr	Ni	Cu	Al	Mo	N
Pole	0.02	0.07	0.2	0.05	0.017	0.08	0.10	0.11	0.03	0.04	0.006
Yoke	0.08	0.25	0.35	0.013	0.012	0.08	0.10	0.11	0.04	0.05	0.007

Main coils

The design of the main coils has been almost completed. Final design, however, may be changed slightly according to the result of the design of the vacuum chamber. They will be formed in size of 3.5 cm in thickness and 55 cm in height to provide enough space for the RF-cavities which will be installed in the narrow space between two sector magnets. The main coils of each sector magnet will be connected in series and excited with maximum current of 1160 A. Maximum current density of copper conductor is 4.5 A/mm^2 .

Deformations

The deformation of the magnet structure as a result of various forces acting on it was computed by FEM-2 code developed by M. Hara. The computed deformation is shown in Fig. 3 and Fig. 4. The maximum displacement relative to the foundation is 0.11 mm vertically and 0.05 mm horizontally. The maximum value for the spacer compression is 0.08 mm for the front one and is 0.05 mm for the rear one. Such difference between the values of the spacer compression will introduce some change in the arrangement of pole pieces. The maximum value of the difference due to the spacer compression is 0.04 mm for parallel alignment and is less than 0.05 mm for defect of the median plane, but such differences entail no problem on the beam dynamics. For the above mechanical analysis the magnet was treated as a solid structure, notwithstanding the magnet consist of 12 separate parts. This treatment is justified for high excitations when different sections of the separate parts are

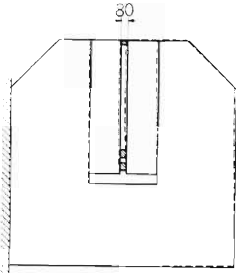


Fig. 3. Computed deformation of the sector magnets under maximum load conditions. The vertical scale is expanded by a factor of 400.

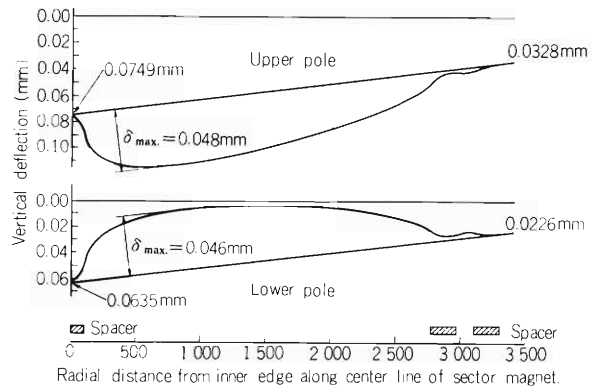


Fig. 4. Computed vertical deflection of the pole faces and the median plane along the center line of the sector magnet. (HARA's FEM-2)

held together by strong magnetic forces between their interfaces. More detailed computations for the mechanical deformation and beam dynamics are now in progress.

Trim coils

For the design of the trim coils extensive calculation by TRIM code were performed. Then a quarter size model was made and field profile has been measured iteratively. Measurements using this model were carried out to obtain the strength and radial profiles of the induced field by trim coils with different coil widths and intervals. In order to obtain the coil configuration and required current of the coils, computer optimization with combination of the above data were tried to form isochronous field. The result obtained was that the maximum deviation from the isochronous field can be made as small as 0.06 %. The resultant phase defect was estimated to be less than one degree.

The trim coils of the SSC magnet consist of 20 pairs of copper plates for isochronous field and 10 pairs of hollow conductors for harmonic field. They have a curved shape for hard-edge pattern of the equilibrium orbit. A preliminary design and configuration of the trim coils is shown in Fig. 5 and required currents of the trim coils are also indicated for the case of $\gamma = 1.20$ (proton). Five power supplies are needed to achieve the isochronous field. Total power of the trim coils is estimated to be 280 kW.

Detailed design study of the trim coil system is now in progress.

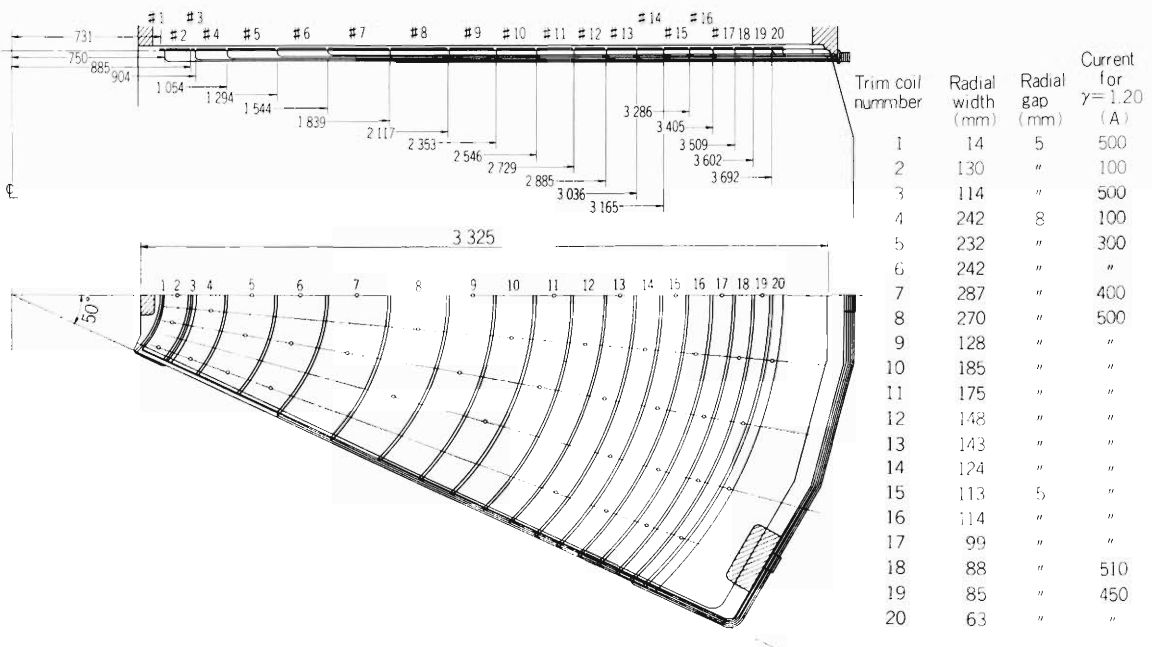


Fig. 5. Configuration of the trim coils for isochronous field, showing required currents for $\gamma = 1.20$.

11-3. Design Study of the Canted Injection Scheme for the IPCR SSC (I)

Y. Yano, A. Goto, T. Wada,
N. Nakanishi, and N. Kishida

We have made a full report on the design of the beam injection system for the IPCR SSC in Ref. 1, in which the beam is injected radially through one of the open valleys of the SSC. After some study on this system, we decided to modify the design as shown in Fig. 1. In the present design, the beams transported from the pre-accelerators are injected vertically down into the open valley and inflected onto the median plane by a couple of 45° bending magnets (BM3 and BM2). After this vertical inflection of 90° the beam is radially guided to the first acceleration orbit by means of a bending magnet (BM1), two magnetic inflection channels (MIC2 and MIC1) and an electrostatic inflection channel (EIC). The MICs are inserted between the poles of the sector magnets to add the necessary bending power to the sector field. The characteristics of these injection elements are listed in Table 1. We call the present system “the canted injection system”. Its advantage is that the beam focusing elements can be arranged down to the central region of the SSC. In radial case, no such elements are allowed to exist along the injection trajectory through the long valley region where beam is being accelerated. The circumstance that the beam line of the linac as the pre-accelerator is about 20 m higher than the median plane of the SSC is also one of primary factors for our decision.

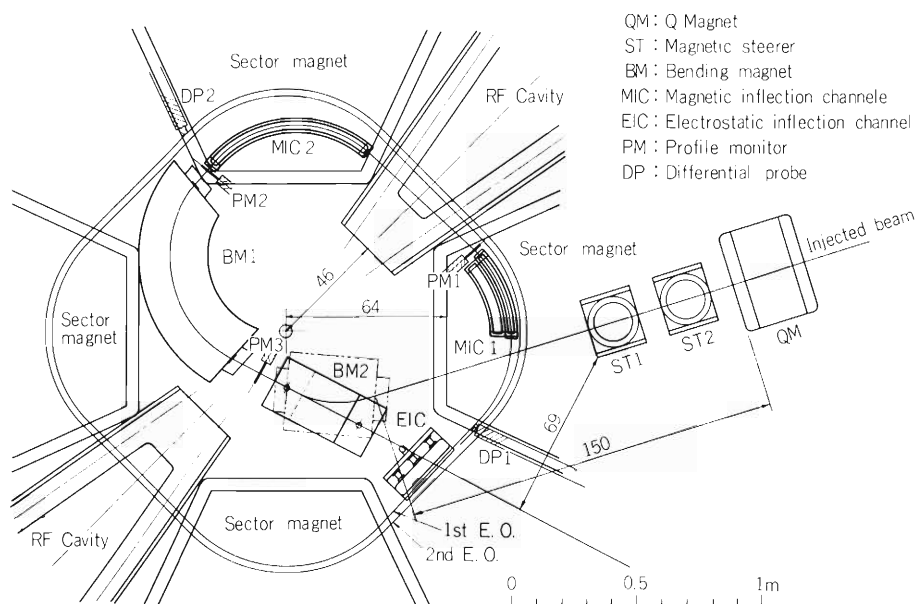


Fig. 1. Layout of injection elements in the central region of the SSC. The injection trajectory drawn through ST1, ST2, and QM is in the plane perpendicular to the median plane.

Table 1. Characteristics of injection elements.

Element	Bend angle	Aperture (cm)		Radius (cm)	Maximum field	Face angle (entrance)/(exit)
		(H)	(V)			
BM2	45°	10	4.2	46	17.1 kG	22.5/22.5
BM1	110°	4	4.2	46	17.1 kG	14/-13
MIC2	86.9°	3	4	43	(15.2)+3 kG	0/0
MIC1	37.2°	3	4	48	(15.2)+1.2 kG	0/0
EIC	3.6°	2	—	450	62 kV/cm	

Besides the principal role to guide the beam onto the first acceleration orbit, the injection system also must satisfy some conditions that are imposed upon the beam at the injection point. These functions are indispensable for one to get well-centered acceleration orbits for particles with wide range of mass and energy, and to extract the beam efficiently. What are to be adjusted for the beam are the position and direction, the dispersion in radial direction, and the beam ellipses in six dimensional phase space. The injection system should be so designed that this matching procedure can be done as easily as possible. The adjustment of the position and direction of the injected beam can be accomplished by the movable MICs and EIC whose location and direction are remotely controlled. Face angles of BM1 are determined so that the necessary radial dispersion of the beam may be obtained. For the easiness in matching the beam ellipses with the eigen-ellipses of the SSC, the properties of the injection elements in the beam optics are desired to be independent of the change of the bending field strength. The quadrupole magnet (QM) between the 45° bending magnets makes the achromatic transport of beam possible.

A 1/1-scale model of BM1 whose bending angle is 50° has been built. The map of the magnetic field produced by this model was obtained. The experimental results for this model test are reported elsewhere in the present progress report. By using the measured field data for the sector magnets and BM1, a more realistic study of the beam injection has been done in terms of numerical orbit calculations (see "Design Study of the Canted Injection Scheme (II)"). The MICs were designed to consist of iron shims and septum coils. A model of MIC has been built and the

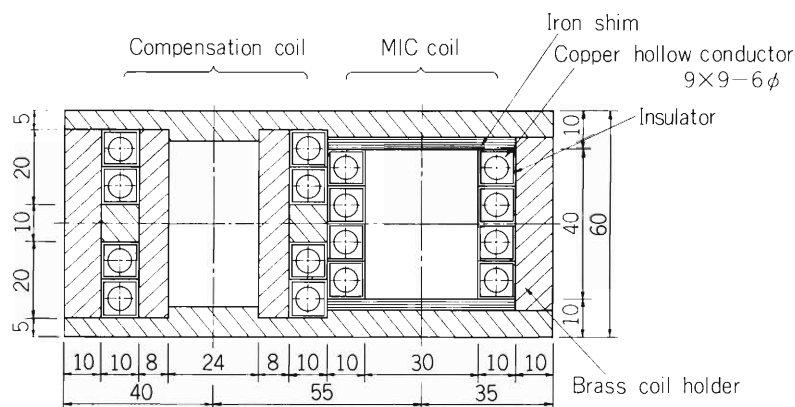


Fig. 2. MIC cross-section; dimensions in mm. The thickness of the iron shim will be determined from the magnetic field measurement for the model MIC.

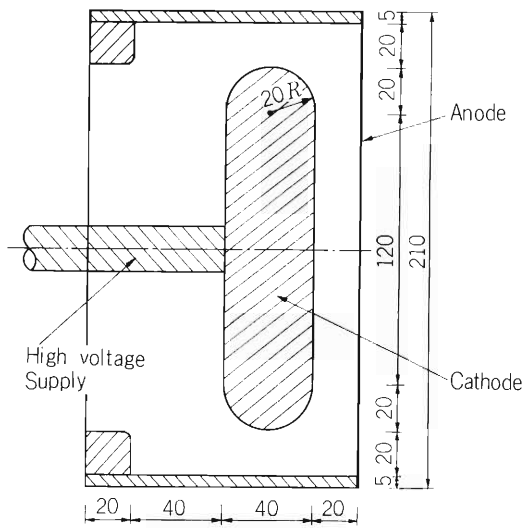


Fig. 3. EIC cross-section; dimensions in mm.

measurement of its magnetic field will be made in November, 1980. The EIC is of conventional structure. The cross sections of the designed MIC and EIC are shown in Figs. 2 and 3.

Reference

- 1) Y. Yano: Sci. Papers I.P.C.R., 74, 13 (1980) .

11-4. Design Study of the Canted Injection Scheme for the IPCR SSC (II)

A. Goto, Y. Yano, T. Wada, and N. Nakanishi

For the detailed study of the injection trajectories, we have developed a computer program for the numerical orbit calculation.¹⁾ In this program, the motion of charged particles in electro-magnetic fields is calculated with time as the independent variable. The fields of each injection element can be superimposed onto those of the sector magnets (the base fields) at arbitrary positions. This program can deal with the acceleration of particles and can calculate individually the paths of 17 particles consisting of a central particle and two groups of 8 particles describing phase ellipses in both (r, r') and (z, z') phase spaces.

As injected particles to be used in the design of injection system we chose three kinds of particles, i.e. 0.84 MeV/u $^{238}\text{U}^{40+}$, 7 MeV/u $^{12}\text{C}^{6+}$, and 4 MeV/u $^{12}\text{C}^{6+}$. The field data used are as follows: The magnetic fields of the four sectors are given by the isochronous fields²⁾ for each particle beam, which were calculated on the basis of the field data of the 1/4-scale model magnet.³⁾ The magnetic fields of BM1 are given by those of the 1/1-scale model bending magnet. For the fields of MICs and EIC we adopted the analytic expression for fringe field.⁴⁾ The accelerating voltage of the resonators is given by the sinusoidal function of time.

We have designed the injection system in such a way that the beam is injected onto the equilibrium orbit. The determination of the characteristics of the injection elements and their arrangement was made by tracing the beam backwards from the middle of the open valley where EIC exists (the exit of EIC) through MICs up to the entrance of BM1. Further, a certain number of acceleration orbits were calculated in order to estimate the magnitudes of turn separation (i.e. the radial separation between two central particle orbits) and beam separation (i.e. the radial separation between two beam envelopes).

Table 1. Characteristics of injection elements derived with the numerical orbit calculation.
Parameters of BM2 are obtained with TRANSPORT.

Element	Bend angle	Aperture (cm)		Radius (cm)	Maximum field		Face angle (entrance)/(exit)
		(H)	(V)				
BM2	45°	10	4.2	46	17.1	kG	22.5/22.5
BM1	94°	4	4.2	46	17.1	kG	14/-13
MIC2	84.5°	3	4	44	3.0	kG	0/0
MIC1	35.2°	3	4	51	1.1	kG	0/0
EIC	2.9°	2		300	58.0	kV/cm	

The characteristics of EIC, MIC1, MIC2, and BM1 thus determined are listed in Table 1 together with those of BM2 obtained with TRANSPORT code⁵⁾. Figure 1 (a)-(c) illustrate the injection paths from the entrance of BM1 to the exit of EIC followed by the first few turns for 0.84 MeV/u $^{238}\text{U}^{40+}$, 7 MeV/u $^{12}\text{C}^{6+}$, respectively. The radial distances of the injected and the first accelerated beams from the machine center and their sizes at the entrance and exit of each element are listed in Table 2 together with the turn separations and the beam separations of those beams at the exits of MIC1 and EIC. It was found that the positions of EIC, MIC1 and the exit of MIC2 should be radially adjustable by 20, 8, and 3 mm, respectively, and that the beam separation of 29 mm at the exit of MIC1 and 12 mm at that of EIC can be obtained even in the severest case. These beam separations assure the accelerated beam to clear these elements.

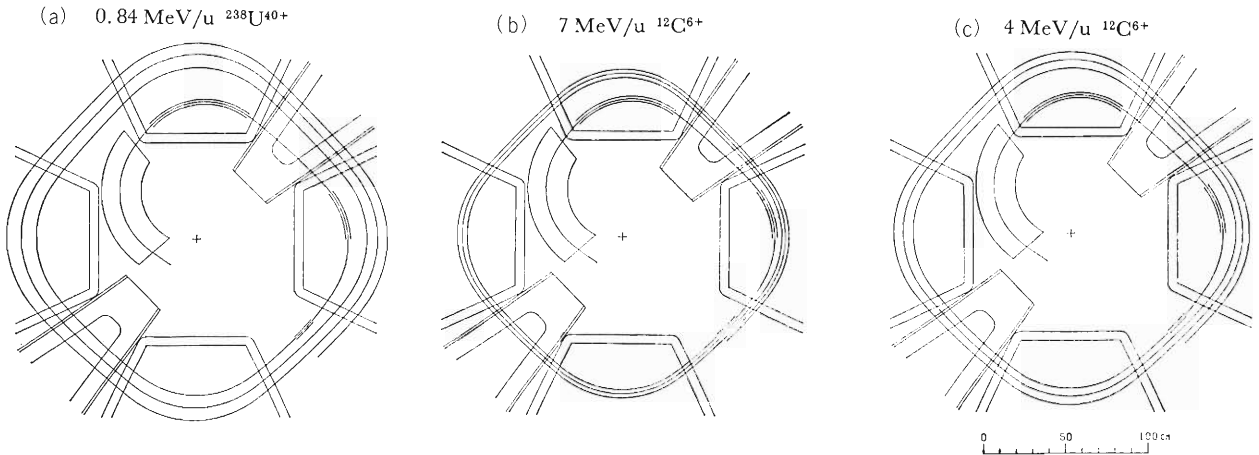


Fig. 1 (a). Injection path through the injection elements and the first few acceleration turns of 0.84 MeV/u $^{238}\text{U}^{40+}$.

Fig. 1 (b). Injection path through the injection elements and the first few acceleration turns of 7 MeV/u $^{12}\text{C}^{6+}$.

Fig. 1 (c). Injection path through the injection elements and the first few acceleration turns of 4 MeV/u $^{12}\text{C}^{6+}$.

Table 2. Calculated radial distances of the injected and the first accelerated beams from the machine center and their sizes at the entrances and the exits of injection elements together with their turn separations and beam separations at the exits of EIC and MIC1 for 0.84 MeV/u $^{238}\text{U}^{40+}$, 7 MeV/u $^{12}\text{C}^{6+}$, and 4 MeV/u $^{12}\text{C}^{6+}$. The areas of phase spaces are set to be 25π mm·mrad.

Particle	Injection energy (MeV/u)		EIC		MIC1		MIC2	
			Exit	Entrance	Exit	Entrance	Exit	
$^{238}\text{U}^{40+}$	0.84	{	Injected orbit	856	862	925	869	820
			(width)	(8.0)	—	(10.8)	—	—
			1st acc. orbit	919	—	1041	—	—
			(width)	(8.3)	—	(11.6)	—	—
			Turn separation	63	—	117	—	—
			Beam separation	55	—	106	—	—
$^{12}\text{C}^{6+}$	7	{	Injected orbit	836	846	927	877	823
			(width)	(7.8)	—	(10.9)	—	—
			1st acc. orbit	856	—	967	—	—
			(width)	(7.8)	—	(10.4)	—	—
			Turn separation	20	—	40	—	—
			Beam separation	12	—	29	—	—
$^{12}\text{C}^{6+}$	4	{	Injected orbit	847	855	926	871	823
			(width)	(7.9)	—	(10.8)	—	—
			1st acc. orbit	887	—	1003	—	—
			(width)	(8.2)	—	(10.3)	—	—
			Turn separation	40	—	77	—	—
			Beam separation	32	—	66	—	—

(Units: mm)

References

- 1) A. Goto, Y. Yano, T. Wada, and N. Nakanishi: Sci. Papers I.P.C.R., 74, 124 (1980).
- 2) N. Nakanishi and S. Motonaga: IPCR Cyclotron Progr. Rep., 13, 12 (1979).
- 3) N. Kumagai, S. Motonaga, K. Ogiwara, H. Takebe, T. Wada, and J. Fujita: Reports I.P.C.R., (in Japanese), 55, 27 (1979).
- 4) H. A. Enge: Rev. Sci. Instr., 35, 278 (1964).
- 5) K. L. Brown, F. Rothacker, D. C. Carey, and Ch. Iselin: SLAC Report, No. 91 (1974).

11-5. Model Study of the Injection Bending Magnet of the IPCR SSC

Y. Yano, H. Takebe, T. Wada, J. Fujita,
A. Goto, Y. Obana, and S. Motonaga

The injection bending magnet (BM1), one of the injection elements of the SSC is required to have the following performances: 1) It can produce the maximum magnetic field up to 17.1 kG. On the other hand, its size must be small enough so that it can be set in the limited available space of the SSC central region. 2) Its property in beam optics must be independent of the change of magnetic field between 6 and 17 kG to allow easy injection orbit tuning. We have designed this magnet¹⁾ and constructed its 1/1-scale model with the bending angle of 50°. It is being tested whether the designed magnet fills the above requirements. The dimensions of the pole and coil cross sections and the pole profile at the beam entrance and exit are given in Figs. 1, 2.

Figure 3 shows the magnetic excitation curve measured for the model magnet. While the current density ran

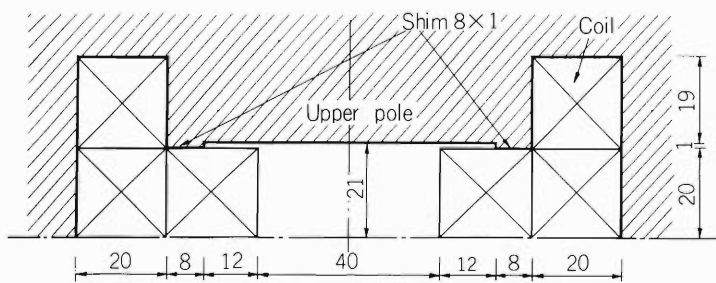


Fig. 1. Transversal dimensions (mm) of pole and coil configuration around beam aperture (upper half only).

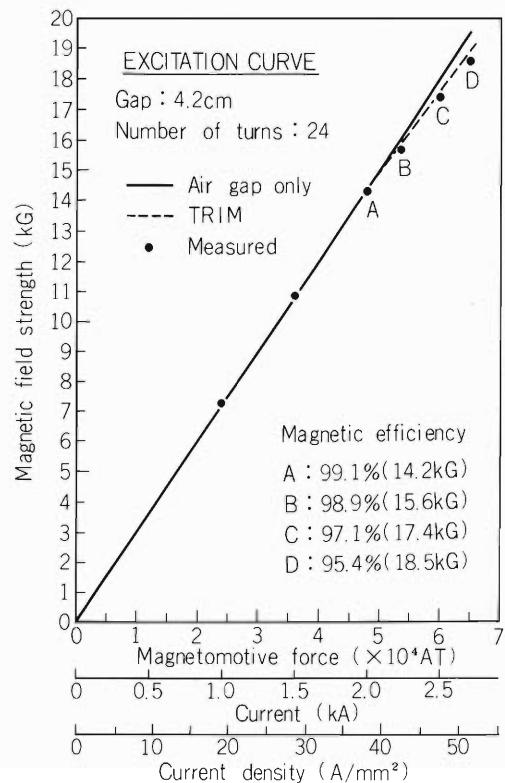


Fig. 3. Magnetic field strength vs magnetomotive force measured for the model bending magnet with the gap of 42 mm. The data (solid circles) are plotted together with the theoretical curve calculated by taking only the reluctance of air-gap into account (solid line) and that predicted by the TRIM code (dashed line). The magnetic efficiency denotes the proportion of the measured field strength to the field strength on the above solid line at certain magnetomotive force.

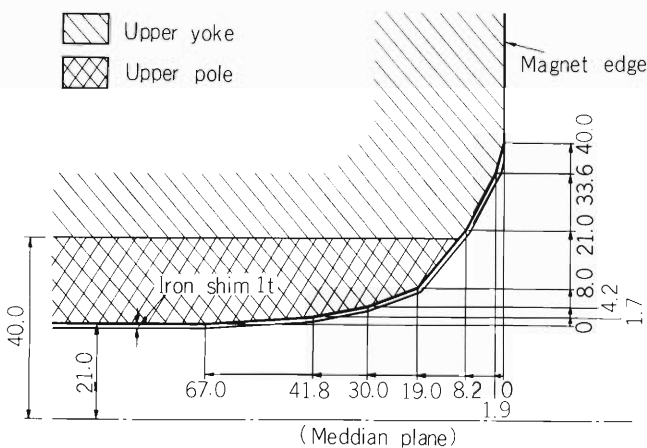


Fig. 2. Longitudinal profile of pole edge; dimensions in mm. The curve of Rogowski is approximated by combining six straight lines.

up to 52 A/mm^2 when the magnet was excited to 18.5 kG, the maximum temperature of coils could be kept below 50°C with the water velocity of 3.9 m/sec. The estimation for the temperature rise of coils by the empirical formulae¹⁾ agreed quite well with the measured value.

For the detailed examination of the optical property of this magnet, the measurement of the magnetic field distributions was made at 7, 12, 15, and 17 kG. The magnetic field strength was measured with the Hall generators of BHT-910 series (F.W. Bell Inc.) that were of high temperature stability. The data in azimuthal direction were taken automatically by using computer-controlled driving system. When θ is defined as the azimuth angle on the inner side from the magnet edge and r as the radial distance taken from the assumed circular orbit centered in the pole width, the map of magnetic field obtained was in the area of $-17 \text{ mm} < r < +46 \text{ mm}$ for $-25^\circ < \theta < -3^\circ$ and $-17 \text{ mm} < r < +17 \text{ mm}$ for $-3^\circ < \theta < +25^\circ$. The mesh points were taken by a step of about 0.4° azimuthally and by a step of 2 mm or 3mm radially. The accuracy of measurements of field strength was within $\pm 1.5 \times 10^{-4}$.

Figure 4 shows the magnetic field distribution in radial direction measured at $\theta=25^\circ$, the central position of the magnet in azimuthal direction. The uniformity better than 1×10^{-3} was obtained in $-10 \text{ mm} < r < +10 \text{ mm}$.

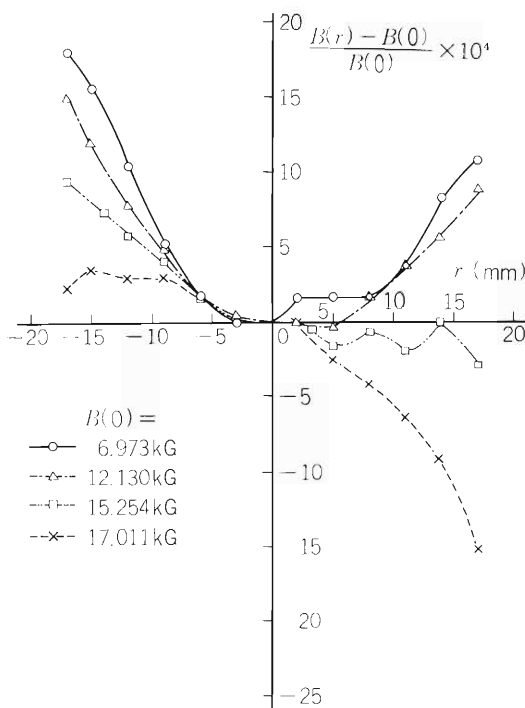


Fig. 4. Magnetic field distribution in radial direction measured at the azimuth of 25° to the inner side from the magnet edge. r denotes the distance outer from the center of horizontal aperture.

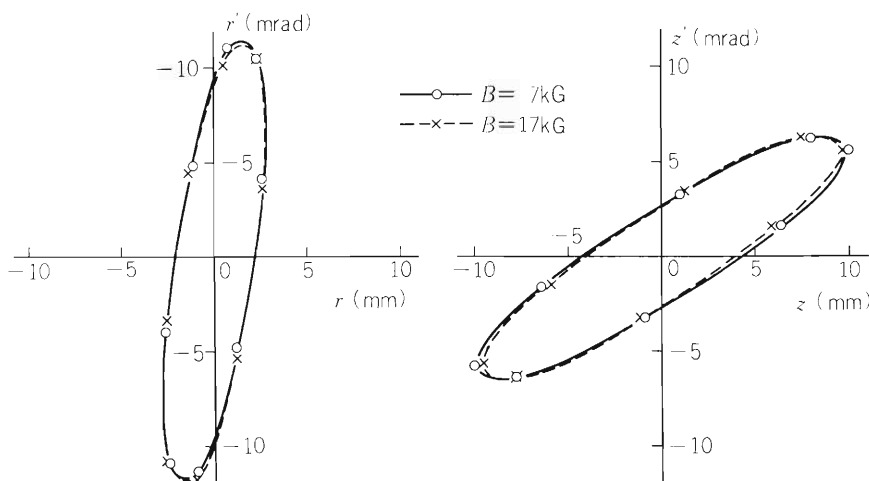


Fig. 5. The phase ellipses in both transverse directions at exit of the 90° bending magnet for the beam just after passing through the magnet. Leave the detail to the text.

This was just as we had expected in the design study including the estimation of field uniformity required for beam optics. The further examination was performed by tracing a beam through the measured magnetic field in terms of numerical orbit calculations. Because the magnet (BM1) will have the bending angle of about 90° , we have generated the magnetic field of a 90° bending magnet on the basis of the model data. The measured data were used in the region of $-25^\circ < \theta < +25^\circ$ near both edges of this 90° magnet and the radial field distribution throughout the central region was assumed to be the same as that at $\theta = 25^\circ$. In the numerical calculations, a beam starts from a position 46 cm, which is equal to the radius of curvature of this magnet, apart from one side of the magnet edges and passes through the magnet. At the starting position the beam is assumed to have phase ellipses of circular shape of $5 \text{ mm} \times 5 \text{ mrad}$ in both transverse directions. The transformation of phase ellipses of the beam was calculated at exit boundary of the 90° magnet. Calculation was made for the maximum field strengths of 7 kG and 17 kG. Quite satisfactory results have been obtained in which the shapes of ellipses were found almost same inspite of the large change of field strength as shown in Fig. 5. Table 1 gives the variation of the position of effective boundary and the effective bending angle with change of magnetic fields for this magnet. Only negligible change of the above quantities was seen. From the present study, the designed magnet has proved to have sufficient performances as the injection bending magnet.

Table 1. The variation of the position of effective boundary (x_{eff}) and the effective bending angle (θ_{bend}) with different magnetic field strengths for the 90° bending magnet. The map of magnetic field of this magnet was generated on the basis of the field data measured for the 50° model magnet. Δx_{eff} is defined as the displacement to the outer side from the magnet edge. Δx_{eff} and $\Delta \theta_{\text{bend}}$ denote the maximum variations of x_{eff} and θ_{bend} , respectively.

B (kG)	x_{eff} (mm)	θ_{bend} (deg)
6.973	-0.42	89.89
12.130	-0.50	89.86
15.254	-0.39	89.89
17.011	-0.37	89.90
Δx_{eff} (mm)	0.13	
$\Delta \theta_{\text{bend}}$ (deg)	0.04	

Reference

- 1) Y. Yano: Sci. Papers I.P.C.R., 74, 13 (1980).

11-6. Magnetic Field Measuring System for the Model Injection-Bending Magnet of the SSC

H. Takebe, Y. Yano, T. Wada, J. Fujita,
Y. Obana, and S. Motonaga

An automatic measuring system of magnetic field was constructed to measure the magnetic field of an injection-bending model magnet.

This system consists of a mechanical part, two Hall generators and electronic devices, an NMR gauss meter, and a microcomputer, LSI-11. Figure 1 (a) shows a schematic diagram of the system, and a setup of this system is shown in Fig. 1 (b). The relative accuracy of the set of field measurement was found to be better than 2×10^{-4} for a period of a few days and the absolute accuracy of 1×10^{-3} for in the period over four months was obtained using a Hall generator, BHT-910, without a temperature stabilizer. The mechanical part and the procedure for the calibration of the Hall generator are described below.

Two Hall generators are mounted in a probe assembly together with a Pt-thermometer. The probe assembly is fixed on a goniometer which is driven by a pulse motor controlled by the computer. The radial position of the Hall assembly is changed by replacing a fixed point of the probe assembly on the goniometer. The position of the goniometer in the azimuthal direction is detected within the accuracy of 0.15 mm along the arc path using an optical rotary encoder.

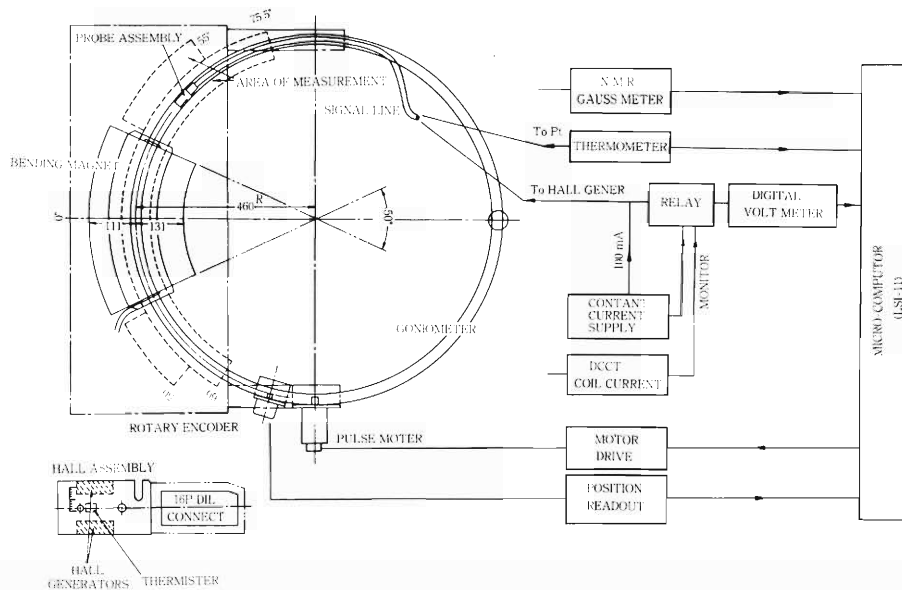


Fig. 1. (a) Schematic diagram of the system for the magnetic field measurement of the injection-bending model magnet.

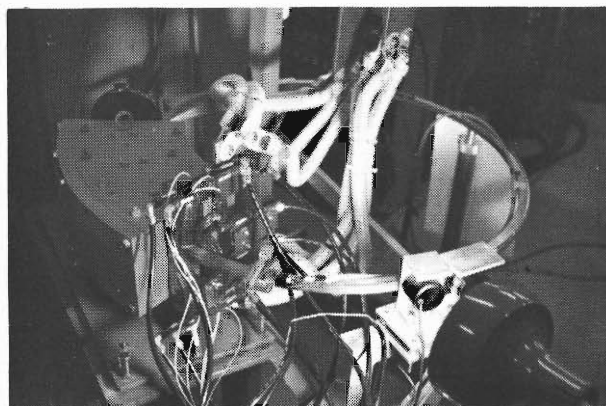


Fig. 1. (b) Setup of the system.

Two Hall generators are powered in series by a 100 mA current regulated power supply with a stability of 10^{-5} . Figure 2 shows an example of stability check of the system at the field of 11.8 kG. Magnetic field, current of the magnet coil, temperatures of the magnet coil and the probe assembly and Hall voltages are plotted by the computer. The error in the measurement of the Hall voltage was found to be better than 1×10^{-4} for an hour. The Hall voltage was calibrated with the NMR gauss meter. Calibration was made at field intervals of approximately 1.5 kG from 3 kG to 18 kG by changing temperature of probe assembly from 20°C to 35°C in step of 5°C. The data was fitted to the 5th-order polynomial relating to the Hall voltage and magnetic field. Figure 3 shows the difference $B - B_{cal}$ plotted against B , where B is the magnetic field observed by the NMR gauss meter and B_{cal} the field obtained from the observed Hall voltage by the above least-squares fitting. The relative accuracy was found to be 2×10^{-4} for one Hall generator (No. 3186) and 1.3×10^{-4} for the other (No.3187) at fields larger than 2.5 kG.

In order to check the long term stability of the system, measurements of Hall voltage against the magnetic field were performed over ten times from April to July. The difference $V_H - V_{cal}$ is plotted against B in Fig. 4.

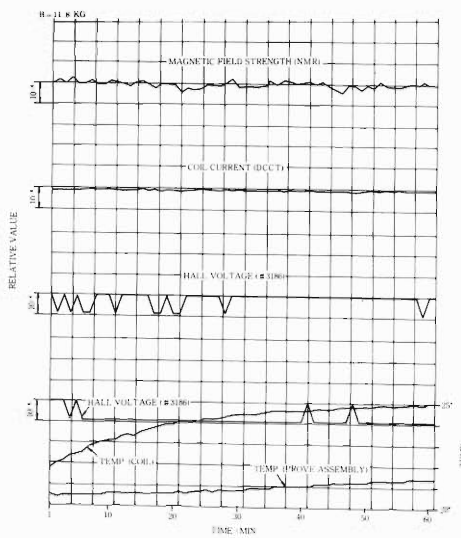


Fig. 2. Characteristics of the magnetic field measuring system. Resolution of the Hall voltage is about 10^{-4} at the digital volt meter resolution of $1 \mu V$ at 11 mV in the field of 11.8 kG.

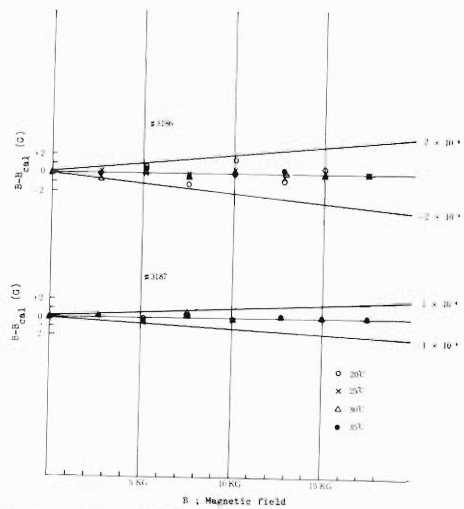


Fig. 3. The difference $B - B_{cal}$ against the magnetic field observed for different temperatures: \circ indicates the data for 20°C, \times for 25°C, Δ for 30°C, and \bullet for 35°C.

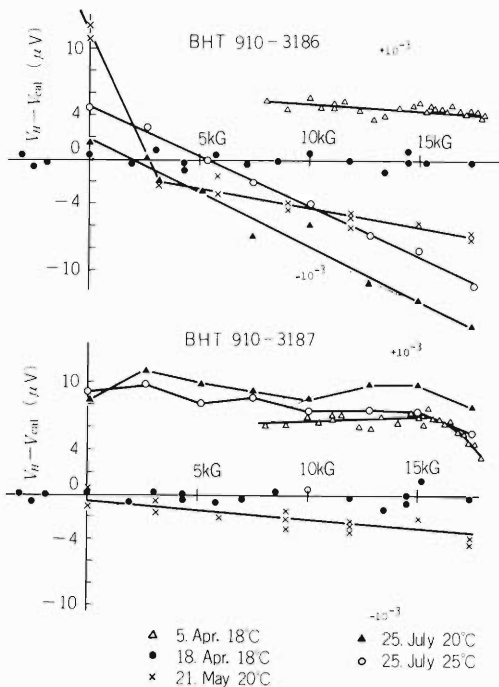


Fig. 4. Hall voltage change on standing. Points indicate $V_H - V_{cal}$, where V_H is the Hall voltage observed for each measurement and V_{cal} is the calculated voltage using 5th-order polynomial least-squares fits to the data on 18. April, 1980.

V_{cal} was obtained from the 5th-order polynomial fit to the data of 18. April. As can be seen Fig. 4, the observed absolute accuracy is better than 10^{-3} in the range from 7 to 18 kG. This accuracy is satisfactory for the calculation of beam trajectory.

An example of the results of measurements is shown in Fig. 5. With the present system it takes about 8 h to complete a set of measurements.

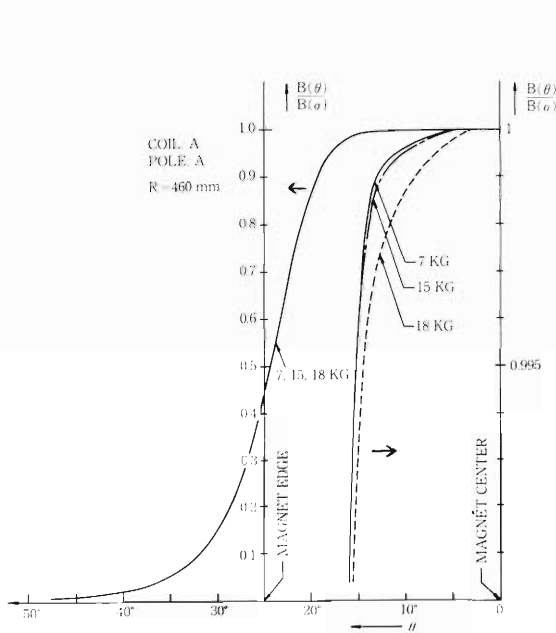


Fig. 5. (a) Azimuthal distribution of the magnetic field measured along a circle of radius 460 mm at maximum field of 7, 12, 15, and 18 kG.

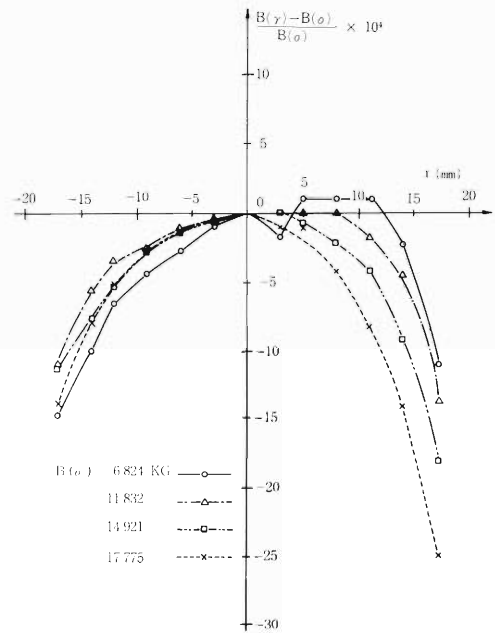


Fig. 5. (b) Observed variation of magnetic field along the radius at the magnet center for the field of 7, 12, 15, and 18 kG.

11-7. Microcomputer System with CAMAC for Measuring Magnetic Field of a SSC Model Magnet

J. Fujita, T. Wada, and H. Takebe

Measurement of magnetic field distribution of a model magnet of the SSC has been carried out with an electronic system using OKI-4500 minicomputer. It was, however, difficult to occupy the OKI computer long enough to carry through this measurement. A floppy based LSI-11 microcomputer system of DEC was, therefore, introduced. Block diagrams of these two systems are shown in Fig. 1 and Fig. 2, respectively.

The OKI computer system has been reported previously.¹⁾ Two NIM modules interface the computer with general measuring instruments. Interconnection between a digital scanning controller and the computer is performed by RG58A/U coaxial cables for control signals and a shielded 50 parallel wire cable for digital data signals.

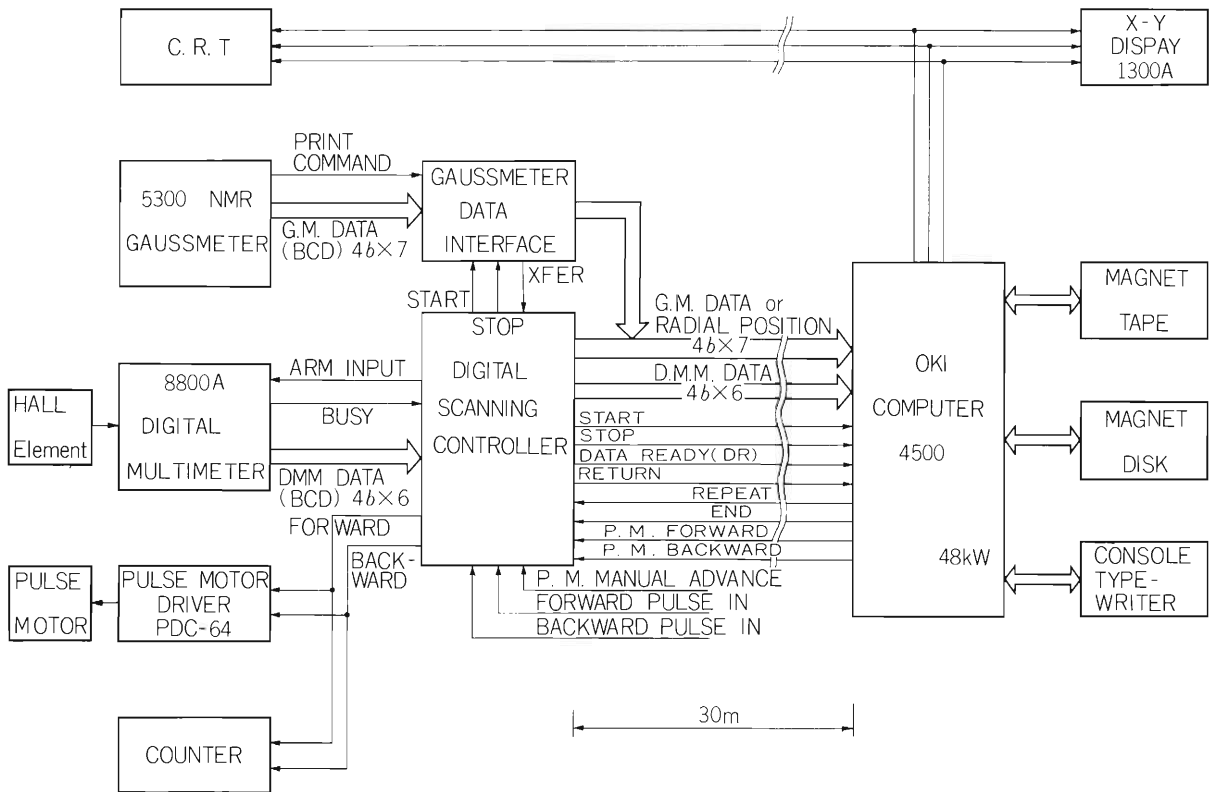


Fig. 1. Block diagram of the electronic system using OKI-4500 for measurement of magnetic fields.

The LSI-11 microcomputer system consists of MOS RAM 28 K words, DSD400 dual floppy disks with total storage capacity of 1 MB and a LA36 DEC writer. In addition to these basic devices, three interface boards are installed in the LSI-11 bus. One is a DRV11-B DMA interface which displays data on a screen of a cathode ray tube through two digital to analogue converters with a resolution of 8 bits. The second is an IBV11-A that interfaces the LSI-11 bus with the instrument bus, or GP-IB bus, as described in IEEE Standard 488-1975 Digital Interface for Programmable Instrumentation. A FLUKE 8502A digital voltmeter is connected

encoder is received through the 6 positioned connector.

Four NIM modules interface the CAMAC modules with specially purposed units. A dual 4 to 1 relay module switches analogue voltage signals generated by maximum four HALL elements to the FLUKE 8502A digital voltmeter according to binary codes from the 3222 output register. The digital scanning controller is modified to a Pulse Motor / OKI Controller which transforms D.C. pulses from the 3222 output register into A.C. pulses compatible to each unit. 8 Inputs OR/ Latch detects negative spikes or levels of up to eight inputs and holds these levels until they are reset by a CLEAR pulse from the output register. A Plotter Controller / OKI Data Buffer interfaces the KINETIC 3061 register with a IWASAKI DPL-602 digital plotter and digital I/O ports in the OKI-4500 minicomputer whose selection is made by a switch on its front panel.

All application programs for the measurements are developed by T. Wada on the basis of RT-11 operating system provided by DEC. The microcomputer system with CAMAC showed good performance in measuring magnetic field for a long time extending over a few days if required by the application program.

Details concerning electronics of the measuring system will be described in SSC reports.

Reference

- 1) T. Wada, T. Nomura, H. Kamitsubo, Y. Chiba, and F. Yoshida: IPCR Cyclotron Progr. Rep., 7, 83 (1973).

11-8. Design Study of RF Resonator for the SSC

M. Hara, K. Ogiwara, and T. Fujisawa

In designing the RF resonator for the SSC at IPCR, resonators of three different types were investigated. These are a resonator of a single gap type, a $\lambda/4$ type with a single vertical stem, and a $\lambda/2$ type with two vertical stems in opposite sides. The first one is the variable frequency H_{101} mode rectangular parallelpiped. This is expected to have a simple structure and high Q value. In our case, however, it is difficult to realize because of the following reasons. The injection radius is so small that the spatial restriction near the central region makes the voltage at the dee gap low near the injection orbit (about a half of the maximum voltage at most). Moreover, compared with other types, a voltage twice as high is needed to keep the same energy gain per turn, and this demands wide gaps. The relatively high cutoff frequency requires the use of large harmonic number. Then transit time effects become severe.

The second one has some advantages but detailed analyses have proved that it has fatal drawbacks which is shown elsewhere.¹⁾ The third one is supposed to be realizable.

The half wavelength resonator is designed under the following conditions:

- 1) The frequency range is 17 to 45 MHz for the synchronous operation with the injectors.
- 2) Harmonic numbers are 9, 6, and 4.
- 3) Maximum energy gain is 1 MeV/turn per unit charge.
- 4) 20° delta shaped two dees are located at opposite valley spaces between 50° sector magnets.

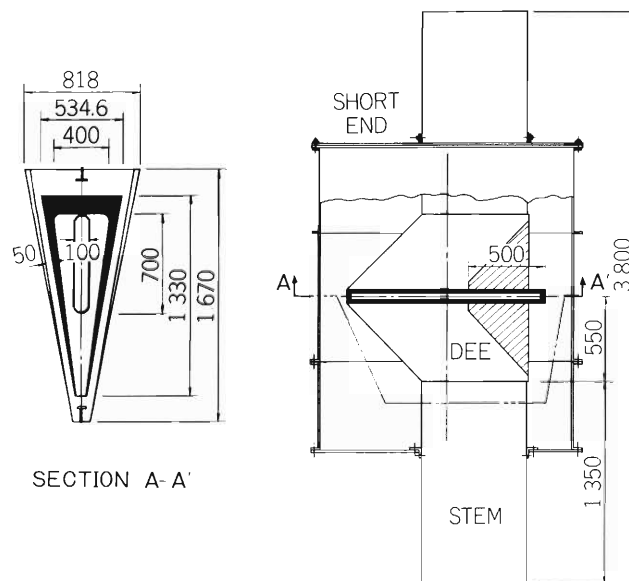


Fig. 1. Cross sectional views of the half scale half wavelength resonator. Hatched part is cut off to improve the radial RF electric field distribution.

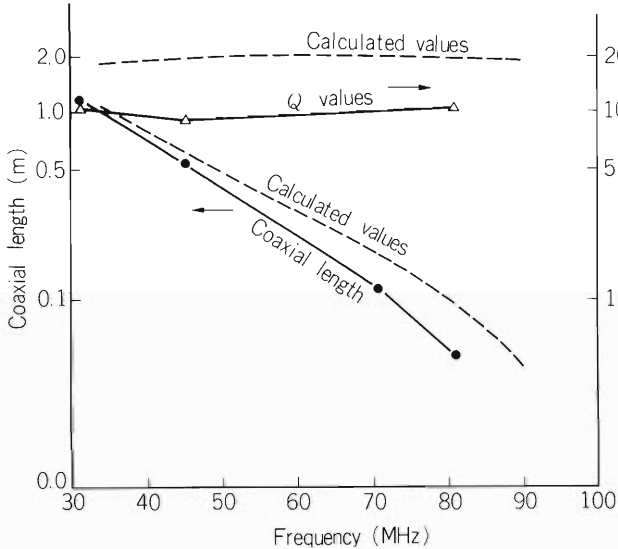


Fig. 2. Measured and calculated Q values and stem lengths. Q values are measured by decay time method. Dotted lines indicate calculated values.

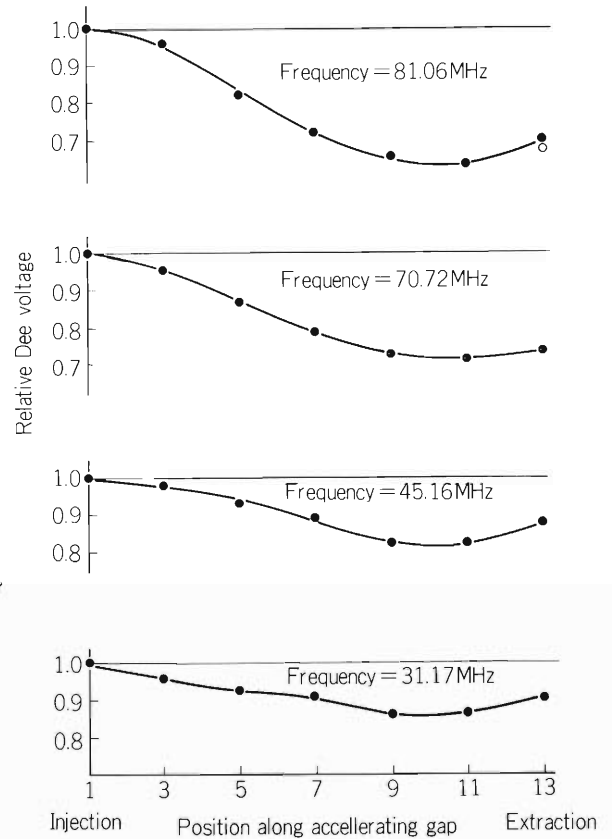


Fig. 3. Relative distribution of RF electric field along the dee edge of half scale model resonator. Measurements were done by perturbation method using ceramic block.

5) Radial length of the accelerating gap should be longer than 2.6 m corresponding to the distance between injection and extraction radii.

6) Maximum current density at short ends should be less than 50 A/cm.

7) Compact, simple in structure and easy to handle.

8) A constant or radially increasing voltage distribution is desirable.

Calculations based on the distributed constant circuit theory were done for three types of stems, the cross sections of which were circular, rounded triangle and racetrack. The racetrack stem was found to be favourable.

A half scale model resonator was constructed to investigate RF characteristics. This model is shown in Fig.1. At several stem lengths, resonance frequencies, Q values, and the radial distributions of RF electric field were measured and shown in Fig. 2 and Fig. 3. The RF electric field distributions had maximum at small radial position and this was not desirable. In order to improve the distributions, parts of the stems are cut off as shown in Fig. 1 (hatched). Data shown in Fig. 4 indicate fairly good results.

In conclusion, the calculation and measurements show that the half wavelength resonator with double vertical stems satisfies the desired conditions. We are developing a computer code to solve the problem of three dimensional electromagnetic wave in a resonator on the basis of finite element method in order to obtain the radial electric field distributions.

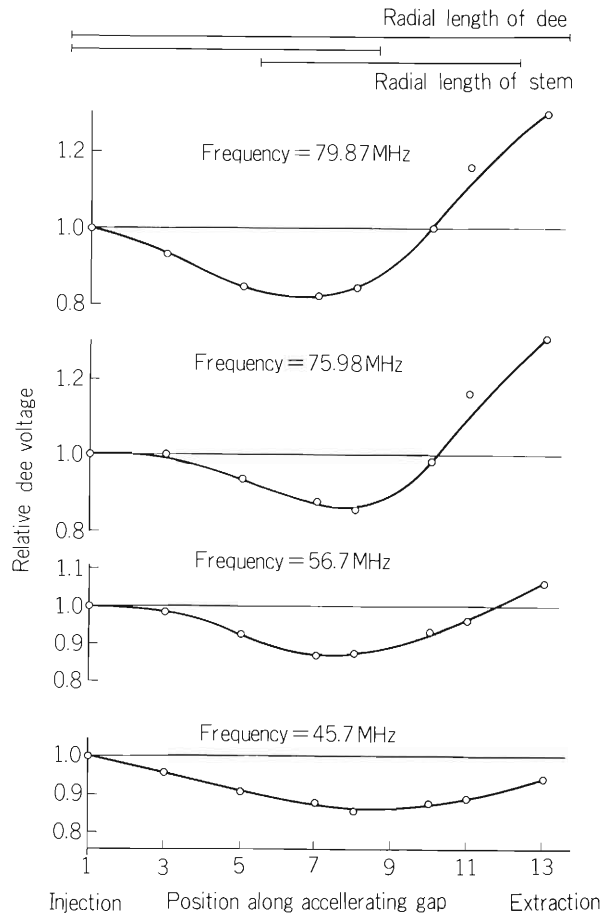


Fig. 4. Relative distribution of RF electric field along the dee edge for the cut-off model resonator. The electric field at the extraction radius became strong, and the distributions were improved.

Reference

- 1) K. Ogiwara, T. Fujisawa, and M. Hara: IPCR Cyclotron Progr. Rep., 14, 187 (1980).

11-9. Design Study of Oscillator for the SSC

M. Hara, K. Ogiwara, and T. Fujisawa

The design study of RF system for the SSC is performed. The resonator is described elsewhere.¹⁾ RF amplifier and coupling system between the power amplifier and the resonator are designed according to the following conditions:

- 1) The frequency is variable from $f_{\min} = 17$ MHz to $f_{\max} = 45$ MHz.
- 2) The maximum output RF power is 300 kW.

Two oscillator systems are considered; one is a self-exciting system and the other is MOPA (master oscillator and power amplifier) system. The latter is employed because of the necessity of synchronous operation with the injectors (the linac and AVF cyclotron). The oscillator is designed intending to use a tetrode, which is to be chosen among RCA 4648, Eimac 4CW-250000 and Eimac X 2170. Length of more than 2 m for the feeder line is necessary from the power amplifier to the resonator. Only a traveling wave should be excited on the feeder line because the frequency must be variable and the feeder line is so long. The circuit is schematically shown in Fig. 1. The impedance of the power feeder is fixed to 50Ω for convenience' sake. The impedance matching between the resonator and the feeder line can be obtained by a variable capacitor (C_f). Figure 2 shows the expected shunt impedance of the resonator and the corresponding coupling capacitance for impedance matching. The impedances can be matched between the main amplifier and the feeder line by a variable capacitor (C_v). The tuning of plate

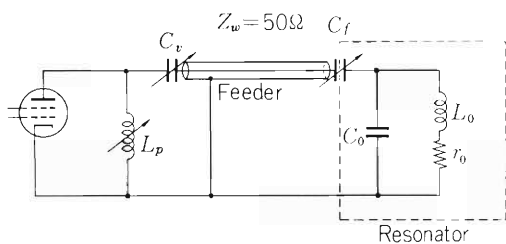


Fig. 1. RF power feeder line and impedance matching circuit for the SSC.

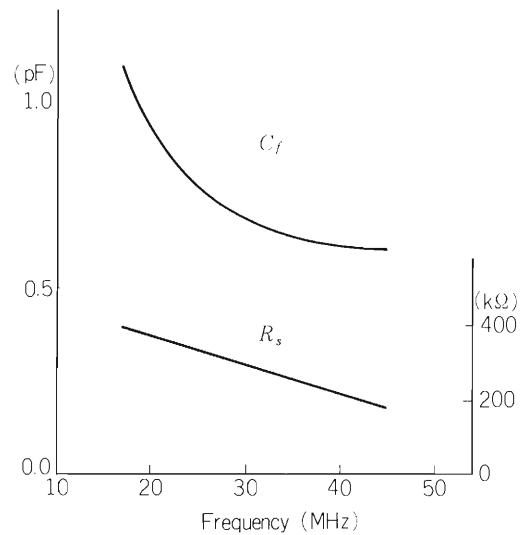


Fig. 2. Coupling capacitance(C_f) to give the impedance matching between the resonator and the feeder line (50Ω). Calculated shunt impedances (R_s) of the resonator are also shown.

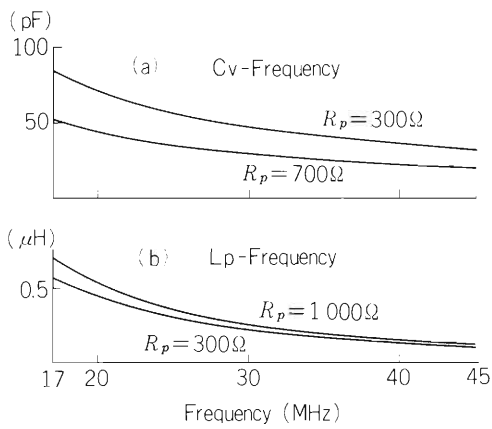


Fig. 3 (a) The capacitance (C_v) to give the desired plate load resistance (R_p). (b) Stub inductance (L_p) to tune the plate circuit.

circuit is done by a tuning stub (L_p). The expected values of the stub inductance (L_p) and the capacitance (C_v) are shown in Fig. 3. The impedance matching at the grid of the tetrode is under consideration and testing. A feeder and an oscillator for a model resonator¹⁾ are under construction to investigate RF circuit characteristics.

In conclusion, power feeder and main amplifier can be realized with the above stated parameters.

Reference

- 1) M. Hara, K. Ogiwara, and T. Fujisawa: IPCR Cyclotron Progr. Rep., 14, 182 (1980); K. Ogiwara, M. Hara, and T. Fujisawa: *ibid.*, p. 187.

11-10. Measurement of RF Field Distribution for a Quarter Wave-Length Vertical Type Resonator

K. Ogiwara, T. Fujisawa, and M. Hara

The half wave-length type resonator for the SSC was investigated last year.¹⁾ We also studied a quarter wave-length resonator this year because it has advantages that the resonator becomes smaller in size and simpler in structure, resulting in lighter vacuum pumping load. However, the model-study described below revealed the following problems:

(1) Vertical electric field may be induced at the accelerating gap and may, further, leak out inside the dee.

(2) At the accelerating gap, the electric field has different strength above and below the median plane.

A half-scale model resonator of a quarter wave-length type was constructed²⁾ and the electric field distributions were measured by the perturbation method using a celamic block in order to eliminate the disturbance from RF magnetic field. Figure 1 shows the field measuring system for this resonator. Figure 2 shows the vertical distribution of the RF field at the accelerating gap. It was found that this resonator had different field strengths above and below the median plane at the accelerating gap. Figure 3 shows the horizontal distribution of the RF field. This resonator was found to have large RF electric field even inside the dee, of which the strength was about 60 % of the dee gap field at the intermediate radius when the resonator was excited at 67.58 MHz corresponding to 33.79 MHz in the case of a full-scale resonator. In order to understand the experimental result, we have also calculated the field distribution inside the dee by assuming that the dee is the rectangular wave guide for simplicity (the electric field is given at both ends). In Fig. 3, the calculated results are shown. The experimental tendency is reproduced fairly well. The field inside the dee must be induced by the RF electric currents flowing above and below the dee aperture. These fatal drawbacks are due to

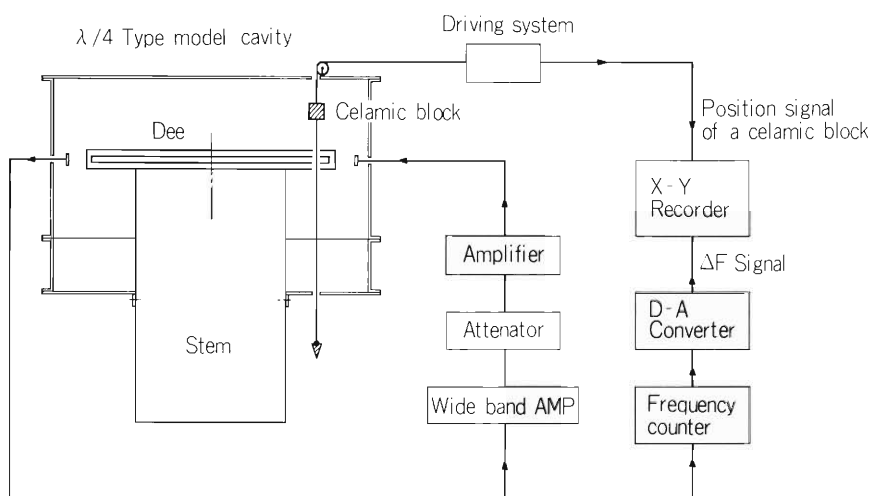


Fig. 1. The block diagram of the field measuring system for this resonator.

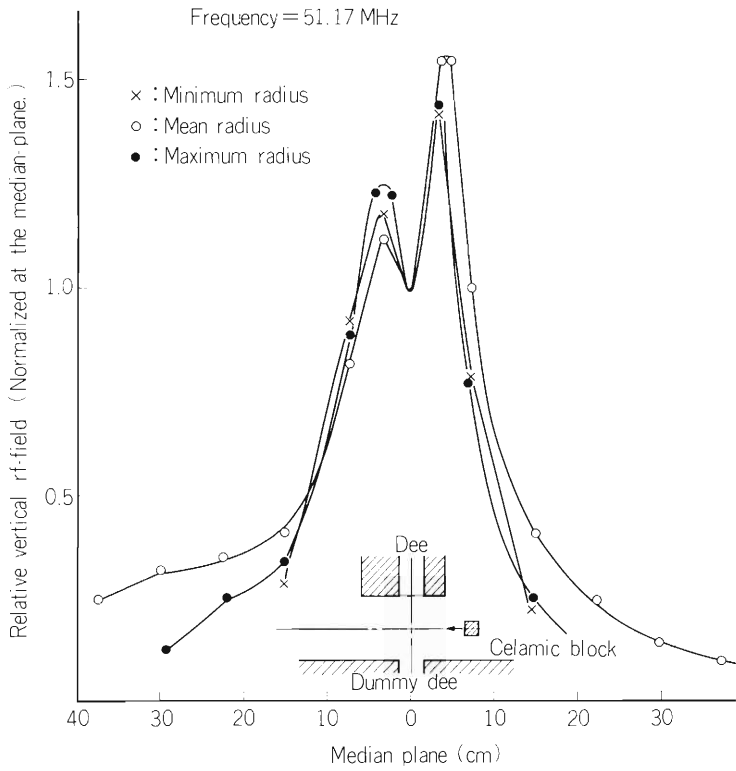


Fig. 2. The vertical distribution of the RF field at the accelerating gap.

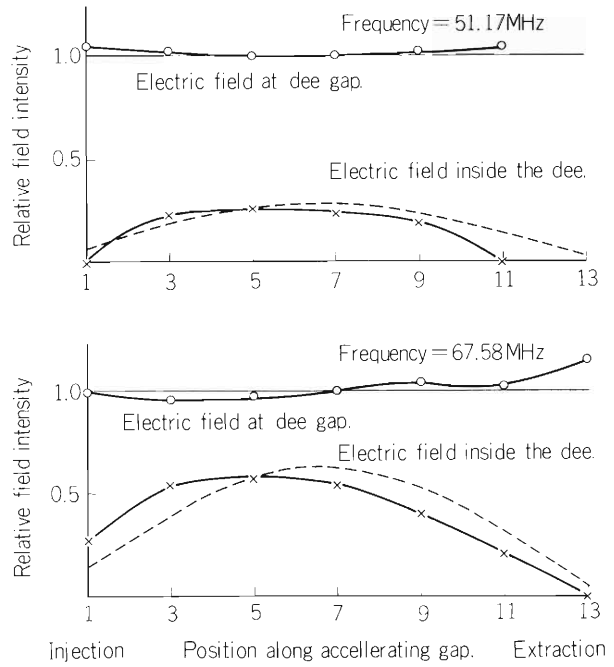


Fig. 3. The horizontal distribution of the RF field. Relative field distribution at the accelerating gap and inside the dee are shown. The broken line shows the result of calculation.

asymmetric structure of this resonator, and made us give up the idea of using a quarter wave-length type resonator.

References

- 1) H. Nakajima, K. Ogiwara, F. Yoshida, and J. Fujita: IPCR Cyclotron Progr. Rep., 12, 16 (1978).
- 2) K. Ogiwara, F. Yoshida, H. Takebe, and T. Fujisawa: *ibid.*, 13, 10 (1979).

11-11. Some Properties of Accelerated-Beam Orbit in the Separated-Sector Cyclotron

N. Nakanishi, T. Wada, A. Goto, and Y. Yano

A computer code AO for an accelerated-beam orbit in the separated-sector cyclotron SSC has been developed¹⁾ and some calculations on the properties of the orbit have been done. The isochronous field, which is employed in the calculation, is numerically produced by an equilibrium orbit code EO²⁾ using the magnetic field measured in a model magnet. Since the model magnet is not exactly of a 1/4 scale in the radial direction, the magnetic fields are not only scaled up but also expanded to those of the full scale magnet. The frequency and position dependences of the accelerating voltage along the gap, which are employed in the calculation, are obtained by using measured data in a model cavity. In the calculation the maximum voltage along the gap is set to be 250 kV. Since the azimuthal angle was taken to be an independent variable in the numerical integration, accuracy in the calculation became worse toward the larger radius. This defect was removed considerably by an improvement in amending the integration method³⁾ without much increase of the calculation time.

Some results of the calculation will be described in brief. Injection conditions of an accelerated reference orbit should be determined to minimize the oscillation amplitude of the turn separation. The turn separations of an accelerated p^+ beam at the injection energy of 9 MeV are shown in Fig. 1. The beam is transported from an injector cyclotron and accelerated up to the energy of 184 MeV at the harmonic number $h = 6$ in the SSC. As can be seen, the amplitude of the turn separation is nearly 1 cm in the case of injection onto its first equilibrium orbit. However the amplitude is reduced to zero if the beam is injected under a specific condition. The radial displacement and radial component of momentum are taken to be, respectively, 0.0 cm and 0.00215 cyclotron unit against the first equilibrium orbit at the injection point,

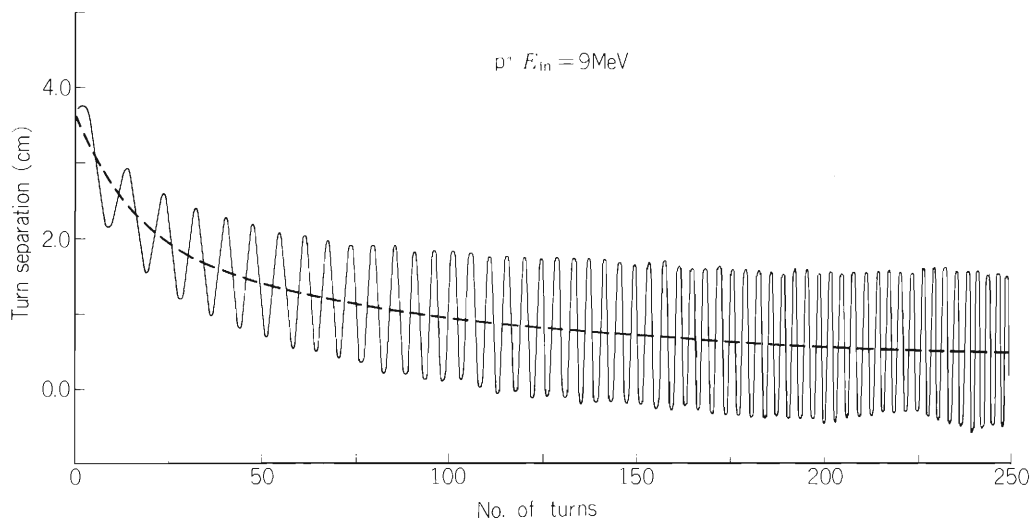


Fig. 1. Turn separation of accelerated p^+ beam. The broken and solid lines show the cases with and without optimization of injection conditions, respectively.

and the initial phase is set to be -4.0 deg. Here zero deg is taken to the phase at which the rising RF voltage crosses the base line. In general these conditions are different for various particles and various injection energies.

Behaviors of the beam in the 6-dimensional phase space are shown in Fig. 2 for the p^+ beam. These curves show transformation of phase space pattern when the beam is injected on to the first equilibrium orbit in the center of the open valley. In this calculation the reference orbit and typical eight orbits on the eigen ellipse are traced toward the extraction region. Figure 2 (a), (b), and (c) show the phase patterns for the (x, x') , (z, z') and $(\Delta E/E, \Delta\varphi)$ spaces, respectively. Emittances are assumed to be $\epsilon_{x, z} = 20 \text{ mm}\cdot\text{mrad}$ and $\Delta E/E \cdot \Delta\varphi = 0.0015 \times 1.5 \text{ deg}$. In these examples, the two-dimensional spread in each phase space only is taken into account at the starting point. The contribution of the spread in the radial phase space to the behavior in the $(\Delta E/E, \Delta\varphi)$ space is shown Fig. 2 (d).

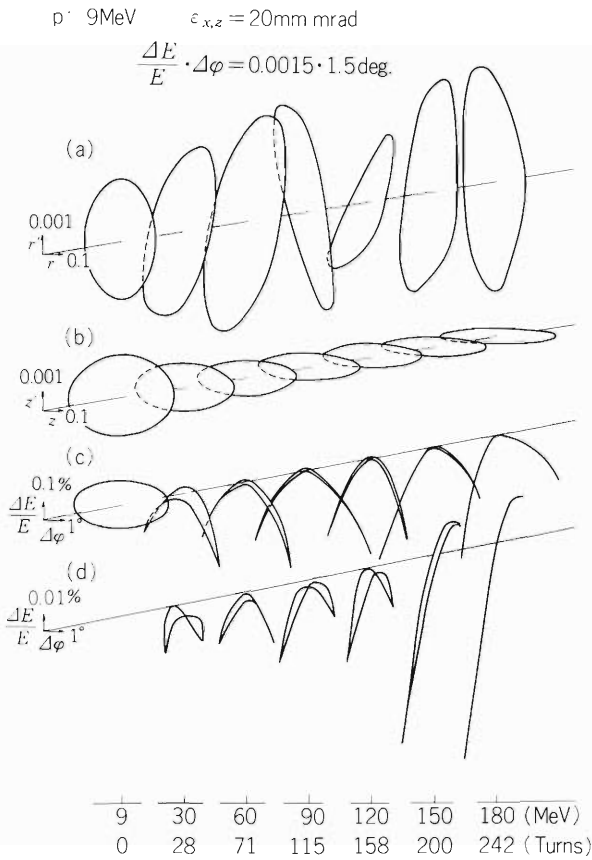


Fig. 2. Transformation of phase space pattern projected on the (x, x') plane (a), (z, z') plane (b), $(\Delta E/E, \Delta\varphi)$ plane (c and d).

The isochronous magnetic field is composed of the fields induced by the main magnet and trim coils which are mounted on the magnet pole faces. The maximum deviation $\Delta B_{\text{max}} = |B(r) - B_0(r)|_{\text{max}}$ between the real and ideal isochronous fields should be suppressed to a value as small as possible. In order to estimate the permissive tolerance, a simple model is introduced. It is assumed that the radial variation induced by the trim coils can be expressed by a sinusoidal curve

$$B(r) = B_0(r) \left[1 + \frac{\Delta B_{\text{max}}}{B_0} \sin \left\{ \frac{2\pi}{a} (r - r_0) + \varphi_0 \right\} \right],$$

where $B(r)$ and $B_0(r)$ are the real and ideal isochronous fields, respectively, and B_0 is set to be ideal field strength at the injection point for convenience sake. Variables a , r_0 and φ_0 are wave length, injection radius, and initial phase, respectively. The phase slip induced by the field deviation is calculated for the 4 MeV/A C^{6+} beam. The relation between the deviation amplitude and the wave length is shown in Fig. 3 for the cases giving the phase slips of less than 1 and 2 degs. The initial phase φ_0 , which corresponds to the deviation at the injection point, is required to be as small as possible. The value is set to be zero in this case. The phase slip can be estimated for more complicated patterns of the deviation, too.

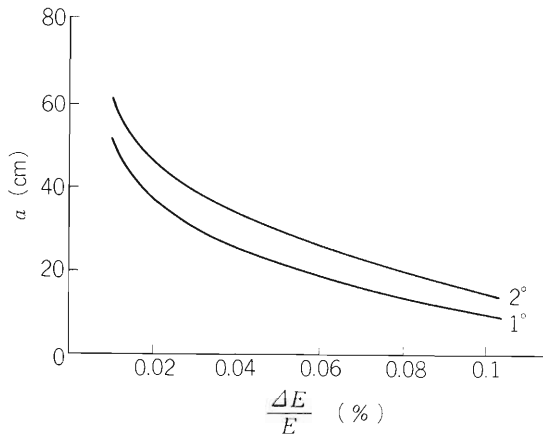


Fig. 3. Relation between the field deviation amplitude and its wave length at the phase slip of less than 1° and 2° .

References

- 1) N. Nakanishi and S. Motonaga: IPCR Cyclotron Progr. Rep., 13, 12 (1979).
- 2) N. Nakanishi and S. Motonaga: *ibid.*, 12, 18 (1978).
- 3) A. Goto, Y. Yano, T. Wada, and N. Nakanishi: *ibid.*, 14, 170 (1980).

11-12. Design of Beam Transport System for the IPCR SSC

N. Kishida, Y. Yano, and T. Wada

The beam transport system for the accelerator complex of the IPCR heavy-ion facility has been designed. This complex consists of a separated-sector cyclotron (SSC), RILAC (Riken heavy-ion linac facility) and an AVF cyclotron. RILAC and the AVF cyclotron function as pre-accelerators. The beam lines of accelerators are not on the same horizontal plane and a three dimensional layout is taken into account. Horizontal and vertical distances between RILAC and the SSC are about 25 m and 19 m, respectively, and those between the AVF cyclotron and the SSC are about 25 m and 8.5 m, respectively. The designed beam transport systems are shown in Figs. 1 and 2. The systems consist of two kinds of quite symmetric subunits. One is an achromatic bending section and the other is a straight beam guiding section with some quadrupole magnets. Charge stripping and charge selection parts are installed between SL0 and SL2 (cf. Fig. 1) and between SC0 and SC3 (cf. Fig. 2) in order to decrease the magnetic rigidity of pre-accelerated ions and to increase the attainable maximum energy of the SSC. The horizontal and vertical phase-space matching is performed in the section between SL10 and SL11, where the beam is achromatic. Dispersion matching is carried out in the subsequent beam injection system.¹⁾

The calculations of ion-optics in the beam transport system have been made with the aid of computer program TRANSPORT.²⁾ This program is based on the matrix formalism for the beam

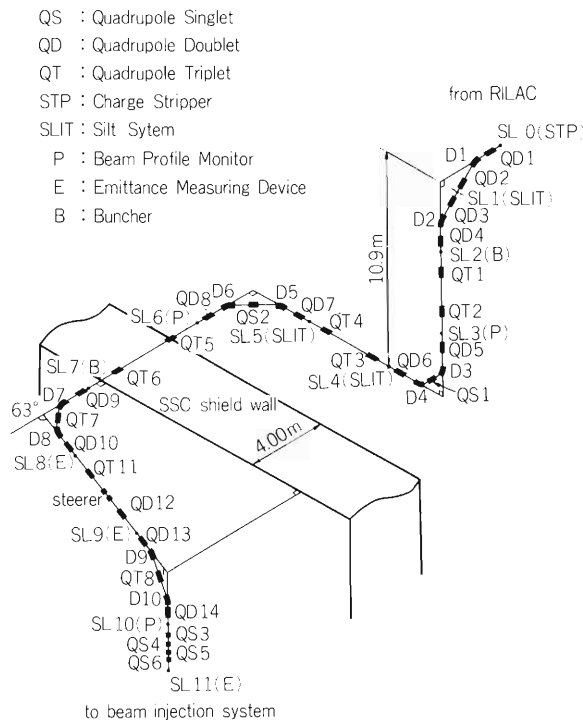


Fig. 1. Layout of the beam transport system from RILAC to the SSC. The entrance of the beam transport system (SL0) is about 15 m distant from the exit of linac. The beam line from the AVF cyclotron flows into this system at switching magnet D8.

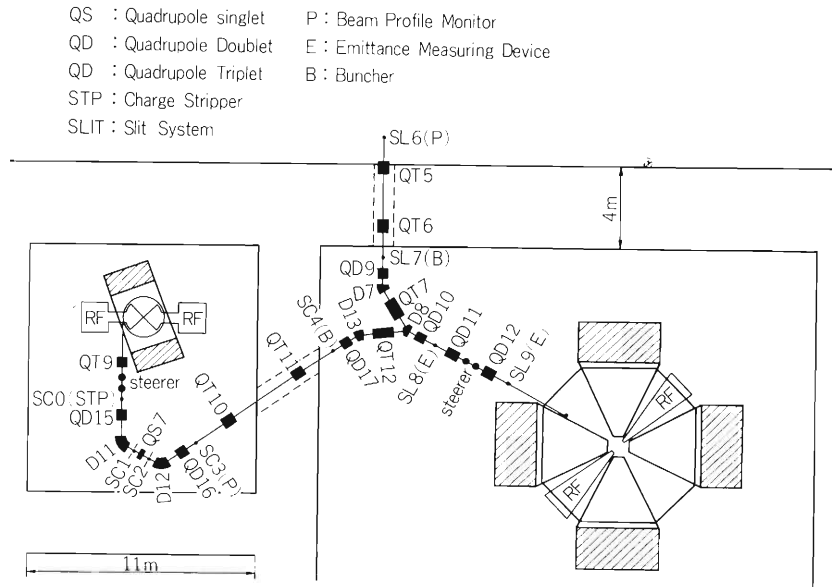


Fig. 2. Layout of the beam transport system from the AVF cyclotron to the SSC.

optics. The calculations have been performed within the first-order approximation. Further, the second-order calculations have been also performed in order to estimate aberrations. Every subsystem before the beam matching section is formed by a double-telescopic transport system whose transformation matrix is the unity or negative unity diagonal one.

As an example, the structure diagram of charge stripping and charge selection part from SL0 to SL2 is shown in Fig. 3. This system is also a 90°-bending achromatic transport system with a mirror symmetry with respect to the point SL1. Figure 4 shows that $^{238}\text{U}^{40+}$ and $^{238}\text{U}^{39+}$

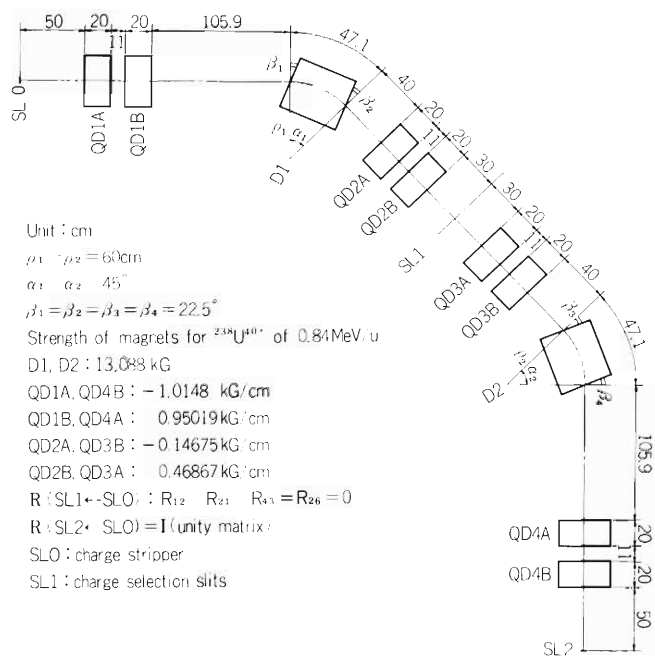


Fig. 3. Charge stripping and charge selection part with two rectangular dipole magnets and eight quadrupole magnets in the system I. This is also a 90°-bending achromatic transport system.

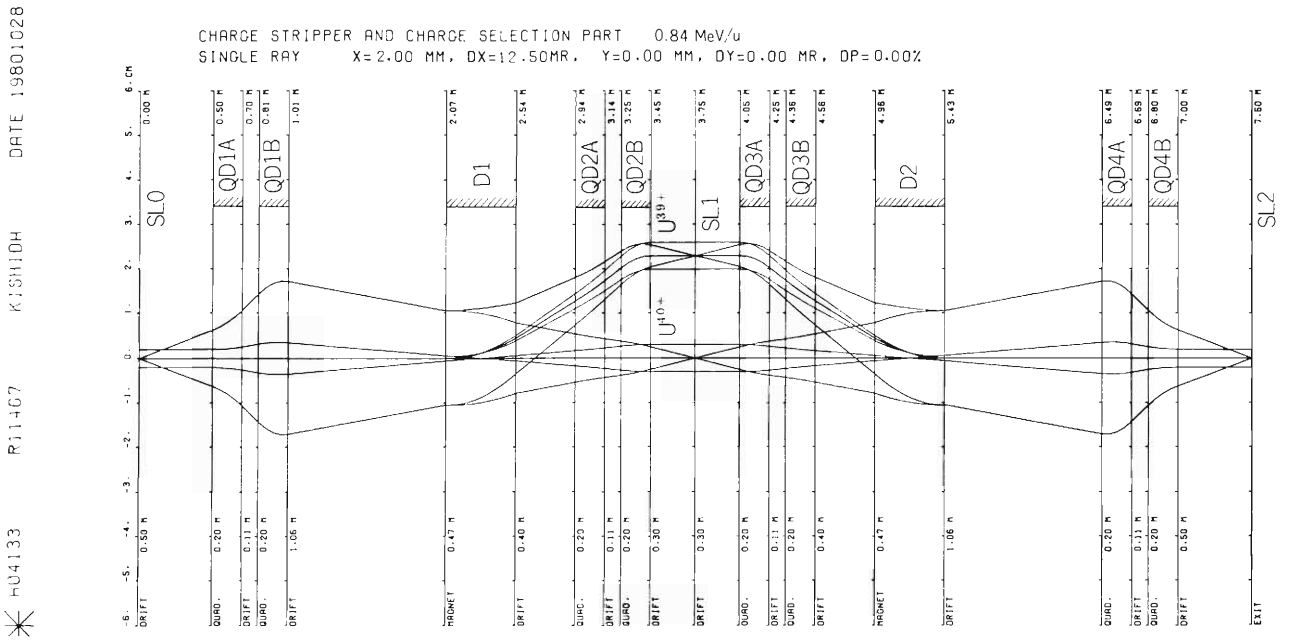


Fig. 4. Single ray plot for the $^{238}\text{U}^{40+}$ and $^{238}\text{U}^{39+}$ beams of 0.84 MeV/u. Both beams are clearly separated at the charge selection slit S2. This figure also indicates that this system is an achromatic system.

beams whose object sizes are 0.4 cm are clearly separated at the charge selection slit (SL1). The distance between two beams is about 2.5 cm.

The more detailed information has been published in Ref. 3 .

References

- 1) Y. Yano: Sci. Papers I.P.C.R., 74 , 13 (1980); A. Goto, Y. Yano, T. Wada, and N. Nakanishi: *ibid.*, p.124.
- 2) K. L. Brown, F. Rothacker, D. C. Carey, and Ch. Iselin: SLAC Report, No. 91 (1974).
- 3) N. Kishida, Y. Yano, and T. Wada: Sci. Papers I.P.C.R., 74, 105 (1980).

11-13. Vacuum System of the SSC (I)

Vacuum Considerations in Some Aspects

S. Nakajima and K. Ikegami

An accelerator chamber is designed for the separated-sector cyclotron (SSC). Vacuum considerations for the chamber are as follows:

1) Pressure in the chamber

Beam loss in an accelerator can be estimated from the following relation:

$$N(X) = N_0 \exp (-3.54 \times 10^{-16} \sum_i \sigma_i \times P_i \times X_i)$$

where N_0 is the number of incident particles and $N(X)$ is that of surviving particles after travelling a distance of X_i (cm). σ_i (cm^2) is the cross section which describes the beam loss due to an interaction with any remaining gas molecules. P_i (Torr) is the pressure of the gas in question. Because σ_i and X_i take various values depending on the species of the colliding particles and the conditions of acceleration, such a universal chart as that shown in Fig. 1 will be of considerable use to estimate the required pressure in the chamber. Particles accelerated will move a distance of

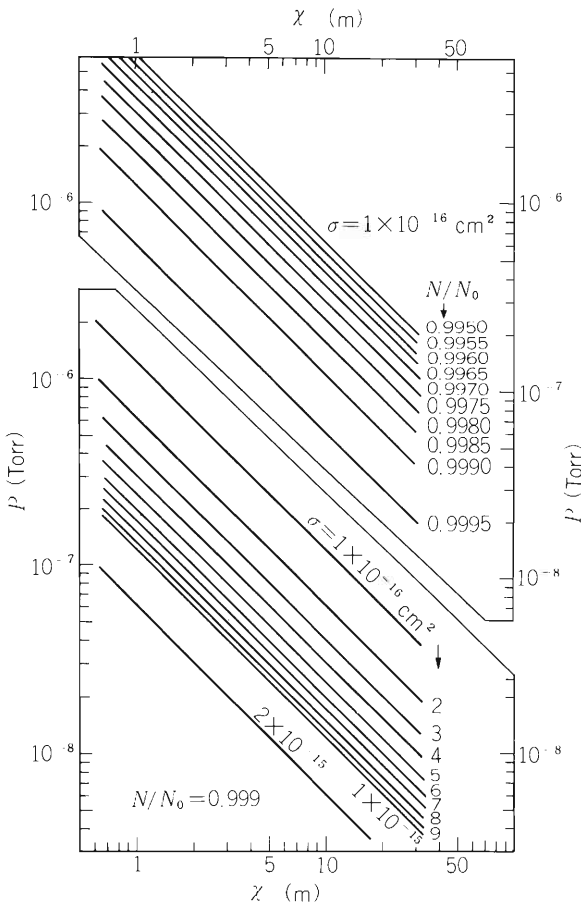


Fig. 1. Relation between the pressure in the chamber and the travelling distance of the particles. σ_i or $N(X)/N_0$ is taken as parameter.

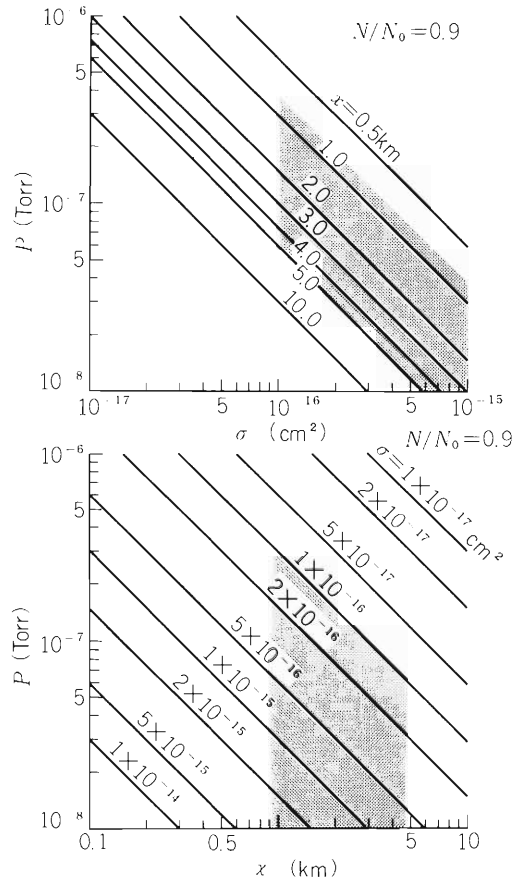


Fig. 2. Pressure to secure 90% survival of the accelerated particles as a function of cross section, and total travelling distance in the SSC.

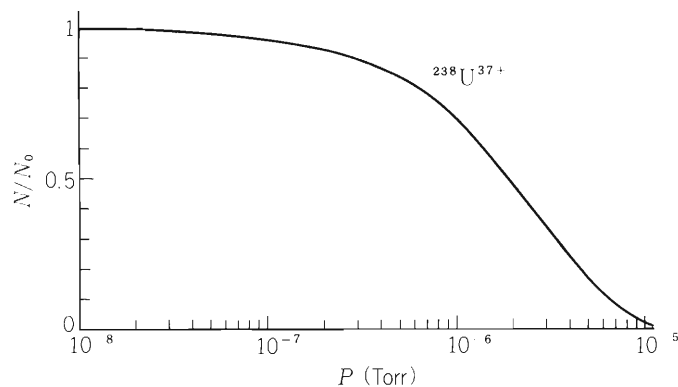


Fig. 3. Calculated attenuation for $^{238}\text{U}^{37+}$ through the SSC as a function of pressure.

several km through the SSC. When we can consider the value of σ_i to be almost constant during acceleration, Fig. 2 will be more convenient. The shaded region will be available to the SSC. It is seen that the pressure in the chamber should be kept below 1×10^{-7} Torr to suppress the beam loss to a value as low as 10 percent of the incident beam. Beam attenuation through the SSC can be also calculated as a function of pressure. An example for $^{238}\text{U}^{37+}$ is shown in Fig. 3 where $\sigma_i \times (V/C)$ is taken to be $1 \times 10^{-17} \text{ cm}^2$ (V is the velocity of the particles and C is that of light).

2) Outgassing rate and pumping speed

We considered a plan in which the main coils are placed outside of the vacuum chamber. The total surface area exposed to the vacuum will be $\sim 550 \text{ m}^2$ for the chamber. The evolution of gas from the constituent materials are estimated as given in Table 1. If we assume that leakage through the chamber walls is $1 \times 10^{-3} \text{ Torr}\cdot\ell/\text{sec}$, the total outgassing rate in the chamber amounts approximately $17 \times 10^{-3} \text{ Torr}\cdot\ell/\text{sec}$. The trim-coils on the magnets are not taken into account in the estimation because the details of these system are not determined yet. It may be possible to put them in the vacuum chamber. The gas evolution increases further in that case.

Table 1. Surface areas exposed to the vacuum and outgassing load from these surfaces.

Component (Material)	Surface area (m^2)	Outgassing rate after 20 h pumping ($\text{Torr}\cdot\ell/\text{sec}\cdot\text{cm}^2$)	Total outgassing rate ($\text{Torr}\cdot\ell/\text{sec}$)
Vacuum Chamber (Stainless steel)	180	2.5×10^{-10}	0.5×10^{-3}
Resonators (Copper)	300	1.8×10^{-10}	0.6×10^{-3}
Magnets (Mild steel)	60 (when nickel plated)	2.0×10^{-8} (2.1×10^{-10})	12×10^{-3} (0.13×10^{-3})
Elastomer seals	2.5	1.2×10^{-10}	3×10^{-3}
Total	550		16×10^{-3}

The major contributors to the degassing rate are the elastomer seals and the magnet poles composed of mild steel. It is desirable to use metal gaskets instead of elastomer seals if possible and to cover the pole surfaces with nickel plating. Even with such a procedure, the outgassing rate can not be decreased to a value less than $6 \sim 7 \times 10^{-3}$ Torr·ℓ/sec. Total pumping speed of $6 \sim 7 \times 10^4$ ·ℓ/sec is therefore required to maintain the pressure in the chamber at 1×10^{-7} Torr. Cryopumps and turbomolecular pumps with high pumping speed will satisfy the demand. Because conductance in the magnet gaps is very low (1000 ~ 2000 ℓ/sec, at the best), it is impossible to exhaust the chamber through these gaps. Pump will be installed to every RF resonator and every valley section of the chamber.

11-14. Vacuum System of the SSC (II)

A Preliminary Design of the Vacuum Chamber for the SSC

K. Ikegami, S. Nakajima, and Y. Ikegami

IPCR separated sector cyclotron, which is designed to accelerate all elements up to uranium, consists of four sector magnets with a sector angle of 50° and a pole gap of 80 mm, two delta resonators of half wave length type with a dee angle of 20° , injection and ejection systems, and a vacuum chamber. The operating pressure required in the chamber for sufficient transmission of heavy ions is less than 10^{-7} Torr.¹⁾

The vacuum chamber for the SSC should be designed by taking into accounts the following conditions:

- 1) The chamber must accommodate the magnetic and electric injection channels of the injection system at the central region.
- 2) Space is narrowly limited between the sector magnet and RF resonator at central region.
- 3) To make overhaul or repair, the two resonators must be pulled out from the chamber.

In order to fulfil the above conditions, we have designed a vacuum chamber made of stainless steel which has the delta-shaped horizontal flanges to accommodate two resonator sections.

Figure 1 shows a plan view of the vacuum chamber for the SSC.

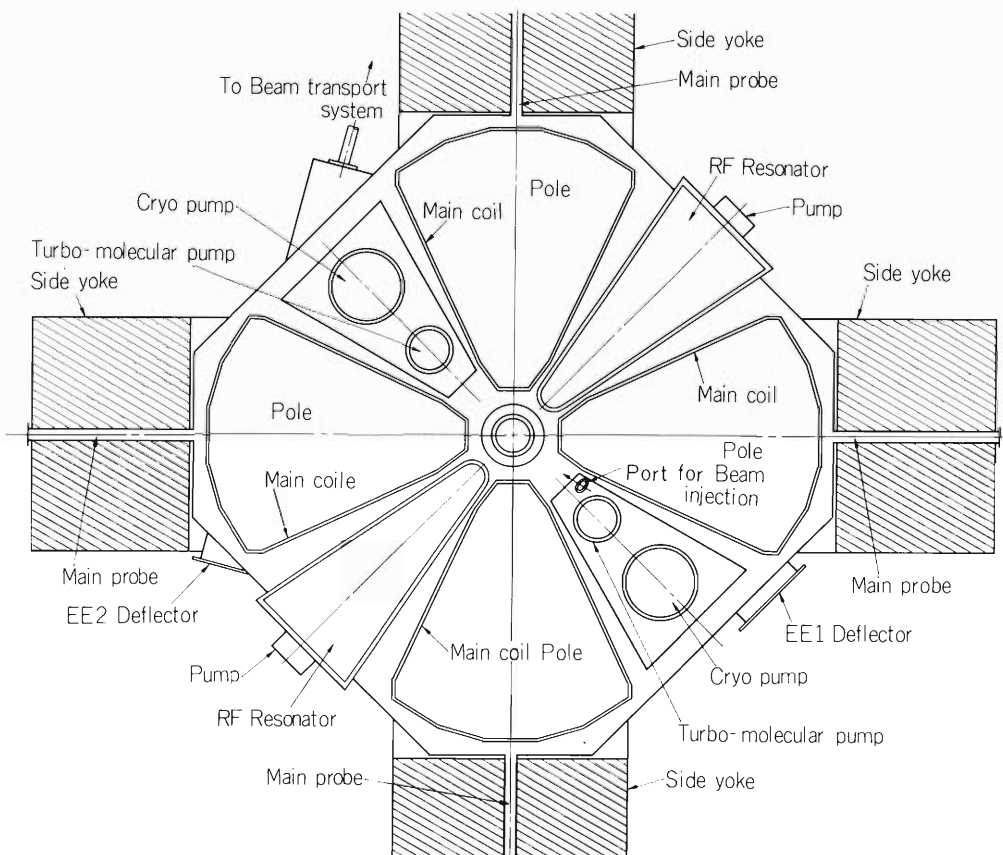


Fig. 1. Plan view of the vacuum chamber for the SSC.

The size of the chamber is as follows:

diameter	9 m
height magnet and valley sections	1.6 m
resonator sections	7.4 m
total volume	78 m ³
total surface area	550 m ²

Magnet section

Side flanges of the chamber are welded around the pole so that the main coil is placed out of the chamber. The size of the main coil is about 35 mm × 550 mm. The magnet section is connected to the valley and resonator sections vacuum-tight by welding or elastomer seals. In this case, trim coils of 32 pairs are in the vacuum. Figure 2 shows a cross-sectional view of the

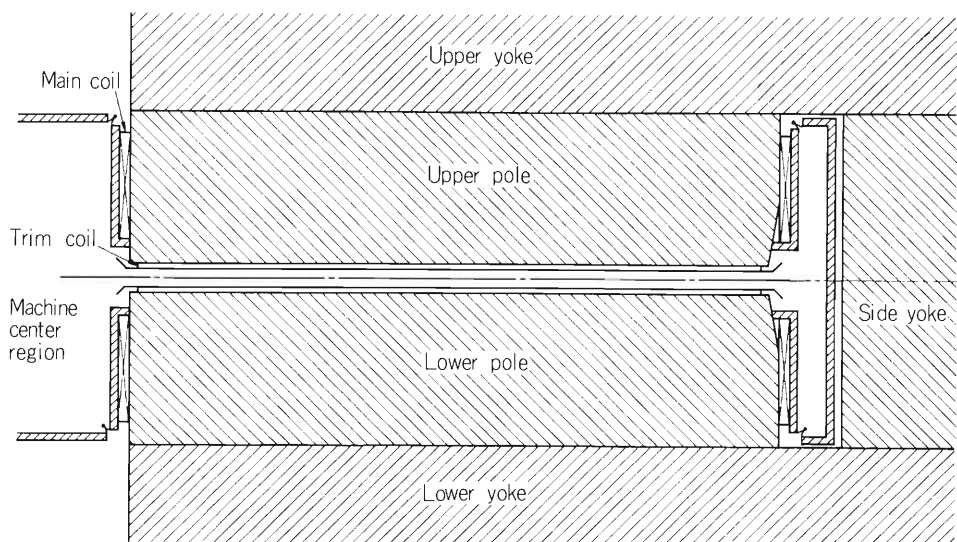


Fig. 2. Cross-sectional view of the vacuum chamber for the magnet section.

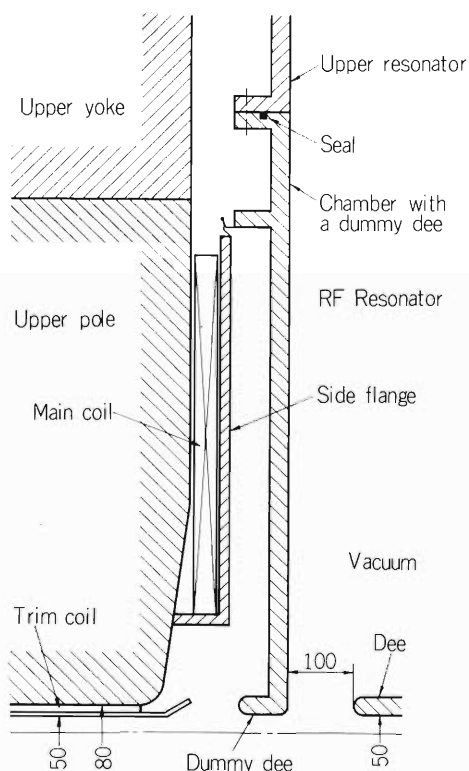


Fig. 3. Cross-sectional view of the vacuum chamber showing connection scheme between the sector-magnet and RF resonator sections at the minimum radius.

vacuum chamber for the magnet section and Fig. 3 a cross-sectional view of the vacuum chamber showing connection scheme between the sector magnet and RF resonator sections at the minimum radius.

RF resonator section

In the present design, the RF resonator section is made of three parts: the upper (lower) part of the section can be moved upward (downward) about 1 m to pull out from the main chamber. Upper and lower parts will be connected using the elastomer seal to the main chamber section.

Pumping system

The pumping system of the SSC is composed of high vacuum pumping system and rough pumping system. High vacuum pumping system consists of cryo-pumps and turbo-molecular pumps connected in parallel. These pumping systems will be installed at the valley and resonator sections.

Reference

- 1) S. Nakajima and K. Ikegami: IPCR Cyclotron Progr. Rep., 14, 195 (1980).

11-15. Design and Operational Performance of Superconducting Coil for Model Sector Magnet of the IPCR SSC

N. Yasumitsu, T. Minakuchi, E. Toyota, and N. Kishida

At an early stage of the design of the separated-sector cyclotron (SSC), it was intended to accelerate the ions injected from the heavy-ion linac by using 8th harmonics. The maximum field strength of sector magnets was 17.5 kG and the power necessary for the four main coils was estimated to be about 1 MW. This power consumption was too large from viewpoint of the present energy circumstances. Thereupon we tried to adopt superconducting coils of the sector magnets in order to decrease the power consumption.

A superconducting coil was designed for a 1/4 scale model sector magnet of the SSC. The design parameters of the coil are listed in Table 1. Direct immersion cooling method in a liquid helium bath was used. Figures 1 and 2, respectively, show outline and cross sectional views of the cryostat. It is designed so as to have the same dimensions as normal copper coils already used in the model magnet. A welded helium can is completely enclosed by a copper can wrapped

Table 1 Specification of superconducting coil.

Max. excitation	:	32500 AT
Conductor	:	NbTi, 1.6 × 2.5 mm
Copper ratio	:	4 : 1
Operating max. current	:	650 A
Critical current	:	1000 A at 5T
Number of turns	:	50
Max. current density	:	162.5 A/mm ²
Weight	:	30 kg/coil

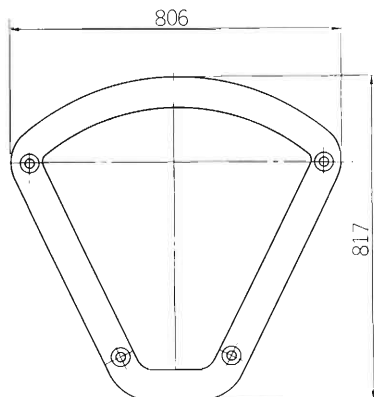


Fig. 1. Outline of the cryostat.

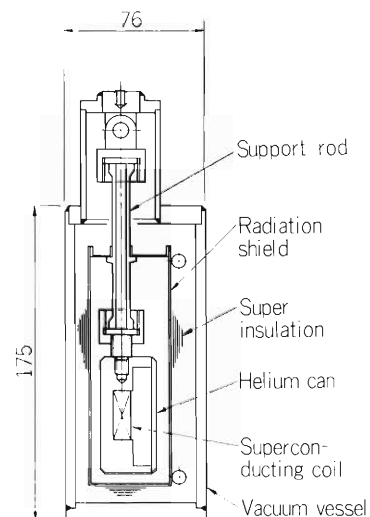


Fig. 2. The cross sectional view of the cryostat.

with 16 layers of super insulation to shield from heat radiation. This copper shield is housed in a vacuum chamber cryostat made of stainless steel. The coil is suspended by four FRP rods of 10 mm diameter.

The strength of magnetic leakage flux through the coil was estimated from the calculations of the magnetic induction of model magnet by using program TRIM.¹⁾ The stabilization design of the coil was carried out with the aid of the results of calculations. The maximum magnetic induction on the coil surface was estimated to be about 4 kG.

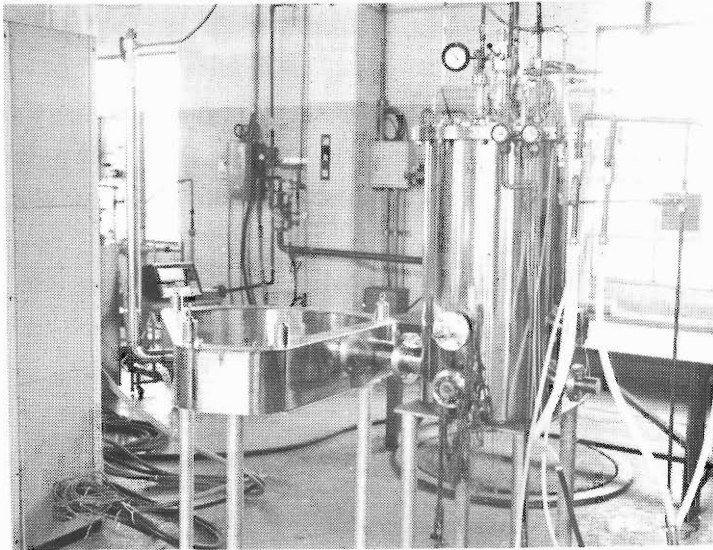


Fig. 3. Fully assembled superconducting coil.

Test of the coil was made by applying a current without mounting it in the model magnet. Figure 3 shows the fully assembled superconducting coil. The cryostat of the coil is connected with a liquid He vessel to supply electric current and liquid He. The coil reached the designed maximum current without any quench. The coil was cooled from room temperature to that of liquid N₂ in 40 min. It took another 110 min to cool the coil down to liquid He temperature. The total thermal loss amounted to 4.7 W in operation for supplying a current of 650 A. This result agreed with the estimating value. Several strain gauges were set on the coil bobbin in order to measure the deformation of the coil due to magnetmechanical force. But they did not function well.

Recently the design of the SSC has been modified so that ions are accelerated by means of harmonic number 9 in place of 8. The modification allows to use a wide space in the central region of the SSC and to save the power consumption.²⁾ As a result of this choice, the total power consumed in the main coils of the sector magnets has been reduced by more than one-half, from 960 kW to 450 kW. It is estimated that the initial and operating cost of superconducting coil system exceeds that of normal copper coil system. Hence the merit which might have been given by introduction of superconducting coil has been lost. The construction group of the SSC decided to adopt normal copper coil.

References

- 1) J. S. Colonias and J. H. Porst: Magnet Design Applications of the Magnetostatic Program Called TRIM, UCRL-16382 (1965).
- 2) H. Kamitsubo: Proc. of 3rd Symp. on Accelerator Science and Technology, at RCNP, Osaka, Aug., p.325 (1980).

11-16. Present Status of Radiation Shielding for the Riken SSC Facility

S. Fujita, S. Yamaji, and T. Shikata

The Riken SSC will accelerate protons in the energy range up to 200 MeV, deuterons, alpha particles, carbon, nitrogen, and neon ions up to 135 MeV/A, and heavier ions in lower energy region. The maximum beam current will be 1 μ A.

In considering the problem of radiation protection, we decided to take the value of 100 mrem/W (2 mrem/h when one week is considered as 48 h) for the allowed radiation levels in the radiation control area, 30 mrem/W (0.6 mrem/h when one week is considered as 48 h) on the outer surfaces of the shielding walls, and 10 mrem/W (0.06 mrem/h when one week is considered as 168 h) at the boundary with inhabitants.

In addition to these values, we adopted internally a value of 5 mrem/Y at the boundary with inhabitants as the design goal of the shielding calculation. This means that we will design the shielding of the cyclotron and experimental facilities to reduce radiations from them at the boundary below this value.

Table 1. Calculated number of neutrons per steradian and per 20 MeV energy range produced by the interaction of 1000 ions of a) 200 MeV p with ^{27}Al and of b) 135 MeV/A ^{12}C with ^{56}Fe , respectively. Table 1 (a) was obtained from Fig. 1 of Ref. 2.

Table 1 (b) was approximately obtained by increasing the energy of emitted neutrons in Table 7 of Ref. 3 by the amount of 35 MeV, as the incident energy of ^{12}C accelerated in the Riken SSC is by 35 MeV/A higher than that given in Ref. 3.

(a)

Energy (MeV) \ θ	θ				
	$0^\circ - 20^\circ$	$20^\circ - 40^\circ$	$40^\circ - 60^\circ$	$60^\circ - 120^\circ$	$120^\circ - 180^\circ$
0 - 20	42.7	24.0	26.0	5.4	1.34
20 - 40	16.8	10.0	8.0	2.6	0.30
40 - 60	13.4	7.4	5.4	0.88	0.04
60 - 80	12.0	6.0	3.6	0.16	0.0
80 - 100	9.5	5.4	2.3	0.013	0.0
100 - 120	8.01	4.6	1.24	0.0	0.0
120 - 140	7.55	3.5	0.52	0.0	0.0
140 - 160	7.02	2.2	0.18	0.0	0.0
160 - 180	5.59	0.8	0.032	0.0	0.0
180 - 200	1.67	0.1	0.0034	0.0	0.0

(b)

Energy (MeV) \ θ	θ				
	$0^\circ - 20^\circ$	$20^\circ - 40^\circ$	$40^\circ - 60^\circ$	$60^\circ - 120^\circ$	$120^\circ - 180^\circ$
35 - 55	30	33	29.4	23.4	25.2
55 - 75	122	49	22	11	18.1
75 - 95	100	27	9.2	5	9.4
95 - 115	24	7.4	2.5	1.2	1.4
115 - 135	5.8	1.7	0.3	0.24	1.1
135 - 155	1.6	0.6	0.14	0.06	0.73
155 - 175	0.52	0.2	0.04	0.01	0.04

Table 2. Conversion factors from particle flux density to dose rate for neutrons.

Neutron energy (MeV)	Conversion factor (n/cm ² sec/mrem/h)	Neutron energy (MeV)	Conversion factor (n/cm ² sec/mrem/h)
2.5×10^{-8}	265	3×10^0	7.0
1×10^{-7}	242	5×10^0	6.8
1×10^{-6}	222	1×10^1	6.8
1×10^{-5}	231	2×10^1	6.5
1×10^{-4}	239	5×10^1	6.1
1×10^{-3}	272	1×10^2	5.55
1×10^{-2}	283	2×10^2	5.10
1×10^{-1}	48	5×10^2	3.60
5×10^{-1}	14	1×10^3	2.25
1×10^0	8.5	2×10^3	1.55
2×10^0	7.0		

Since the most penetrating component of radiation is high-energy neutrons,¹⁾ our effort is concentrated on the shielding against neutrons.

Among the neutrons ejected by nuclear reaction between energetic ion beams and targets, the number of high energy neutrons will differ by no more than a factor of two for various combinations of target materials and incident particles with the same energy per nucleon, after Refs. 2, 3, and 4. So we considered following two typical reactions as sources of neutrons to estimate the thickness of the shielding wall: 1) proton beams incident on a thick aluminum target and 2) carbon beams incident on a thick iron target. Spectra of neutrons which will be emitted in the above two cases are shown in Table 1.^{2), 5)}

There are two kind of radiations which have to be considered: the direct radiation coming through the shielding wall and the skyshine due to the backscattering of radiation from the atmosphere. In order to calculate the radiation levels in the control area and on the outer surface of the shielding, the skyshine was neglected because of its smallness compared with the direct radiation in the region near the neutron source. The direct radiation due to the attenuation can be estimated by the relation

$$\phi_D = \frac{\phi_0}{r^2} \exp(-\mu x). \quad (1)$$

Here ϕ_D is the neutron flux density (n/cm²) at distance r from the source, ϕ_0 is the neutron flux density (n/sr) at the source, μ is the linear absorption coefficient of ordinary concrete (cm⁻¹),⁶⁾ and x is the thickness of walls. In this calculation, factors for converting neutron flux density to dose equivalent shown in Table 2⁷⁾ was used. The results obtained are shown in Fig. 1. Here, a larger value between the calculated values of $r^2 \cdot \text{dose-rate}$ for both cases (p on Al and C on Fe) was selected in each angular region. From these curves one can easily determine the shield thicknesses in various directions with respect to the beam. For example, the design of a beam dump shield is shown in Fig. 2. The radiation level just outside the beam dump shield was taken to be 2 mrem/h.

The radiation level at the boundary with inhabitants was estimated only by the contribution from skyshine, neglecting that of the direct radiation, because the latter decreases more rapidly than the former as the distance between the source and the observing point increases. Also the fact that the building of the SSC is designed to be buried in the ground reduces the contribution of the direct radiation.

For our calculation of the skyshine effect, we used the following empirical expression given by Thomas⁸⁾ which is to be used at distances larger than about 50 meters:

$$\phi_s = \frac{aQ}{4\pi r^2} \left\{ 1 - \exp\left(-\frac{r}{\alpha}\right) \right\} \exp\left(-\frac{r}{\lambda}\right) \quad (\text{n/cm}^2 \cdot \text{sec}) \quad (2)$$

$$\text{for } r \gtrsim 50 \text{ m,}$$

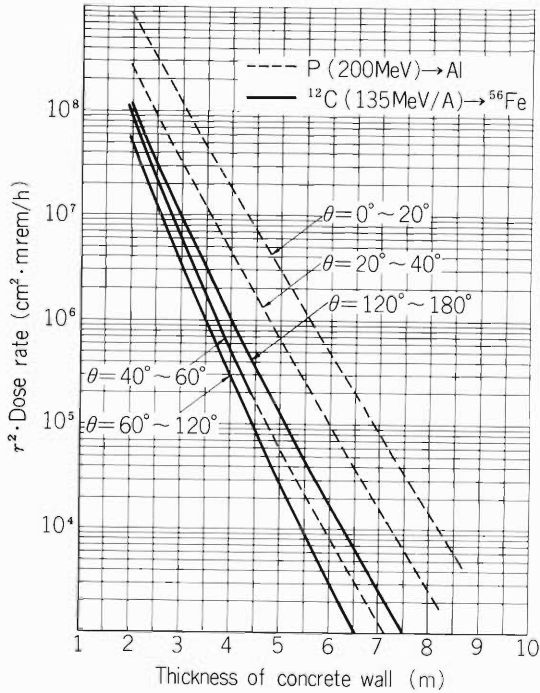


Fig. 1. Dose rate multiplies by r^2 vs thickness of concrete wall.

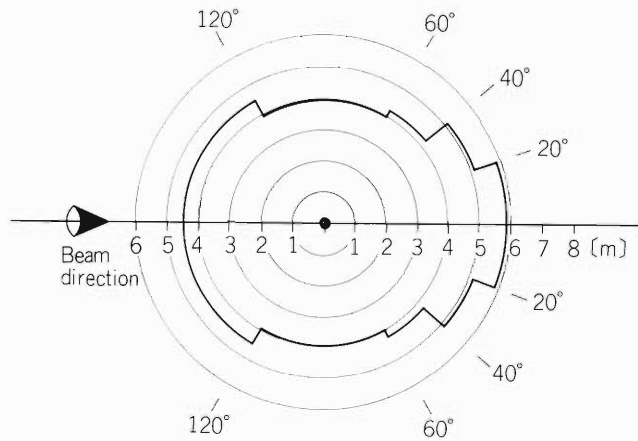


Fig. 2. The design of a beam dump shield of iso-dose rate contours, where the shield material is ordinary concrete. ($\rho = 2.4 \text{ g/cm}^3$)

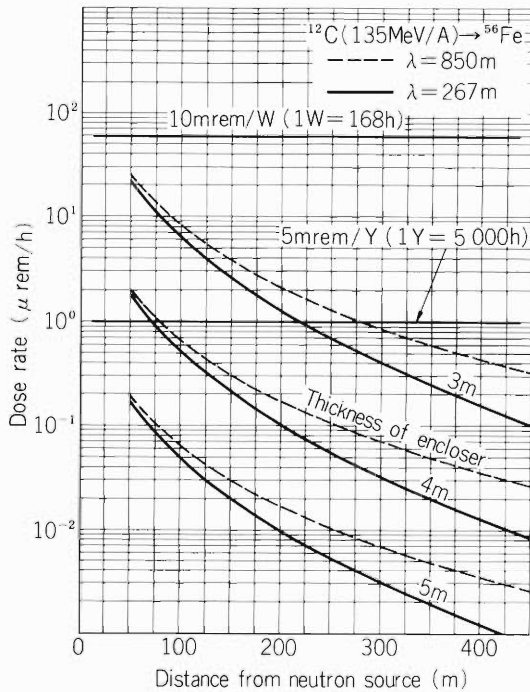


Fig. 3. Spatial distribution of neutron skyshine. Values of 267 m and 850 m for the attenuation length λ were adopted as minimum and maximum values, respectively.

where Q stands for neutron source strength in unit of n/sec , a and α stand for fitting parameters which reproduce the experimental data, λ stands for attenuation length in air and r stands for the distance from the source. Following values are taken for a , α , and λ :

- $a = 2.8,$
- $\alpha = 56 \text{ m},$
- $\lambda = 267 \text{ m or } 850 \text{ m}.$

Equation (2) is considered to be the most reliable one at present, although we have not yet obtained satisfactory results due to the complexity of the skyshine problem.

As the yield of neutron skyshine for the case of carbon was by a factor of about 10 larger than that for proton, the result for carbon was chosen in our calculation. The result together with the radiation levels for design criterion is shown in Fig. 3. As there are several observed values for the attenuation length λ , the calculation was performed for two extreme values of $\lambda = 267$ m and 850 m and the corresponding results are shown by solid and dashed curves, respectively. Using this figure, the required roof thickness can be estimated to be more than 4 m, if the nearest boundary with inhabitants is located at 100 m from the SSC facility.

References

- 1) R. G. Alsmiller: Nucl. Instr. and Meth., 72, 213 (1969).
- 2) H. A. Smith: IUCF Internal Rep., No. 74-6 (Radiation Shielding Note 1).
- 3) S. J. Lindenbaum: Ann. Rev. Nucl. Sci., 11, 213 (1961).
- 4) T. Nakamura: INS-NUMA-5, p.321 (1977).
- 5) J. Drouet and A. Leleux: "Rapport de synthese des calculs effectues pour la determination des blindages de l'accelerateur GANIL", D. CEN-S/SPR/SRI/78-342 GRA-066JD/AI 5 mai (1978).
- 6) R. Wallace: Nucl. Instr. and Meth., 18-19, 405 (1962).
- 7) H. W. Patterson and R. H. Thomas: "Accelerator Health Physics", Academic Press, p.69 (1973).
- 8) H. W. Patterson and R. H. Thomas: *ibid.*, p.442.

12. LIST OF PUBLICATIONS

1. Machine development and accelerator physics
 - 1) Y. Yano: "Design of Injection System for Separated Sector Cyclotron Proposed at the Institute of Physical and Chemical Research (I)", Sci. Papers I.P.C.R., 74, 13 (1980).
 - 2) N. Kishida, Y. Yano, and T. Wada: "Design of Beam Transport System for the IPCR SSC(I)", Sci. Papers I.P.C.R., 74, 105 (1980).
 - 3) A. Goto, Y. Yano, T. Wada, and N. Nakanishi: "Design of Injection System for the IPCR SSC (II)", Sci. Papers I.P.C.R., 74, 124 (1980).

2. Nuclear physics and nuclear instrumentation
 - 1) M. Yanokura, I. Kohno, H. Nakahara, and K. Yanakoshi: "Heavy Ion Identification System by Using a Gas Proportional Telescope", Oyo Buturi, 49, 1095 (1980).
 - 2) H. Ohnuma, T. Kubo, N. Kishida, T. Hasegawa, N. Ueda, T. Fujisawa, T. Wada, K. Iwatani, and T. Suehiro: "Vector Analyzing Power and Polarization Measurements for the $^{116}\text{Sn}(d, p)^{117}\text{Sn}$ Reaction and Deuteron D-State Effects", Phys. Lett., 97B, 192 (1980).
 - 3) T. Wada, H. Kumagai, and T. Inamura: "Data Processing System for IPCR Linac", Genshikaku Kenkyu, 25, No.2 (1980).
 - 4) H. Kamitsubo: "Heavy Ion Reaction - Quasi Elastic and Deep Inelastic Collision", Butsuri, 35, 981 (1980).

3. Atomic and solid-state physics
 - 1) M. Uda, K. Maeda, H. Endo, Y. Sasa, and M. Kobayashi: "Chemical Effect on Ion-Induced L X-Ray Spectra of Transition Elements", Proc. Intern. Conf. X-Ray Processes and Inner-Shell Ionization, Plenum Pub. Co., New York (1980).
 - 2) Y. Awaya: "Systematics of Multiple Ionization in Heavy Ion Collisions", Electronic and Atomic Collisions, North-Holland Pub. Co., Amsterdam, p.325 (1980).
 - 3) T. Okada and H. Sekizawa: "Mössbauer Study of ^{119}Sn in Chromium and Manganese Dioxides", J. Magn. Magn. Mat., 15-18, 649 (1980).
 - 4) Y. Awaya, T. Katou, H. Kumagai, T. Tonuma, Y. Tendow, K. Izumo, A. Hashizume, T. Takahashi, and T. Hamada: "Ratio of Single K-Shell Ionization Cross Section to Double K-Shell Ionization Cross Section in Heavy-Ion-Atom Collision", Phys. Lett., 75A, 478 (1980).
 - 5) H. Endo, M. Uda, and K. Maeda: "Influence of the Chemical Bond on the Intensities of F $K\alpha$ X-Ray Satellites Produced by Electron and Photon Impacts", Phys. Rev. A, 22, 1436 (1980).
 - 6) T. Tonuma, Y. Awaya, T. Kambara, H. Kumagai, M. Kase, A. Yagishita, and I. Kohno: "Krypton $K\beta/K\alpha$ Intensity Ratios for 6 MeV/amu Ion Bombardment", Atomic Collision Research in Japan (Progr. Rep.), 6, 86 (1980).
 - 7) T. Kambara, Y. Awaya, A. Hitachi, M. Kase, I. Kohno, and T. Tonuma: "X-Rays from 110 MeV Ne Ions Passing through Gaseous Targets", Atomic Collision Research in Japan, (Progr. Rep.), 6, 91 (1980).
 - 8) H. Fukushima and N. Shiotani: "Positron Annihilation in Amorphous Alloys", Solid State Phys., 15, 475 (1980).

- 9) K. Maeda and M. Uda: "Application of Anomalous Oxygen $K\alpha$ 532 eV Peak for the Determination of Metal Oxide Thickness", *Spectrochimica Acta*, 35B, 561 (1980).
4. Radiochemistry, radiation chemistry and radiation biology
- 1) F. Ambe and S. Ambe: "Mössbauer Emission Studies of Defect ^{119}Sn , ^{119}Sb , and $^{119\text{m}}\text{Te}$ Atoms after Nuclear Decays and Reactions in SnSb , SnTe , and Sb_2Te_3 ", *J. Chem. Phys.*, 73, 2029 (1980).
 - 2) F. Yatagai, T. Takahashi, and A. Matsuyama: "Effect of Heavy Ions on Bacterial Spores", *Int. J. Radiat. Biol.*, 37, 558 (1980).
 - 3) T. Takahashi, F. Yatagai, and A. Matsuyama: "Possible Long Range Effects in the Inactivation of Bacterial Cells by Heavy Ions", *Sci. Papers I.P.C.R.*, 74, 51 (1980).
5. Heavy ion linear accelerator
- 1) M. Kase, Y. Miyazawa, M. Hemmi, and M. Odera: "Initial Performance of the Heavy-Ion Source for the Riken Linac, RILAC", *Proc. 4th Symp. on Ion Sources and Ion Application Technology*, (Ed. T. Takagi), *Inst. Electrical Eng. Japan*, p.257 (1980).
 - 2) M. Odera: "Riken Variable Frequency Linac, RILAC", *Proc. 3rd Symp. on Accelerator Science and Technology*, (Ed. M. Kondo), *RCNP, Osaka Univ.*, p.23 (1980).
 - 3) N. Kishida, Y. Yano, T. Wada, S. Motonaga, and H. Kamitsubo: "Design of the Beam Transport System for the IPCR SSC", *Proc. 3rd Symp. on Accelerator Science and Technology*, (Ed. M. Kondo), *RCNP, Osaka Univ.*, p.41 (1980).
 - 4) T. Kambara, M. Odera, and S. Takeda: "Control System of Riken Linac", *Proc. 3rd Symp. on Accelerator Science and Technology*, (Ed. M. Kondo), *RCNP, Osaka Univ.*, p.131 (1980).
 - 5) M. Yanokura, I. Yokoyama, I. Takeshita, and M. Odera: "Beam Buncher and Chopper of the Riken Variable Frequency Linac, RILAC", *Proc. 3rd Symp. on Accelerator Science and Technology*, (Ed. M. Kondo), *RCNP, Osaka Univ.*, p.147 (1980).
 - 6) M. Kase, I. Yokoyama, M. Hemmi, M. Yanokura, J. Schimizu, and M. Odera: "Beam Diagnostic Probes of the RILAC", *Proc. 3rd Symp. on Accelerator Science and Technology*, (Ed. M. Kondo), *RCNP, Osaka Univ.*, p.151 (1980).
 - 7) M. Hemmi, Y. Miyazawa, M. Kase, T. Inoue, and M. Odera: "Injector Terminal of the RILAC", *Proc. 3rd Symp. on Accelerator Science and Technology*, (Ed. M. Kondo), *RCNP, Osaka Univ.*, p.245 (1980).
 - 8) N. Yasumitu, T. Minakuchi, E. Toyota, and N. Kishida: "Design and Operational Performance of Superconducting Coil for SSC Sector Magnet", *Proc. 3rd Symp. on Accelerator Science and Technology*, (Ed. M. Kondo), *RCNP, Osaka Univ.*, p.319 (1980).
 - 9) M. Odera: "Status of Riken Variable Frequency Heavy Ion Linac, RILAC", *Proc. 5th Linac Technology Conf.*, (Ed. T. Tomimasu), (in Japanese), *Electro-Technical Laboratory, Tsukuba*, p.1 (1980).

(Papers Presented at Meetings)

1. Machine development and accelerator physics
 - 1) Y. Yano, H. Takebe, T. Wada, Y. Obana, S. Motonaga, and H. Kamitsubo: "Model Test of the Injection Bending Magnet of the IPCR SSC", Ann. Meeting of Phys. Soc. Japan, Tokyo, Mar. (1980).
 - 2) N. Nakanishi, N. Iida, S. Motonaga, and H. Kamitsubo: "Orbit Calculation III in IPCR SSC", Ann. Meeting of Phys. Soc. Japan, Tokyo, May (1980).
 - 3) I. Kohno and K. Ikegami: "Multiply-charged Metal Ion Source for Cyclotron", 4th Symp. on Ion Sources and Ion Application Technology, Tokyo, June (1980).
 - 4) I. Kohno, K. Ikegami, and T. Kageyama: "Heavy Ion Source for the IPCR Cyclotron", 3rd Symp. on Accelerator Science and Technology, Osaka, Aug. (1980).
 - 5) Y. Yano, A. Goto, T. Wada, H. Takebe, Y. Obana, N. Kishida, S. Motonaga, and H. Kamitsubo: "Design of Injection System for the IPCR SSC (I)", 3rd Symp. on Accelerator Science and Technology, Osaka, Aug. (1980).
 - 6) A. Goto, Y. Yano, T. Wada, H. Takebe, Y. Obana, N. Kishida, N. Nakanishi, S. Motonaga, and H. Kamitsubo: "Design of Injection System for the IPCR SSC (II)", 3rd Symp. on Accelerator Science and Technology, Osaka, Aug. (1980).
 - 7) M. Hara, K. Ogiwara, and T. Fujisawa: "RF Cavity for IPCR SSC", 3rd Symp. on Accelerator Science and Technology, Osaka, Aug. (1980).
 - 8) N. Nakanishi, K. Yamashita, T. Wada, A. Goto, Y. Yano, S. Motonaga, and H. Kamitsubo: "Orbit Calculations for the IPCR SSC", 3rd Symp. on Accelerator Science and Technology, Osaka, Aug. (1980).
 - 9) I. Kohno: "Ion Source for Accelerator", Symp. on Ion Beam Engineering, Wako, Dec. (1980).

2. Nuclear physics and nuclear instrumentation
 - 1) A. Hashizume, T. Katou, Y. Gono, and Y. Tendow: "The Ground State Band in ^{158}Yb Excited by the $^{142}\text{Nd}(^{20}\text{Ne}, 4n)$ Reaction", Ann. Meeting of Phys. Soc. Japan, Tokyo, Mar. (1980).
 - 2) H. Utsunomiya, T. Nomura, M. Ishihara, Y. Gono, T. Sugitate, and K. Ieki: "Relaxation Phenomenon of Angular Momentum in Heavy-Ion Reactions 2", Ann. Meeting of Phys. Soc. Japan, Tokyo, Mar. (1980).
 - 3) K. Ieki, M. Ishihara, T. Nomura, Y. Gono, H. Utsunomiya, and T. Sugitate: "Spin Alignment of Heavy Fragment in Heavy Ion Reactions", Ann. Meeting of Phys. Soc. Japan, Tokyo, Mar. (1980).
 - 4) T. Sugitate, T. Nomura, M. Ishihara, H. Utsunomiya, Y. Gono, and K. Ieki: "Polarization Phenomena of Protons in Heavy-Ion Reactions", Ann. Meeting of Phys. Soc. Japan, Tokyo, Mar. (1980).
 - 5) S. Yamaji, A. Iwamoto, K. Harada, and S. Yoshida: "Microscopic Calculation of Frictional Tensors for Ar + Au and Cu + Au", Ann. Meeting of Phys. Soc. Japan, Tokyo, Apr. (1980).
 - 6) T. Fujisawa, S. Motonaga, N. Ueda, S. Yamada, T. Hasegawa, and M. Sekiguchi: "Performance of the IPCR Polarized Proton and Deuteron Source", 5th Intern. Symp. on

- Polarization Phenomena in Nucl. Phys., Santa Fe, (New Mexico), Aug. (1980).
- 7) T. Fujisawa, N. Kishida, K. Kudo, T. Hasegawa, M. Sekiguchi, N. Ueda, M. Yasue, Y. Wakuta, and A. Nagao: "Spin Flip Asymmetry in the Inelastic Scattering of Protons on ^{12}C at Energies from 22.0 to 29.0 MeV", 5th Intern. Symp. on Polarization Phenomena in Nucl. Phys., Santa Fe, (New Mexico), Aug. (1980).
 - 8) N. Ueda, S. Yamada, T. Hasegawa, M. Sekiguchi, T. Fujisawa, and S. Motonaga: "Acceleration of the Polarized Proton and Deuteron at the INS SF Cyclotron", 5th Intern. Symp. on Polarization Phenomena in Nucl. Phys., Santa Fe, (New Mexico), Aug. (1980).
 - 9) T. Sugitate, T. Nomura, M. Ishihara, Y. Gono, H. Utsunomiya, K. Ieki, and S. Kohmoto: "Polarization of Preequilibrium Proton Emission in the $^{93}\text{Nb} + ^{14}\text{N}$ Reaction", Intern. Conf. on Nucl. Phys., Berkeley, Aug. (1980).
 - 10) S. Yamaji, A. Iwamoto, K. Harada, and S. Yoshida: "Microscopic Calculation of Frictional Tensors Including Mass Asymmetry", Intern. Conf. on Nucl. Phys., Berkeley, Aug. (1980).
 - 11) T. Nomura: "Evidence for the Hot-Spot Formation in Heavy-Ion Fusion-Like Reactions", Intern. Conf. on Nucl. Phys., Berkeley, Aug. (1980).
 - 12) S. Kohmoto, M. Ishihara, H. Kamitsubo, T. Nomura, Y. Gono, H. Utsunomiya, T. Sugitate, and K. Ieki: "Lifetime Measurement of a Heavy-Ion Preequilibrium System via α - α Correlation", Intern. Conf. on Nucl. Phys., Berkeley, Aug. (1980).
 - 13) Y. Nagame, M. Watanabe, H. Kudo, H. Muramatsu, H. Nakahara, and I. Kohno: "Heavy-Ion Reactions between 115 MeV ^{14}N and ^{62}Ni ", Discussion Meeting on Radiochem., Hirosaki, Oct. (1980).
 - 14) Y. Nagame, H. Kudo, H. Nakahara, M. Yanokura, and I. Kohno: "Heavy-Ion Reactions between ^{20}Ne and ^{50}Cr (I)", Discussion Meeting on Radiochem., Hirosaki, Oct. (1980).
 - 15) H. Kudo, Y. Nagame, H. Muramatsu, H. Nakahara, K. Miyano, and I. Kohno: "Study on the Proton-Induced Fission of ^{232}Th (III), Mass Yield", Discussion Meeting on Radiochem., Hirosaki, Oct. (1980).
 - 16) H. Kudo, Y. Nagame, H. Muramatsu, H. Nakahara, K. Miyano, and I. Kohno: "Study on the Proton-Induced Fission of ^{232}Th (IV), Angular Distribution", Discussion Meeting on Radiochem., Hirosaki, Oct. (1980).
 - 17) H. Utsunomiya, T. Nomura, M. Ishihara, T. Sugitate, S. Kohmoto, and K. Ieki: "Measurement of Spin Alignment Following Preequilibrium α -Particle Emission in Heavy-Ion Reactions", Ann. Meeting of Phys. Soc. Japan, Fukushima, Oct. (1980).
 - 18) S. Kohmoto, M. Ishihara, H. Kamitsubo, T. Nomura, Y. Gono, H. Utsunomiya, T. Sugitate, and K. Ieki: "Final State Interaction between Two Particles Emitted from Heavy Ion Reactions", Ann. Meeting of Phys. Soc. Japan, Fukushima, Oct. (1980).
 - 19) Y. Nagame, I. Kohno, M. Yanokura, H. Kudo, and H. Nakahara: "Heavy Particle Emissions in Reactions between ^{20}Ne and ^{50}Cr ", Autumn Divisional Meeting of Phys. Soc. Japan, Fukushima, Oct. (1980).
 - 20) T. Sugitate, T. Nomura, M. Ishihara, H. Utsunomiya, K. Ieki, and S. Kohmoto: "Polarization Phenomena of Protons in Heavy-Ion Reactions II", Autumn Divisional Meeting of Phys. Soc. Japan, Fukushima, Oct. (1980).
 - 21) A. Iwamoto, S. Yamaji, K. Harada, and S. Yoshida: "Friction Tensors for $\text{Ar} + \text{Au}$ ",

Autumn Divisional Meeting of Phys. Soc. Japan, Fukushima, Oct. (1980).

- 22) H. Kudo, Y. Nagame, H. Nakahara, K. Miyano, and I. Kohno: "Angular Distributions of Fission Fragments in the Proton-Induced Fission of ^{232}Th ", Autumn Divisional Meeting of Phys. Soc. Japan, Fukushima, Oct. (1980).

3. Atomic and solid-state physics

- 1) Y. Awaya: "Present Studies and Plannings on Atomic Collision in the IPCR", Symp. on Atomic Collisions by Using Accelerators, Tokyo, Jan. (1980).
- 2) Y. Awaya: "Comments on Multiple Inner-Shell Ionization", Symp. on Atomic Collisions in Solids, Tokyo, Jan. (1980).
- 3) T. Okada, H. Sekizawa, F. Ambe, and S. Ambe: "Mössbauer Study of ^{119}Sb in $\alpha\text{-Fe}_2\text{O}_3$ ", Ann. Meeting of Phys. Soc. Japan, Tokyo, Mar. (1980).
- 4) M. Kamiya, A. Kuwako, M. Sebata, K. Ishii, S. Morita, Y. Awaya, and T. Tonuma: "K-Shell Ionization of Elements Ranging from Ca to Ni by 5, 6, and 7 MeV/amu α -Particles and N^{7+} Ions", Ann. Meeting of Phys. Soc. Japan, Tokyo, Mar. (1980).
- 5) N. Shiotani, T. Okada, N. Sakai, H. Sekizawa, and T. Nakamichi: "Compton Profile and Positron Annihilation in Nb-20 at. % Mo", Ann. Meeting of Phys. Soc. Japan, Tokyo, Mar. (1980).
- 6) M. Hara and K. Mori: "Test of Position Sensitive Detector for Spectrometer II", Ann. Meeting of Phys. Soc. Japan, Tokyo, Mar. (1980).
- 7) T. Tonuma, Y. Awaya, T. Kambara, H. Kumagai, and I. Kohno: "The $\text{K}\beta/\text{K}\alpha$ Intensity Ratio of Kr X-Rays Induced by 6 MeV/amu Heavy Ions", Ann. Meeting of Phys. Soc. Japan, Tokyo, Mar. (1980).
- 8) H. Shiraiishi, H. Shinno, N. Yamamoto, N. Kainuma, R. Watanabe, H. Kamitsubo, I. Kohno, and T. Shikata: "Effect of Aging on Helium Embrittlement of Precipitation-Strengthened Fe-Ni-Cr Alloys", Ann. Meeting of the Atomic Energy Soc. Japan, Nagoya, Mar. (1980).
- 9) M. Hara and K. Mori: "Observation of VUV Spectra by Position Sensitive Detector", Spring Meeting of Appl. Phys. Soc. Japan, Kofu, Apr. (1980).
- 10) M. Hara and K. Mori: "Multichannel Detection in Normal Incidence Vacuum Ultraviolet Region", V11th Intern. Conf. on Vacuum Ultraviolet Radiat. Phys., Charlottesville, June (1980).
- 11) T. Mizoguchi, N. Shiotani, U. Mizutani, T. Kudo, and S. Yamada: "Structure and Physical Properties of a Simple Metal-Metal Amorphous Alloy $\text{Mg}_{70}\text{Zn}_{30}$ ", 4th Intern. Conf. on Liquid and Amorphous Metals, Grenoble, July (1980).
- 12) T. Tonuma, Y. Awaya, T. Kambara, H. Kumagai, M. Kase, A. Yagishita, and I. Kohno: "Kr $\text{K}\beta/\text{K}\alpha$ Intensity Ratios by 6 MeV/amu Ion Bombardment", Symp. at the Soc. for Atomic Collision Research, Tokyo, July (1980).
- 13) T. Tonuma, Y. Awaya, T. Kambara, H. Kumagai, M. Kase, A. Yagishita, and I. Kohno: "Krypton $\text{K}\beta/\text{K}\alpha$ X-Ray Intensity Ratio by Impact of 6 MeV/amu He, N, and Ne Ion Bombardment", Intern. Conf. on X-Ray Processes and Inner-Shell Ionization, Glasgow, Aug. (1980).
- 14) M. Uda, K. Maeda, H. Endo, Y. Sasa, and M. Kobayashi: "Chemical Effect on Ion-Induced L X-Ray Spectra of Transition Elements", Intern. Conf. on X-Ray Processes and Inner-Shell Ionization, Glasgow, Aug. (1980).
- 15) N. Shiotani and T. Mizoguchi: "Positron State in Amorphous $\text{Mg}_{70}\text{Zn}_{30}$ ", Ann. Meeting of Phys. Soc. Japan, Fukui, Oct. (1980).

- 16) T. Okada, H. Sekizawa, F. Ambe, and S. Ambe: "Mössbauer Study of ^{119}Sb in Cr_2O_3 ", Autumn Divisional Meeting of Phys. Soc. Japan, Fukui, Oct. (1980).
 - 17) T. Kambara, Y. Awaya, A. Hitachi, M. Kase, I. Kohno, and T. Tonuma: "X-Rays from Collision of 110 MeV Ne Ions with Gas Targets", Autumn Divisional Meeting of Phys. Soc. Japan, Fukui, Oct. (1980).
 - 18) N. Yamamoto, N. Kainuma, H. Shiraishi, H. Yoshida, H. Kamitsubo, I. Kohno, and T. Shikata: "Aging Behaviour of Helium-Injected Precipitation-Strengthened Fe-Ni-Cr Alloys", Autumn Divisional Meeting of the Japan Institute of Metals, Fukuoka Oct. (1980).
 - 19) H. Shiraishi, H. Shinno, N. Yamamoto, H. Yoshida, H. Kamitsubo, I. Kohno, and T. Shikata: "Change of Embrittlement Response Due to Composition Modification and Pre-injection Treatments in Helium-Injected Fe-Ni-Cr Alloys", Japan-US Seminar (E-10) on Materials – Results of Irradiation Work and Exploration of Ferritic Status, Tokai-mura, Oct. (1980).
 - 20) Y. Awaya, K. Ando, T. Tonuma, A. Yagishita, A. Hitachi, and H. Kumagai: "Atomic-Collision Equipments of the Cyclotron and the Linear Accelerator of IPCR", Symp. of Atomic Collisions by Using Accelerators, Wako, Dec. (1980).
 - 21) T. Kambara, M. Kase, A. Hitachi, I. Kohno, T. Tonuma, and Y. Awaya: "X-Rays Following Collisions of 110 MeV Ne Ions with Gaseous Targets", Symp. of Atomic Collisions by Using Accelerators, Wako, Dec. (1980).
4. Radiochemistry, radiation chemistry and radiation biology
- 1) T. Takahashi: "Analysis of Survival Curves and Track Structure of High LET Particles", Symp. on the Theor. Aspects of Survival Curves, Kumatori, Jan. (1980).
 - 2) T. Nozaki and M. Iwamoto: "Some Fundamental Data Concerning the Formation of Low Z Radionuclides", 3rd Intern Symp. Radiopharm. Chem., St. Louis, June (1980).
 - 3) T. Nozaki, Y. Itoh, and A. Yusa: "Oxygen Depth Profile in Silicon and Its Change in Heat Treatment Measured by Charged Particle Activation Analysis", Discussion Meeting on Radiochem., Hirosaki, Oct. (1980).
 - 4) T. Nozaki and M. Iwamoto: "Recoil Range of ^{18}F Formed by Various Reactions", Discussion Meeting on Radiochem., Hirosaki, Oct. (1980).
 - 5) F. Ambe, S. Ambe, T. Okada, and H. Sekizawa: " ^{119}Sn -Mössbauer Emission Spectra of ^{119}Sb Adsorbed on Magnetic Oxides Surface", Discussion Meeting on Radiochem., Hirosaki, Oct. (1980).
 - 6) Y. Itoh, T. Nozaki, and A. Yusa: "Measuring the Change of Oxygen Depth Profile in Silicon by Applying Heat Treatment", 41th Ann. Meeting of Japan Soc. Appl. Phys., Nagoya, Oct. (1980).
 - 7) T. Takahashi, F. Yatagai, and A. Matsuyama: "Application of Katz's Theory to the Analysis of Inactivation of Bacterial Cells – Possible Long Range Effect of Heavy Ions", 41th Ann. Meeting of Japan Soc. Appl. Phys., Nagoya, Oct. (1980).
 - 8) I. Kaneko, T. Ohno, K. Suzuki, T. Taira, K. Nakano, and F. Yatagai: "Effects of Nitrogen-Ion Beam Accelerated with IPCR Cyclotron on Human Diploid Fibroblast", 23rd Ann. Meeting of Japan Radiat. Res. Soc., Nagasaki, Oct. (1980).

5. Heavy ion linear accelerator

- 1) M. Kase, Y. Miyazawa, M. Hemmi, M. Yanokura, and M. Odera: "Initial Performance of the Heavy Ion Source for the Riken Linac, RILAC", 4th Symp. on Ion Sources and Ion Application Technology, Tokyo, June (1980).
- 2) M. Kase, I. Yokoyama, M. Hemmi, M. Yanokura, J. Schimizu, and M. Odera: "Beam Diagnostic Probes of the RILAC", 3rd Symp. on Accelerator Science and Technology, Osaka, Aug. (1980).
- 3) M. Yanokura, I. Yokoyama, M. Hemmi, I. Takeshita, and M. Odera: "Beam Buncher and Chopper of the Riken Variable Frequency Linac, RILAC", 3rd Symp. on Accelerator Science and Technology, Osaka, Aug. (1980).
- 4) T. Kambara, M. Odera, and S. Takeda: "Control System of Riken Linac", 3rd Symp. on Accelerator Science and Technology, Osaka, Aug. (1980).
- 5) M. Hemmi, Y. Miyazawa, M. Kase, T. Inoue, and M. Odera: "Injector Terminal of the RILAC", 3rd Symp. on Accelerator Science and Technology, Osaka, Aug. (1980).
- 6) M. Odera: "Riken Variable Frequency Linac, RILAC", 3rd Symp. on Accelerator Science and Technology, Osaka, Aug. (1980).
- 7) M. Odera: "Status of Riken Variable Frequency Heavy Ion Linac, RILAC", 5th Linac Technology Conf., Tsukuba, Aug. (1980).
- 8) M. Odera: "Heavy Ion Linacs in Japan", Japan-China Accelerator Science and Technology Symp., Atami, Sept. (1980).
- 9) M. Odera: "On the Accelerators for Research of Materials for Fission and Fusion Reactors", Material Research Accelerator Work Shop at Ooarai Research Facility of Tohoku Univ., Metal Laboratory, Ibaragi, Nov. (1980).

13. LIST OF OUTSIDE USERS AND THEIR THEMES

(Jan. – Dec. 1980)

- | | |
|--|---|
| 1) M. Shimada
“Cyclotron Irradiation for Study of
Fast Breeder Reactor Material Embrittlement” | Toshiba R & D Center |
| 2) A. Hishinuma and T. Furuta
“Helium Implantation Effect on Creep
Repture Properties of Modified 316 Stainless
Steel for Fast Reactor Material” | Japan Atomic Energy Research Inst. |
| 3) K. Suganuma and S. Yajima*
“Development of Ferritic Stainless Steel for
Atomic Reactor” | Research Inst. for Iron, Steel and Other
Metals, Tohoku Univ.
*Irradiation Research Lab., in JMTR |
| 4) M. Harada and H. Matsutani*
“Study of Effect by Bombarding High Energy
Proton on a Solar Cell” | Japan Trust Center for Electronic Parts
*Electronic Parts Div., Sharp Co., Ltd. |
| 5) H. Nakahara, H. Kudo, and K. Muramatsu
“Production of ^{112}Pd , ^{115}Cd , $^{119\text{m}}\text{Sn}$, and
^{196}Au ” | Faculty of Science, Tokyo Metropolitan
Univ. |
| 6) Y. Homma
“Production of ^{52}Mn ” | Kyoritsu College of Pharmacy |
| 7) K. Yuita
“Production of ^{77}Br ” | National Inst. of Agricultural Sciences |
| 8) H. Emori
“Radiochemical Analysis of ^{16}O in Ga AS” | Mitsubishi Metal Co., Ltd. |
| 9) T. Watanabe
“Production of ^{18}F ” | Mitsubishi Aluminum Co., Ltd. |

- 10) M. Watanabe
“Radiochemical Analysis of ^{14}N in Si
Crystal”
Toshiba R & D Center
- 11) T. Abe
“Radiochemical Analysis of ^{14}N in Si
Crystal”
Shinetsu Semiconductor Co., Ltd.

14. LIST OF SEMINARS

(Apr. – Dec. 1980)

- 1) S. Kosugi, Tokyo Institute of Technology (Tokyo), 15 April
“The Study of the Imaginary Part of the Optical Potential”
- 2) T. Udagawa, Univ. Texas (USA), 12 May
“Break-up Processes in Heavy-Ion Collisions”
- 3) D. Youngblood, Texas A & M Univ. (USA), 20 May
“E0 Giant Resonances”
- 4) M.N. Harakeh, KVI Gröningen (Netherlands), 27 May
“Giant Resonances of s, d-Shell Nuclei”
- 5) H. Taketani, Tokyo Institute of Technology (Tokyo), 9 July
“The Study of the Fine Structures of Analogue Resonances Excited by (p, d) Reactions”
- 6) M. Koike, INS (Tokyo), 22 July
“ π -on Production in Nuclear Collision”
- 7) K. Shimizu, Univ. Tübingen (BRD), 22 July
“ π -on Absorption and Two Nucleon Correlation”
- 8) S. Nagamiya, LBL (USA), 25 July
“Recent Topics on Relativistic Heavy-Ion Collisions”
- 9) R.C. Tribble, Texas A & M Univ. (USA), 28 July
“Mass Measurements of Nuclei Far from Stability and Exotic Spectroscopy”
- 10) H. Yoshida, Tokyo Institute of Technology (Tokyo), 10 September
“Contribution of Excitations of the Emitted Particles to the Nucleon Transfer in Heavy-Ion Reactions”
- 11) H. Yamada, Vanderbilt Univ. (USA), 18 September
“Massive Transfer Reaction and the Applications to Studies of High Spin States”
- 12) S. Fukumoto, KEK (Tsukuba), 22 September
“Applications of Accelerators”
- 13) P. Grand, BNL (USA), 9 October
“Applications of Accelerators to Energy Problems”

- 14) H. Tawara, Kyushu Univ. (Fukuoka), 14 October
“Collision Phenomena of Highly Ionized High Energy Heavy-Ions and Its Applications”
- 15) R.A. Jameson, LASL (USA), 17 October
“Accelerator Developments in LASL”
- 16) K. Ogawa, INS (Tokyo), 22 October
“Predicted High Spin Isomers in the $A = 95 - 100$ Nuclei”
- 17) P. Radvanyi, LNS (France), 28 October
“On Saturn II”
- 18) M. Muraoka, INS (Tokyo), 18 November
“Mechanism of High Energy Heavy-Ion Collision and Energy Spectra of Low Energy Pion”
- 19) H. Adachi and K. Taniguchi, Osaka Electro-Communication Univ. (Osaka), 25 November
“Analyses of X-Ray Spectra Using the DV X_{α} -Methods”
- 20) M. Ichimura, Univ. of Tokyo (Tokyo), 26 November
“Alpha Spectra from the $^{12}\text{C}(^{16}\text{O}, \alpha)$ Reaction”
- 21) S. Hanashima, JAERI (Tokai), 1 December
“Computer Control System of Tandem Van de Graaff at JAERI”
- 22) K. Yagi, Univ. of Tsukuba (Tsukuba), 3 December
“Studies of Nuclear Reaction Mechanism Using the Polarized Beam”
- 23) H. Sasaki, KEK (Tsukuba), 9 December
“Applications of 500 MeV Proton Beam from the Booster at KEK”
- 24) G. Igo, UCLA (USA), 22 December
“Third Observable in Polarized Proton Scattering on ^{40}Ca at 500 MeV”
- 25) I. Hamamoto, Nordita (Copenhagen), 25 December
“Properties of Rotating Nuclei and the Role of High - J Shell”

15. LIST OF PERSONNEL

Members of the Board

DOE Toshihiko 土手敏彦 (Chairman)	HAMADA Tatsuji 浜田達二
KAMITSUBO Hiromichi 上坪宏道	KOHNO Isao 河野功
NOZAKI Tadashi 野崎正	ODERA Masatoshi 小寺正俊

Users Committee

HAMADA Tatsuji 浜田達二 (Chairman)	IMAMURA Masashi 今村昌
KAMITSUBO Hiromichi 上坪宏道	KOHNO Isao 河野功
MORI Kazuo 森一夫	NOZAKI Tadashi 野崎正
ODERA Masatoshi 小寺正俊	SAKAIRI Hideo 坂入英雄
SEKIZAWA Hisashi 関沢尚	

Operation and Machine Maintenance Group

FUJITA Shin 藤田新	IKEGAMI Kumio 池上九三男
KAGEYAMA Tadashi 影山正	KOHARA Shigeo 小原重夫
KOHNO Isao 河野功	OGIWARA Kiyoshi 荻原清
TAKEBE Hideki 武部英樹	

Scientific and Engineering Personnel

Cyclotron Laboratory

FUJISAWA Takashi 藤沢高志	FUJITA Jiro 藤田二郎
GOTO Akira 後藤彰	HARA Masahiro 原雅弘
ICHIMURA Atsushi 市村淳	IKEGAMI Yuji 池上祐司
INAMURA Takashi 稲村卓	ISHIHARA Masayasu 石原正泰
KAMITSUBO Hiromichi 上坪宏道	KARASAWA Takashi 唐沢孝
KISHIDA Norio 岸田則生	KOHMOTO Susumu 河本進
KOHNO Isao 河野功	MOTONAGA Shoshichi 元永昭七
NAKAJIMA Shunji 中島諄二	NAKANISHI Noriyoshi 中西紀喜
NOMURA Toru 野村亨	SHIKATA Takashi 四方隆史
WADA Takeshi 和田雄	YAMAJI Shuhei 山路修平
YANO Yasushige 矢野安重	

(Visitors)

HAYAKAWA Shunichiro 早川俊一郎 (Dept. Phys., Waseda Univ.)
 HIRUTA Kotaro 蛭田幸太郎 (Dept. Phys., Tokyo Gakugei Univ.)
 ICHIMURA Munetake 市村宗武 (Inst. Phys., College General Education, Univ. of Tokyo)
 KAMMURI Tetsuo 冠哲夫 (Dept. Phys., Osaka Univ.)
 NAKAHARA Hiromichi 中原弘道 (Dept. Chem., Tokyo Metropolitan Univ.)
 OHNUMA Hajime 大沼甫 (Dept. Phys., Tokyo Inst. Technol.)

SATO Kenichi 佐藤憲一 (Dept. Phys., Tohoku College of Pharmacy)
 SHIRAISHI Haruki 白石春樹 (Nat. Res. Inst. for Metals)
 TAKEMASA Tadashi 武政尹士 (Dept. Phys., Saga Univ.)
 YOSHIDA Shiro 吉田思郎 (Dept. Phys., Tohoku Univ.)

(Students)

HOSOYAMA Michio 細山三千男 (Facul. Sci. and Eng., Chuo Univ.)
 IEKI Kazuo 家城和夫 (Dept. Phys., Kyoto Univ.)
 NAGAME Yuichiro 永目諭一郎 (Dept. Chem., Tokyo Metropolitan Univ.)
 OBANA Yoshiki 小花芳樹
 SUGITATE Toru 杉立徹 (Dept. Phys., Tokyo Inst. Technol.)
 UTSUNOMIYA Hiroaki 宇都宮弘章 (Dept. Phys., Kyoto Univ.)

Linac Laboratory

CHIBA Yoshiaki 千葉好明	CHIBA Toshiya 千葉利哉
GONO Yasuyuki 郷農靖之	HEMMI Masatake 逸見政武
IKEZAWA Eiji 池沢英二	INOUE Toshihiko 井上敏彦
KAMBARA Tadashi 神原正	KASE Masayuki 加瀬昌之
KUBO Toshiyuki 久保敏幸	MIYAZAWA Yoshitoshi 宮沢佳敏
ODERA Masatoshi 小寺正俊	SASAGASE Masaji 笹ヶ瀬正二
TONUMA Tadao 戸沼正雄	YAGISHITA Akira 柳下明
YANOKURA Minoru 矢野倉実	YOKOYAMA Ichiro 横山一郎

(Visitors)

DOKE Tadayoshi 道家忠義 (Sci. and Eng. Res. Lab., Waseda Univ.)
 EJIRI Hiroyasu 江尻宏泰 (Dept. Phys., Osaka Univ.)
 FUKUZAWA Fumio 福沢文雄 (Dept. Nucl. Eng., Kyoto Univ.)
 HARADA Kichinosuke 原田吉之助 (Japan Atomic Energy Res. Inst.)
 HAYASHIBE Shogo 林部昭吾 (Dept. Phys., Tohoku Univ.)
 HISATAKE Kazuo 久武和夫 (Tokyo Inst. Technol.)
 ISHII Keishi 石井慶之 (Dept. Nucl. Eng., Kyoto Univ.)
 ITO Noriaki 伊藤慶昭 (Dept. Crystalline Materials, Nagoya Univ.)
 KAWAI Nanao 河合七雄 (Osaka Univ.)
 MASUDA Kozo 升田公三 (Tsukuba Univ.)
 MATSUI Masao 松井正夫 (Nagaoka Sci. and Tech. Univ.)
 MORITA Susumu 森田右 (Dept. Phys., Tohoku Univ.)
 OHNO Shinichi 大野新一 (Japan Atomic Energy Res. Inst.)
 OZAWA Kunio 小沢国夫 (Japan Atomic Energy Res. Inst.)
 SAKISAKA Masakatsu 向坂正勝 (Dept. Nucl. Eng., Kyoto Univ.)
 TAKEDA Shigeru 竹田繁 (Nat. Lab. High Energy Phys.)
 TAWARA Hiroyuki 俵博之 (Dept. Nucl. Eng., Kyushu Univ.)
 TSURUBUCHI Seiji 鶴淵誠二 (Dept. Eng., Tokyo Univ. Agric. Tech.)
 YOSHIZAWA Yasukazu 吉沢康和 (Dept. Phys., Hiroshima Univ.)

(Studnet)

NAKAMURA Tomohisa 中村友久 (Dept. Facul. Sci. and Technol., Sophia Univ.)

Radiation Laboratory

AWAYA Yohko 粟屋容子
 HASHIZUME Akira 橋爪朗
 IZUMO Koichi 出雲光一
 KONNO Satoshi 金野智
 OKANO Masaharu 岡野真治
 TENDOW Yoshihiko 天道芳彦

HAMADA Tatsuji 浜田達三
 HITACHI Akira 月出章
 KATOU Takeo 加藤武雄
 KUMAGAI Hidekazu 熊谷秀和
 TAKAHASHI Tan 高橋 昇

(Visitors)

DOKE Tadayoshi 道家忠義 (Sci. and Eng. Res. Lab., Waseda Univ.)
 FUJIOKA Manabu 藤岡学 (Dept. Phys., Tohoku Univ.)
 HAYASHIBE Shogo 林部昭吾 (Dept. Phys., Tohoku Univ.)
 ISHII Keizo 石井慶造 (Cyclotron, Tohoku Univ.)
 MORITA Susumu 森田右 (Dept. Phys., Tohoku Univ.)
 NAGAHARA Teruaki 永原照明 (Inst. Atomic Energy, Rikkyo Univ.)
 TAWARA Hiroyuki 俵博之 (Dept. Nucl. Eng., Kyushu Univ.)
 WATANABE Tsutomu 渡部力 (Dept. Eng., Univ. of Tokyo)

Thermonuclear Fusion Laboratory

ANDO Kozo 安藤剛三

MORI Kazuo 森 一夫

Metal Physics Laboratory

KOYAMA Akio 小山昭雄
 YAGI Eiichi 八木栄一

SHIOTANI Nobuhiro 塩谷巨弘

Magnetic Materials Laboratory

ASAI Kichizo 浅井吉藏
 SAKAI Nobuhiko 坂井信彦

OKADA Takuya 岡出卓也
 SEKIZAWA Hisashi 関沢 尚

(Visitor)

MIZOGUCHI Tadashi 溝口 正 (Dept. Phys., Gakushuin Univ.)

Solid State Chemistry Laboratory

ENDO Hiroshi 遠藤 寛
 KOBAYASHI Masayoshi 小林雅義
 SASA Yoshihiko 佐々嘉彦

FUWA Koh 不破 耕
 MAEDA Kuniko 前田邦子
 UDA Masayuki 宇田 応之

Radiochemistry Laboratory

AMBE Fumitoshi 安部文敏
 ARATANI Michi 荒谷美智
 IWAMOTO Masako 岩本正子
 TERAJ Yoshiro 寺井善郎

AMBE Shizuko 安部静子
 ITO Yoshiko 伊東芳子
 NOZAKI Tadashi 野崎 正

(Visitors)

HIRAIWA Atsushi 平岩篤 (Central Lab., Hitachi Ltd.)

MUKAI Kiichiro 向喜一郎 (Central Lab., Hitachi Ltd.)

TAKI Ko 滝幸 (Dept. Hygen., Kitazato Univ.)

TOYODA Minoru 豊田稔 (Central Res. Lab., Mitsubishi Chemical Ind.)

TSUKAZAKI Toshimasa 塚崎敏正 (Central Res. Lab., Mitsubishi Chemical Ind.)

USAMI Katsuhisa 宇佐美勝久 (Hitachi Res. Lab., Hitachi Ltd.)

YAJIMA Fumikazu 矢島文和 (Central Res. Lab., Mitsubishi Chemical Ind.)

Radiation Chemistry Laboratory

IMAMURA Masashi 今村昌

KIMURA Kazuie 木村一宇

Radiobiology Laboratory

HATTORI Yukihiko 服部行彦

KANEKO Ichiro 金子一郎

KITAYAMA Shigeru 北山滋

NAKANO Kazushiro 中野和城

YATAGAI Fumio 谷田貝文夫

(Visitors)

ONHO Tadao 大野忠夫 (National Inst. Radiological Sciences)

Safety Control Affairs Office

IGARASHI Kazui 五十嵐一茂

KOYAMA Masashi 小山政史

SAKAMOTO Ichiro 坂本一郎

USUBA Isao 薄葉勲

Beam Analysis Center

IWAKI Masaya 岩木正哉

SAKAIRI Hideo 坂入英雄

AUTHOR INDEX

- ADACHI Shizuko 安達静子 61
- AMBE Fumitoshi 安部文敏 86, 96, 98, 154
- AMBE Shizuko 安部静子 86, 96, 98
- ANDO Kozo 安藤剛三 149
- AWAYA Yohko 粟屋容子 67, 70, 72, 77, 88
- CHIBA Yoshiaki 千葉好明 117, 120, 123
- FUJISAWA Takashi 藤沢高志 13, 182, 185, 187
- FUJITA Jiro 藤田二郎 164, 173, 176, 179
- FUJITA Shin 藤田新 2, 104, 203
- GONO Yasuyuki 郷農靖之 16, 19, 22, 28, 31, 64, 141
- GOTO Akira 後藤彰 167, 170, 173, 189
- HAGIWARA Kohji 萩原弘二 9
- HAMADA Tatsuji 浜田達二 67
- HARA Masahiro 原雅弘 151, 182, 185, 187
- HARADA Kichinosuke 原田吉之助 44, 47
- HASEGAWA Takeo 長谷川武夫 13
- HASHIZUME Akira 橋爪朗 59, 67, 77
- HATTORI Yukihiro 服部行彦 101
- HEMMI Masatake 逸見政武 115, 126, 129, 135
- HITACHI Akira 月出彰 67, 77, 88
- IEKI Kazuo 家城和夫 16, 19, 22, 25, 28, 31, 64
- IGARASHI Kazui 五十嵐一茂 104
- IIDA Shigenori 飯田重規 11
- IKEGAMI Kumio 池上九三男 2, 4, 195, 198
- IKEGAMI Yuji 池上祐司 164, 198
- INOUE Toshihiko 井上敏彦 135
- ISHIHARA Masayasu 石原正泰 16, 19, 22, 25, 28, 31, 64
- ITOH Yoshiko 伊東芳子 94
- IWAKI Masaya 岩木正哉 154
- IWAMOTO Akira 岩本昭 44, 47
- IWAMOTO Masako 岩本正子 93
- IZUMO Koichi 出雲光一 67, 72, 77
- KAGEYAMA Tadashi 影山正 2, 4
- KAMBARA Tadashi 神原正 72, 88, 110, 138
- KAMITSUBO Hiromichi 上坪宏道 16, 79, 162
- KAMMURI Tetsuo 冠哲夫 50
- KANEKO Ichiro 金子一郎 102
- KARASAWA Takashi 唐沢孝 11
- KASE Masayuki 加瀬昌之 72, 88, 115, 117, 132, 138
- KATOU Takeo 加藤武雄 59, 67, 70
- KISHIDA Norio 岸田則夫 13, 167, 192, 201
- KITAYAMA Shigeru 北山滋 148
- KOHARA Shigeo 小原重夫 2, 9
- KOHMOTO Susumu 河本進 16, 19, 22, 25, 28, 31, 64
- KOHNO Isao 河野功 2, 4, 34, 37, 40, 72, 79, 88, 141
- KOYAMA Akio 小山昭夫 82, 146

- KOYAMA Masashi 小山政史 104
- KUBO Toshiyuki 久保敏幸 13, 123
- KUDO Hisaaki 工藤久昭 34, 37, 40
- KUMAGAI Hidekazu 熊谷秀和 59, 67, 72, 77, 156
- MAEDA Kuniko 前田邦子 74
- MATSUOKA Kazuo 松岡和夫 50
- MINAKUCHI Tadayoshi 水口忠良 201
- MIYAZAWA Yoshitoshi 宮沢佳敏 126, 129, 132, 135
- MIZOGUCHI Tadashi 溝口正 84
- MORI Kazuo 森一夫 149, 151
- MOTONAGA Shoshichi 元永昭七 164, 173, 176
- NAGAME Yuichiro 永目諭一郎 34, 37, 40
- NAGAO Akihiro 長尾明博 13
- NAKAHARA Hiromichi 中原弘道 34, 37, 40
- NAKAJIMA Shunji 中島諄二 195, 198
- NAKAMURA Tomohisa 中村友久 143
- NAKANISHI Noriyoshi 中西紀喜 167, 170, 189
- NAKANO Kazushiro 中野和城 102
- NISHIDA Masami 西田雅美 67, 77
- NOMIYA Yoshio 野宮芳雄 9
- NOMURA Toru 野村亨 16, 19, 22, 25, 28, 31, 64
- NOZAKI Tadashi 野崎正 11, 91, 93, 94
- OBANA Yoshiki 小花芳樹 164, 173, 176
- ODERA Masatoshi 小寺正俊 108, 110, 113, 126, 138
- OGIWARA Kiyoshi 荻原清 2, 6, 182, 185, 187
- OHNO Tadao 大野忠夫 102
- OKADA Takuya 岡田卓也 84, 86
- SAITO Motozou 齋藤始三 138
- SAKAI Nobuhiko 坂井信彦 84
- SAKAIRI Hideo 坂入英雄 82
- SAKAMOTO Ichiro 坂本一郎 104, 106
- SANO Mitsuo 佐野光男 53
- SASAGASE Masaji 笹ヶ瀬正二 159
- SATO Kenichi 佐藤憲一 56
- SEKIGUCHI Masayuki 関口雅行 13
- SEKIZAWA Hisashi 関沢尚 84, 86
- SHIKATA Takashi 四方隆史 79, 82, 146, 203
- SHINNO Hitoshi 新野仁 79
- SHIOTANI Nobuhiro 塩谷亘弘 84
- SHIRAISHI Haruki 白石春樹 79
- SUGITATE Toru 杉立徹 16, 19, 22, 25, 28, 31, 64
- TAKAHASHI Tan 高橋丹 77
- TAKEBE Hideki 武部英樹 2, 6, 164, 173, 176, 179
- TAKEDA Shigeru 竹田繁 110
- TAKEMASA Tadashi 武政尹士 53
- TAKESHITA Isao 竹下勇夫 9, 70, 141
- TAKIGAWA Noboru 滝川昇 56
- TENDOW Yoshihiko 天道芳彦 59, 67, 70

- TERAJ Yoshiro 寺井善郎 91
 TONUMA Tadao 戸沼正雄 67, 72, 77, 88, 117
 TOYOTA Eijiro 豊田英二郎 201
 UDA Masayuki 宇田応之 74
 UEDA Nozomu 上田望 13
 USAMI Katsuhisa 宇佐美勝久 93
 USUBA Isao 薄葉勲 104
 UTSUNOMIYA Hiroaki 宇都宮弘章 16, 19, 22, 25, 28, 31, 64
 WADA Takeshi 和田雄 156, 164, 167, 170, 173, 176, 179, 189, 192
 WAKUTA Yoshihisa 和久田義久 13
 WATANABE Michito 渡辺道人 37
 YAGISHITA Akira 柳下明 67, 72, 143
 YAMADA Yutaka 山田豊 6
 YAMAJI Shuhei 山路修平 44, 47, 203
 YAMAMOTO Norikazu 山本徳和 79
 YANO Yasushige 矢野安重 167, 170, 173, 176, 189, 192
 YANOKURA Minoru 矢野倉実 34, 37, 40, 113, 117, 141
 YASUE Masaharu 安江正治 13
 YASUMITSU Naoki 安光直樹 201
 YATAGAI Fumio 谷田貝文夫 101, 102, 148
 YOKOYAMA Ichiro 横山一郎 115, 138
 YORO Kenji 養老憲二 53
 YOSHIDA Heitaro 吉田平太郎 79
 YOSHIDA Shiro 吉田思郎 44, 47, 56, 61

IPCR Cyclotron Progress Report

理化学研究所サイクロトン年次報告 第14巻 (1980)

印刷 昭和56年(1981)3月25日

発行 昭和56年(1981)3月31日

発行者 理化学研究所

代表者 宮 島 龍 興

〒351 埼玉県和光市広沢2番1号

電話(0484)62-1111

編集者 理化学研究所加速器運営委員会

印刷所 丸 星 印 刷 株 式 会 社

〒130 東京都墨田区亀沢1丁目3番3号

定価 4,000円

理化学研究所

埼玉県 和光市 広沢